NASA CR-66907





FAIRCHILD HILLER
REPUBLIC AVIATION DIVISION
FARMINGDALE, LONG ISLAND, NEW YORK

# Investigation of the Aerodynamic Characteristics and Wing-Deployment Transients of the NASA DL-4 Body With a Sailwing Landing Aid

Final Report

FHR 3907 January 30, 1970

FAIRCHILD HILLER
Republic Aviation Division
Farmingdale, Long Island, New York 11735

Prepared under Contract NASI-9099
for
The National Aeronautics and Space Administration
Langley Research Center
Hampton, Virginia 23365

# Investigation of the Aerodynamic Characteristics and Wing-Deployment Transients of the NASA DL-4 Body With a Sailwing Landing Aid

Final Report

FHR 3907 January 30, 1970

## FOREWORD

This report was prepared by the Republic Aviation Division of Fairchild Hiller Corporation for the NASA-Langley Research Center in accordance with Contract NAS 1-9099. The work reported herein was conducted under the technical cognizance of Mr. George Ashby, project engineer for NASA.

The contract effort was conducted under the management of Dr. Robert J. Sanator of Fairchild Hiller. A major subcontracting effort was supplied by Princeton University under the direction of Professor Thomas Sweeney.

The principal investigators were Messrs. Domenick T. Torrillo of Fairchild Hiller, and Jeff Bohn and Albert Jobst of Princeton University.

Acknowledgement is extended to the staff of the NASA-Langley 7 x 10 - 300 mph wind tunnel, under the direction of Mr. Dudley Hammond, for their cooperation and support.

The contributions of Messrs. Eli Grossman, Jean McComas,and George Mead of Fairchild Hiller are gratefully acknowledged.

## SUMMARY

The results are presented of an investigation of the aerodynamic characteristics and wing deployment transients of the NASA DL-4 body fitted with a sailwing landing aid having an aspect ratio of 3.27. Longitudinal and lateral-directional static stability and control characteristics for the body alone and for the sailwing-body combination were determined by tests in the NASA-Langley 7 x 10 foot 300 mph wind tunnel. Tests were also made to determine the buildup of aerodynamic and structural forces during deployment of the wing at different dynamic pressures and deployment rates. A design study was conducted to evaluate the relative merits of two different sized sailwings versus their rigid wing counterparts as landing aids on a scaled-up DL-4 body. The vehicle size and weight were established by satisfying design requirements representative of current space shuttle system guidelines.

The test results show that the sailwing significantly improves the lift-to-drag ratio of the DL-4 body, and that adequate lateral control is afforded by the wing-warp technique. The sailwing was found to add to both the directional stability and to the effective dihedral parameter of the body. For the size sailwing tested the body elevons would have to be increased in size to provide trim capability over the whole angle of attack range tested. For a downsized sailwing, however, which would still greatly augment the aerodynamic performance of the DL-4 body, the elevons tested would be adequate. The deployment tests demonstrated the feasibility of sailwing deployment at dynamic pressures of up to 60 psf at realistic deployment rates without difficulty.

The results of the design study indicate that a downsized sailwing, which would provide a landing speed of 134 knots, would weigh less than an equivalent rigid wing. This weight advantage of the sailwing could be increased by optimizing the cantilever type structural design of the sailwing.

Scaling factors are also presented for use in applying sailwing test data to full scale configurations.

CONTENTS


| Section | | Page |
|---|---|---|
| 1 | INTRODUCTION | 1 |
| 2 | SYMBOLS | 3 |
| 3 | MODEL AND TESTS | |
| | A. Model Description | 7 |
| | B. Test Conditions | 9 |
| 4 | BODY-ALONE CHARACTERISTICS | |
| | A. Longitudinal | 18 |
| | B. Lateral - Directional | 20 |
| 5 | WING-BODY CHARACTERISTICS | |
| | A. Longitudinal | 44 |
| | B. Lateral - Directional | 47 |
| | C. Cable Tension and Hinge Moment | 50 |
| 6 | DEPLOYMENT CHARACTERISTICS | 101 |
| 7 | BODY-ALONE AND WING-BODY LIFT-CURVE SLOPES COMPARISON | 121 |
| 8 | SAILWING VS. RIGID WING TRADE STUDY | |
| | A. Vehicle Sizing Guidelines | 124 |
| | B. Configuration Studies | 128 |
| | C. Loads | 135 |
| | D. Weight Analyses | 137 |
| 9 | CONCLUSIONS | 150 |
| 10 | REFERENCES | 153 |
| | APPENDIX | 154 |

LIST OF FIGURES


| Figure | | Page |
|---|---|---|
| 2-1 | System of axes and positive sense of angles, forces and moments. | 6 |
| 3-1 | Sketch of model of NASA DL-4 body with sailwing. | |
| | (a) Complete Configuration | 11 |
| | (b) DL-4 basic body design | 12 |
| | (c) Typical cross-section of wing | 13 |
| 3-2 | DL-4 model, showing internal arrangement. | 14 |
| 3-3 | Deployment system schematic. | 15 |
| 3-4 | Photograph of model installed in wind tunnel. | |
| | (a) Body alone | 16 |
| | (b) Body with sailwing deployed | 17 |
| 4-1 | Body-alone longitudinal aerodynamic characteristics for several dynamic pressures. | |
| | (a) Variation with angle of attack | 22 |
| | (b) Drag polar | 23 |
| | (c) Lift-drag ratio | 24 |
| 4-2 | Experimental and predicted body-alone lift curves. | 25 |
| 4-3 | Variation of body-alone drag with $C_L^2$. | 26 |
| 4-4 | Comparison of predicted and experimental body-alone polars. | 27 |
| 4-5 | Effect of dynamic pressure and elevons on body base pressure coefficient. | 28 |
| 4-6 | Body-alone longitudinal aerodynamic characteristics for various elevon deflections. | |
| | (a) Variation with angle of attack | 29 |
| | (b) Drag polar | 30 |
| | (c) Lift-drag ratio | 31 |
| 4-7 | Body-alone lift curve with and without elevons. | 32 |
| 4-8 | Drag increment due to elevon deflection. | 33 |
| 4-9 | Pitching moment due to elevon deflection. | 34 |
| 4-10 | Effect of aft-end modifications on pitching moment. | 35 |

LIST OF FIGURES (Continued)


| Figure | | Page |
|---|---|---|
| 4-11 | Variation of body-alone side force coefficient with angle of attack for several elevon deflections. q = 60 psf. | |
| | (a) $\beta = 1°$ | 36 |
| | (b) $\beta = 6°$ | 37 |
| 4-12 | Variation of body-alone yawing moment coefficient with angle of attack for various elevon deflections. q = 60 psf. | |
| | (a) $\beta = 1°$ | 38 |
| | (b) $\beta = 6°$ | 39 |
| 4-13 | Variation of body-alone rolling moment coefficient with angle of attack for various elevon deflections. q = 60 psf. | |
| | (a) $\beta = 1°$ | 40 |
| | (b) $\beta = 6°$ | 41 |
| 4-14 | Variation of body-alone lateral - directional stability parameters with angle of attack. $\delta_{e_{L,R}} = 0°$, q = 60 psf. | 42 |
| 4-15 | Rolling moment due to elevon deflection. $\beta = 1°$. | 43 |
| 5-1 | Wing-body longitudinal aerodynamic characteristics for several dynamic pressures. To = 80 lbs. | |
| | (a) Variation with angle of attack | 52 |
| | (b) Drag polar | 53 |
| | (c) Lift-drag ratio | 54 |
| 5-2 | Wing-body longitudinal aerodynamic characteristics for several cable tensions. q = 30 psf. | |
| | (a) Variation with angle of attack | 55 |
| | (b) Drag polar | 56 |
| | (c) Lift-drag ratio | 57 |
| 5-3 | Wing-body longitudinal aerodynamic characteristics for several cable tensions. q = 60 psf. | |
| | (a) Variation with angle of attack | 58 |
| | (b) Drag polar | 59 |
| | (c) Lift-drag ratio | 60 |
| 5-4 | Drag increment due to wing-tip deflection. | 61 |

LIST OF FIGURES (Continued)


| Figure | | Page |
|---|---|---|
| 5-5 | Effect of wing-tip deflection on pitching moment coefficient. | 62 |
| 5-6 | Effect of sail elasticity on pitching moment coefficient. | 63 |
| 5-7 | Body-alone and wing-body pitching moment comparison. | |
| | (a) Nominal sailwing | 64 |
| | (b) Downsized sailwing | 65 |
| 5-8 | Effect of dynamic pressure on rolling moment coefficient, $\delta WT_R = 0°$, $\beta = 1°$. | 66 |
| 5-9 | Variation of wing-body rolling moment coefficient with angle of attack for various wingtip deflections. q = 30 psf. | |
| | (a) $\beta = 1°$ | 67 |
| | (b) $\beta = 6°$ | 68 |
| | (c) $\beta = -6°$ | 69 |
| 5-10 | Variation of wing-body rolling moment coefficient with angle of attack for various wingtip deflections. q =60 psf. | |
| | (a) $\beta = 1°$ | 70 |
| | (b) $\beta = 6°$ | 71 |
| | (c) $\beta = -6°$ | 72 |
| 5-11 | Rolling moment due to wing tip deflection. $\beta = 1°$. | |
| | (a) q = 30 psf | 73 |
| | (b) q = 60 psf | 74 |
| 5-12 | Rolling moment due to wing tip deflection. q = 60 psf. | |
| | (a) $\beta = 6°$ | 75 |
| | (b) $\beta = -6°$ | 76 |
| 5-13 | Variation of wing-body yawing moment coefficient with angle of attack for various wing tip deflections at q = 30 psf. | |
| | (a) $\beta = 1°$ | 77 |
| | (b) $\beta = 6°$ | 78 |
| | (c) $\beta = -6°$ | 79 |
| 5-14 | Variation of wing-body yawing moment coefficient with angle of attack at q = 60 psf. | |
| | (a) $\beta = 1°$ | 80 |
| | (b) $\beta = 6°$ | 81 |
| | (c) $\beta = -6°$ | 82 |

LIST OF FIGURES (Continued)


| Figure | | Page |
|---|---|---|
| 5-15 | Variation of wing-body side force coefficient with angle of attack for various wing tip deflections at q = 30 psf. | |
| | (a) $\beta = 1°$ | 83 |
| | (b) $\beta = 6°$ | 84 |
| | (c) $\beta = -6°$ | 85 |
| 5-16 | Variation of wing-body side force coefficient with angle of attack at q = 60 psf. | |
| | (a) $\beta = 1°$ | 86 |
| | (b) $\beta = 6°$ | 87 |
| | (c) $\beta = -6°$ | 88 |
| 5-17 | Variation of wing-body lateral-directional stability parameters with angle of attack. $\delta_{WT_R} = 0°$, To = 80 lbs. | 89 |
| 5-18 | Effect of dynamic pressure and angle of attack on cable tension. To = 80 lbs., $\delta_{WT_R} = 0°$. | |
| | (a) $\beta = 1°$ | 90 |
| | (b) $\beta = 6°$ | 91 |
| | (c) $\beta = -6°$ | 92 |
| 5-19 | Effect of initial tension and angle of attack on cable tension. $\delta_{WT_R} = 0°$. | |
| | (a) q = 30 psf. | 93 |
| | (b) q = 60 psf. | 94 |
| 5-20 | Effect of dynamic pressure and angle of attack on hinge moment. To = 80 lbs, $\delta_{WT_R} = 0°$. | |
| | (a) $\beta = 6°$ | 95 |
| | (b) $\beta = -6°$ | 96 |
| 5-21 | Effect of dynamic pressure and angle of attack on hinge moment. To = 80 lbs., $\delta_{WT_R} = 12.5°$ | |
| | (a) $\beta = 6°$ | 97 |
| | (b) $\beta = -6°$ | 98 |

LIST OF FIGURES (Continued)


| Figure | | Page |
|---|---|---|
| 5-22 | Effect of dynamic pressure and angle of attack on hinge moment. To = 80 lbs., $\delta_{WT_R}$ = -7°. | |
| | (a) $\beta$ = 6° | 99 |
| | (b) $\beta$ = -6° | 100 |
| 6-1 | Deployment test run 33. q = 0 psf, fast deployment rate. | 110 |
| 6-2 | Deployment test run 34. q = 15 psf, $\alpha$ = 0°, fast rate. | 111 |
| 6-3 | Deployment test run 36. q = 15 psf, $\alpha$ = 5°, fast rate. | 112 |
| 6-4 | Deployment test run 37. q = 15 psf, $\alpha$ = 10°, fast rate. | 113 |
| 6-5 | Deployment test run 38. q = 15 psf, $\alpha$ = -5°, fast rate. | 114 |
| 6-6 | Deployment test run 42. q = 15 psf, $\alpha$ = 0°, slow rate. | 115 |
| 6-7 | Deployment test run 43. q = 15 psf, $\alpha$ = 10°, slow rate. | 116 |
| 6-8 | Deployment test run 45. q = 30 psf, $\alpha$ = 0°, slow rate. | 117 |
| 6-9 | Deployment test run 46. q = 30 psf, $\alpha$ = 10°, slow rate. | 118 |
| 6-10 | Deployment test run 47. q = 60 psf, $\alpha$ = 0°, slow rate. | 119 |
| 6-11 | Deployment test run 48. q = 60 psf, $\alpha$ = 10°, slow rate. | 120 |
| 7-1 | DL-4 body with various size wings. | 122 |
| 7-2 | Wing-body lift-curve slope breakdown. | 123 |
| 8-1 | 170-foot Vehicle with nominal size and downsized sailwings. | 144 |
| 8-2 | 170-foot Vehicle with nominal size and downsized rigid wings. | 145 |
| 8-3 | Lift curves of nominal sailwing and rigid wing. | 146 |
| 8-4 | Lift curves of downsized sailwing and rigid wing. | 147 |
| 8-5 | Typical section through leading edge box. | 148 |
| 8-6 | Sailwing structural loads schematic. | 149 |

# SECTION I
# INTRODUCTION

The use of deployable wings as landing aids appears to be appropriate for many of the lifting re-entry body applications currently being considered. The selection of a particular landing aid for any given application will result from overall system trade studies. These studies must carefully weigh data relative to reliability, landing performance improvement, and impact of the landing aid on overall spacecraft weight and volume, or payload degradation if gross weight is a system constraint.

References 1 and 2 present some important results for a potentially attractive landing aid candidate, the semi-rigid sailwing, devised at Princeton University. This type of wing uses a single spar as the wing leading-edge and main load carrying member, a rib at each tip, a wire trailing edge, and a fabric envelope to form the wing surface. In the studies reported in Reference 1, small-scale models of a lifting body fitted with a deployable sailwing were tested at low dynamic pressures (3 psf for transient wing deployment and 15 psf for steady-state aerodynamic characteristics). These studies revealed no significant problems pertinent to deployment reliability and showed large performance gains attributable to the sailwing addition.

Because of these encouraging results the present investigation was undertaken to further examine this concept by testing a larger scale model of a more realistic sailwing and lifting body combination at higher dynamic pressures under steady-state and deployment conditions. Accordingly, a 5-feet long scaled model of the NASA DL-4 lifting body configuration, with an appropriate sailwing and deployment mechanism, was designed and built. The longitudinal and lateral-directional static stability and control characteristics for the body alone and for the sailwing-body combination were then determined by wind-tunnel tests. Tests were also made of the wing deployment at various dynamic pressures to determine the buildup of both aerodynamic and certain sailwing structural forces and moments. Test results were compared to pre-test predictions of aerodynamic characteristics.

Finally, a design study was conducted to evaluate the relative merits of two different sizes of sailwings, and their equivalent rigid wing counterparts, as landing aids on a scaled-up DL-4 lifting body. The vehicle size and weight were established by satisfying design requirements representative of current space-shuttle system concept guidelines.

## SECTION 2
## SYMBOLS

Figure 2-1 shows the axis system used in the presentation of the data, and the positive directions of the forces, moments, and angles. All values of the force and moment coefficients presented herein are based on the stability-axis system with the exception of the sideslip derivative values. These are based on the body axis system. Unless noted otherwise all force and moment coefficients are based upon body geometric parameters. To enable conversion of these coefficients to wing-based parameters values of the pertinent wing geometric parameters are also given below.

| | |
|---|---|
| A | aspect ratio of theoretical wing, 3.27 |
| b | body width, 19.5 inches; wing total span, 52.5 inches |
| $\bar{c}$ | body length, 5.0 ft; mean aerodynamic chord of wing, $\bar{c} = \frac{2}{S} \int_o^{b/2} c^2 dy$, 18.69 inches |
| $c_{p_b}$ | body base pressure coefficient $\frac{p_b - p_\infty}{q}$ |
| $C_D$ | drag coefficient, Drag/qS |
| $C_{D_o}$ | zero-lift drag coefficient |
| $C_L$ | lift coefficient, Lift/qS |
| $C_\ell$ | rolling-moment coefficient, Rolling moment/qSb |
| $C_m$ | pitching-moment coefficient, Pitching moment/qS$\bar{c}$ |
| $C_n$ | yawing-moment coefficient, Yawing moment/qSb |
| $C_Y$ | side-force coefficient, Side force/qS |
| $C_{\ell_\beta}$ | $\frac{\partial C_\ell}{\partial \beta}$, rolling-moment sideslip derivative, per deg |

| | |
|---|---|
| $C_{n_\beta}$ | $\frac{\partial C_n}{\partial \beta}$, yawing-moment sideslip derivative, per degree |
| $C_{L_\alpha}$ | $\frac{\partial C_L}{\partial \alpha}$, lift-curve slope, per degree |
| $C_T$ | cable tension coefficient, $\Delta T/qS$ |
| HM | chordwise hinge moment at root chord, in-lb |
| $\Delta$HM | increment in hinge moment due to airload |
| K | induced drag factor |
| $\ell$ | body length, 5.0 ft |
| pb/2V | roll-rate parameter |
| p | static pressure, $lb/ft^2$, or rolling velocity rads/sec |
| q | free-stream dynamic pressure, $\rho \frac{V^2}{2}$, $lb/ft^2$ |
| $R_e$/Ft | Reynolds number per ft $\rho \frac{V}{\mu}$ |
| S | body plan area, 5 $ft^2$; theoretical wing area, 5.85 $ft^2$ |
| T | trailing-edge cable tension, lb ($T = T_o + \Delta T$) |
| $\Delta T$ | increment in cable tension produced by air loads |
| V | free-stream velocity |
| $\alpha$ | angle of attack of fuselage reference line (flat upper surface of fuselage), degree |
| $\beta$ | sideslip angle, degree |
| $\delta_e$ | elevon deflection angle, positive with trailing edge down, degree |
| $\delta_{WT}$ | wing tip deflection angle, positive with trailing edge down, degree |
| $\Lambda$ | wing leading-edge sweepback angle, degree |
| $\mu$ | coefficient of viscosity, lb sec/$ft^2$ |
| $\rho$ | mass density of air, slugs/$ft^3$ |

subscripts:

| | |
|---|---|
| exp | exposed area |
| b | body |
| o | preset (wind-off) value |
| R | right (viewed from rear) |
| L | left |
| w | wing |
| $\infty$ | free-stream conditions |

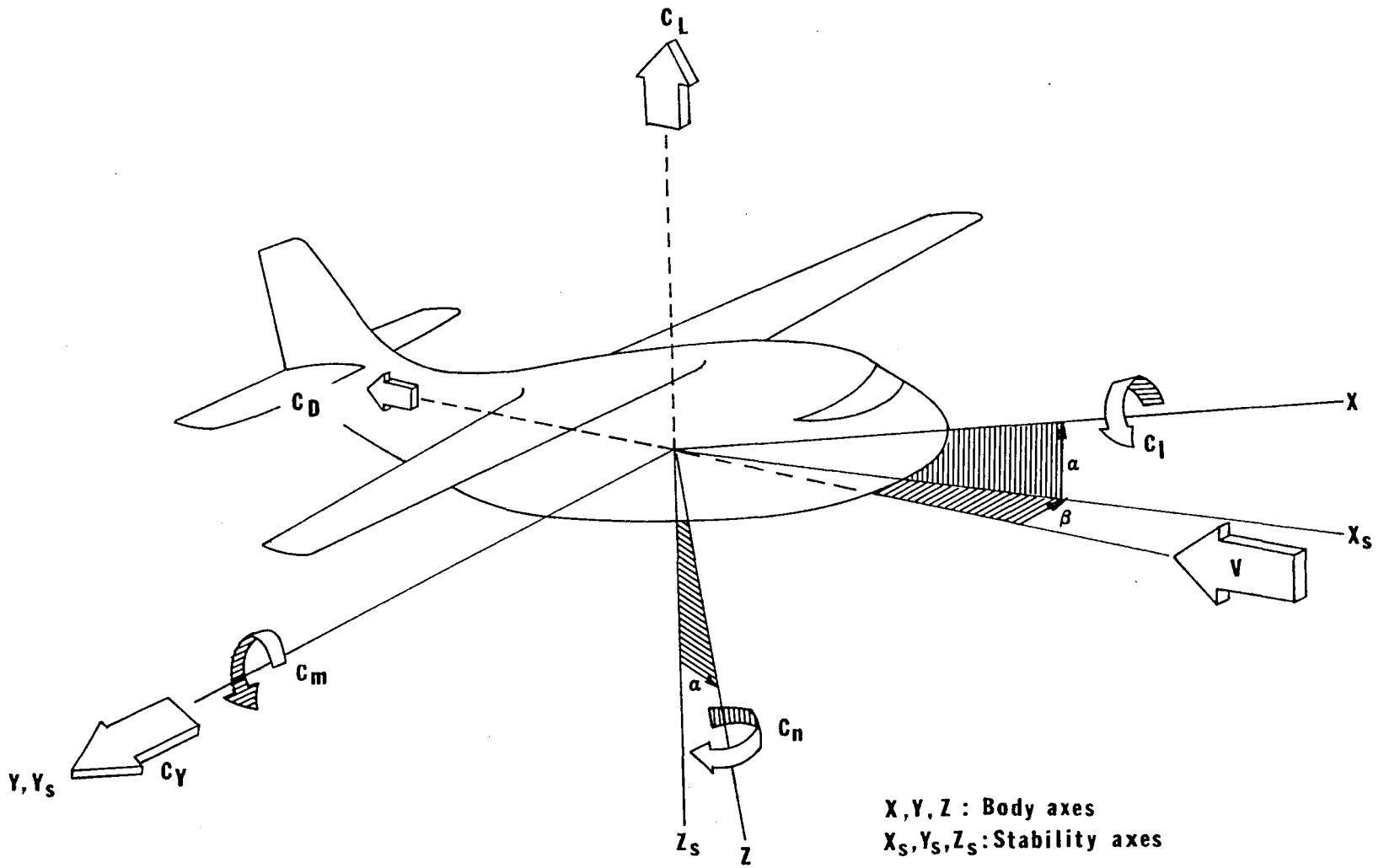


Figure2-1.System of axes and positive sense of angles, forces and moments.

## SECTION 3
## MODEL AND TESTS

### A. Model Description

For this investigation, a five-foot model of the NASA DL-4 lifting body configuration was constructed and fitted with a sailwing. The model was furnished with an actuating mechanism to deploy the sailwing from its stowed position within the body. It was used in the wind-tunnel tests to simulate in-flight deployment of a sailwing. Principal dimensions and general arrangement of the model are shown in Figure 3-1. The body has an aspect ratio of 0.5, a sweepback, as seen in plan view, of 82°, and rather angular features with a large blunt base.

The wing construction consisted of a rigid built-up D-spar which formed the leading edge, a wire-cable for the trailing edge, and a rib at each tip. This framework was covered with a fabric envelope which formed the upper and lower surfaces of the wing. The fabric used was untreated Dacron sailcloth which was folded around the leading edge and sewn together at the trailing edge to form a seam. Inside this seam ran a cable which, in each wing panel, was fastened to the wing-tip rib at one end, and secured to an eyebolt inside the body at the other end. The shape of the trailing edge, together with the length of the cable which could be adjusted by means of the eyebolt attachment, were such that when the spar was deployed by the actuator mechanism and reached its design sweepback angle, the cable was pulled to a pre-determined tension. In this way the fabric was stretched tight in both chordwise and spanwise directions forming a taut lifting surface. A typical cross section of the wing showing the loaded, and unloaded ($q = o$), contours which it assumes is presented in Figure 3-1(b). A sketch of the internal arrangement of the model is shown in Figure 3-2.

The wing had an aspect ratio of 3.27 and a leading edge swept back at 20°. In the stowed position, with the spars inside the body cavity, the sweepback angle was about 83°. This cavity was left open for wing deployment tests and was covered over with tape for body-alone tests. The wing was located above the longitudinal axis of the vehicle and placed longitudinally such that the estimated .25 mac (mean aerodynamic

chord) point of the wing was at the model moment reference center shown in Figure 3-1(a). Such positioning was only intended to be approximate because it was known that the wing aerodynamic center would move rearward with angle of attack to about .40 of the wing mac. This is a result of the aeroelastic behavior of the sailwing, which produces an increase of camber with airload.

The wing deployment mechanism was a combination of the pneumatic hydraulic type, and is shown schematically in Figure 3-3. By adjusting the regulator valve, deployment times varying from 0.4 to 5.0 seconds could be obtained. The actuator was designed to deploy the wings under wind-on conditions and establish an initial (pre-set) trailing edge cable tension of up to 120 pounds. Deployments with this mechanism, given constant regulator setting and bottle pressure, were highly repeatable.

To provide data on forces encountered within the model during deployment, strain gauges were installed on the trailing edge cable and in the deployment linkage of the right wing. In addition, a potentiometer was attached to one wing to indicate wing position versus time during deployment.

The model control surfaces consisted of elevons at the base of the body, and, when the wings were deployed, wing tips which could be deflected to act as ailerons. Only the right wing tip was deflected during the tests. It could be set to any one of several pre-determined positions for testing. The axis of the wing tip hinge passed through the inside attachment point of the trailing edge cable, thereby avoiding changing the pre-set cable tension during tip deflection. Elevon and wing tip deflections are measured relative to the vehicle reference line, which lies in the upper surface of the vehicle. This reference also serves as the zero angle of attack datum. Figures 3-4 (a) and (b) present photographs of the model mounted in the wind tunnel test section with the wing in the stowed and deployed positions.

B. Test Conditions

The tests were carried out in the NASA-Langley 7x10 ft - 300 mph wind tunnel. The objectives of the test program were to:

1) determine the low-speed stability and control characteristics of the DL-4 lifting body

2) evaluate the improvement of the lifting body performance afforded by the addition of a flexible, deployable wing (sailwing)

3) investigate the nature of forces and oscillations encountered during the deployment of this wing at various rates and dynamic pressures.

The results of this investigation were to be used to guide the design of a full-scale deployable lifting aid for the DL-4 vehicle.

The model was tested over an angle of attack range from about -8° to 20°, at tunnel dynamic pressures of 15, 30, and 60 lbs/ft$^2$, at sideslip angles of ±6°, and at maximum Reynolds numbers between $1.0 \times 10^6$ and $1.4 \times 10^6$ per foot. Body-alone tests were made with elevons deflected both symmetrically and differentially over a range of -13° to 16°.

No attempt was made to simulate a turbulent boundary layer in these tests. However, because the test Reynolds number, based on body length, varied between $5 \times 10^6$ and $6 \times 10^6$, and because of the angular features of the model and surface irregularities (joints, seals, etc.) it is reasonable to assume that the boundary layer on most of the model surface was a turbulent one. In any case, in view of the large base area and the correspondingly high base drag, the difference in skin friction drag between a laminar and turbulent layer would have been indiscernible.

Model aerodynamic force measurements were made with an internal strain-gage balance located at a postulated vehicle center-of-gravity location. Forces on the deployment linkage were also measured by means of a strain gauge located as shown in Figure 3-2. All data were recorded on magnetic tape. For the wing deployment tests, data were recorded at the rate of 64 points per second and were complemented,

on some runs, by oscillograph records of several selected channels. On regular (static) runs data were taken ten times on magnetic tape at each point and averaged to yield the nominal value at that point.

To provide a visual record of deployment phenomena, black-and-white motion pictures were taken at a rate of 200 frames per second from two locations: one outside the tunnel, giving a 3/4 view of the rear of the model; and one inside the tunnel looking upstream at the right wing trailing edge.

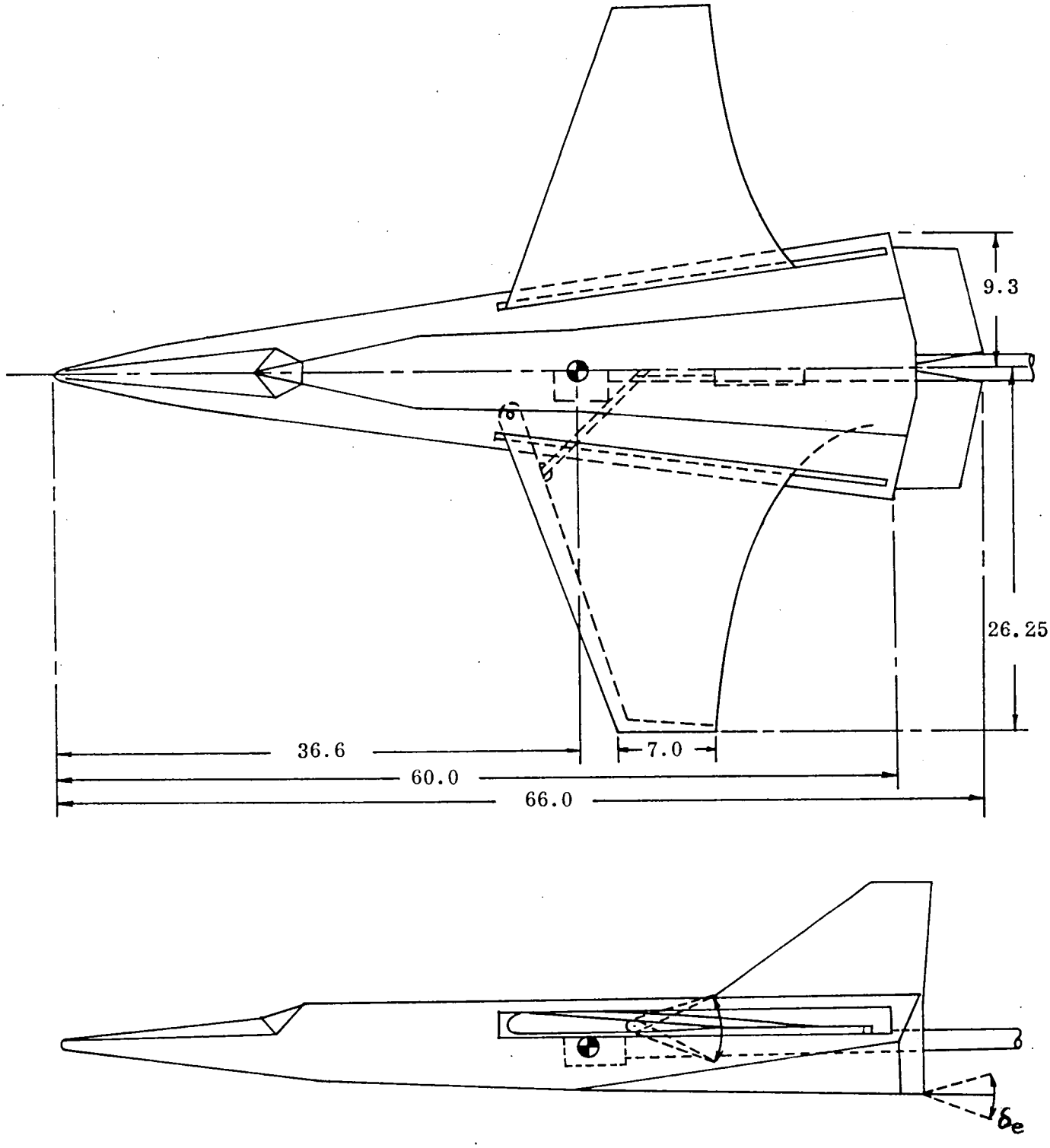


(a) Complete configuration

Figure 3-1. Sketch of model of NASA DL-4 body with sailwing.

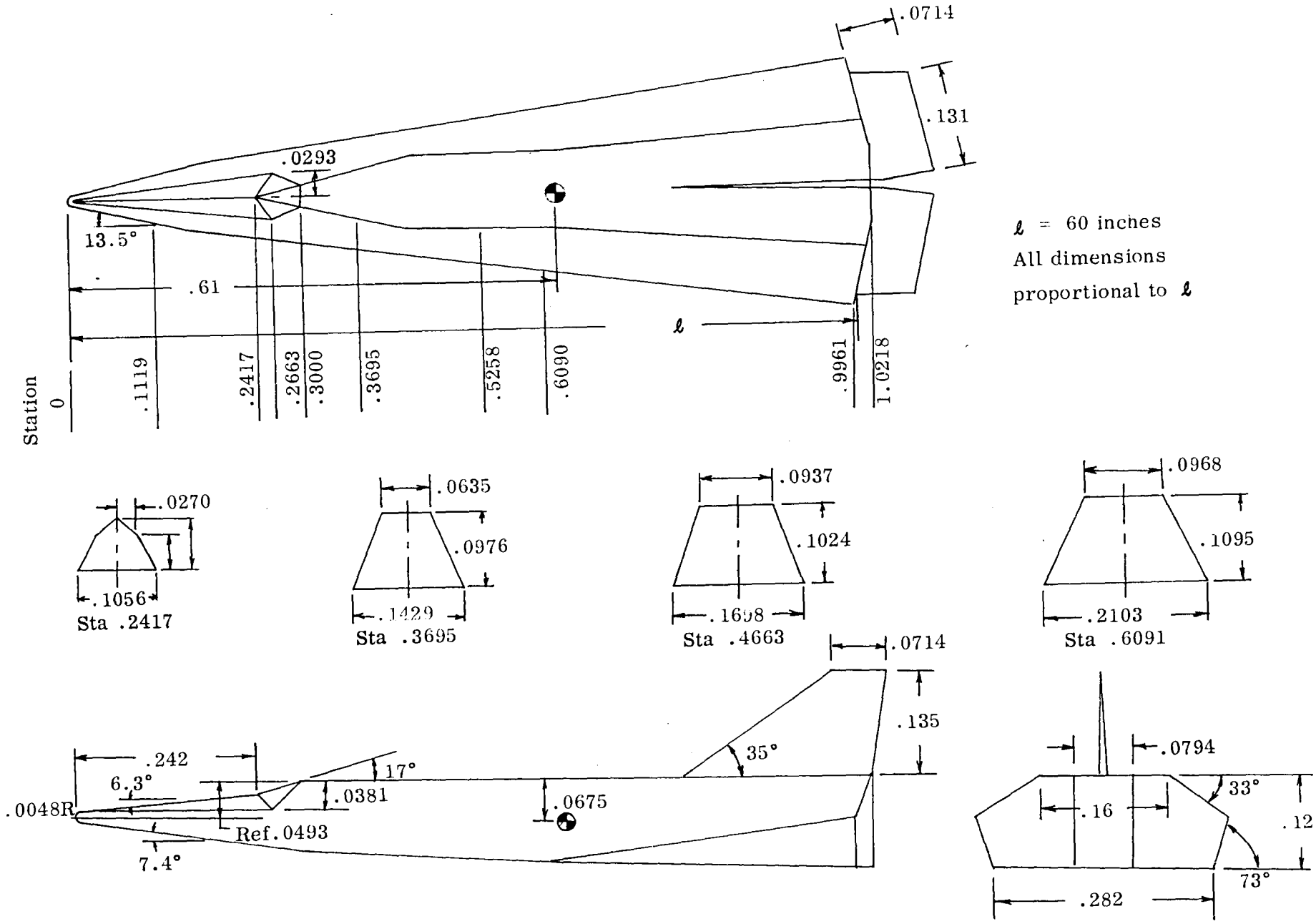


(b) DL-4 basic body design.
Figure 3-1. Continued.

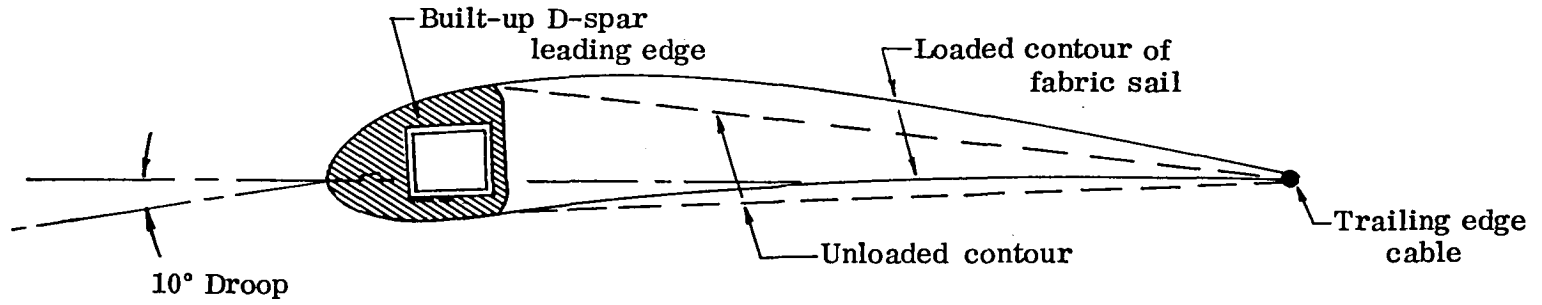


(c) Typical cross section of wing.

Figure 3-1. Concluded.

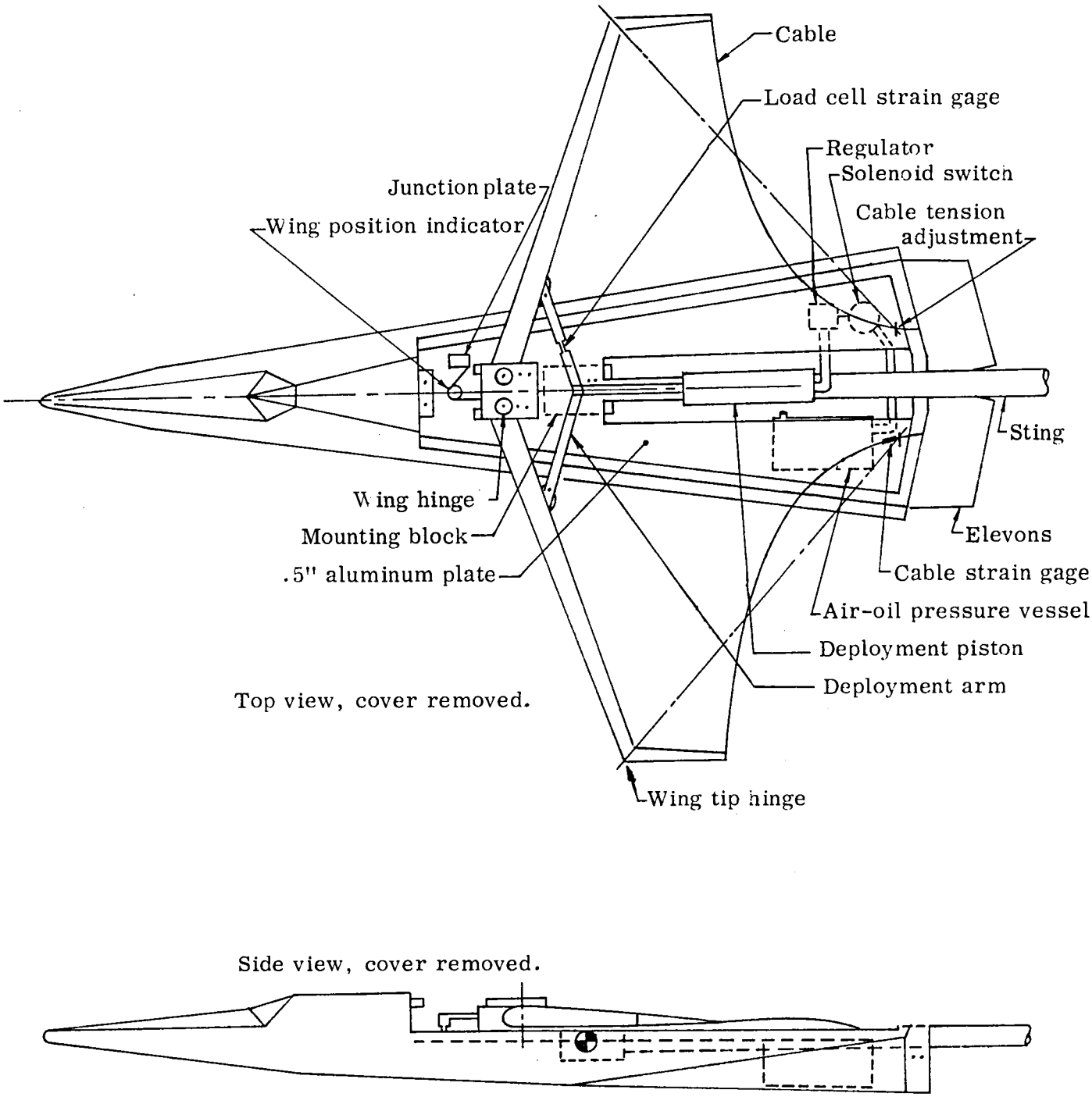


Figure 3-2. DL-4 model, snowing internal arrangement.

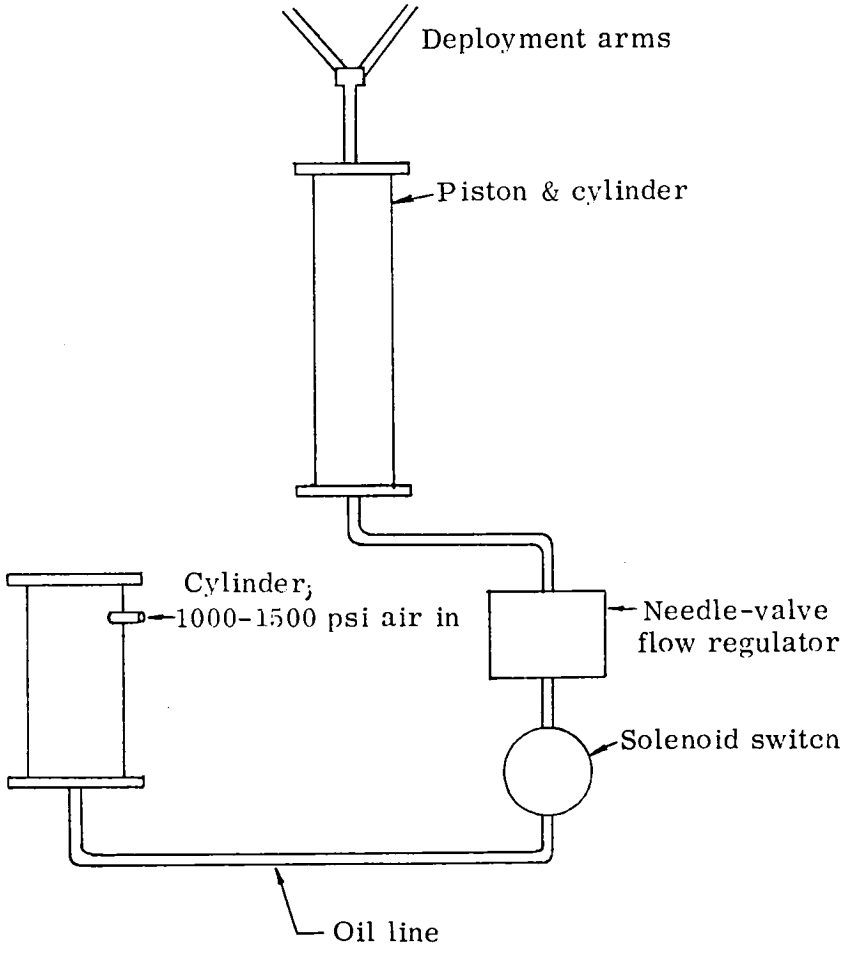


Figure 3-2. Deployment system schematic.

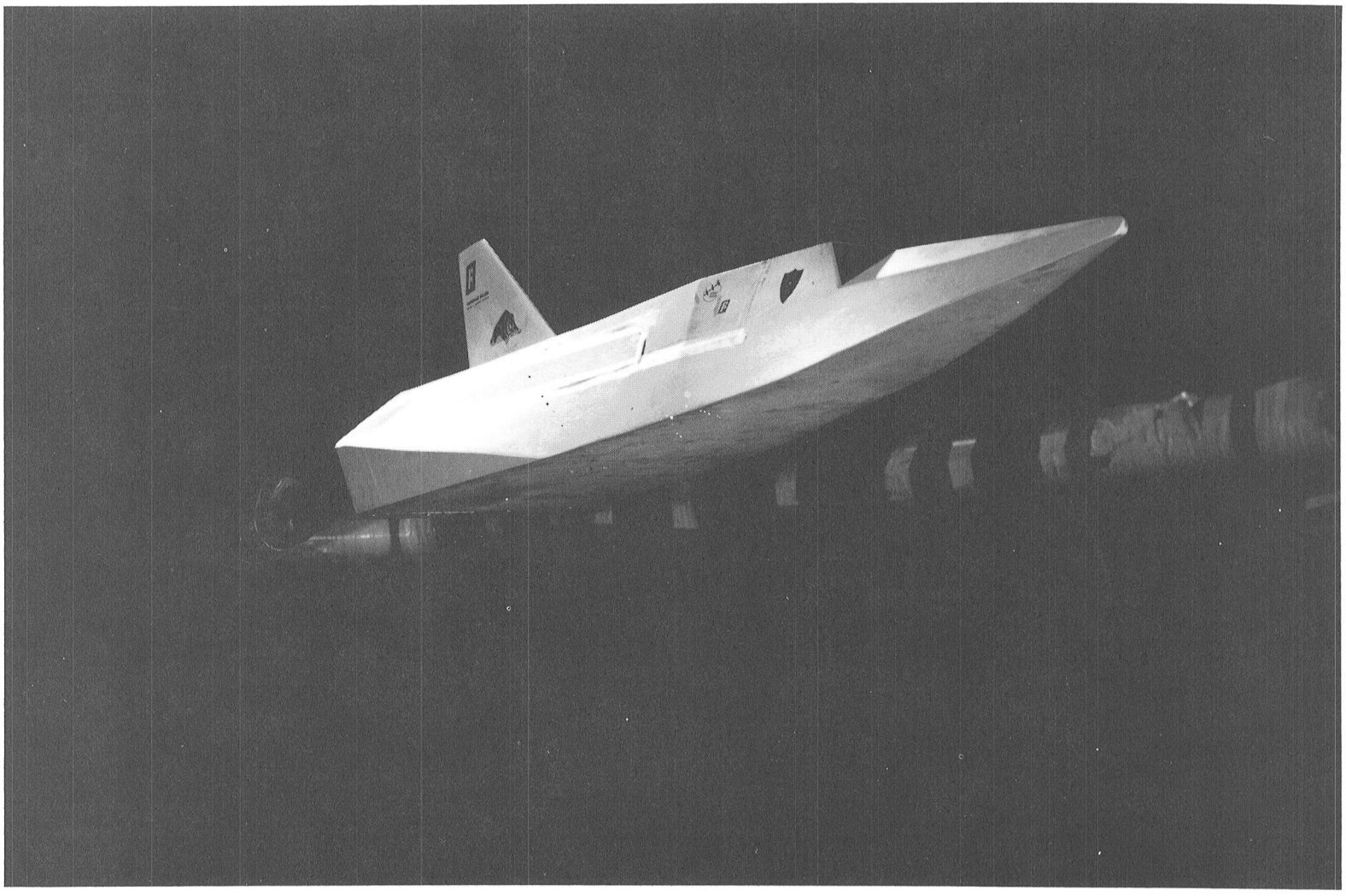

(a) Body alone.

Figure 3-4. Photograph of model installed in wind tunnel.

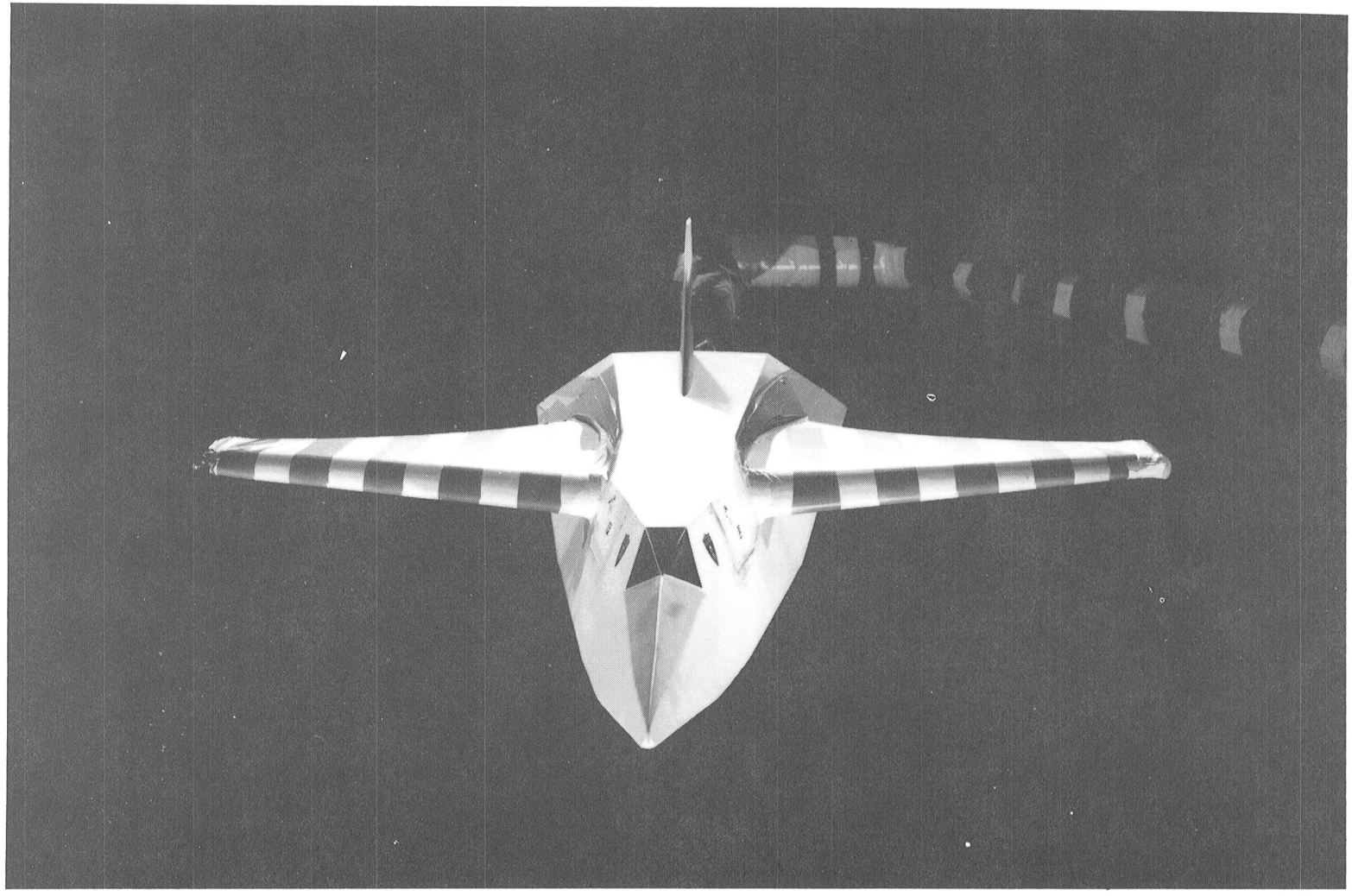

(b) Body with sailwing deployed.
Figure 3-4. Concluded.

## SECTION 4
## BODY-ALONE CHARACTERISTICS

### A. Longitudinal

The longitudinal characteristics of the basic DL-4 lifitng body are summarized in Figures 4-1 through 4-10. In Figure 4-1 (a) is shown the variation with angle of attack of the lift, drag, and pitching moment coefficient for dynamic pressures of 30 and 60 psf with the elevons in neutral ($\ddot{o}_e = 0°$). The lift curve shows the characteristic concave-upward shape of very low aspect ratio bodies; it passes through the origin, climbs smoothly to a lift coefficient of 0.39 at the highest angle of attack tested, $\alpha = 21°$, with no indication of stall. Tunnel-wall interference prevented testing at higher angles of attack. The lift curve slope at $\alpha = 0°$ is about 0.0150 per degree, increasing to 0.0184 per degree at $\alpha = 20°$. Presented in Figure 4-2 is a comparison of the experimental and predicted body-alone lift curve with the elevons in neutral. The predicted values were obtained using slender wing theory modified, as in Reference 3, to account for cross-flow effects which become important at high angles of attack. The agreement is seen to be good.

The body-alone pitching moment curve shows little variation over the angle of attack range. The slope of the $C_m$ versus $\alpha$, or $C_L$, curve varies from zero to slightly positive and negative indicating that the neutral point is located at about the moment reference center.

The body-alone drag data of Figure 4-1 (b) is replotted versus the square of the lift coefficient in Figure 4-3. It can be seen that the drag polar is not parabolic and that it has a slope, K, of about 1.52 at $C_L = 0$; where K is the induced drag factor appearing in the widely used drag polar representation, i.e.,

$$C_D = C_{D_o} + KC_L^2$$

Evidently K varies with $C_L$ due probably to the non-linearity of the lift-curve. On the other hand use of the relation

$$C_D = C_{D_o} + C_L \tan \alpha$$

is seen in Figure 4-4 to agree much better with the experimental polar than the preceding

one. The observed difference between predicted and experimental $C_{D_o}$ is due to uncertainties in the prediction of the base drag.

In this connection, it is pointed out that because the base drag constitutes a significant portion of the drag for this bodyshape the base pressures were measured, and tuft studies made to investigate base flow patterns. The tufts showed circulating flow in the wake region behind the base. The length of this region was found to increase slightly with angle of attack. Figure 4-5 shows the effects of dynamic pressure (Reynolds number) and of the presence of elevons on the body base pressure coefficient. Base pressure measurements were also made with a base shield with the elevons on and off. This base shield consisted of a thin band of sheet metal fastened flush to the surface of the model around its periphery at the back end. The sheet metal extended past the blunt base to form a slight base cavity. Its purpose was to examine what effect, if any, it had on the circulating type flow at the base. Its effect on base pressure coefficient was found to be negligible. The measured values fall right on the elevon-off values shown in Figure 4-5 and for that reason are not plotted therein.

Test data on effects of elevon deflections on the body-alone longitudinal characteristics are plotted in Figure 4-6. From the lift-curve data of Figure 4-6 (a) the elevons are seen to contribute a lift increment of .005 per degree of elevon deflection (elevons deflected in unison). Figure 4-7 shows body-alone lift curves with and without elevons. It is seen that without elevons both the lift coefficient at zero angle of attack and the lift curve slope are lower than for the body with elevons.

Drag due to elevon deflection is considerable at positive angles of attack, as shown in Figures 4-6 (a) and (b). From a small increment at $\alpha = -8°$, the drag due to deflection grows until $\alpha = 8°$. A cross plot taken at $\alpha = 8°$, is presented in Figure 4-8. It shows the drag increment due to deflecting both elevons in unison, and deflecting one elevon while the other is kept in the neutral position.

In Figure 4-6 (b) the maximum lift-to-drag ratio is seen to vary between 1.85 and 2.20 over the range of elevon deflections which were tested. This comparatively low value is characteristic of bodies having a large blunt base such as this one.

From the pitching moment data plotted in Figure 4-6 (a) it is seen that; the elevon power is sufficient to trim the basic DL-4 body at any desired lift coefficient; and that the static longitudinal stability over this range of $C_L$ will vary from a slightly stable condition to a slightly unstable one. Moreover, for the greatest positive elevon deflection tested, the elevons apparently stall at a vehicle lift coefficient of about 0.25; while for the negative deflection case, their effectiveness decreases below a vehicle $C_L$ of about -.05. Cross plots at several angles of attack enable a curve of incremental pitching moment coefficient versus elevon deflection to be drawn, as in Figure 4-9, from which $C_{m_{\delta_e}}$ ($\Delta Cm/\Delta \delta e$) is determined to be -.002 per degree of elevon deflection (in unison). Sideslip was found to have no appreciable effect on elevon effectiveness; any elevon deflection generated a constant pitching moment increment through the range of sideslips tested, namely -6° to 6°.

Figure 4-10 shows additional information relative to the effect of aft-end modifications on body-alone on pitching moment characteristics. It represents data taken during the base-pressure tests with and without elevons, and with the base shield in place, also with and without elevons. It is noted that inhibiting the circulatory flow around the base decreased the effectiveness of the deflected elevons by about 30%.

B. Lateral - Directional

The lateral-directional aerodynamic characteristics of the body alone are presented in Figures 4-11 through 4-15. For various elevon deflections the variation, with angle of attack, of the measured side force, yawing moment, and rolling moment coefficient are presented for sideslip angles of 1° and 6° in Figures 4-11 through 4-13. The 1° sideslip angle was the result of a sting mounting error which was not discovered until midway through the test program when the model was yawed to -6°. The problem was corrected when the model and sting were re-aligned for the final tests in the program.

The sideslip derivatives band on body axes presented in Figure 4-14 were evaluated using the incremental differences between the measured coefficients at $\beta$ = 1° and 6°. From the plot of the directional stability parameter, $C_{n_\beta}$, versus angle of attack it is seen that the directional stability vanishes at angles of attack greater than about 11.5°.

This loss of vertical tail effectiveness is probably due to the flow separating from around the sharp edges of the body in the aft region of the body, resulting in a region of low dynamic pressure in the region of the tail.

The body is found to have positive dihedral effect ($-C_{\ell_\beta} > 0$) which increases slightly with angle of attack. This is probably due to the positive geometric dihedral of the beveled lower edges of the body in its aft region.

The effectiveness of the elevons as roll controllers is shown in Figure 4-13, in which the curves have a slight negative slope due to the aforementioned residual yaw ($\beta = 1°$) in the model mounting. Moreover, the roll contribution of the elevons is seen to be insensitive to angle of attack for $\beta = 1°$, and to vary only slightly at $\beta = 6°$.

From the variation of rolling moment coefficient with elevon deflection shown in Figure 4-15, the elevon roll effectiveness ($C_{\ell_{\delta_e}} = \Delta C_\ell / \Delta \delta_{e_{total}}$) is found to be -.00025 per degree total elevon deflection ($\delta_{e_{total}} = \delta_{e_R} - \delta_{e_L}$). This value is unaffected by sideslip over the range of sideslip angles tested.

In terms of the non-dimensional roll rate parameter $\frac{pb}{2v}$, commonly used for evaluating lateral control effectiveness, the elevons are capable of generating a value of about 0.36. This is based upon an estimated roll damping of $C_{\ell_p} = -.025$ for the body (using the methods of Reference 4) together with the measured rolling moment coefficient of -.009 for a total elevon deflection of 29°.

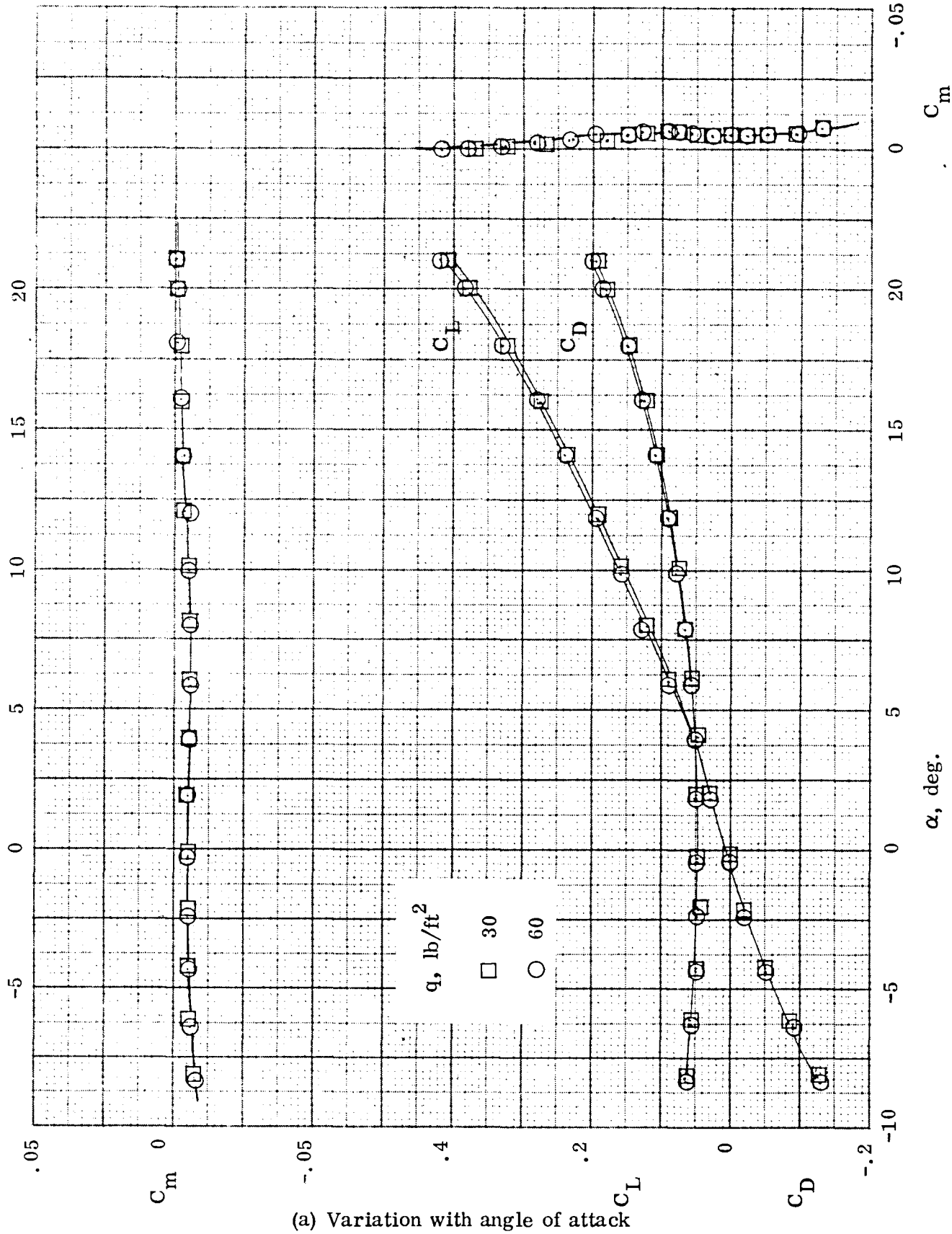


(a) Variation with angle of attack

Figure 4-1. Body-alone longitudinal aerodynamic characteristics for several dynamic pressures.

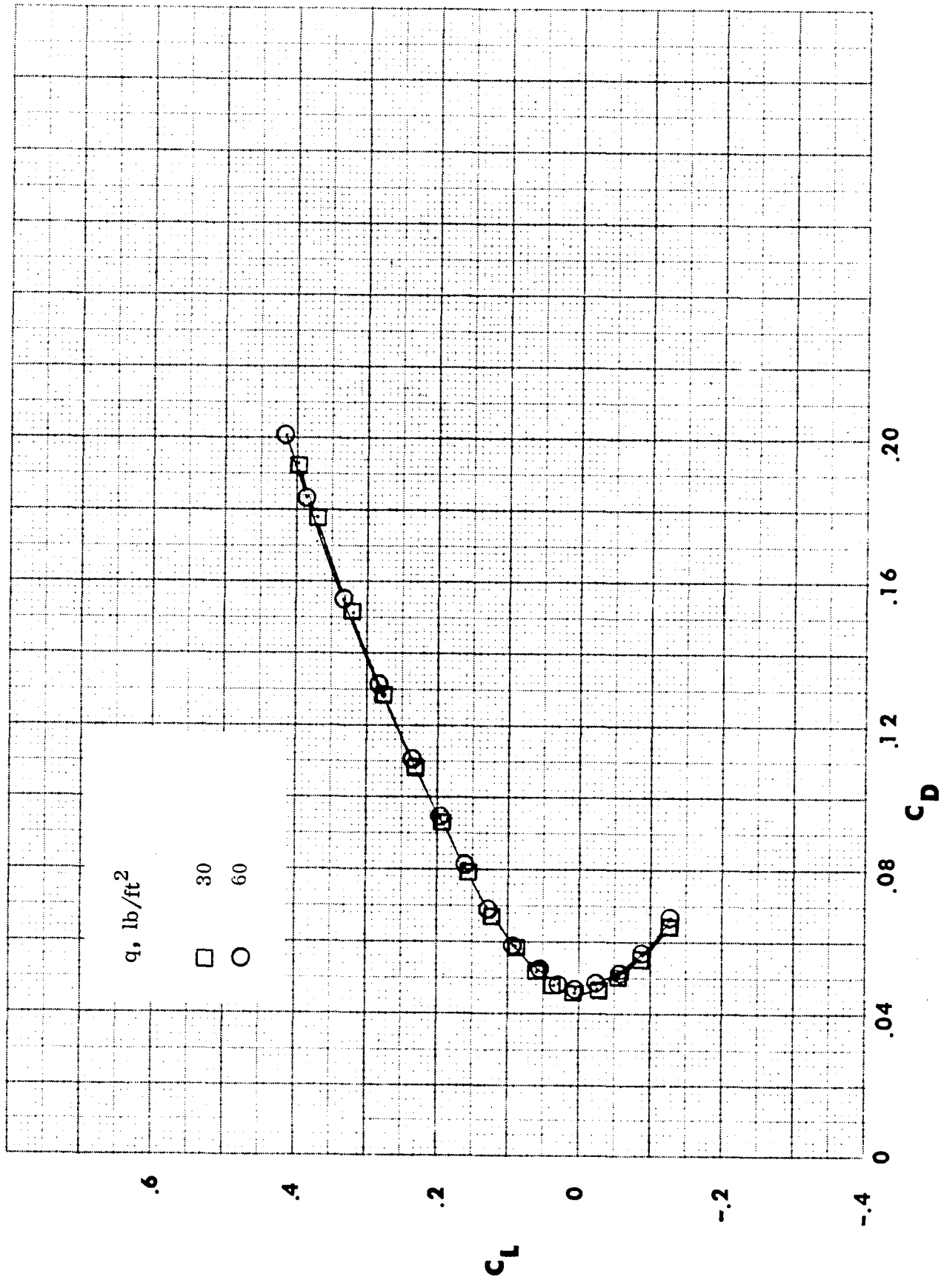


(b) Drag polar

Figure 4-1. Continued.

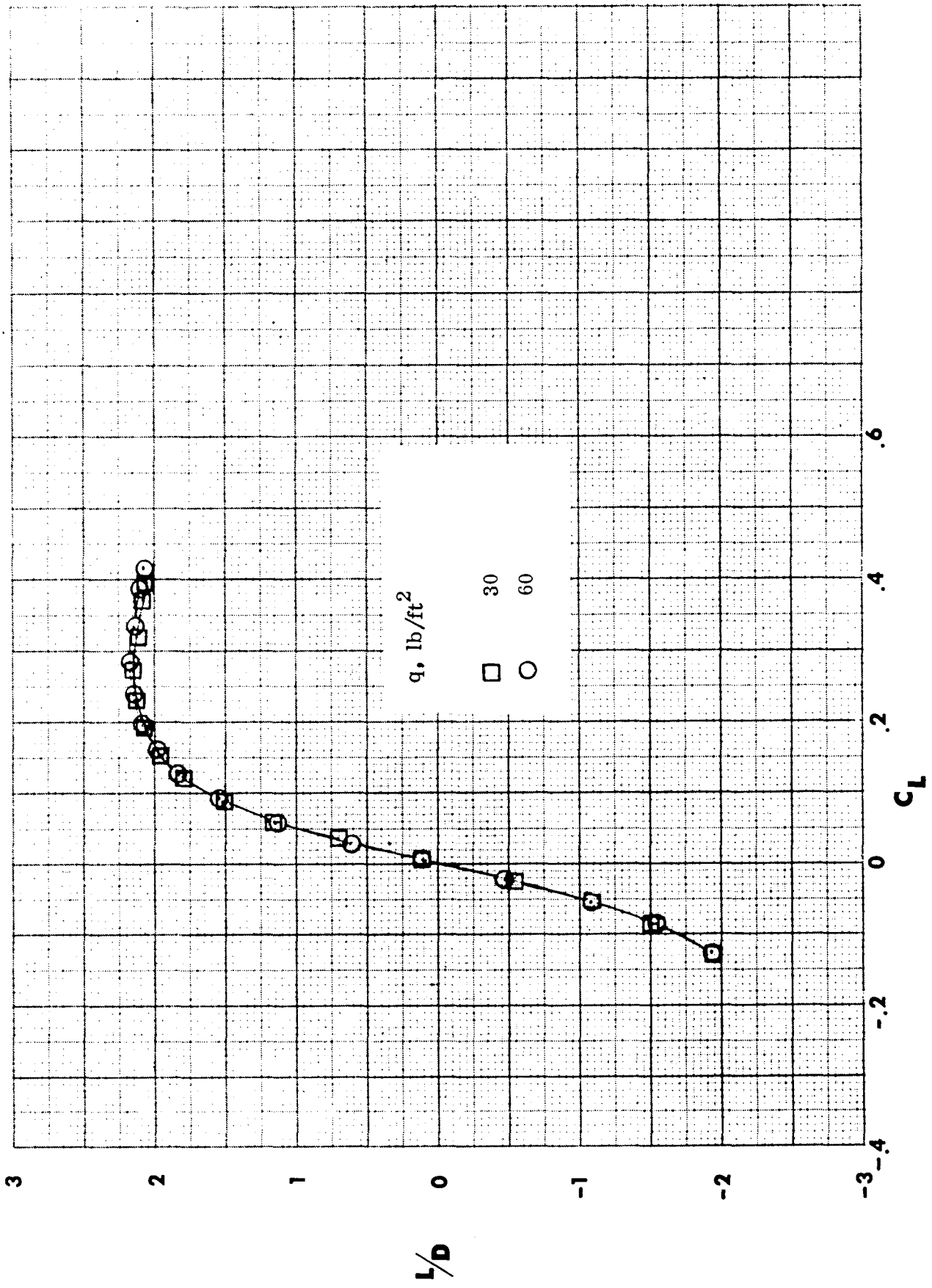


(c) Lift-drag ratio

Figure 4-1. Concluded.

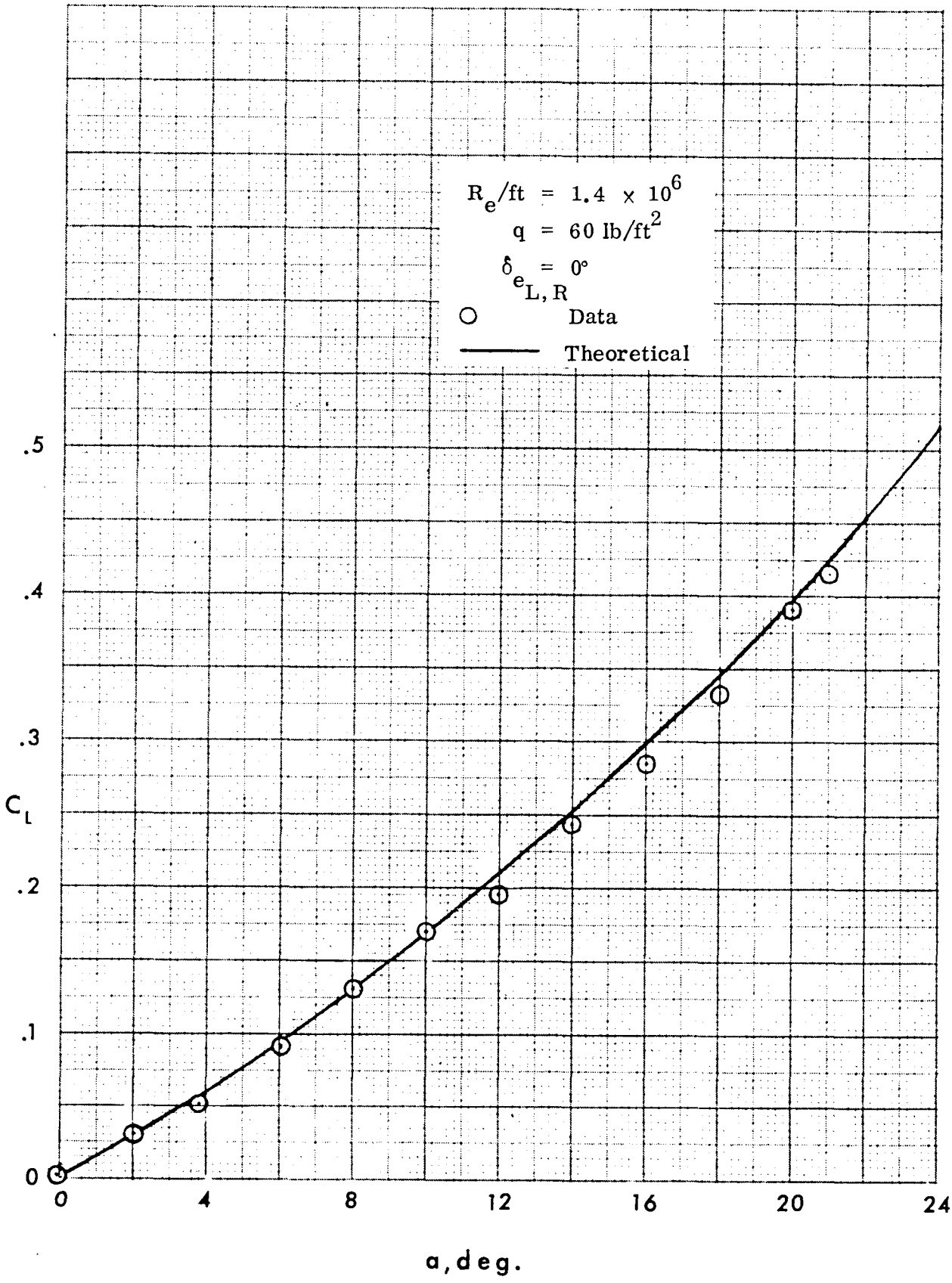


Figure 4-2. Experimental and predicted body-alone lift curves.

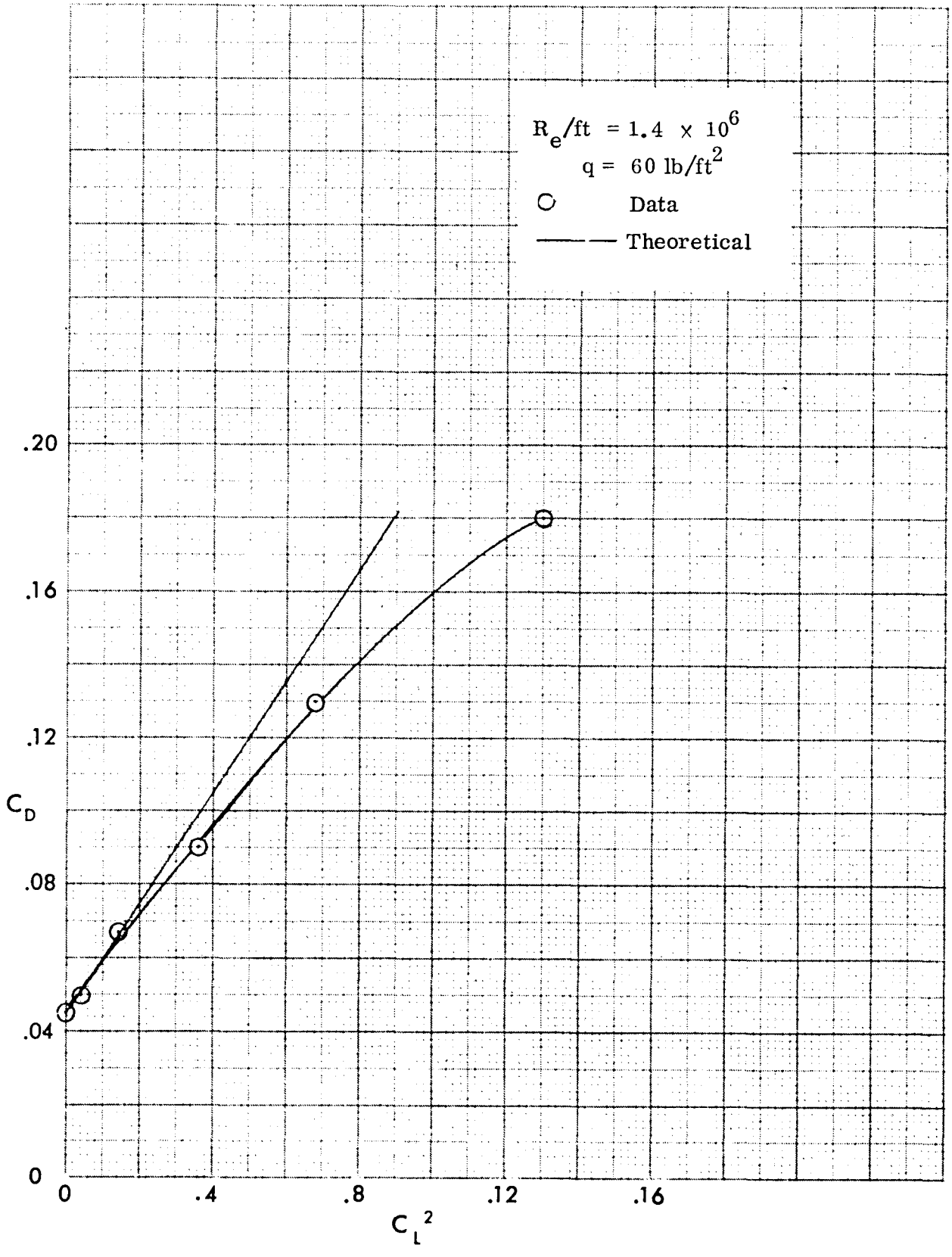


Figure 4-3. Variation of body-alone drag with $C_L^2$.

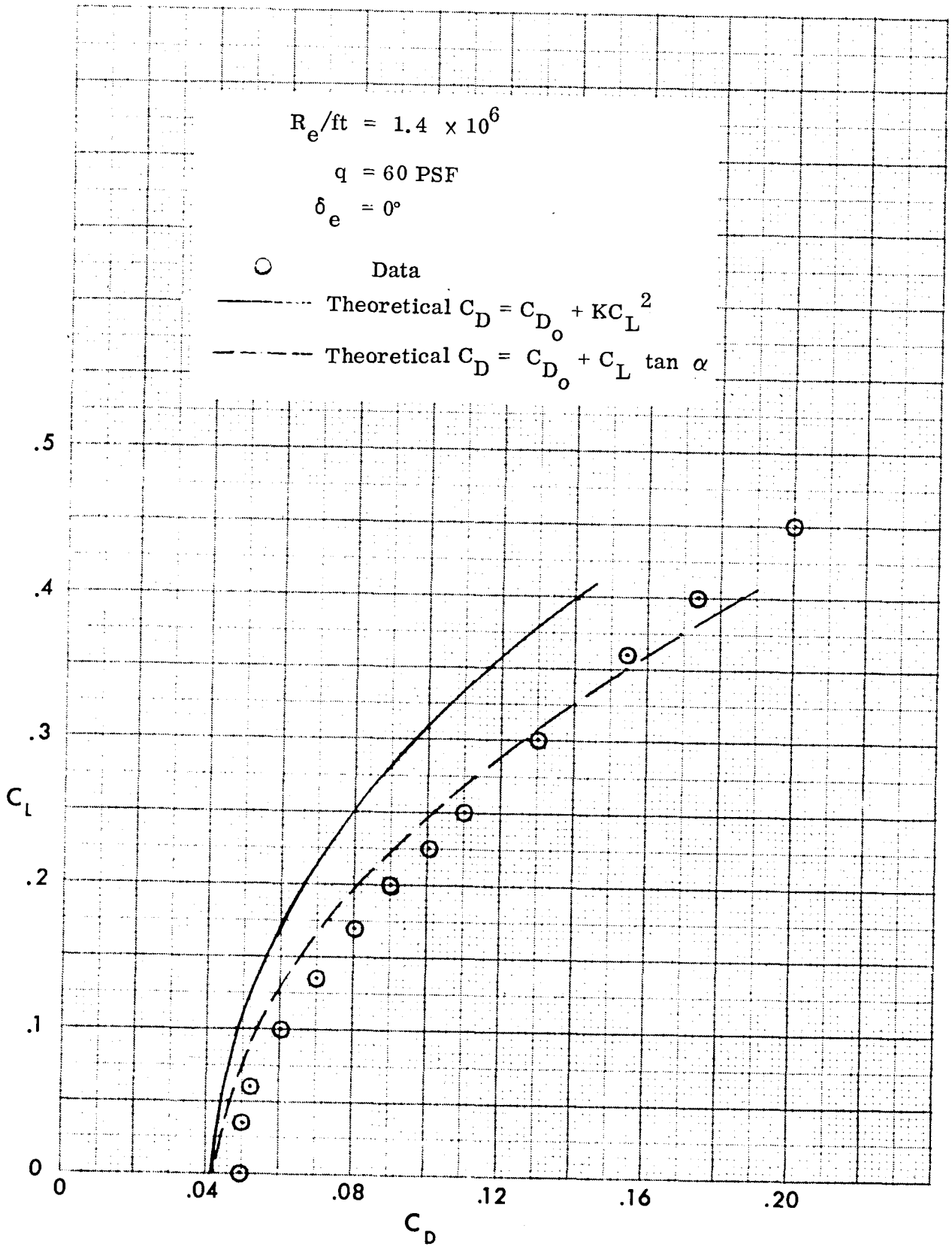


Figure 4-4. Comparison of predicted and experimental body-alone polars.

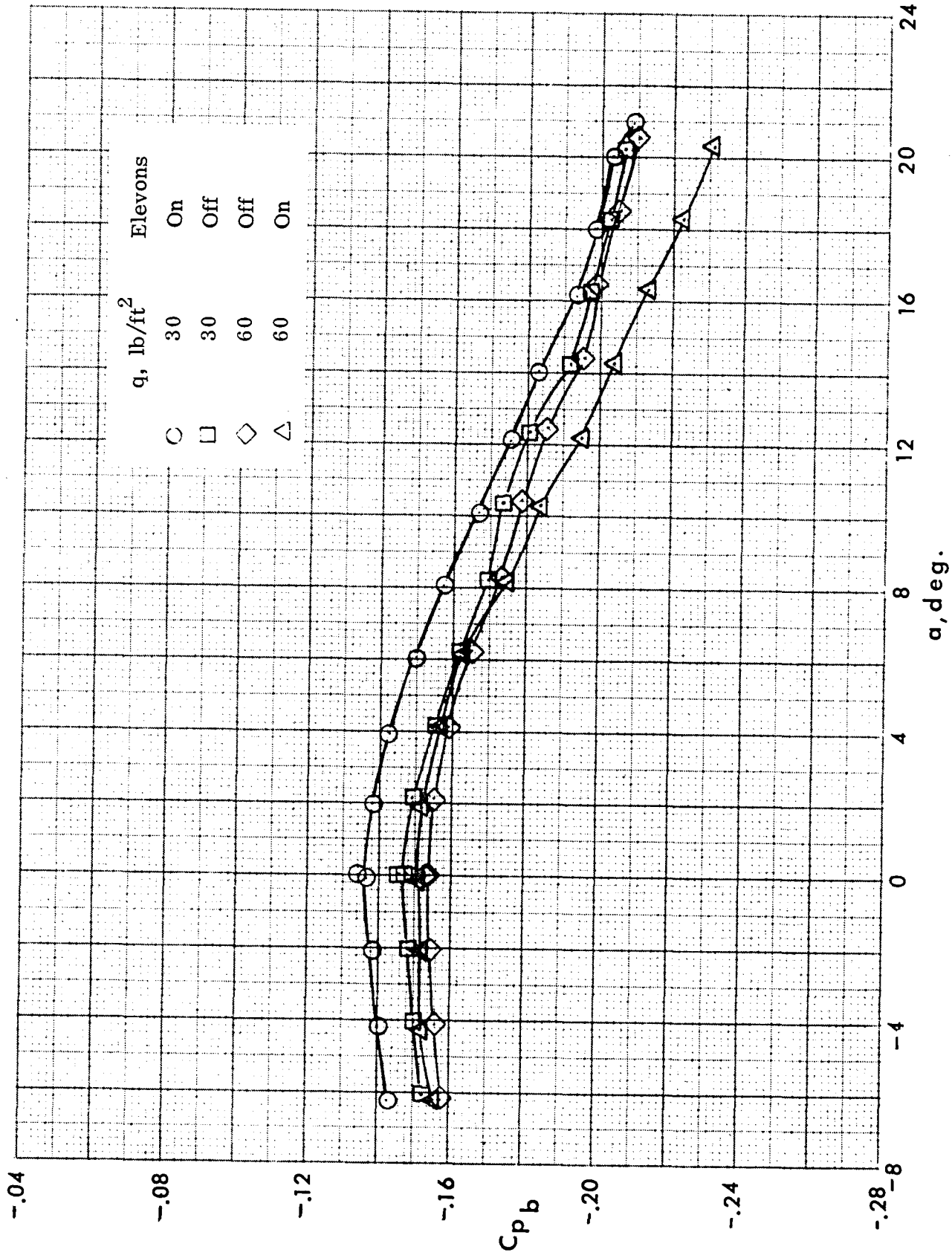


Figure 4-5. Effect of dynamic pressure and elevons on body base pressure coefficient.

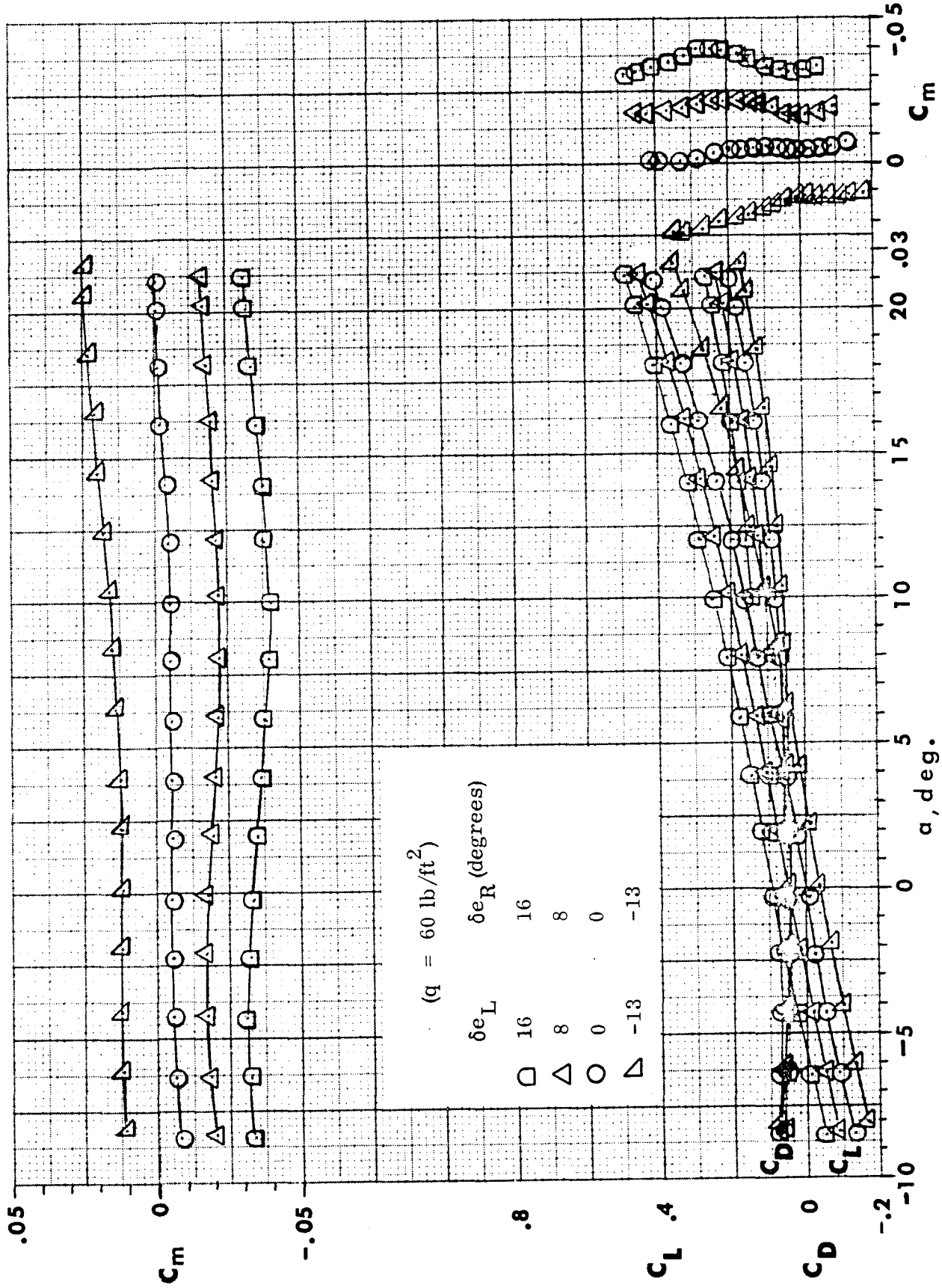


(a) Variation with angle of attack

Figure 4-6. Body-alone longitudinal aerodynamic characteristics for various elevon deflections.

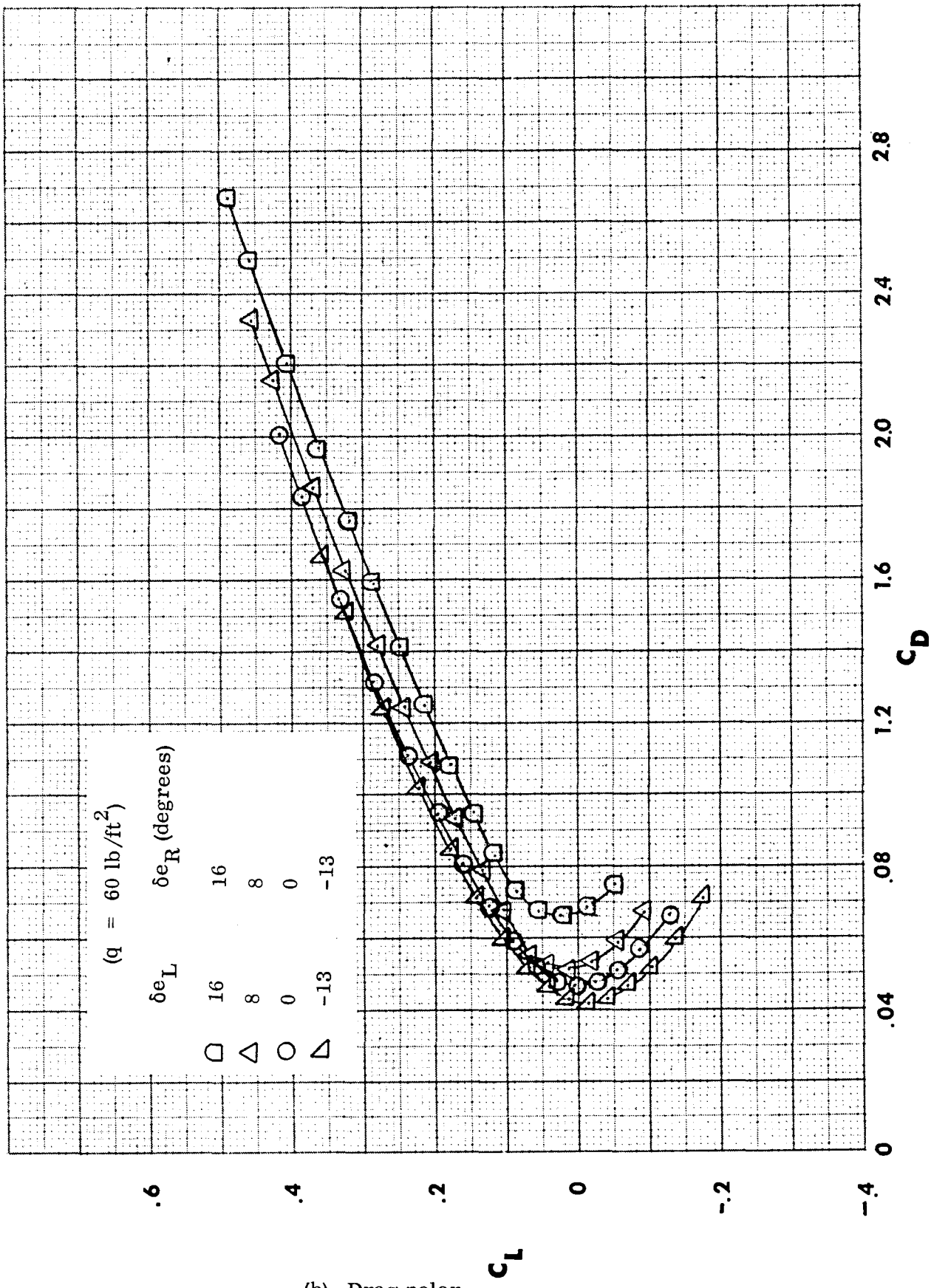


(b) Drag polar.

Figure 4-6. Continued.

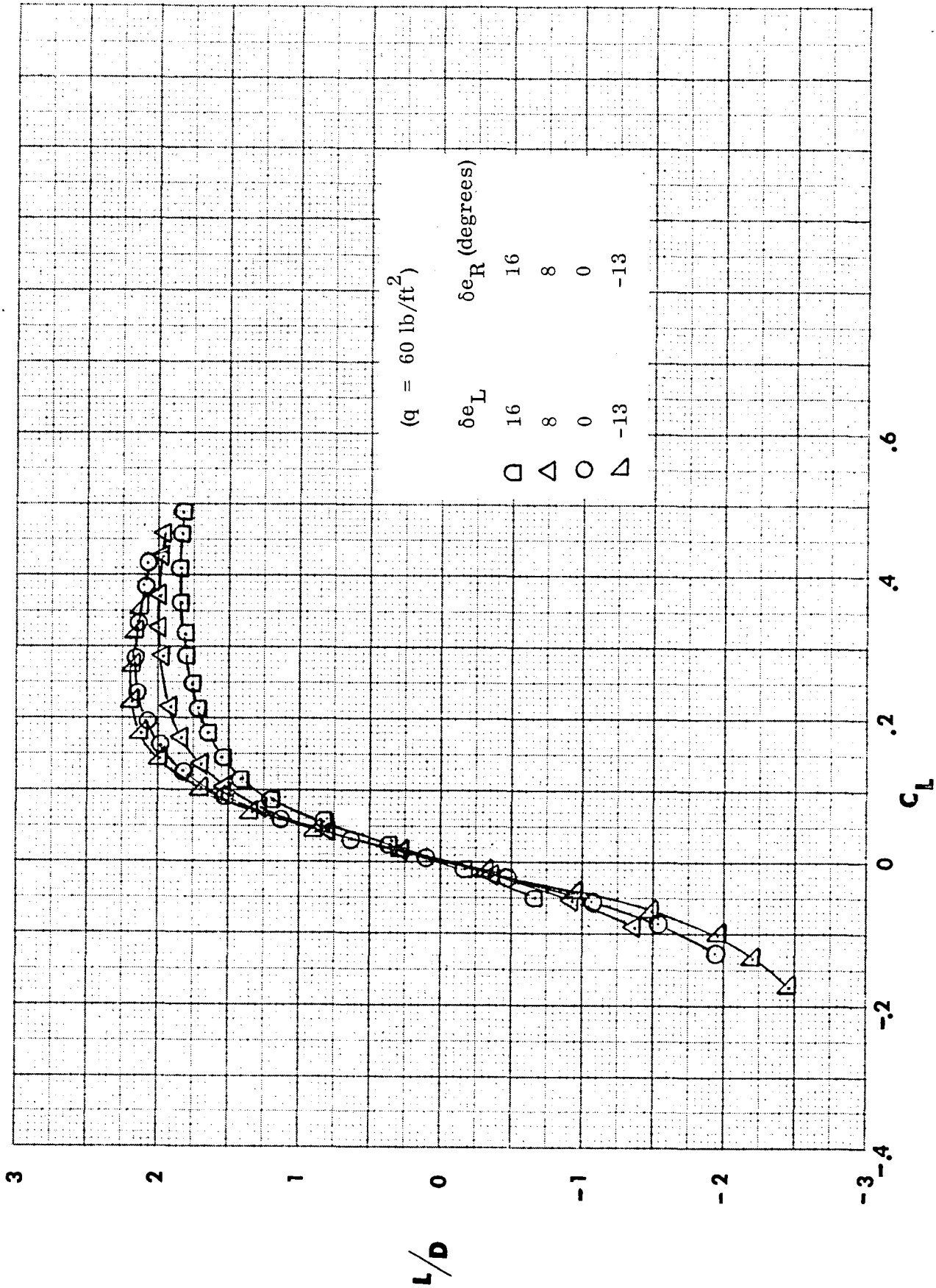


(c) Lift-drag ratio

Figure 4-6. Concluded.

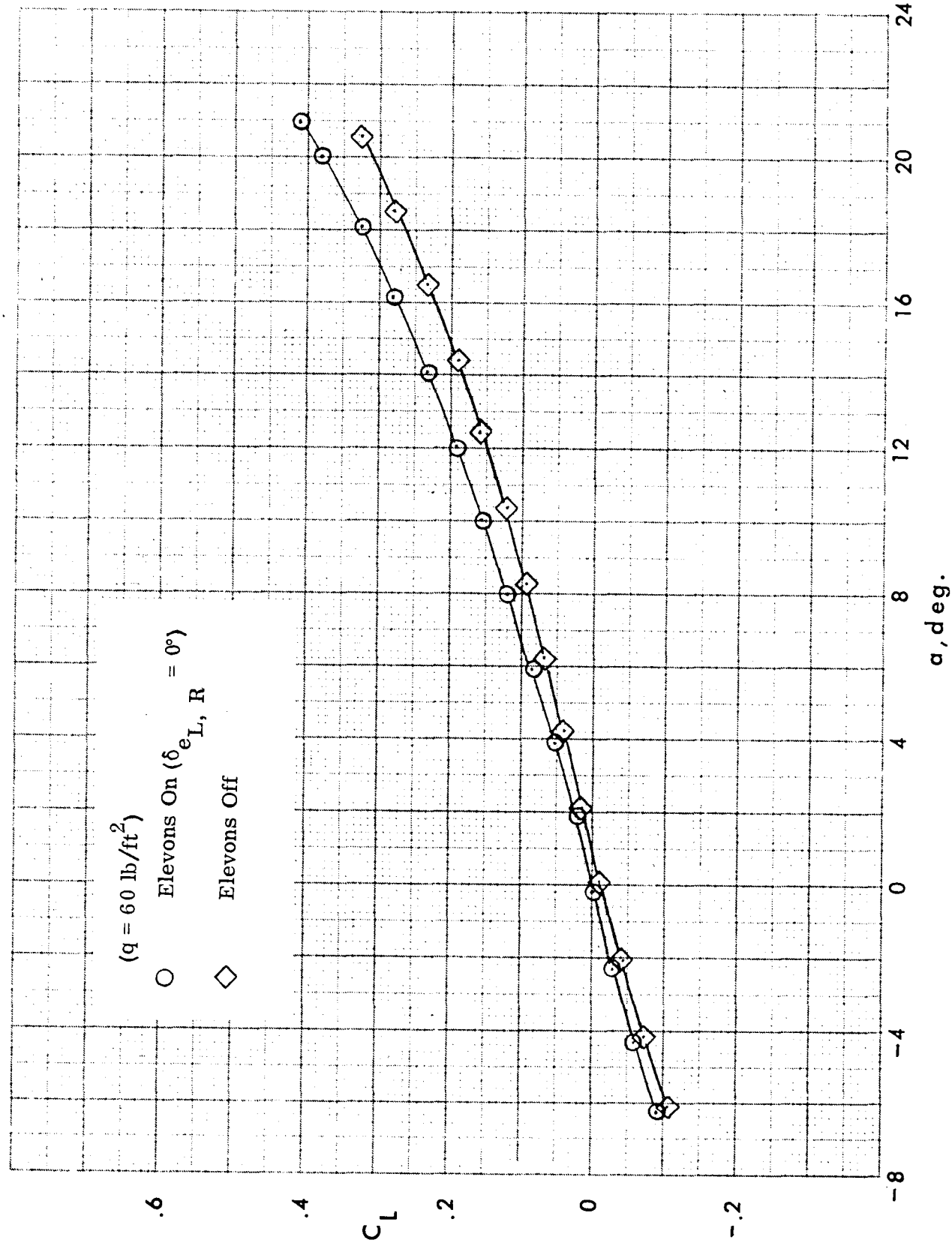


Figure 4-7. Body-alone lift curve with and without elevons.

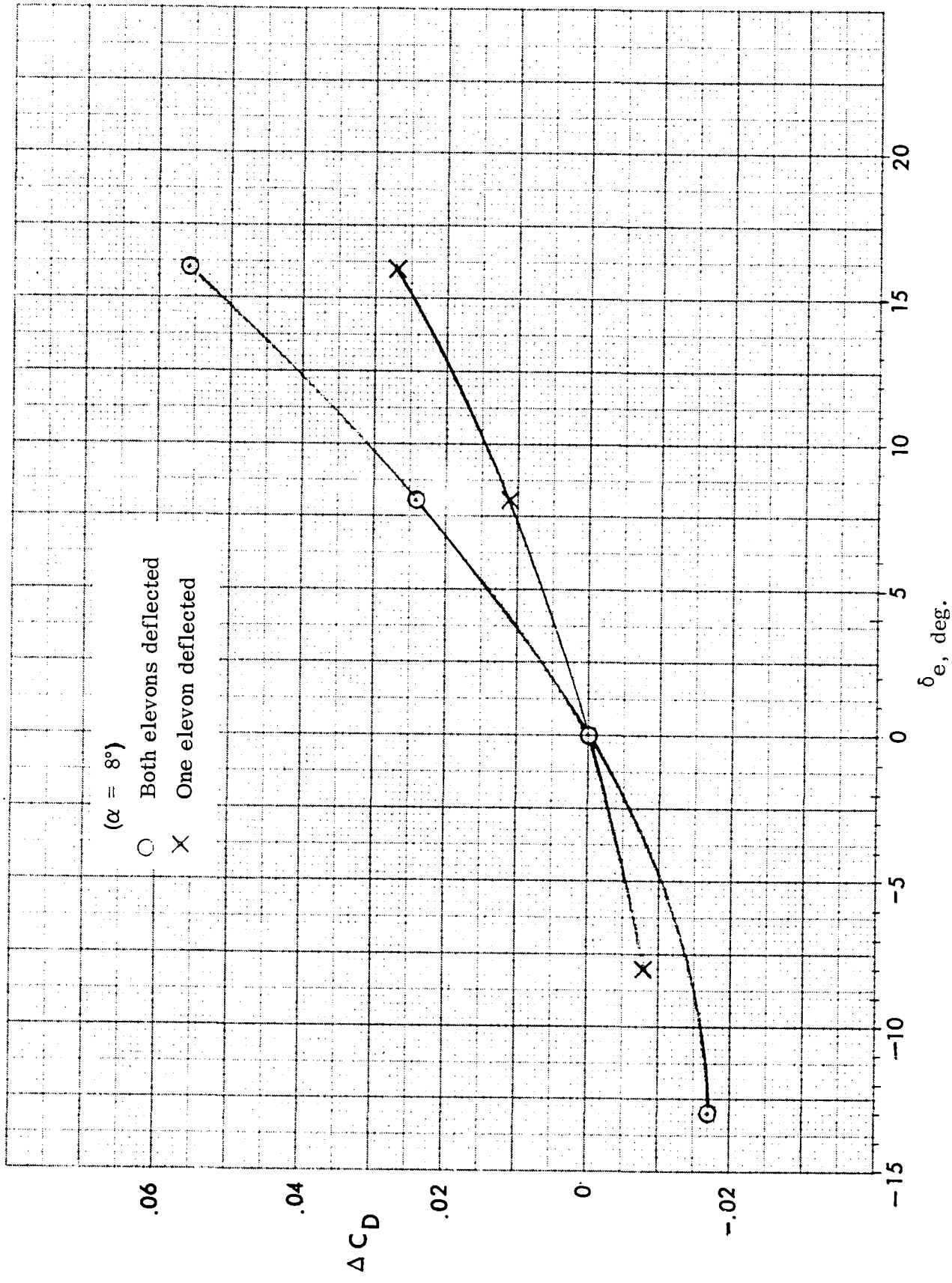


Figure 4-8. Drag increment due to elevon deflection.

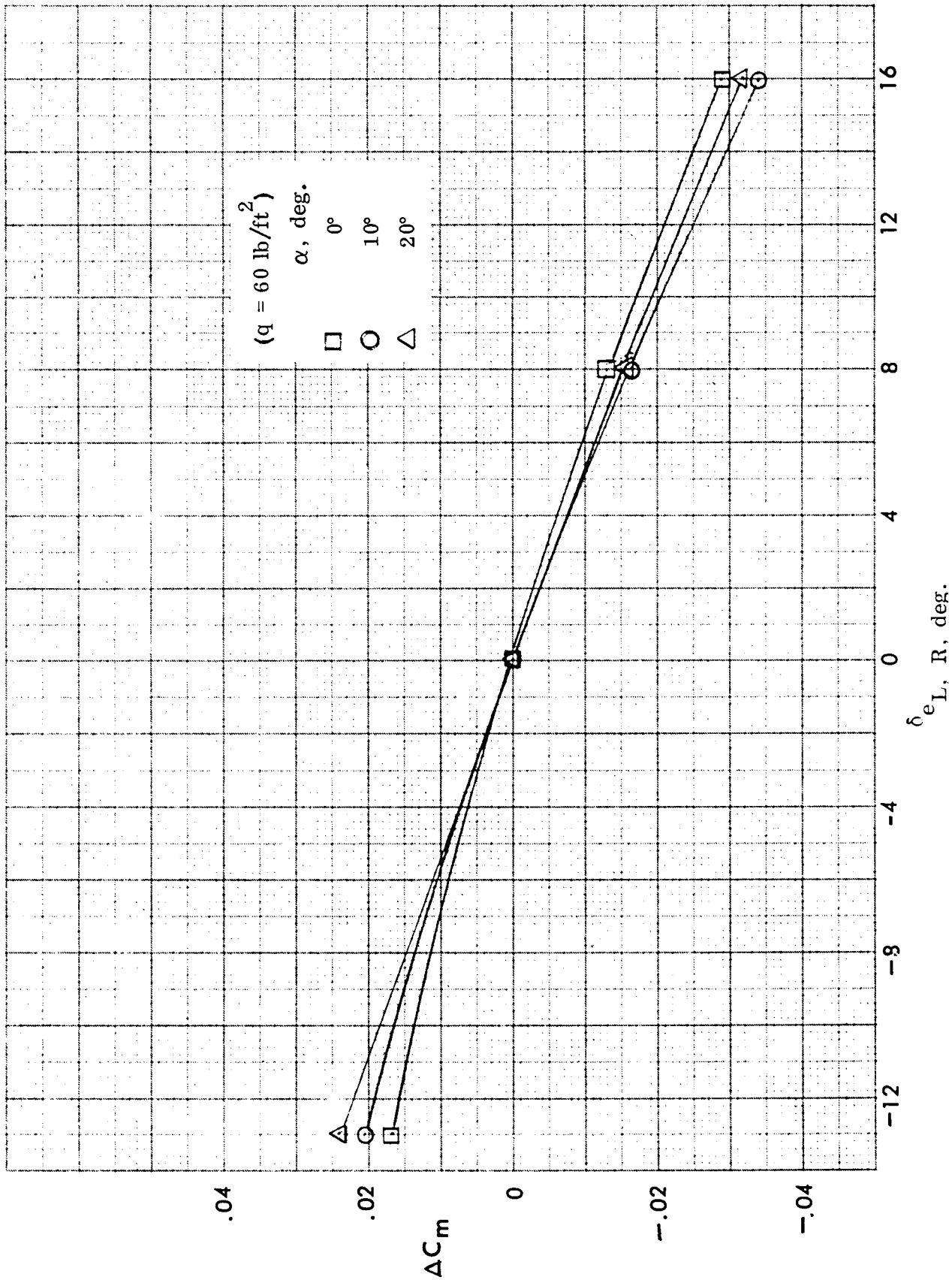


Figure 4-9. Pitching moment due to elevon deflection.

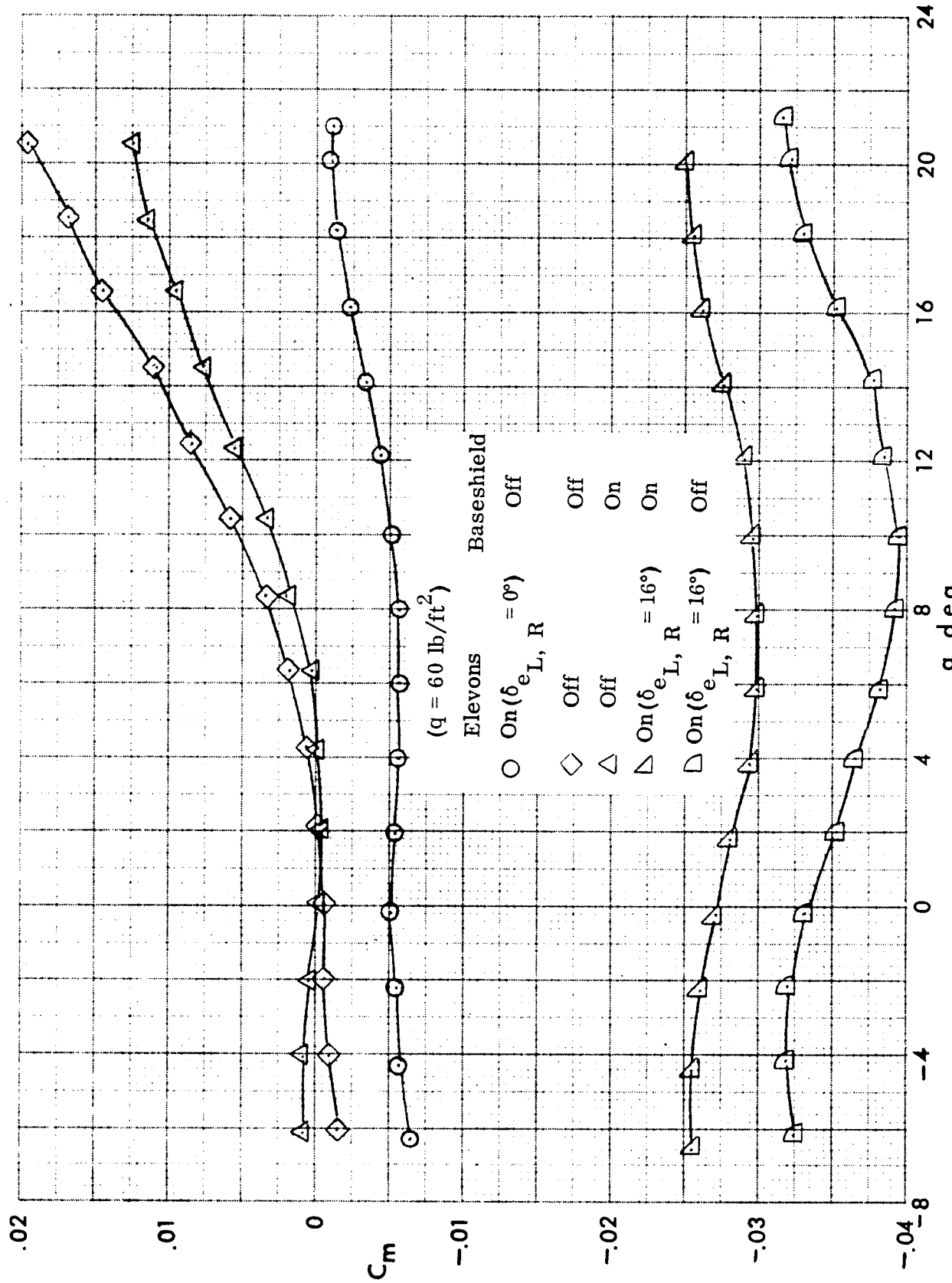


Figure 4-10. Effect of aft-end modifications on pitching moment.

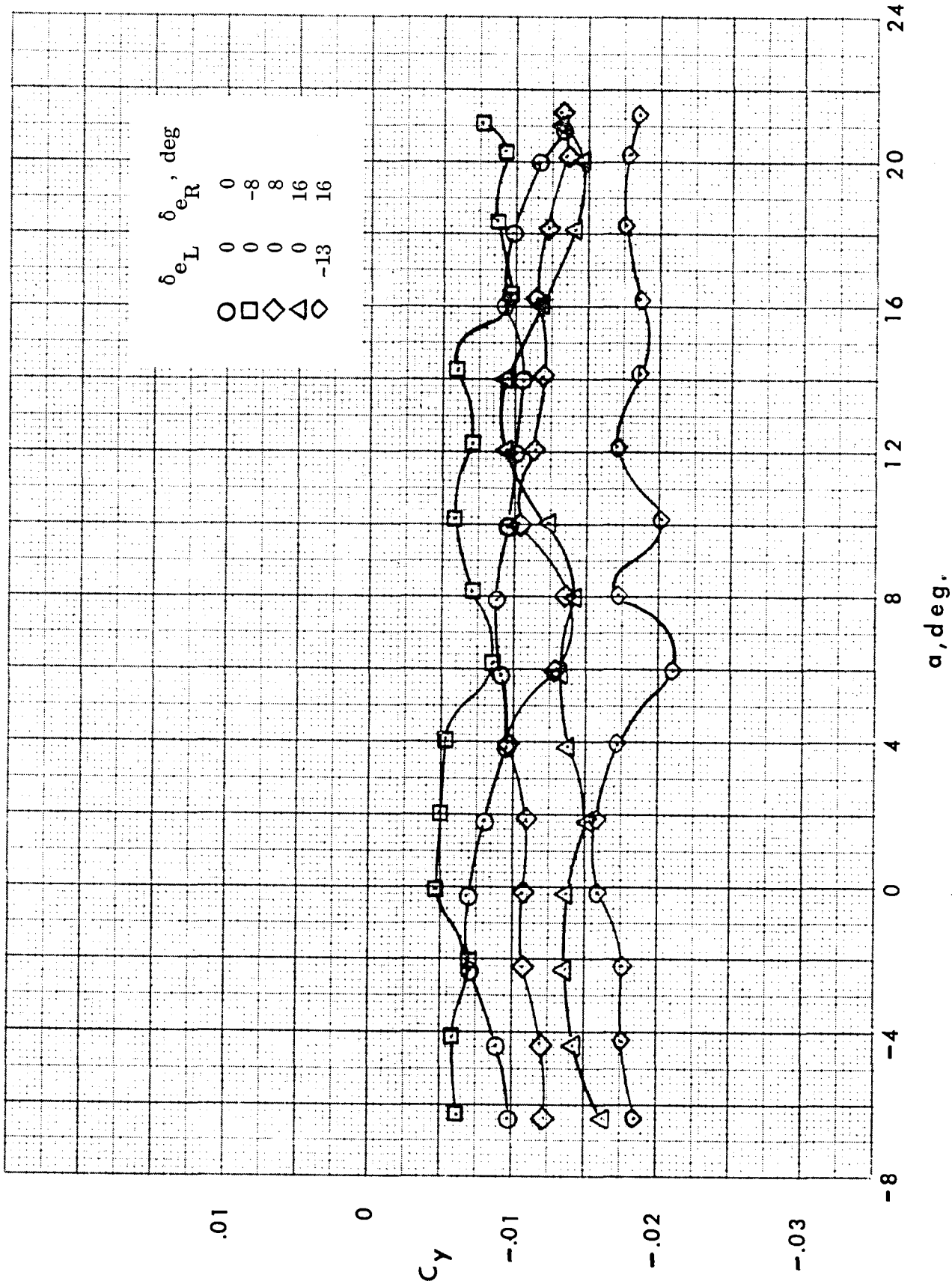


(a) $\beta = 1°$

Figure 4-11. Variation of body-alone side force coefficient with angle of attack for several elevon deflections. q = 60 psf.

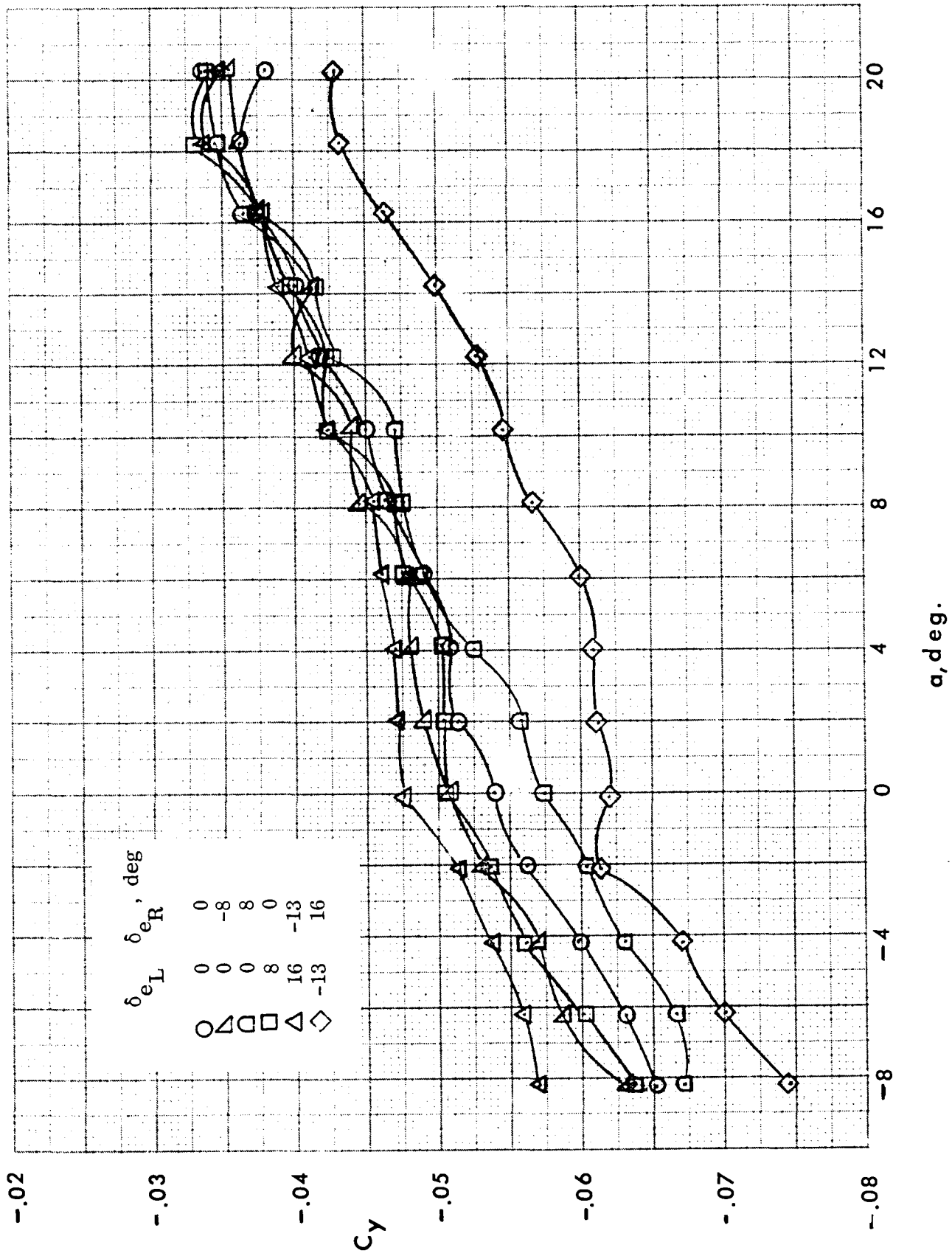


(b) $\beta = 6°$.

Figure 4-11. Concluded.

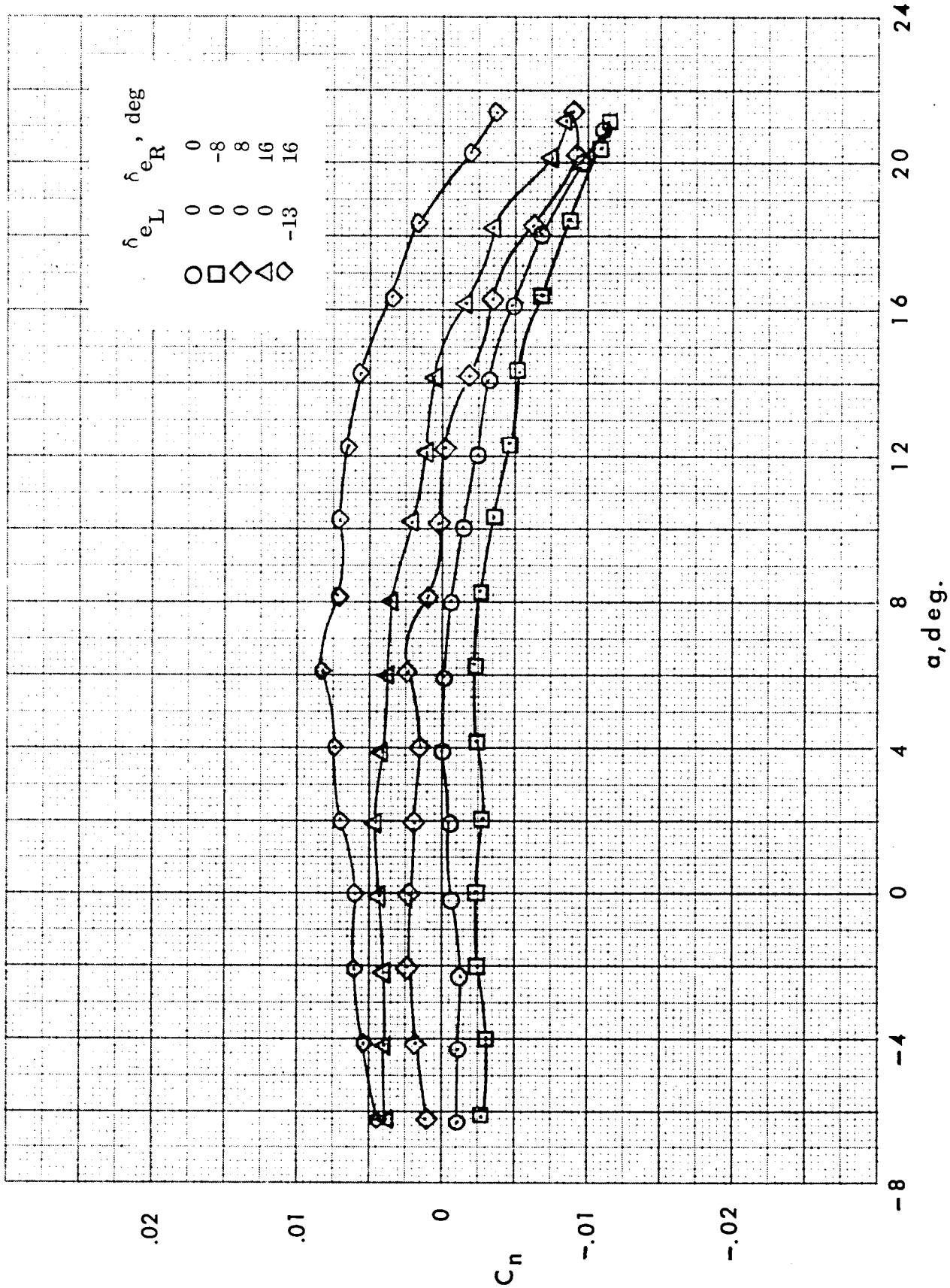


(a) $\beta = 1°$

Figure 4-12. Variation of body-alone yawing moment coefficient with angle of attack for various elevon deflections. q = 60 psf.

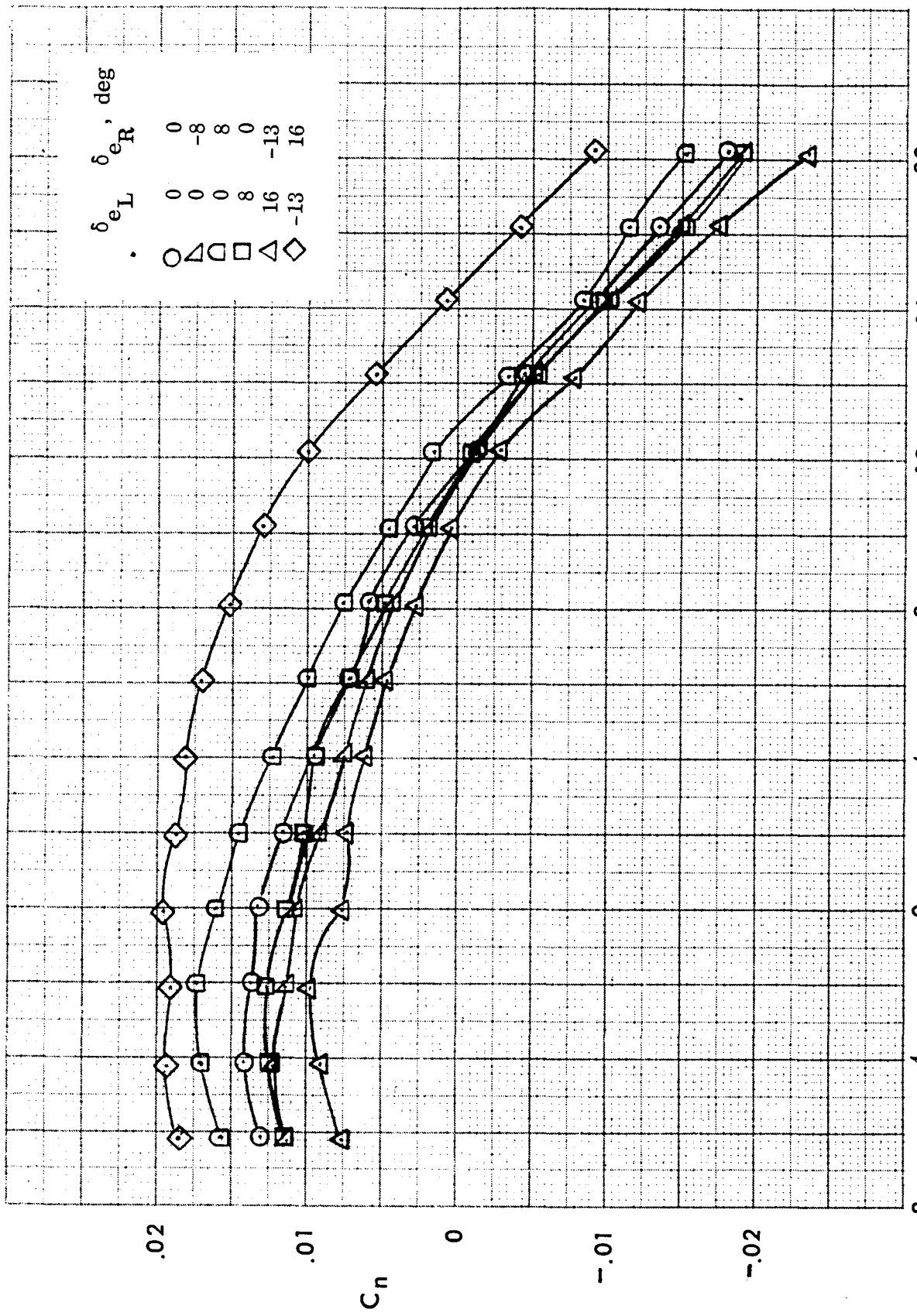


(b) $\beta = 6°$

Figure 4-12. Concluded.

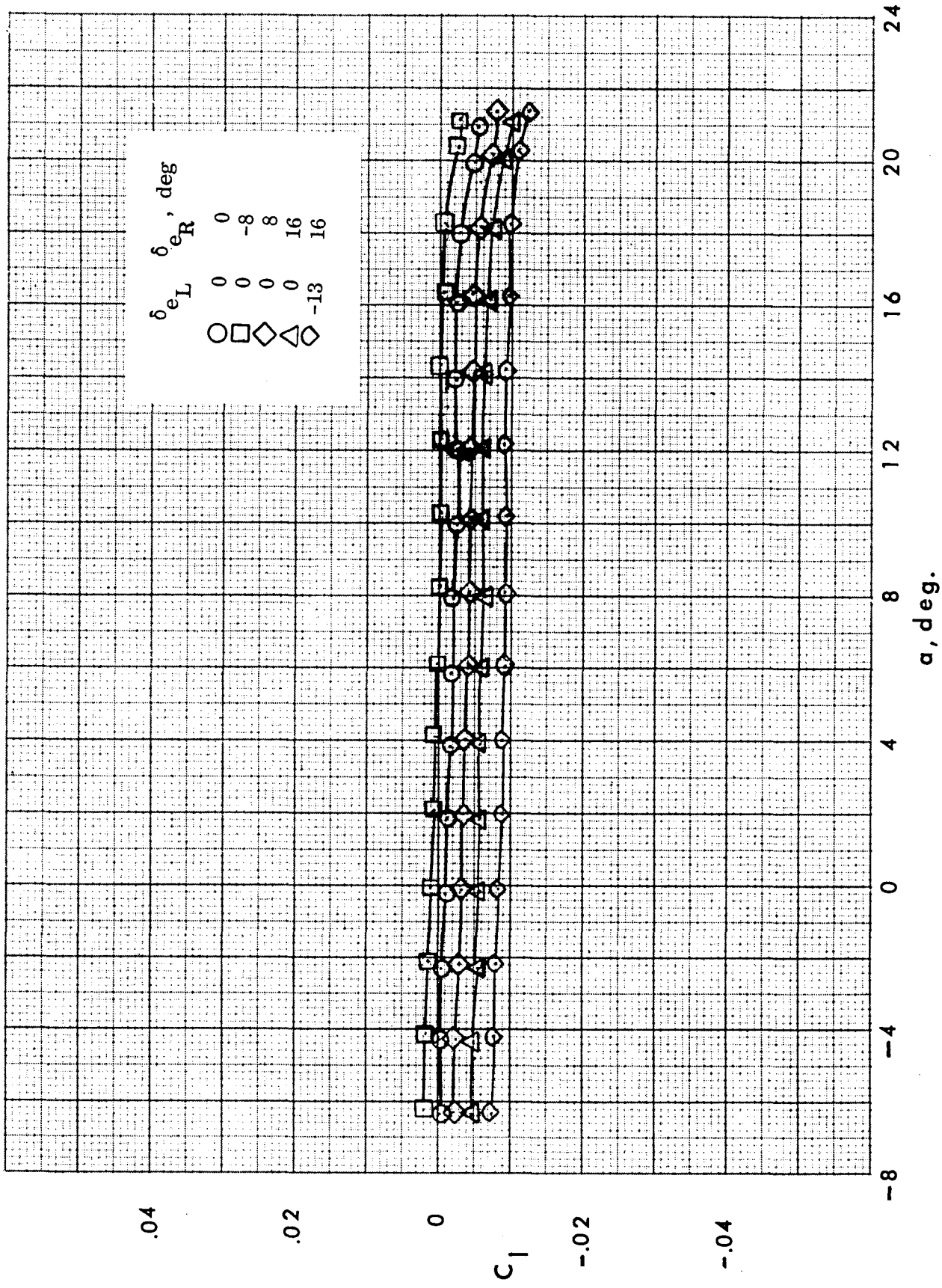


(a) $\beta = 1°$.

Figure 4-13. Variation of body-alone rolling moment coefficient with angle of attack for various elevon deflections. q = 60 psf.

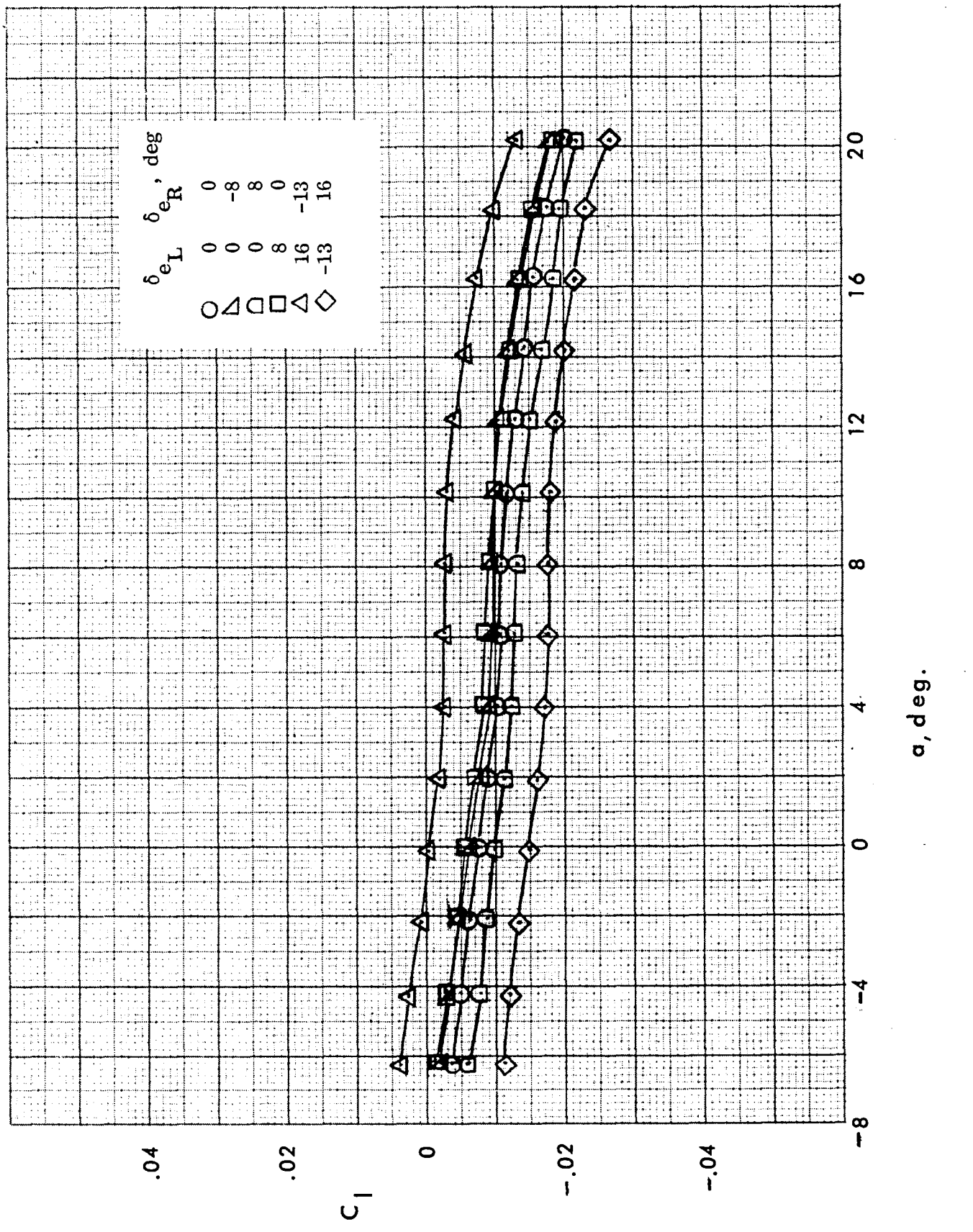


(b) $\beta = 6°$

Figure 4-13. Concluded.

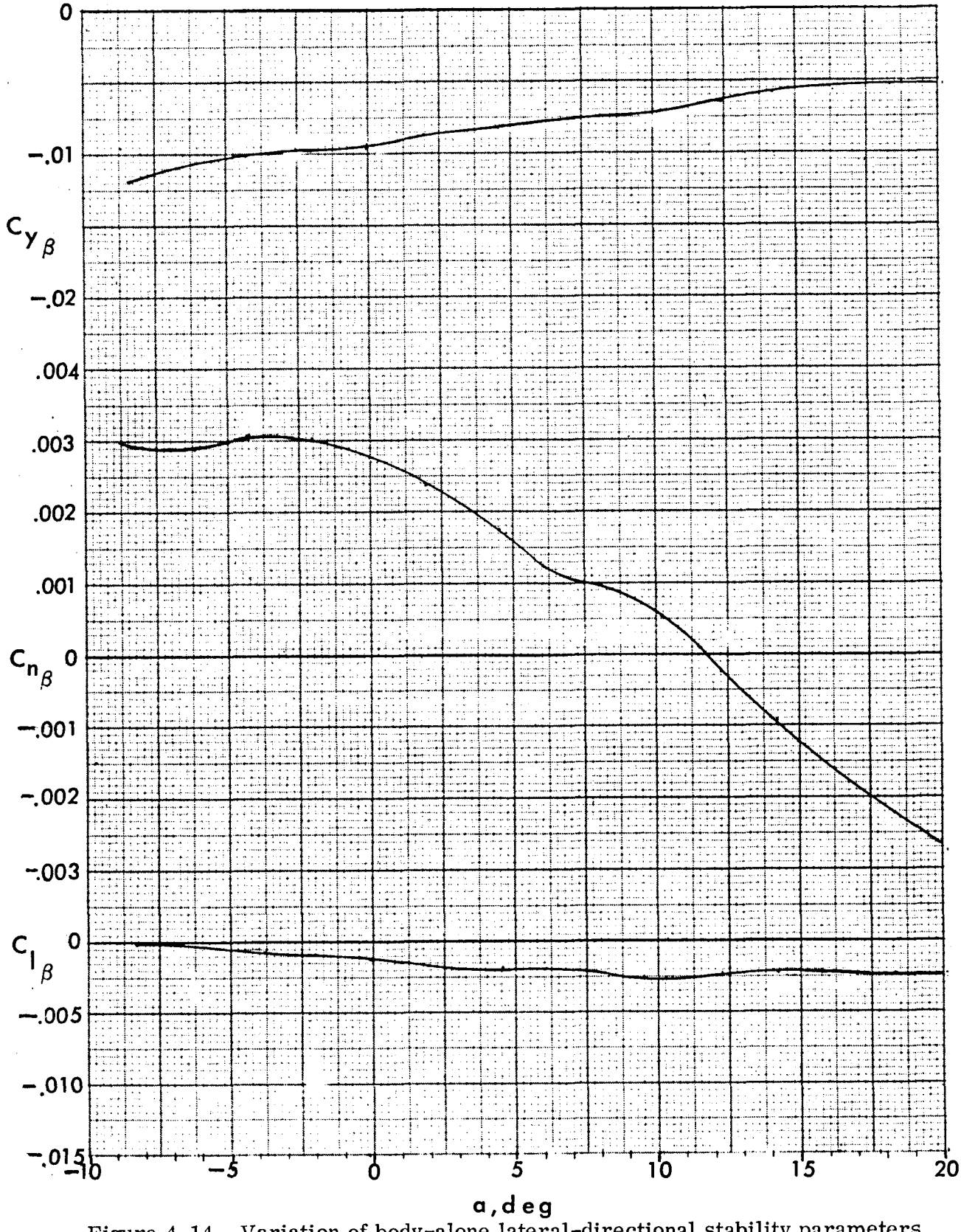


Figure 4-14. Variation of body-alone lateral-directional stability parameters with angle of attack. $\delta_{e_{L,R}} = 0°$, q = 60 psf.

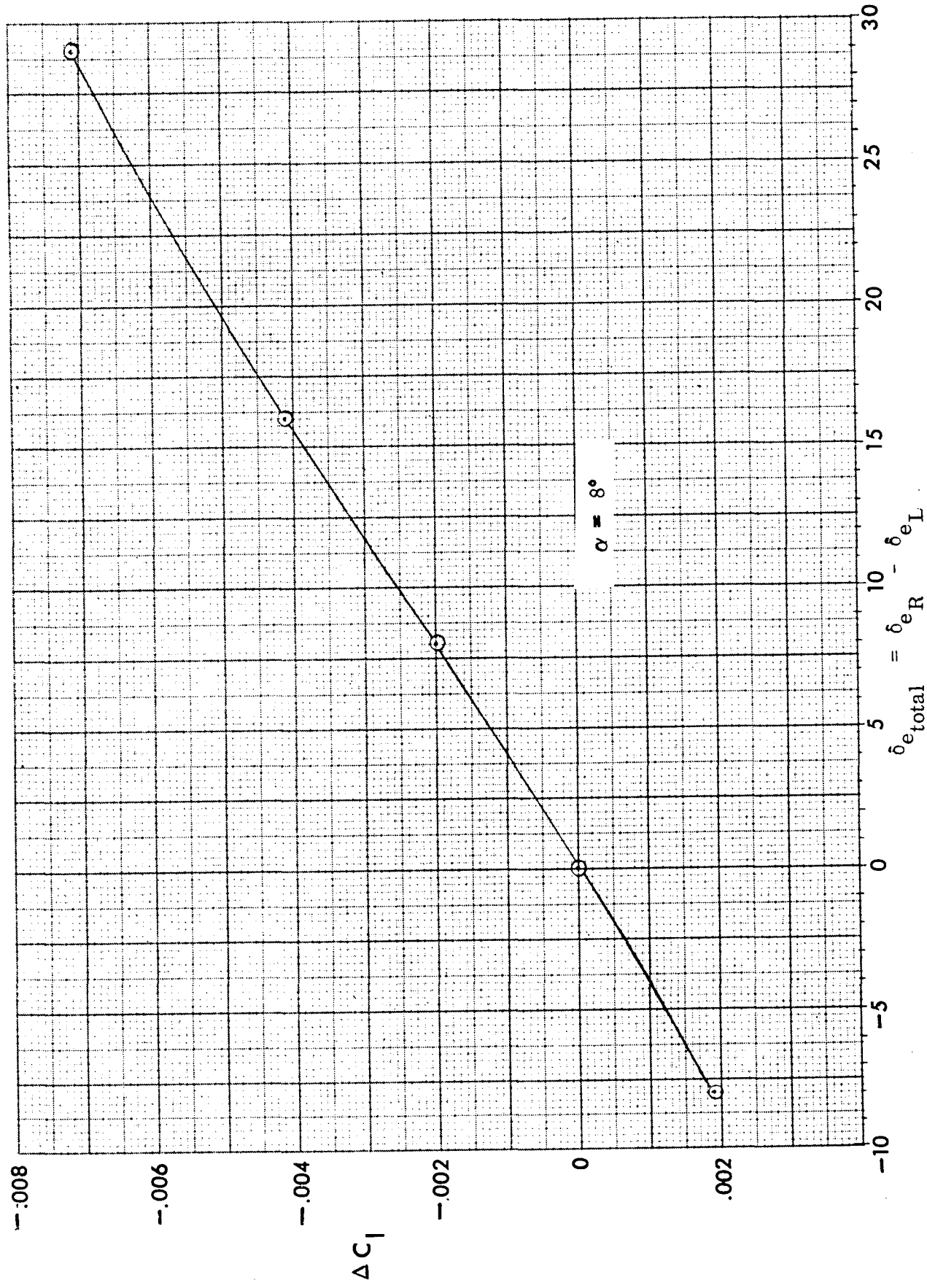


Figure 4-15. Rolling moment due to elevon deflection. $\beta = 1°$.

# SECTION 5
# WING-BODY CHARACTERISTICS

The experimentally determined aerodynamic characteristics of the DL-4 body in combination with the sailwing are presented in this section together with data on the effects of aerodynamic loads on the sailwing trailing-edge cable tension and the associated chordwise hinge moment.

## A. Longitudinal

Figures 5-1 through 5-7 summarize the longitudinal characteristics of the DL-4 body with the sailwing deployed. The effect of dynamic pressure on the variation of lift, drag, and pitching moment coefficients with angle of attack, and on the drag polar and lift-to-drag ratio is shown in Figure 5-1 for a constant initial cable tension, $T_o$, of 80 pounds. It is seen that the lift curve slope at positive angles of attack is fairly constant at about 0.074 per degree, based on body-alone plan form area. Noteworthy is the upward shift of the lift curve with increasing dynamic pressure and the change in lift-curve slope which occurs at about -2.5° angle of attack for q = 60 and 45 psf. Both these effects can be attributed directly to the flexibility and the elasticity of the sailwing. The former indicates that the sailwing takes on greater camber with increasing dynamic pressure. The latter effect is produced by camber reversal and is encountered as the wing goes through the zero-lift air load condition. It depends roughly on the ratio of dynamic pressure to trailing-edge cable tension. For high dynamic pressures the transition from positive to negative camber takes place quite rapidly, resulting in a very steep lift-curve slope in this region. If the sail fabric constraint (tension) is increased by increasing trailing edge cable tension, or by lowering the dynamic pressure, this transition in airfoil section camber shape becomes less pronounced. These effects are visible in Figures 5-1, 5-2, and 5-3. It is noted that trailing edge cable tension does not greatly affect the lifting performance of the wing at positive angles of attack.

The drag data presented in Figures 5-1 through 5-3 indicate the minimum drag coefficient to vary from 0.055 at q = 15 psf to 0.070 at q = 60 psf, with an induced drag factor K of about 0.15. Moreover, the data show a negligible effect of cable

tension on drag coefficient at q = 30 psf, and only a small change at q = 60 psf for small angles of attack. The sense of the change is for decreasing $C_{D_{min}}$ with increasing cable tension, i.e., the drag is lowered as the wing camber decreases. The lateral-directional test runs, in which a range of wing tip deflections were tested to determine the roll control effectiveness of such a wing warping technique, indicated a change in $C_{D_{min}}$ of only 0.01 from full up to full down wing tip deflection. At higher angles of attack the increment in drag due to wing tip deflection is higher, reflecting a change in the flow field caused by the warped wing extremity. A cross plot of such data at an angle of attack of 8° is presented in Figure 5-4 which shows the incremental change in drag coefficient to be about 0.0024 per degree wing tip deflection for deflections greater than 4°.

As shown in Figure 5-3(c), the highest lift-to-drag ratio attained in the longitudinal test runs for the wing-body combination was 7.1, for a pre-set cable tension of 100 pounds and a dynamic pressure of 60 psf. The highest lift-to-drag ratio attained by the DL-4 body alone was only 2.20.

The pitching moment behavior of the sailwing is illustrated by Figures 5-1 through 5-3. Figure 5-1 shows the pitching moment variation with both angle of attack and lift coefficient for a constant trailing-edge cable tension, at dynamic pressures of 15, 30, 45, and 60 psf. The effect to be noted here is the non-linearity which results when the dynamic pressure is increased in the angle of attack range of 0° to -5°. This non-linearity corresponds to the observed changes in the lift-curve slope mentioned earlier which results from the camber reversal of the sailwing. In the angle of attack range of -5° to -2° the pitching moment coefficient (based on body length and planform area) changes from about -.006 to -.034 for a q of 60 psf as shown in Figure 5-1(a). It can be seen that the slope of the moment curve on either side of this discontinuity is positive, indicating a slight static instability about the moment reference center used in the wind tunnel tests. For angles of attack on either side of the discontinuity region the aerodynamic center lies at about 1.25% body length ahead of the moment reference center. In the camber reversal region it moves to about 6% of the body length behind the moment reference center.

The phenomenon of increasing camber with dynamic pressure is readily apparent in Figure 5-1 (a) as a consistently downward shift of the pitching moment curve with increasing dynamic pressure. A change in the flow pattern at an angle of attack of about 16° is indicated by the change in the slope of the pitching moment coefficient, signifying a rearward shift of the aerodynamic center and, possibly, the onset of stall, which is not clearly discernible from the lift data.

A hysteresis was noted in the pitching moment data due to the fact that wing camber reversal occurred at different angles of attack, depending on whether the angle of attack was increasing or decreasing. This hysteresis is not observable in the figures presented here, however. If passage through this angle of attack range was slow, it was noted that the left and right wings could maintain opposite cambers, although this was more often observed if a wing tip was deflected. This, of course, produces a large rolling moment and is discussed below. It is noted that reducing the tension in the trailing edge cable allows the wing to camber more, thus lowering the pitching moment coefficient curve and increasing the slope of the moment curve in the camber reversal region. These effects are seen in Figures 5-2(a) and 5-3(a).

The effect of using wing tip deflection as a roll control device on the vehicle pitching moment may be seen to be small by referring to Figure 5-5. In this figure are plotted $C_m$ versus $\alpha$ at dynamic pressures of 30 and 60 psf for right wingtip deflections of +16, -7, and 0 degrees. The difference between these curves for the two extreme deflections is 10% or less.

The effects of sail elasticity may be clarified by Figure 5-6 which shows the variation of $C_m$ with dynamic pressure for several cable tensions. This plot reveals a negative speed stability derivative $C_{m_V}$ $(= \frac{\partial C_m}{\partial V})$. The figure also indicates the degree to which the sail cloth developed a permanent set following its initial loading in the first group of test runs. It was noted after the conclusion of the first several runs (at $T_o$ = 80 lbs) that the cable tension had dropped from the value at which it had been set before the test; subsequent runs showed no further discrepancies. The initial stretching of the cloth is apparent in Figure 5-6 wherein it is seen that for the points designating $T_o$ = 80 lbs, the $C_m$ value travels from a pre-set value near the higher cable tension toward a value corresponding to a lower cable tension.

A comparison of the pitching moment characteristics of the body alone, and the sailwing-body combination is presented in Figure 5-7 (a) for elevons in the neutral position and for maximum upward deflection. For the body alone, the elevons are capable of producing sufficiently large nose up increment for trim about the moment reference center over the angles of attack range tested. For the body with sailwing, however, the elevons are incapable of trimming the winged vehicle in the intermediate angle of attack range of -4° to +12°. A comparison of the body alone and wing-body curves for elevons in neutral shows that the sailwing introduces a negative pitching moment increment for angles of attack greater than -2°, where the camber is positive, and a positive increment for angles less than -4°, where the sailwing camber has reversed its shape. The elevon control power can be increased, and the static stability helped, by enlarging and relocating the elevons. In this connection, increasing their span so that they extended beyond the sides of the body would make them more effective. The pitching moment increment produced by the sailwing camber could be offset by the addition of stabilizing fins. A combination of these modifications could easily provide the degree of control effectiveness and static stability sought for in a particular application.

Reducing the size of the sailwing, relative to the body size, would reduce the pitching moment due to sailwing camber, and make it possible for the elevons tested to provide trim over the angle of attack range. Thus, as shown in Figure 5-7 (b), the elevons would have sufficient control power for the trimmed flight of a downsized sailwing-body combination. This sailwing would have 50% of the exposed area of the nominal size wing tested. Both these wing sizes were studied in the trade study described in Section 8, in which it is shown that, for the application considered, the downsized wing provides satisfactory landing performance, and weighs less than an equivalent rigid (metallic) wing. The estimated pitching moment curves for the downsized sailwing-body combination shown in Figure 5-7 (b) are based on the body-alone elevon data, together with the nominal sailwing-body data scaled down by the ratio of exposed wing areas.

B. Lateral-Directional

Figures 5-8 through 5-12 present the rolling moment coefficient versus angle of attack for various dynamic pressures and wing tip deflections, with the cable tension

preset to 80 lbs. The rolling moment coefficient is based upon the planform area and span of the body.

Figure 5-8 shows the rolling moment coefficient at dynamic pressures of 15, 30, 45, and 60 psf, for a yaw of one degree (the reason for this was mentioned earlier), and the wingtips in their undeflected positions. It is seen that an undesired rolling moment is present, amounting to a $C_\ell$ of about 0.040. It was found that the left wingtip, in its undeflected position, was misaligned about 2.5°, trailing edge down, from the neutral position, thereby creating a small positive rolling moment. Another contributing factor may have been slight differences in fabric tension between the left and right wing which makes the left wing, through different camber, have a slightly higher effective angle of attack than the right wing, thereby generating a positive rolling moment, and also causing this wing to stall first. This latter point explains the rapid reversal of the sense of the rolling moment at high angles of attack. The left wing stalls, and the right wing, still generating lift, creates a negative rolling moment. The differences in fabric tension that would cause this could not be determined from these tests.

An interesting consequence of these wing structure anomalies is shown by the peaks in two of the curves of Figure 5-8 and those following. Beginning at negative angles of attack we see that as angle of attack is increased the aforementioned camber reversal occurs first in the left wing (because its trailing edge was misaligned downward) causing this wing to produce upward lift while the right wing is still producing downward lift, thereby producing a large positive rolling moment. As the angle of attack is increased further, the right wing undergoes camber reversal, and the rolling moment returns to its "normal" value, determined by the wing tip setting.

Shown in Figures 5-8 and 5-9 are curves of rolling moment coefficient versus angle of attack for various elevon deflections and sideslip angles, at dynamic pressures of 30 and 60 psf respectively. The effect of sideslip is apparent, i.e., a positive sideslip induces a negative rolling moment increment which reduces the positive rolling moment increment produced by the misaligned left wing tip. A negative sideslip angle of -6° generally induces a positive rolling moment as seen in Figure 5-9(c). This figure also shows that, for the positive deflections of the right wing tip (trailing edge down), as the angle of attack increases the rolling moment coefficient changes sign.

This is undoubtedly due to the right wing tip stalling out, making it possible for the positive rolling moment contribution of the left wing panel to overcome the reduced negative one of the right wing. A comparison of Figures 5-9 (a) and 5-10 (a) indicates that the change in rolling moment coefficient that occurs as the angle of attack changes from negative to positive is much less abrupt for the q = 30 psf case than for the 60 psf one. This is due to the more gradual nature of the camber reversal for the lower dynamic pressure than for the higher. In any case, it should be noted that this effect would not have been encountered if the left wing tip had been properly aligned.

The effectiveness of wing tip deflection as a roll control device is indicated in Figures 5-11 and 5-12. Shown plotted in Figure 5-11 (a) and (b) is the increment in rolling moment coefficient for a given increment in the right wing tip deflection for dynamic pressures of 30 and 60 psf respectively. An approximate value of $C_{\ell_{\delta_{WT}}}$ of -.0030 per degree is indicated for a dynamic pressure of 30 psf, and -.0040 for 60 psf. These are valid for angles of attack of 0° and 10° and for right wing tip deflections in the neighborhood of the neutral position. For a dynamic pressure of 30 psf it is seen that the roll effectiveness at 20° angle of attack is markedly lower, due probably to the imminence of stall. At a dynamic pressure of 60 psf, however, the roll effectiveness at this angle of attack is greater than that for the q = 30 psf case.

The effect of sideslip may be seen by comparing Figure 5-12 (a) and (b) to Figure 5-11 (b). It is seen that for the positive sideslip condition of 6° the roll control effectiveness is about the same as for the 1° case; whereas, for the -6° sideslip case the roll control effectiveness is diminished. This is due to the fact that the right wing is leeward for negative sideslip, and a reduction of its lift as compared to the left wing is therefore to be expected in any case.

It is estimated that by using only the deflection of one wing tip (16°) it is possible to obtain a value of the roll rate parameter, $\frac{pb}{2V}$, of about 0.18. If the elevons are used in conjunction with wing tip deflection this value increases only slightly to about 0.21. However, if only the elevons are used for roll control when the wing is deployed, a value of only about 0.03 can be generated, due to the smaller moment arm of the elevons as compared to the wing semispan.

The effect of wing tip deflection on yawing moment and side force coefficients at various angles of attack is shown in Figures 5-13 through 5-16 at dynamic pressures of 30 and 60 psf at sideslip angles of 1, 6 and -6 degrees.

The adverse yaw produced by wing tip deflection is evident in Figures 5-13 and 5-14. A positive wing tip deflection (trailing edge down) produces a positive increment in yawing moment due to the increased drag which accompanies the increased lift on the panel.

The wing-body sideslip derivatives are presented in Figure 5-17. They are based on the body axes system, and were evaluated using the differences between the measured coefficients at $\beta = 1°$ and $6°$. By comparison with the results presented in Figure 4-14 it is seen that the sailwing adds to both the directional stability ($C_{n_\beta}$) of the body, and the effective dihedral parameter ($-C_{\ell_\beta}$). It is observed that with the wing deployed the directional stability vanishes at a higher angle of attack (18°) than for the body alone (11.5°).

C. Cable Tension and Hinge Moment

The variation of trailing-edge cable tension with angle of attack for different dynamic pressures and different initial cable tensions is shown in Figures 5-18 and 5-19. It should be noted that the tension is represented in these figures in coefficient form, $C_T = \Delta T/qS$, in which the increment in tension above the preset value has been non-dimensionalized by the product of dynamic pressure and body planform area. This increment directly reflects the aerodynamic load on the sailwing, which is determined by the camber under a given set of conditions, and thus is high when the camber is high, in the cases of low initial tension or high dynamic pressures. Examination of Figures 5-18 (a) to (c) indicates the effect of sideslip to be small over the angle of attack range tested. It is noted that the cable tension was measured on the left wing, hinge moment on the right wing. This should be remembered when comparing the figures showing the cable tension to those presenting the hinge moment data. The data of Figures 5-18 and 5-19 correspond to both wing tips in their undeflected positions. Unfortunately, because only the right wing tip was deflected to different positions, and the cable tension was measured in the left wing, it was not possible to directly measure the effect of wing tip deflection on the incremental cable tension.

In Figure 5-19 the effect of cable tension is apparent. For the lowest preset cable tension, the camber was greatest, whence, the greater air load and associated incremental tension at a given angle of attack, compared to the other preset values tested.

The measured hinge moment data, expressed in inch-lbs, for the same test conditions corresponding to the cable tension data of Figures 5-18 (b) and (c), is presented in Figures 5-20 (a) and (b). It is noted that the data presented represents the increment in hinge moment above its initial value (produced by the preset cable tension) corresponding to the cable tension increment discussed above. It can be seen that the hinge-moment follows the same variations as the cable tension. No hinge moment data was obtained for the test conditions of Figure 5-18 (a) ($\beta = 1°$) because the strain gage on the right wing deployment link used to obtain hinge moment data proved unreliable in these runs. This gage was subsequently replaced with a load cell which furnished the data presented in Figures 5-20 to 5-22.

In Figures 5-21 and 5-22 hinge moment data is presented for right wing tip deflections of 12.5 and -7 degrees, respectively. The data indicates that, for a given wing tip deflection, the effect of sideslip is slight, as is the effect of wing tip deflection itself.

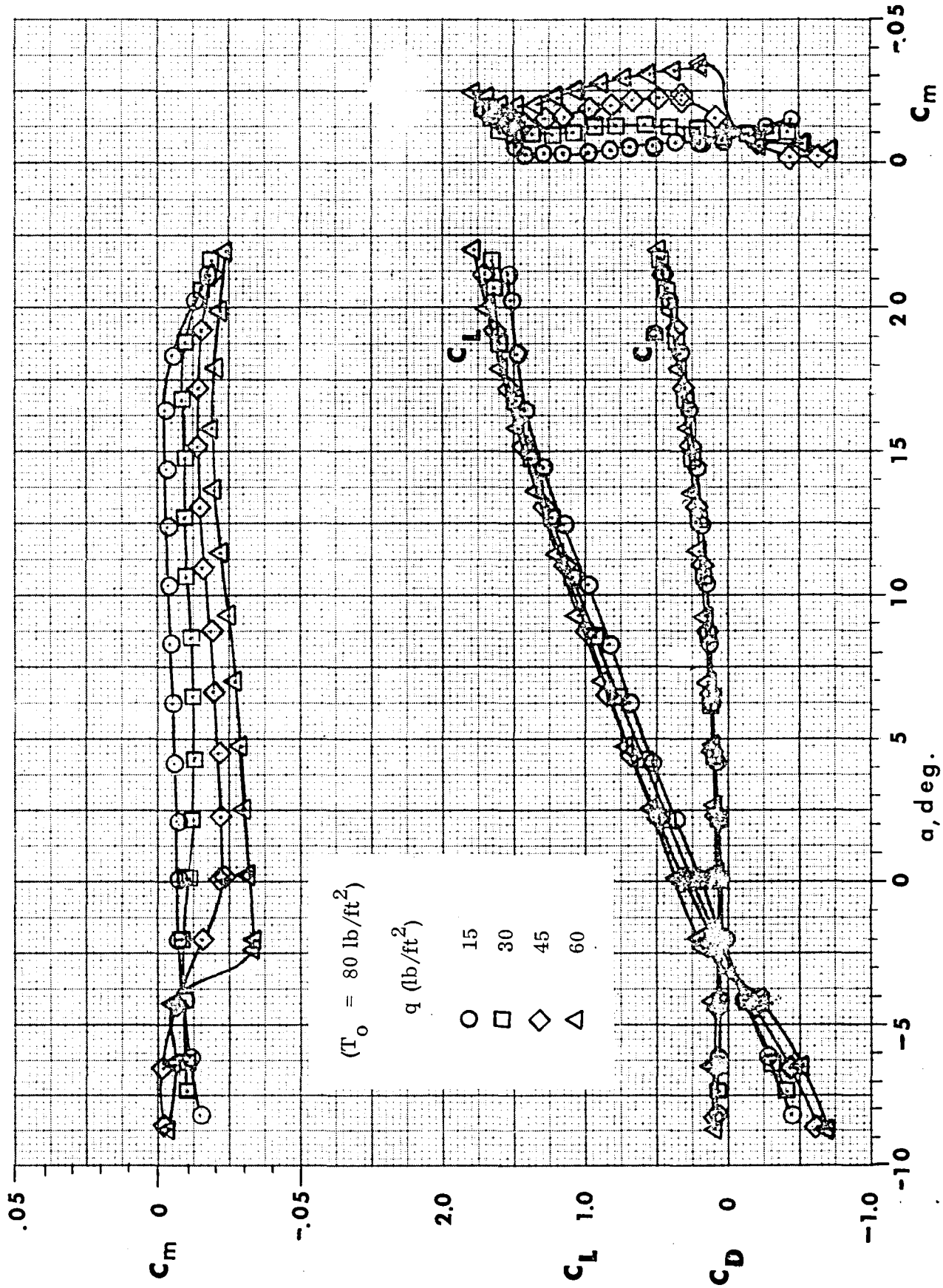


(a) Variation with angle of attack.

Figure 5-1. Wing-body longitudinal aerodynamic characteristics for several dynamic pressures. $T_o$ = 80 lbs.

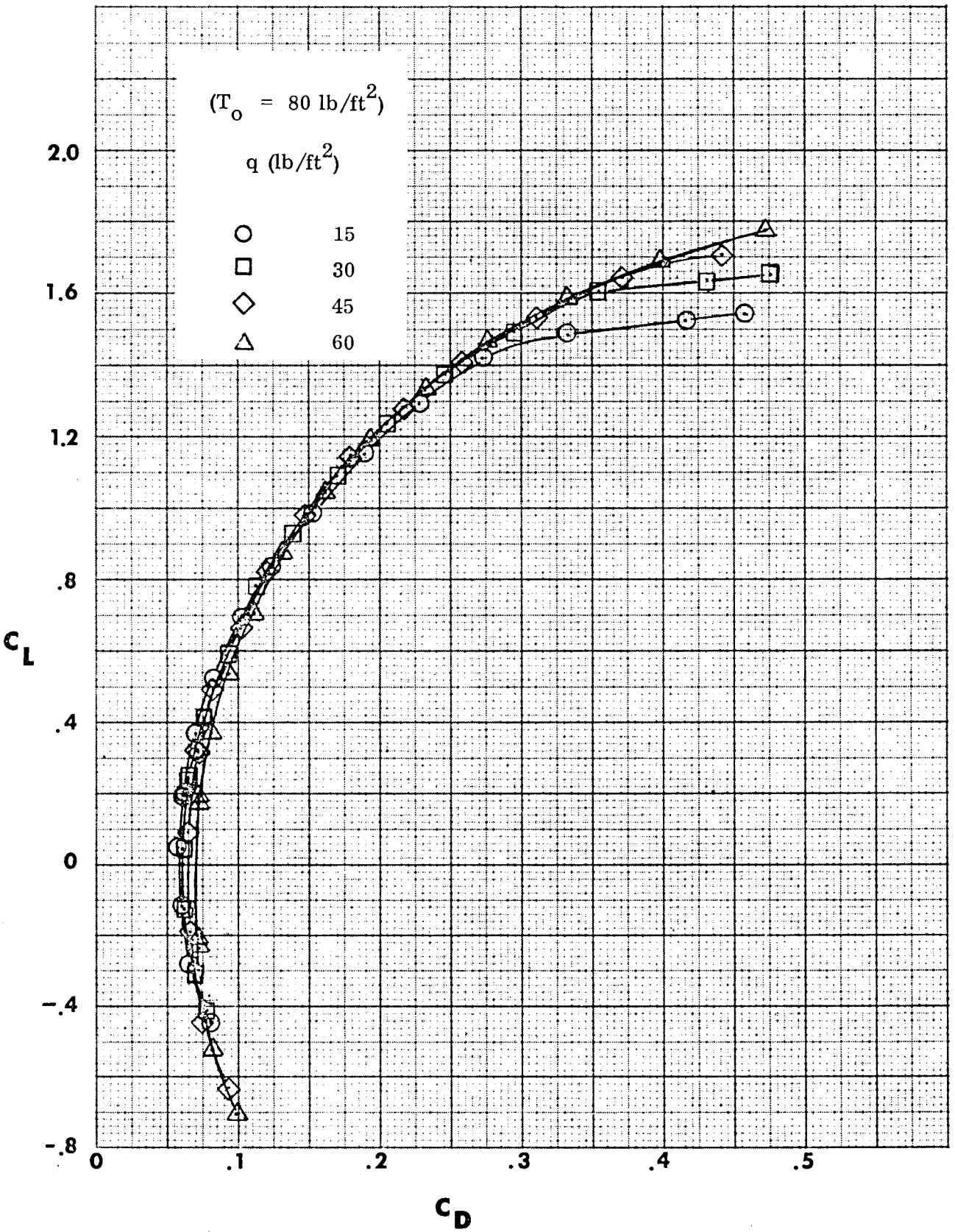


(b) Drag polar.

Figure 5-1. Continued.

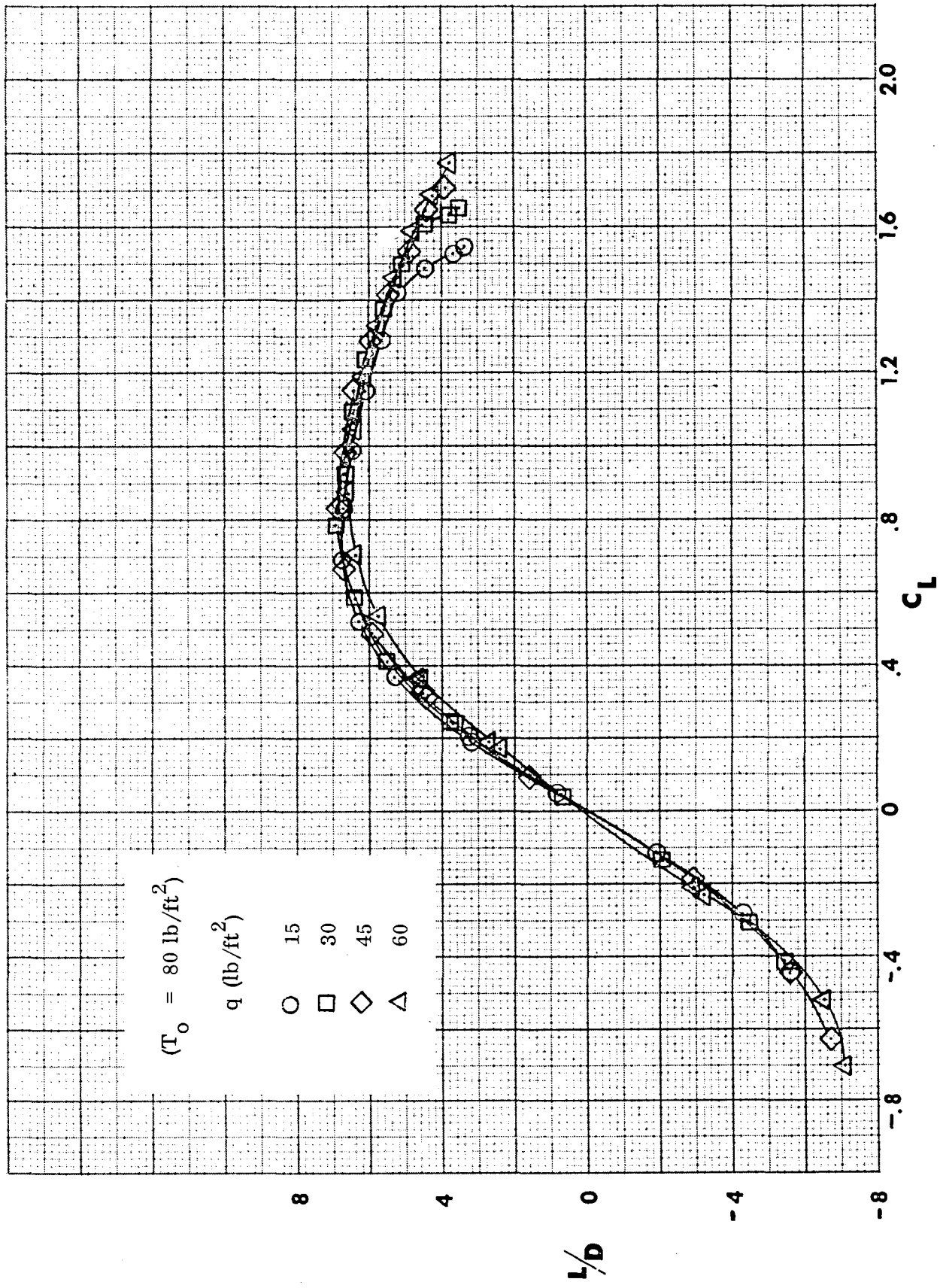


(c) Lift-drag ratio.

Figure 5-1. Concluded.

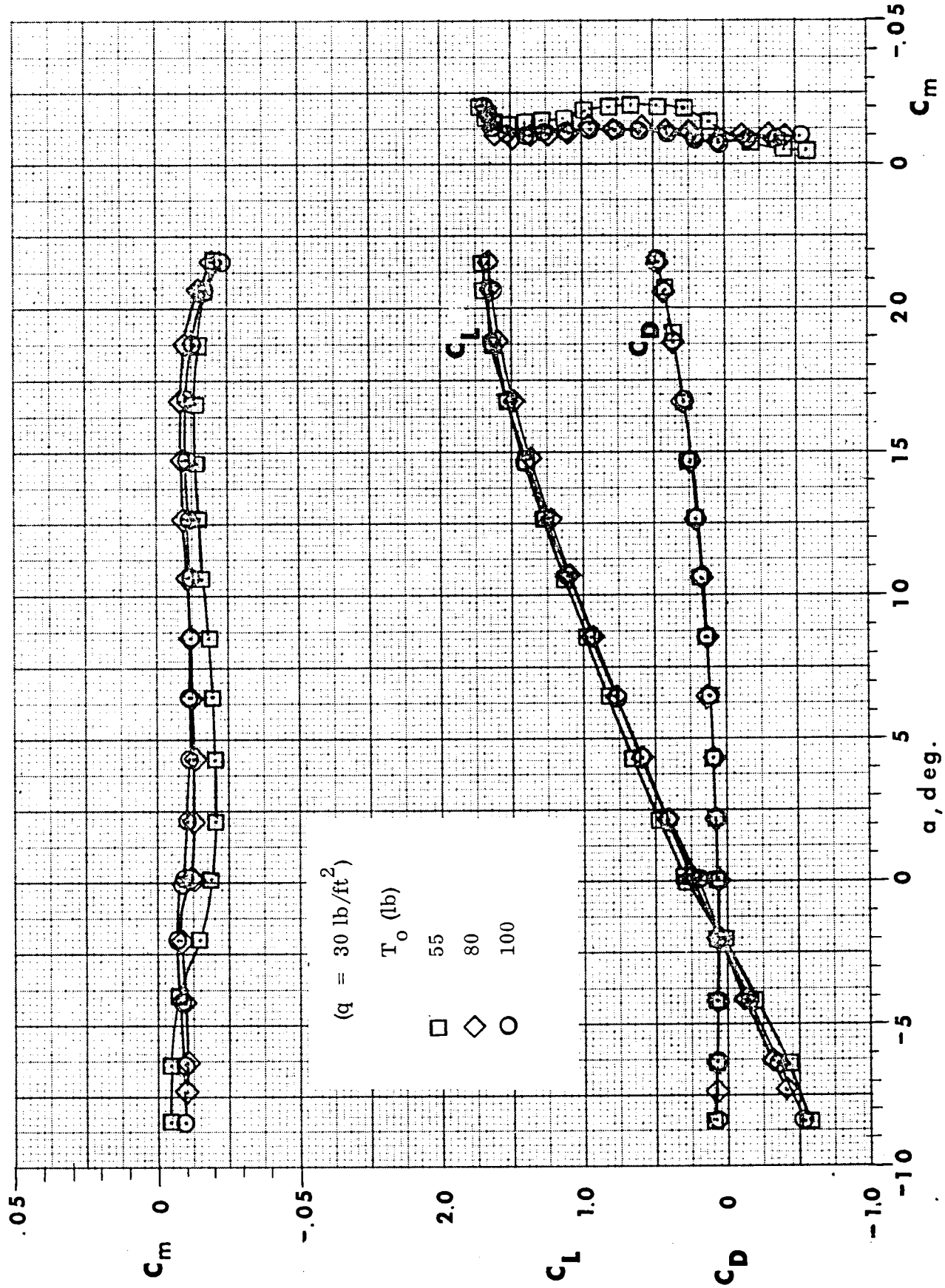


(a) Variation with angle of attack.

Figure 5-2. Wing-body longitudinal aerodynamic characteristics for several cable tensions. q = 30 psf.

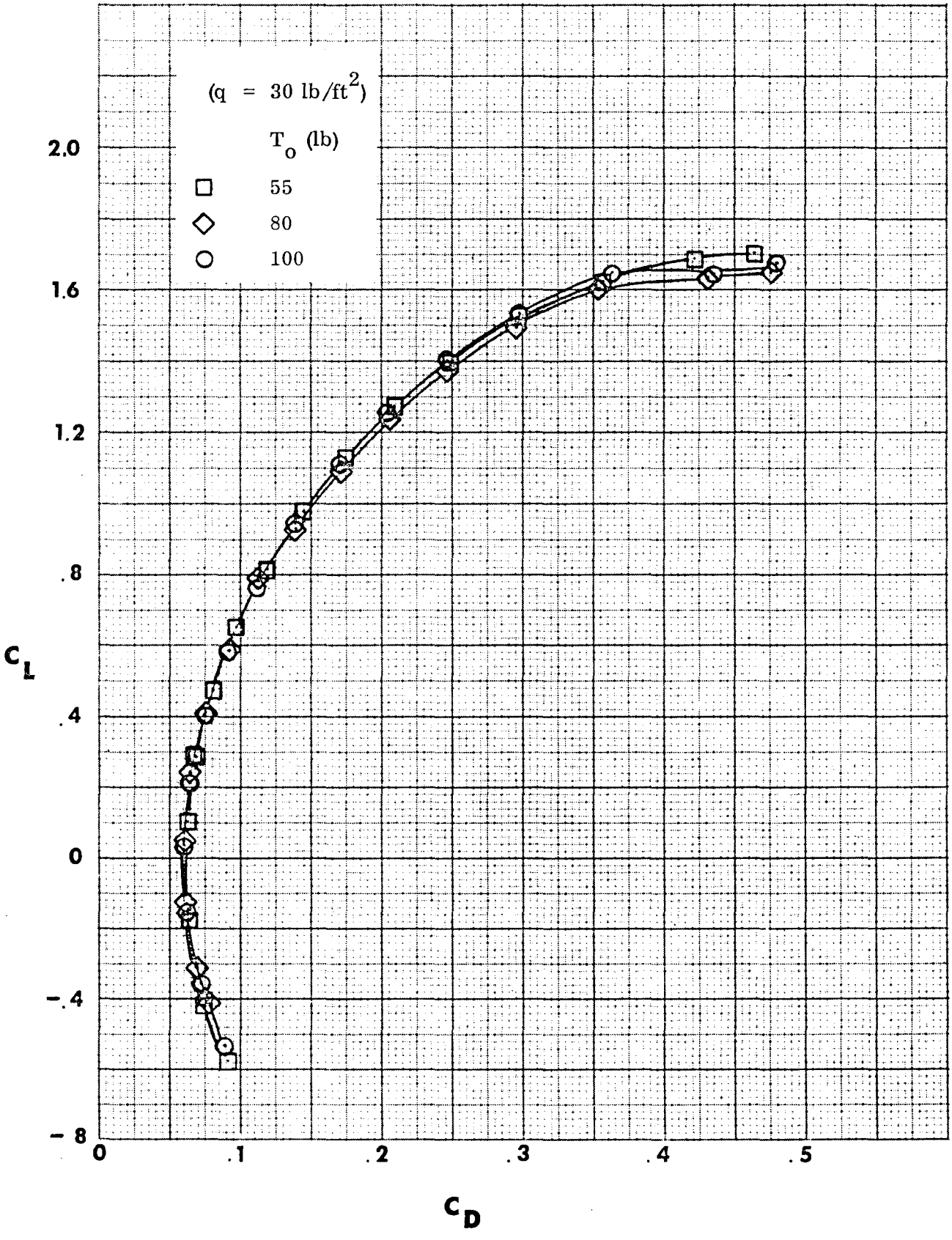


(b) Drag polar

Figure 5-2. Continued.

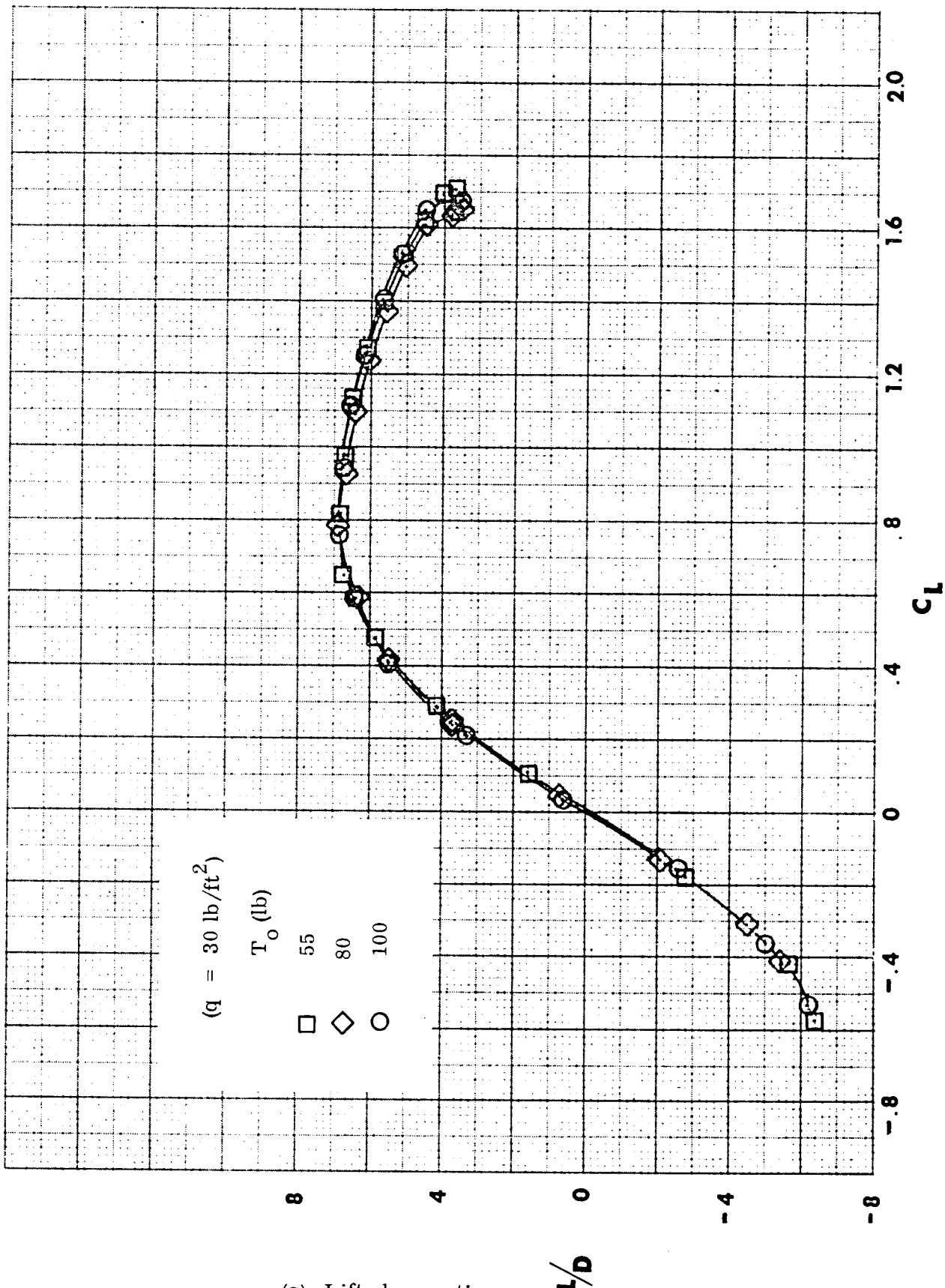


(c) Lift-drag ratio.

Figure 5-2. Concluded

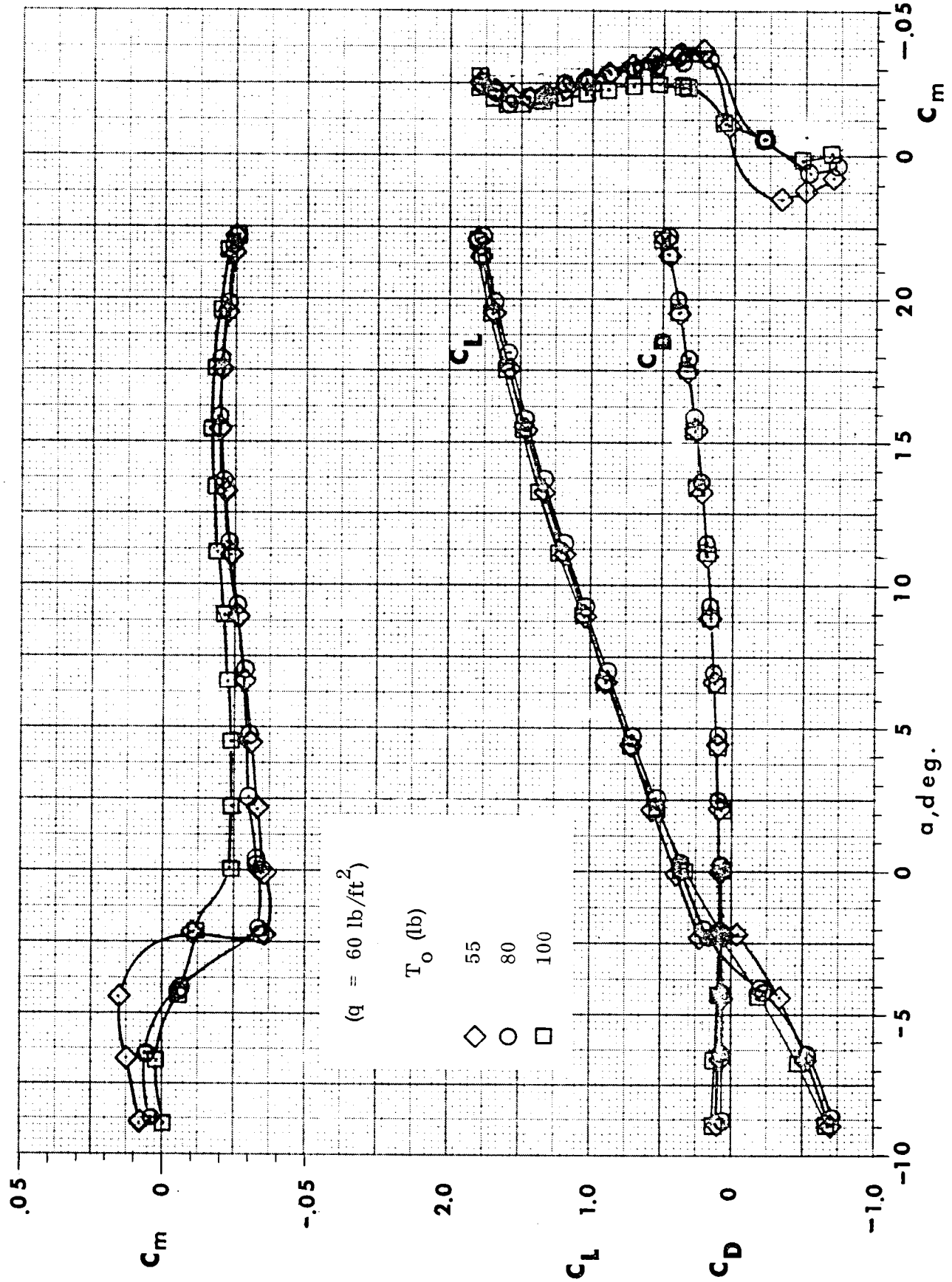


(a) Variation with angle of attack.

Figure 5-3. Wing-body longitudinal aerodynamic characteristics for several cable tensions. q = 60 psf.

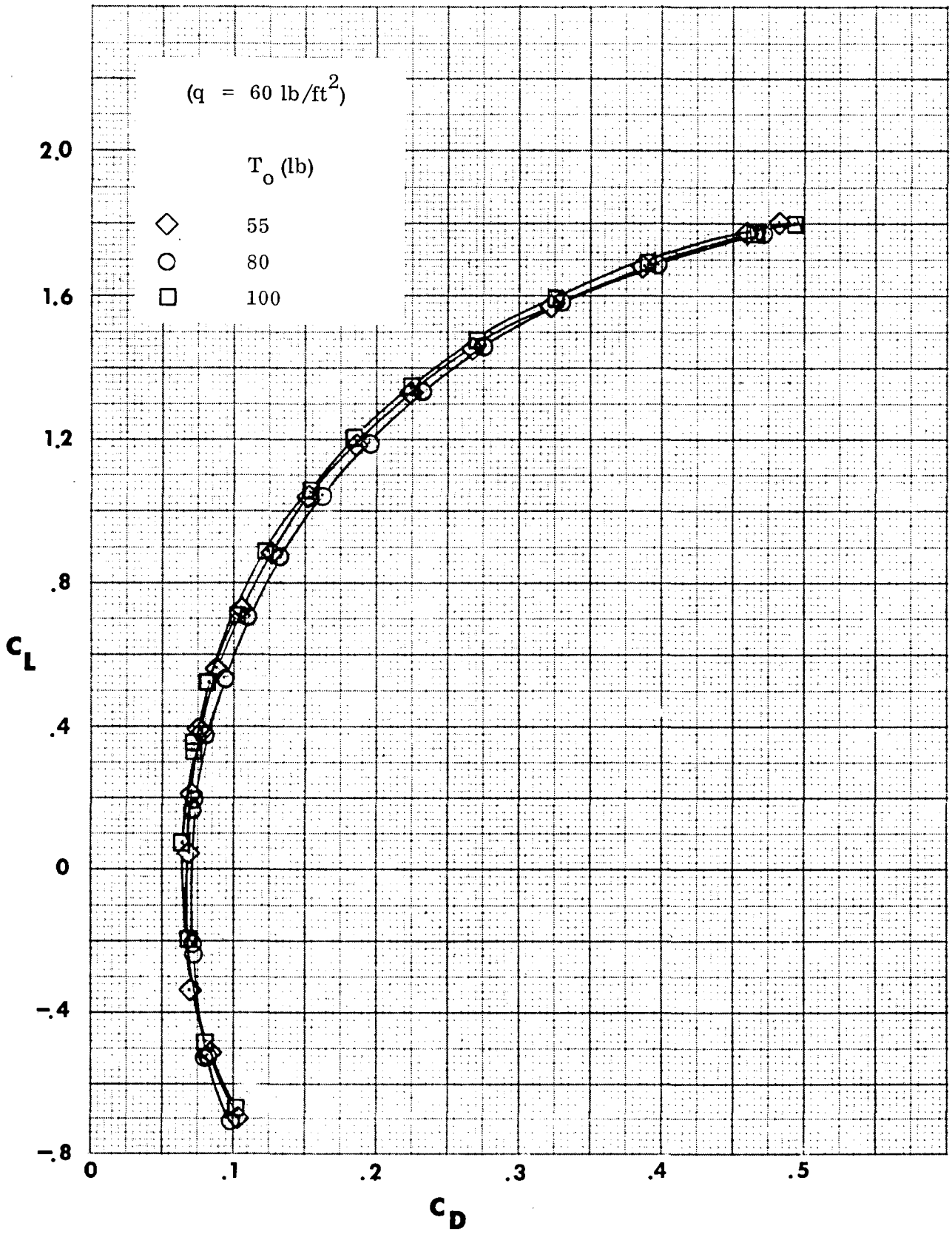


(b) Drag polar.

Figure 5-3. Continued

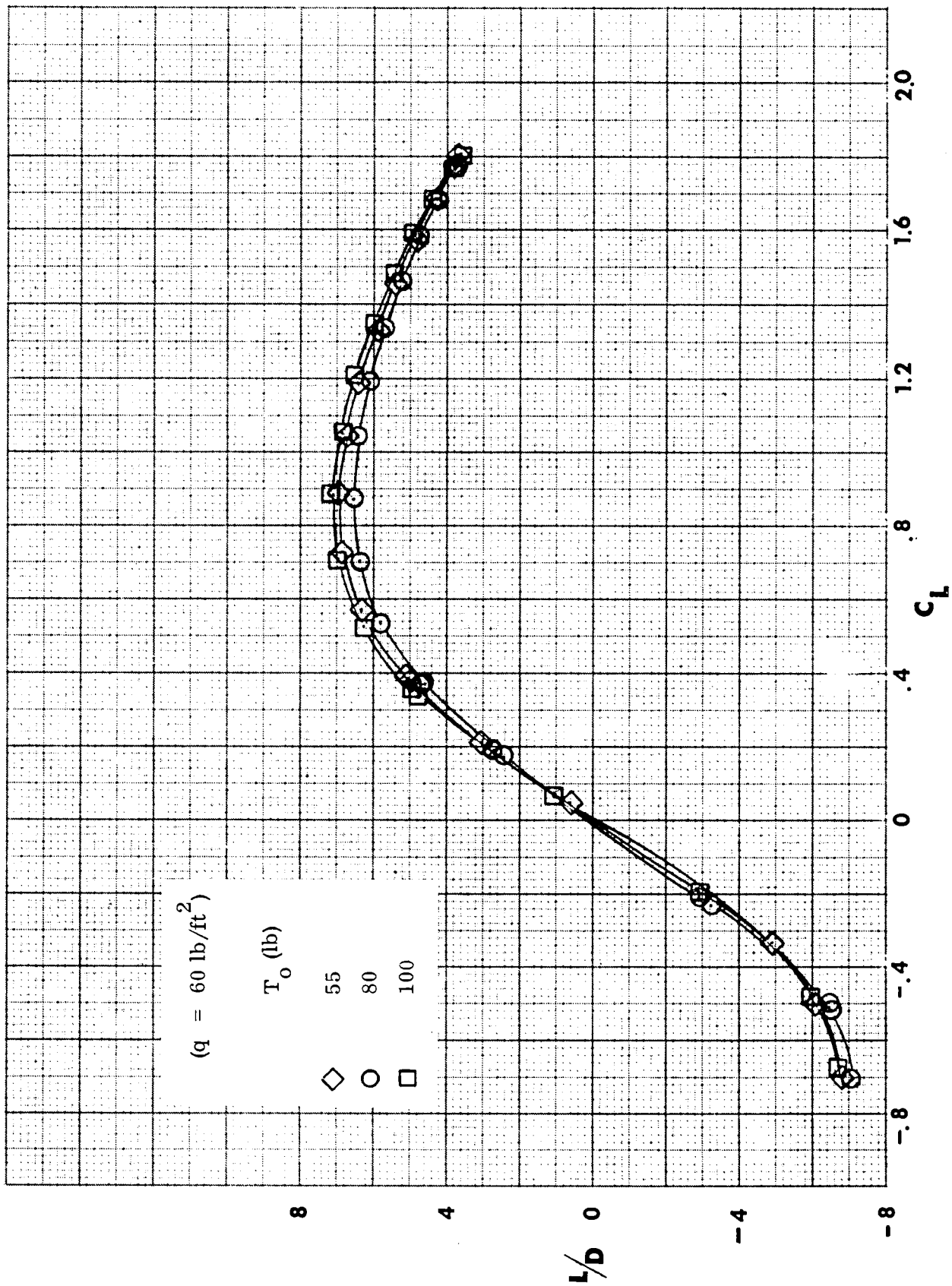


(c) Lift-drag ratio.

Figure 5-3. Concluded.

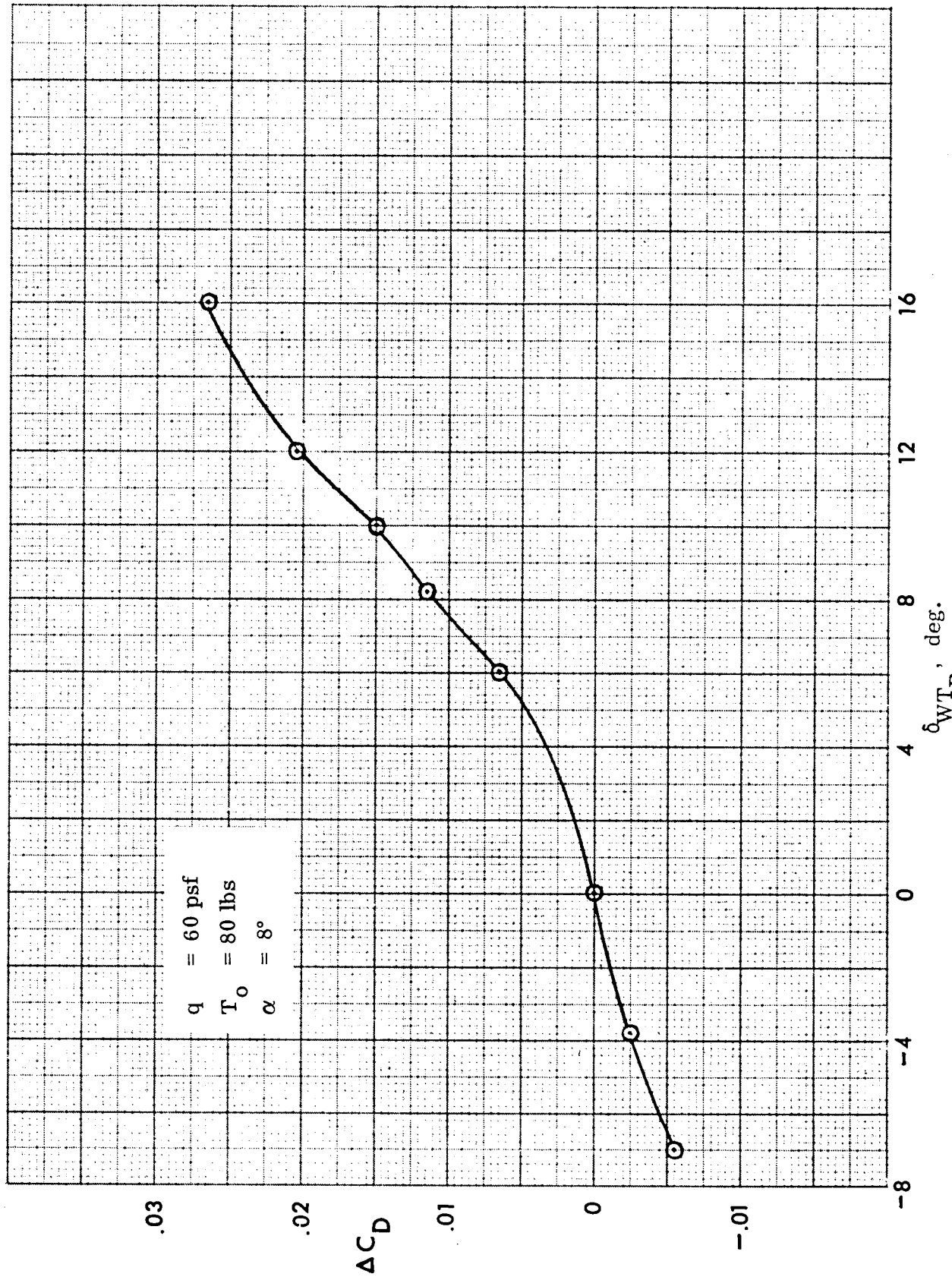


Figure 5-4. Drag increment due to wing-tip deflection.

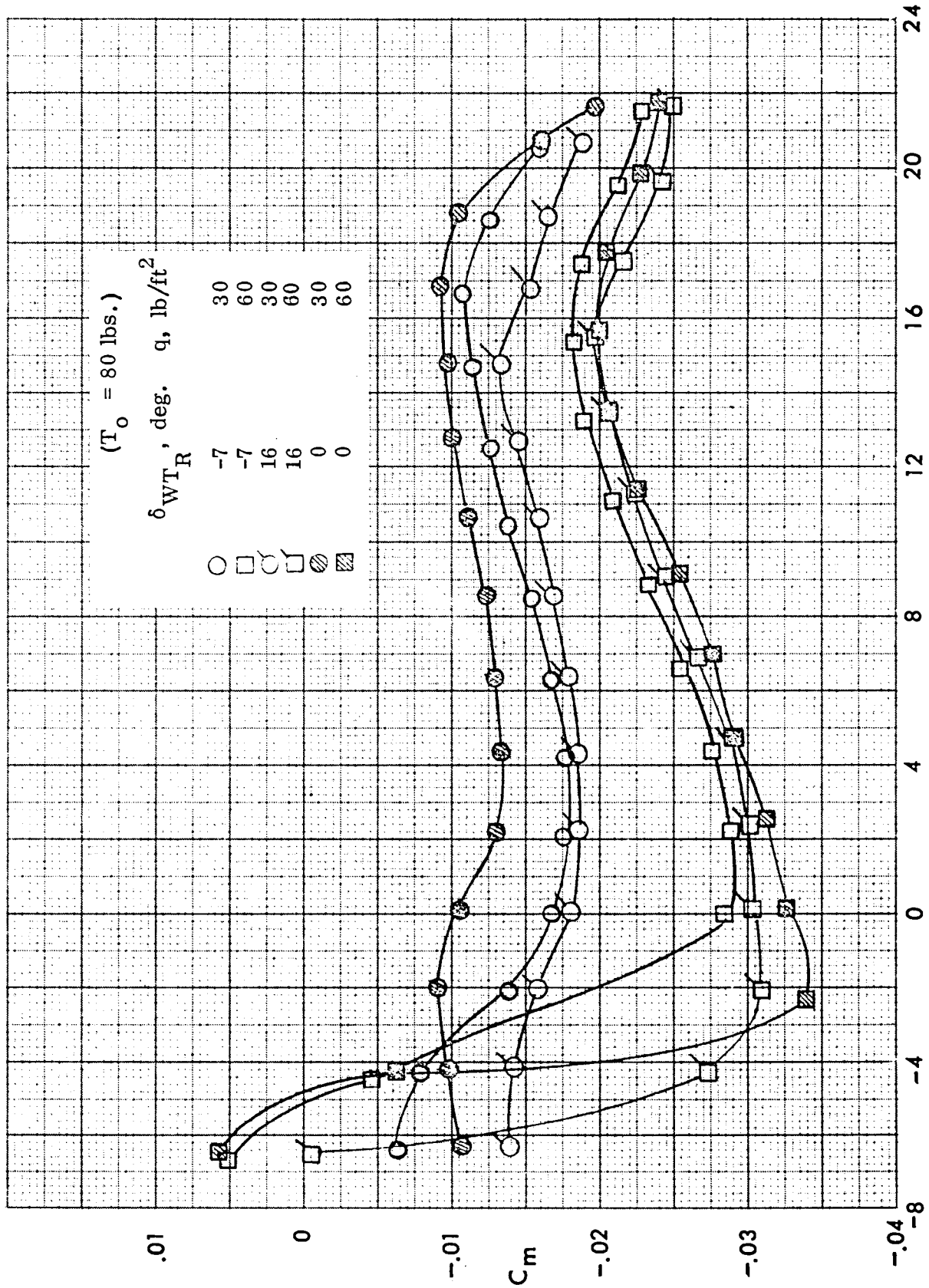


Figure 5-5. Effect of wing-tip deflection on pitching moment coefficient.

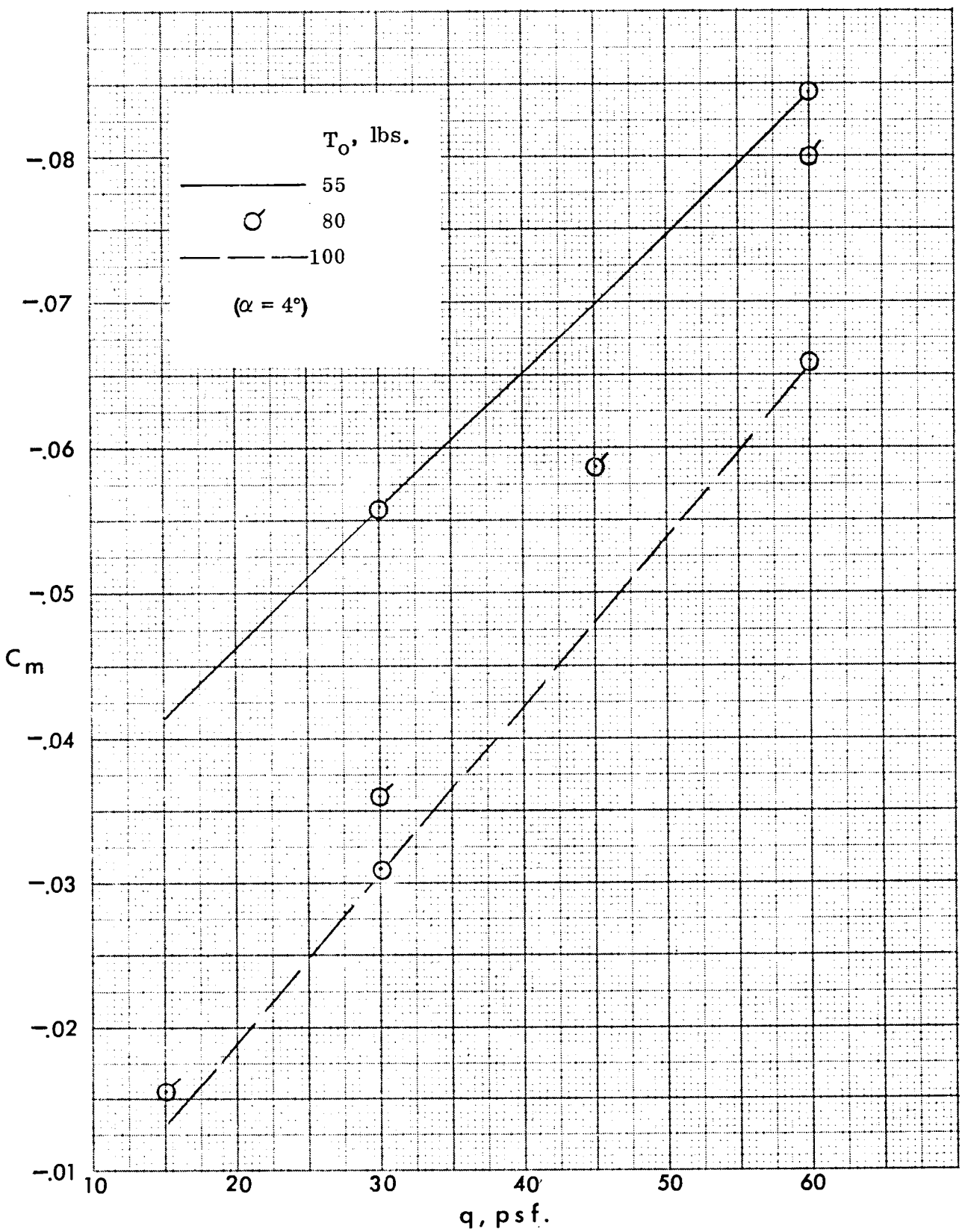


Figure 5-6. Effect of sail elasticity on pitching moment coefficient.

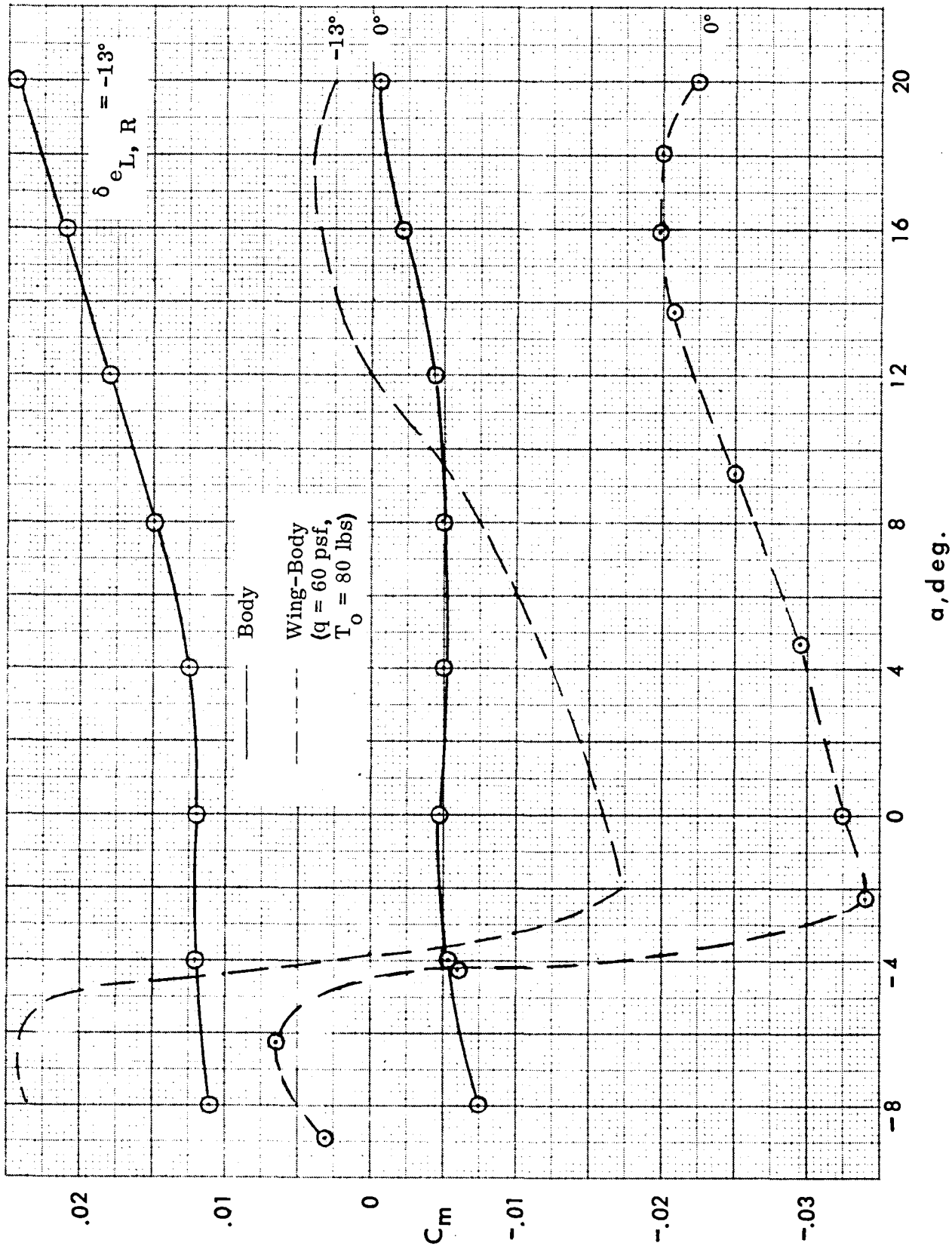


(a) Nominal sailwing.

Figure 5-7. Body-alone and wing-body pitching moment comparison.

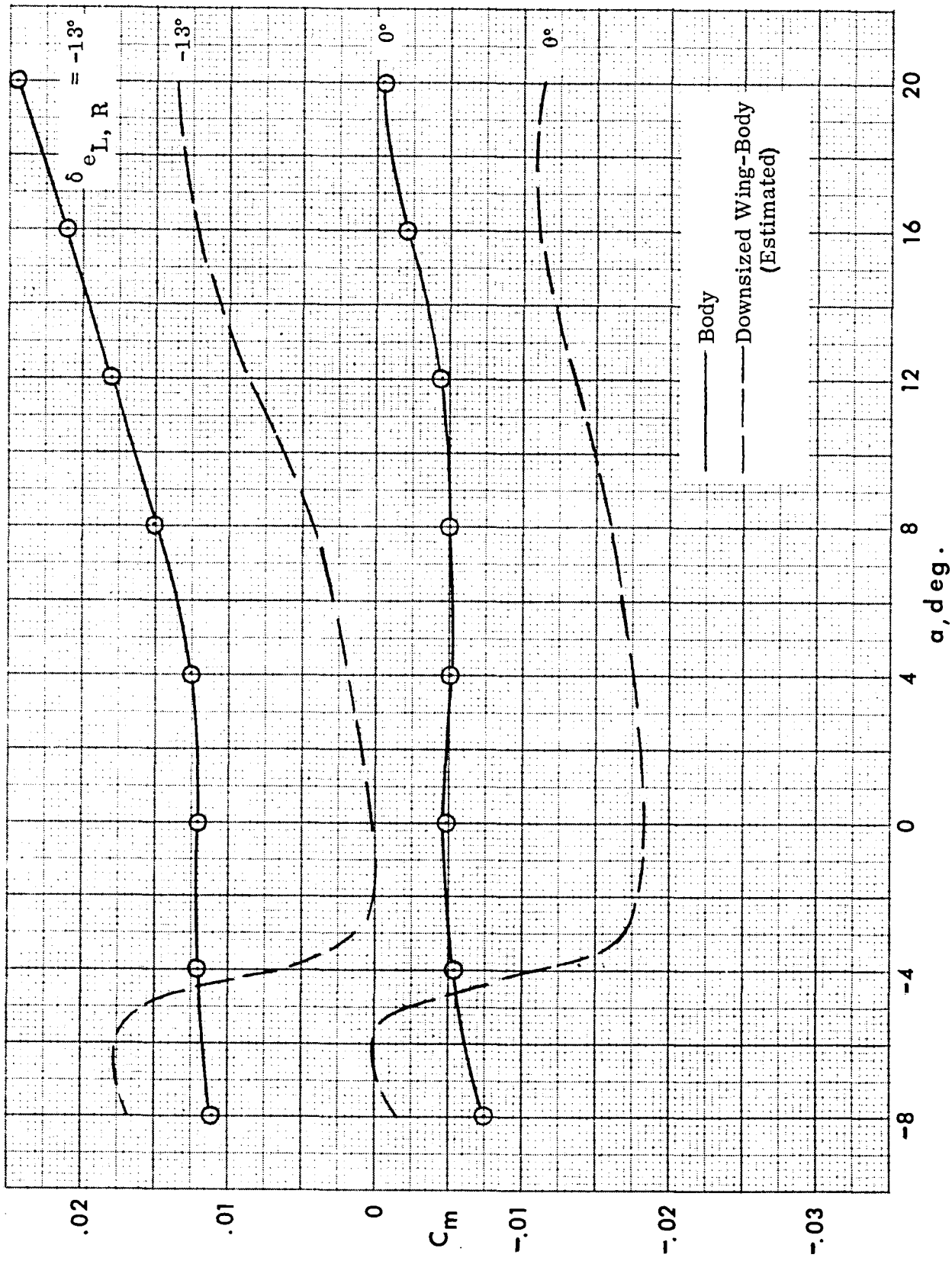


(b) Downsized sailwing.

Figure 5-7. Concluded.

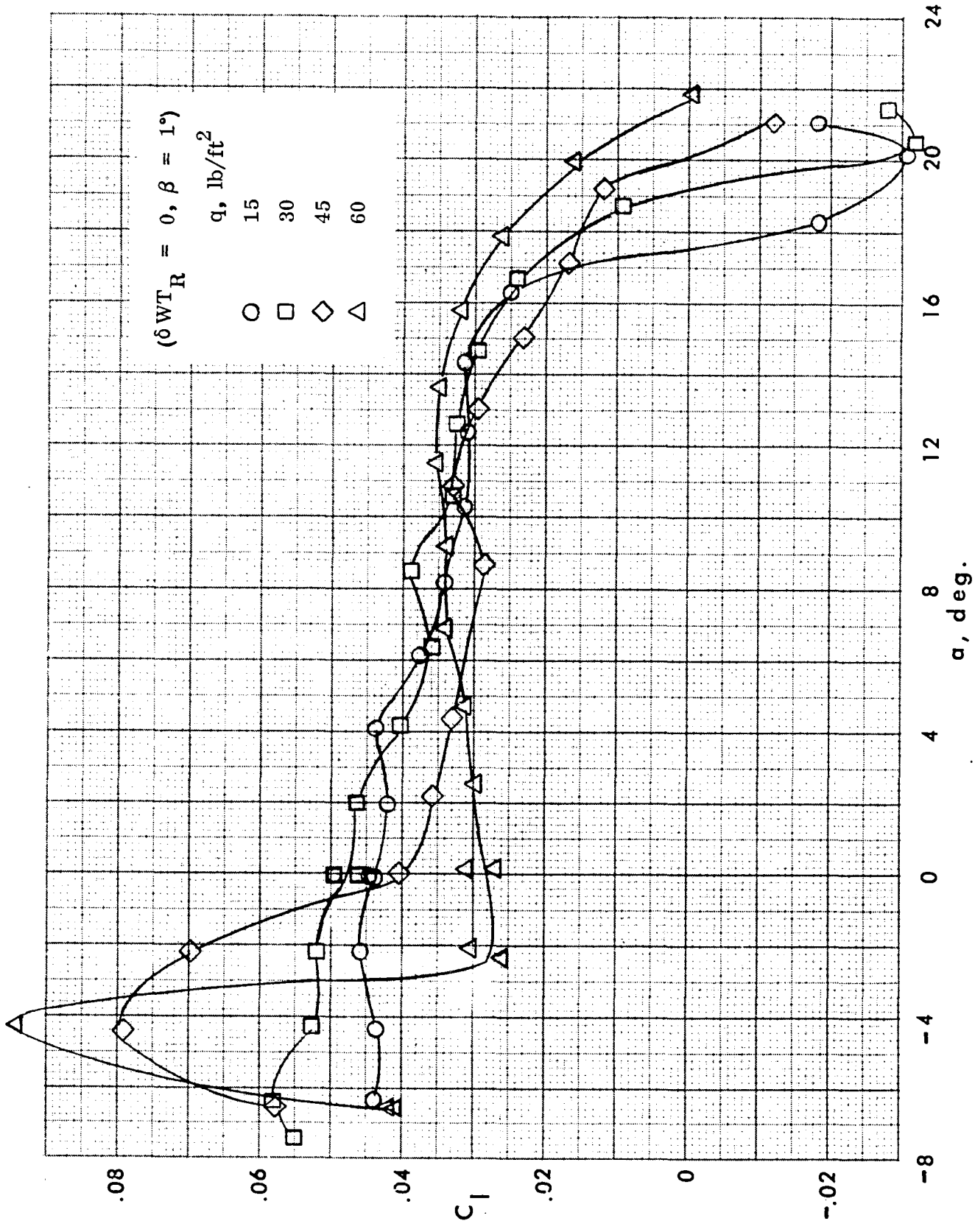


Figure 5-8. Effect of dynamic pressure on rolling moment coefficient, $\delta_{WT_R} = 0°$, $\beta = 1°$.

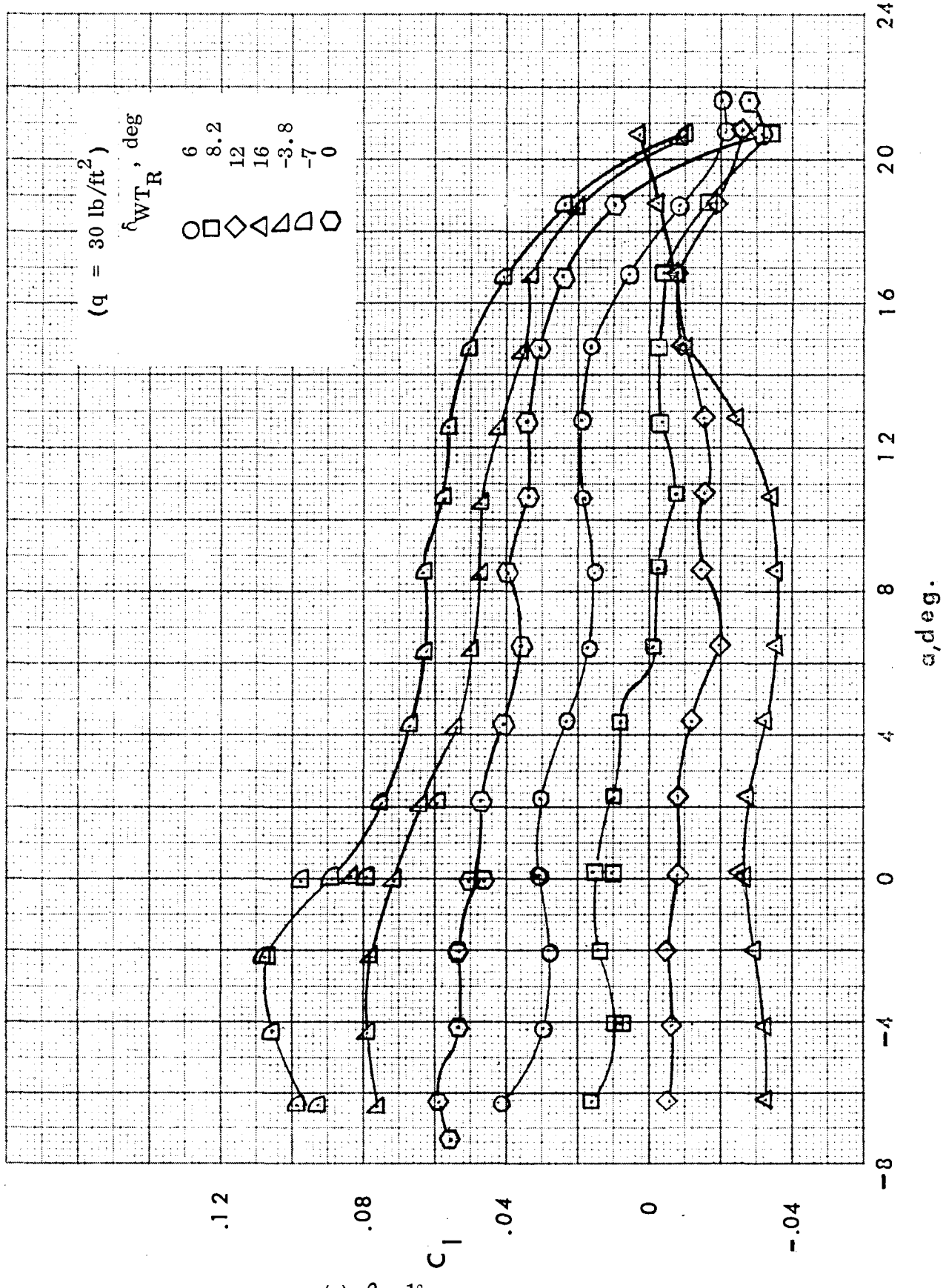


(a) $\beta = 1°$

Figure 5-9. Variation of wing-body rolling moment coefficient with angle of attack for various wing tip deflections. q = 30 psf.

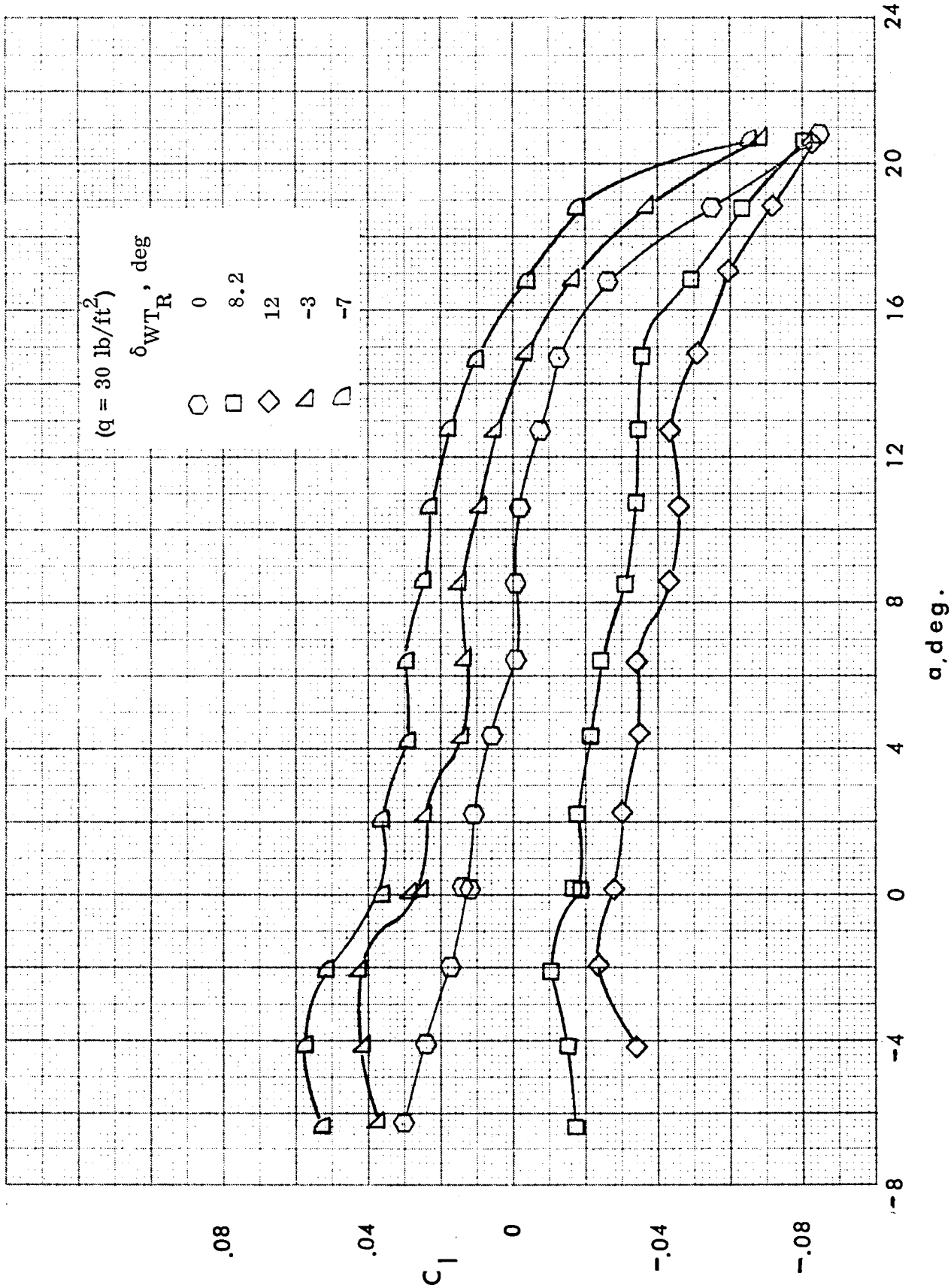


(b) $\beta = 6°$

Figure 5-9. Continued.

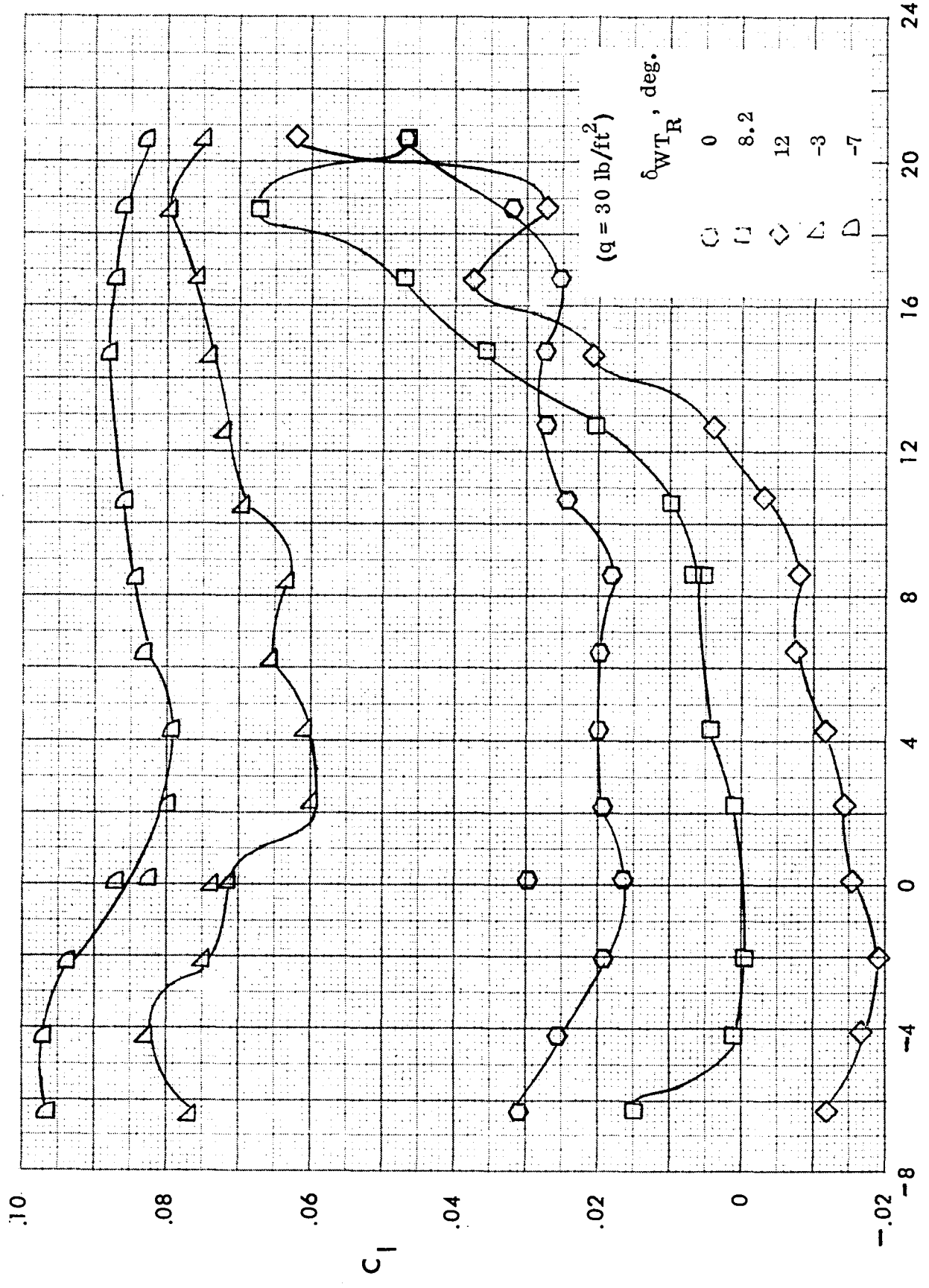


(c) $\beta = -6°$

Figure 5-9. Concluded

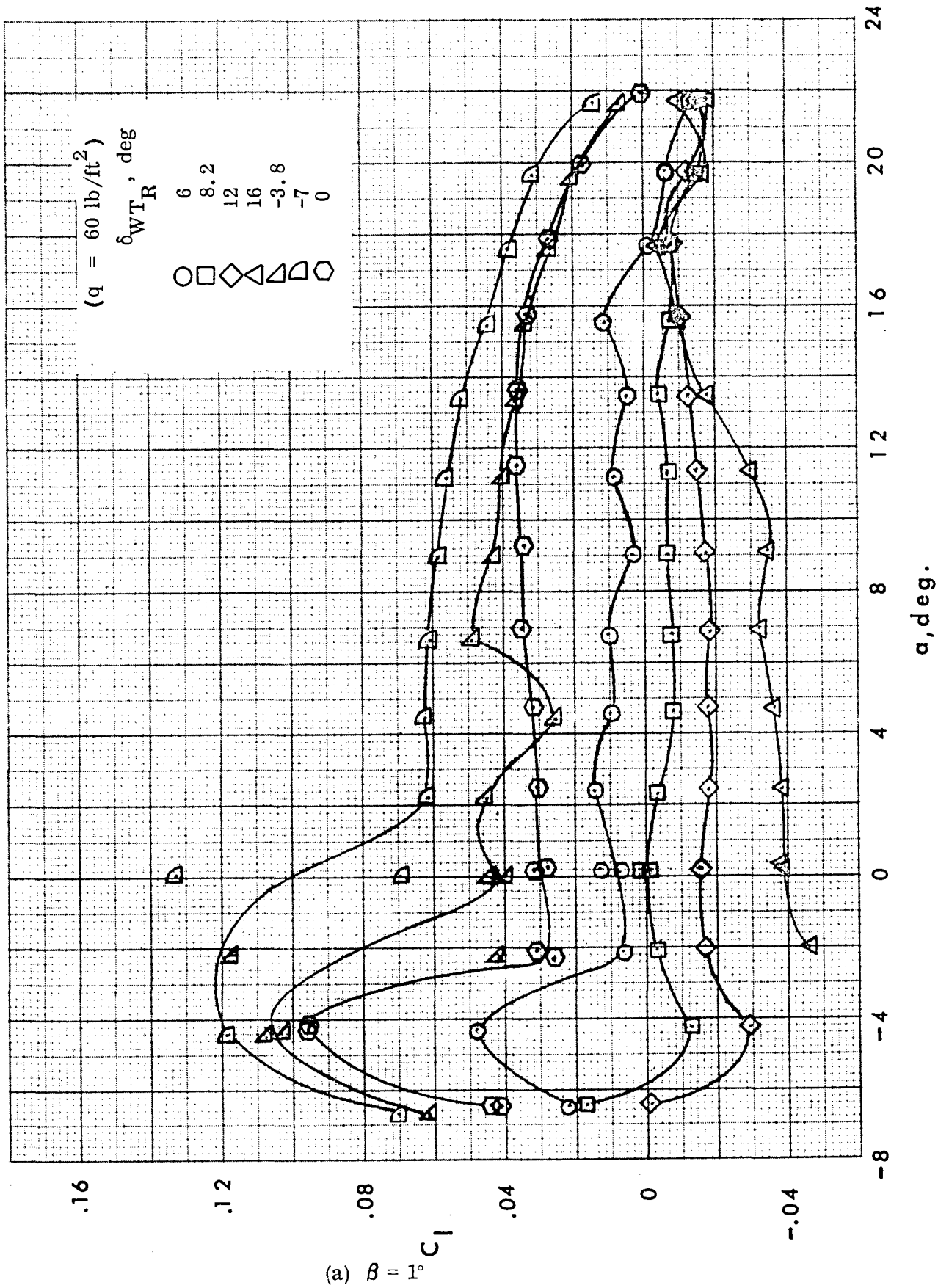


(a) $\beta = 1°$

Figure 5-10. Variation of wing-body rolling moment coefficient with angle of attack for various wing tip deflections. q = 60 psf.

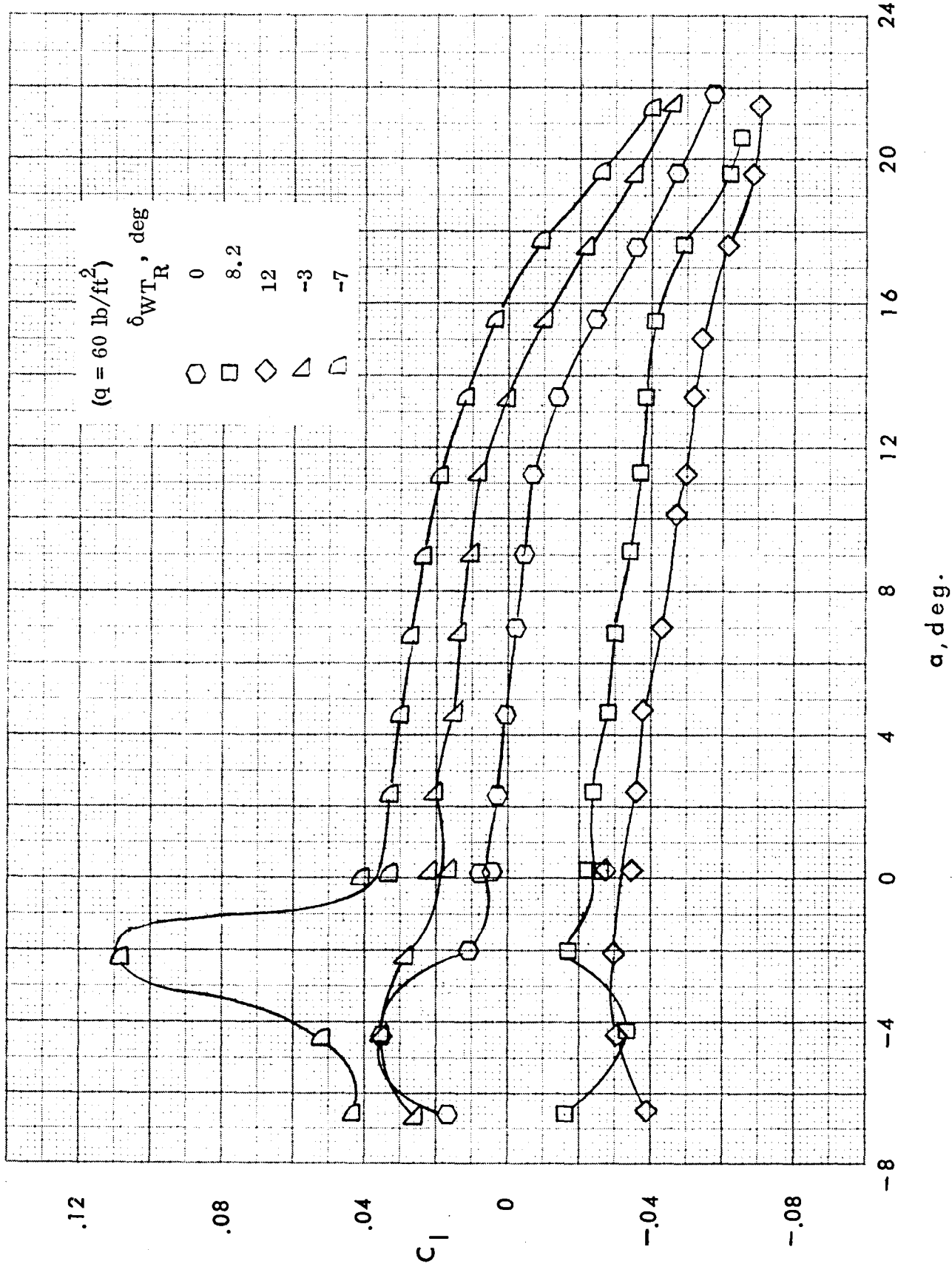


(b) $\beta = 6°$

Figure 5-10. Continued.

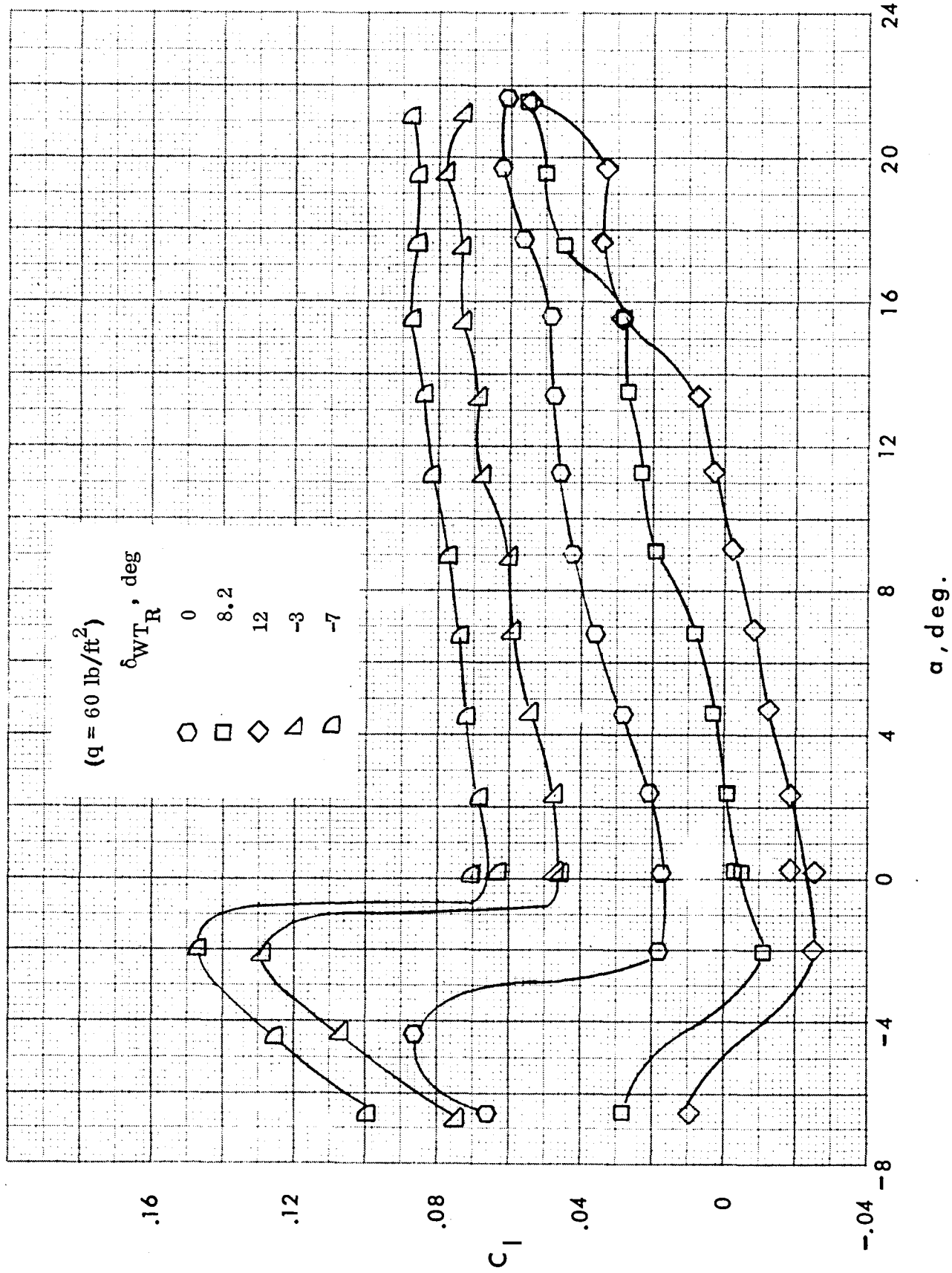


(c) $\beta = -6°$

Figure 5-10. Concluded.

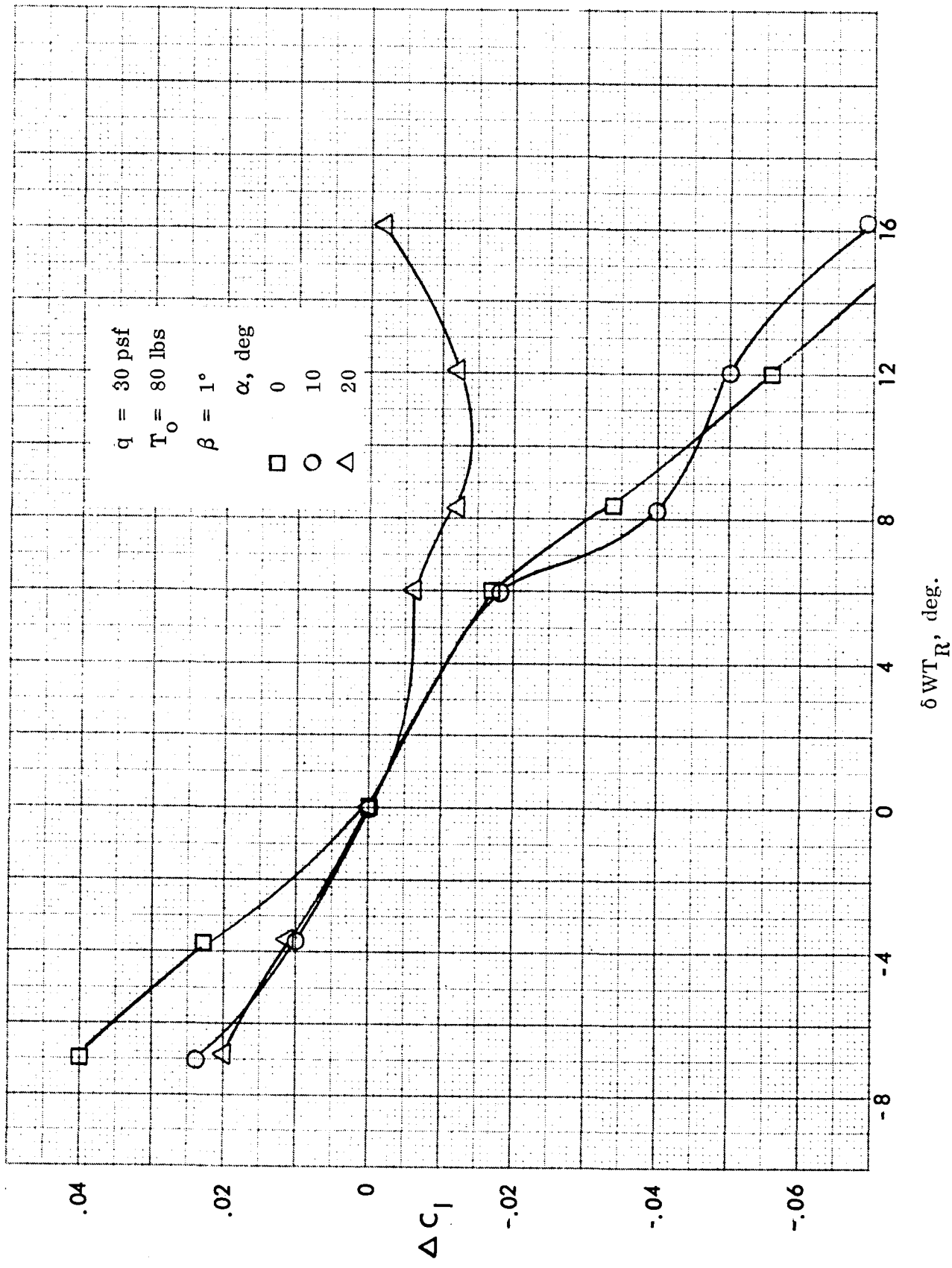


(a) q = 30 psf

Figure 5-11. Rolling moment due to wing tip deflection. $\beta$ = 1°.

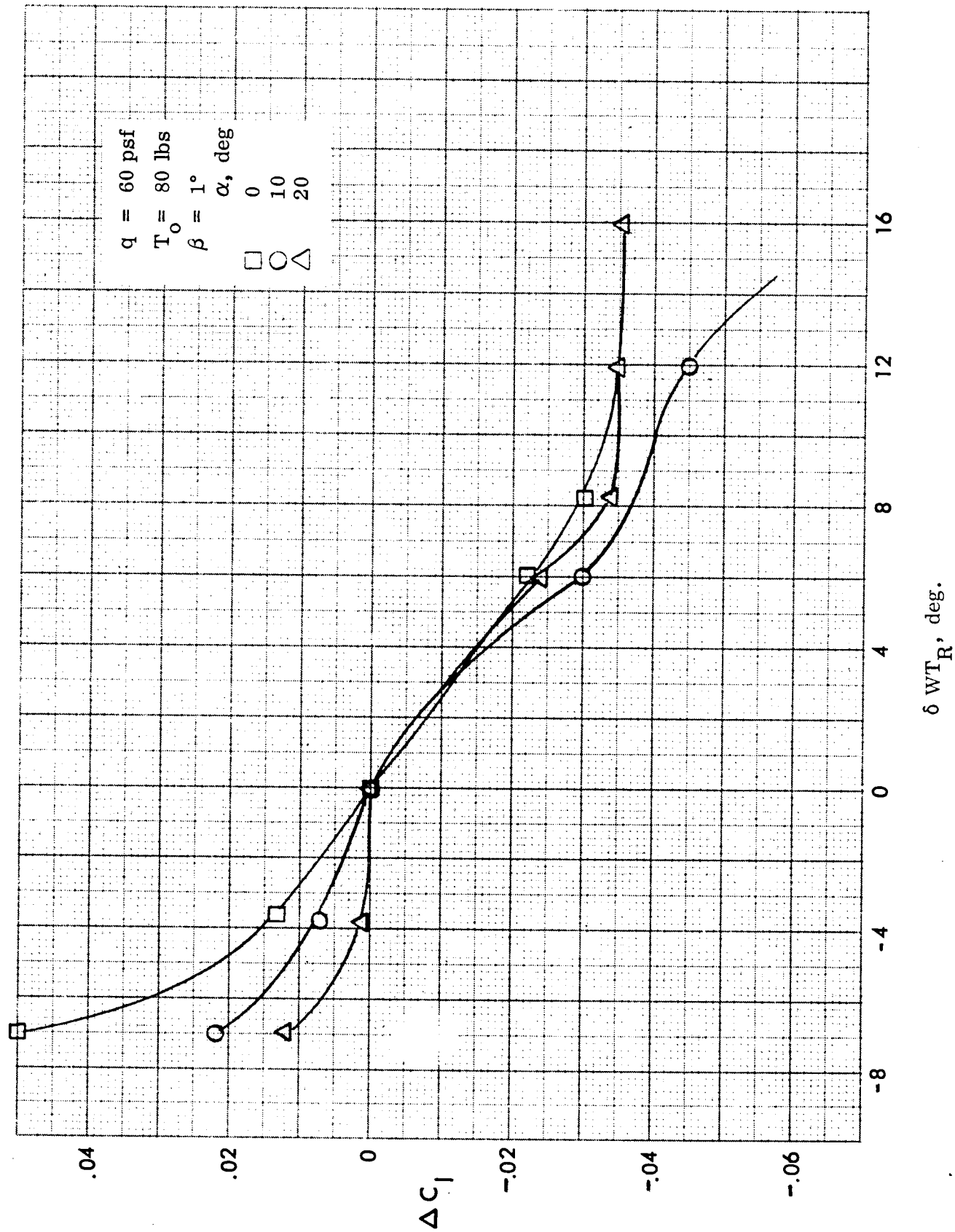


(b) q = 60 psf.

Figure 5-11. Concluded.

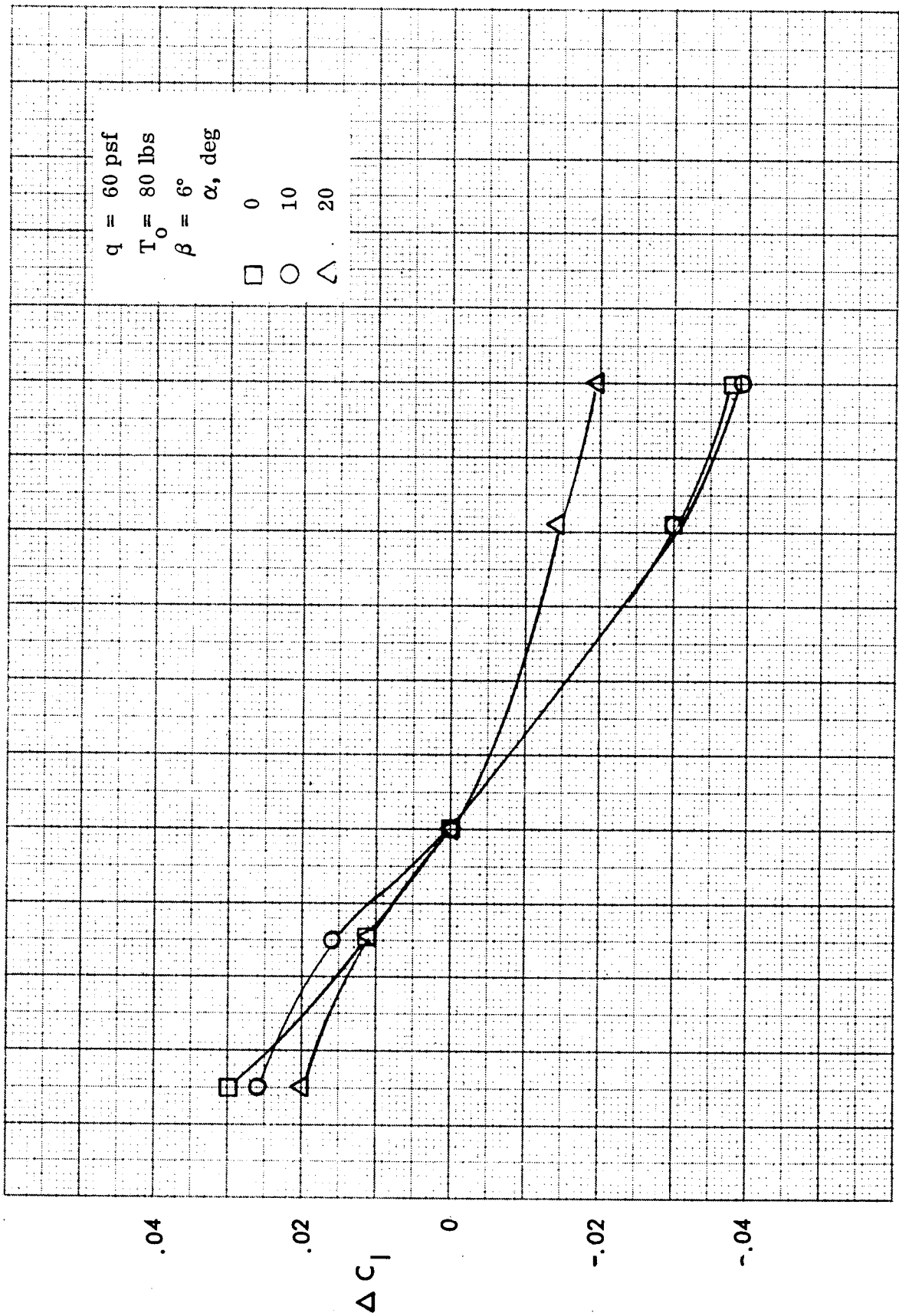


(a) $\beta$ = 6°.

Figure 5-12. Rolling moment due to wing tip deflection. q = 60 psf.

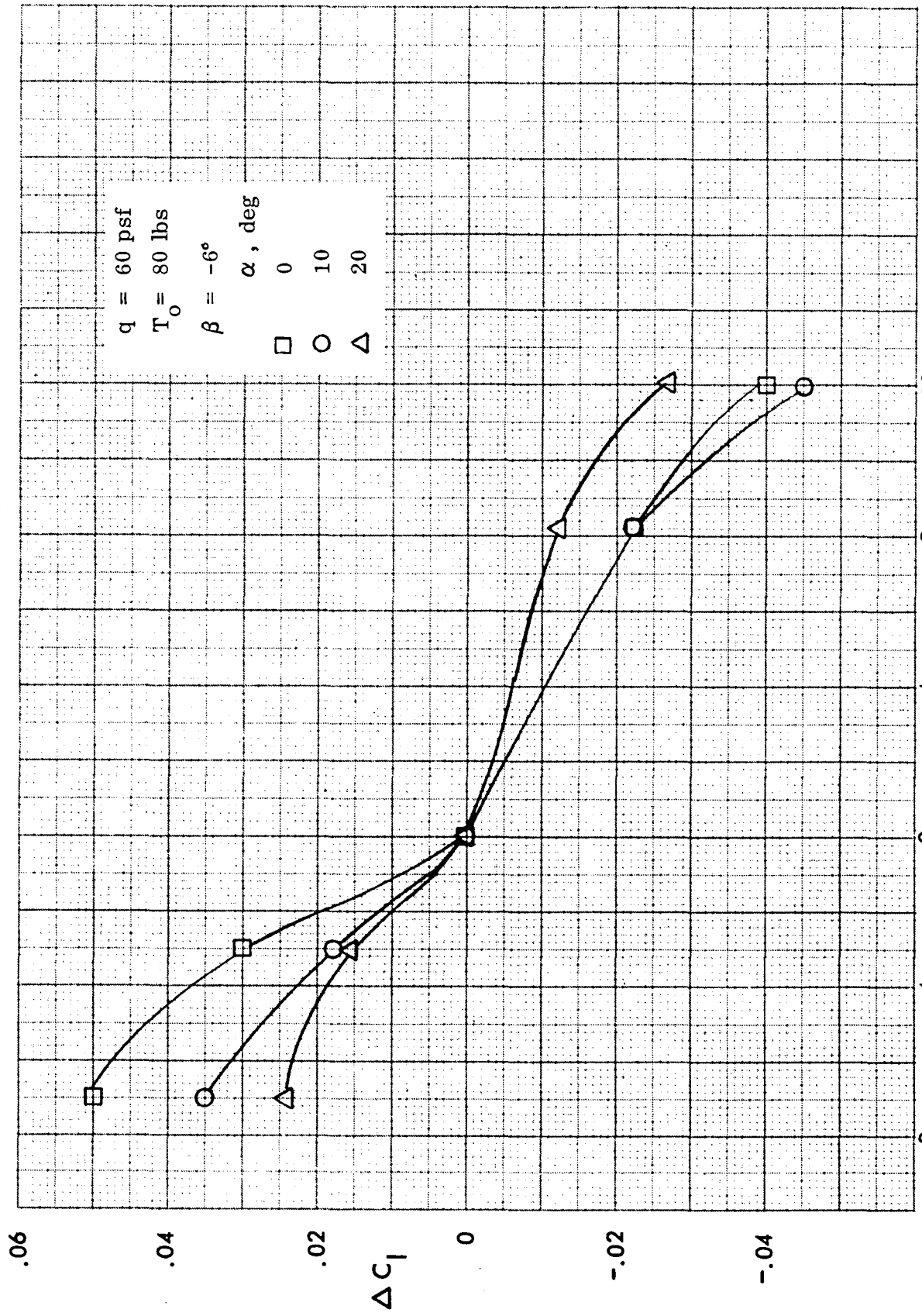


(b) $\beta = -6°$

Figure 5-12. Concluded.

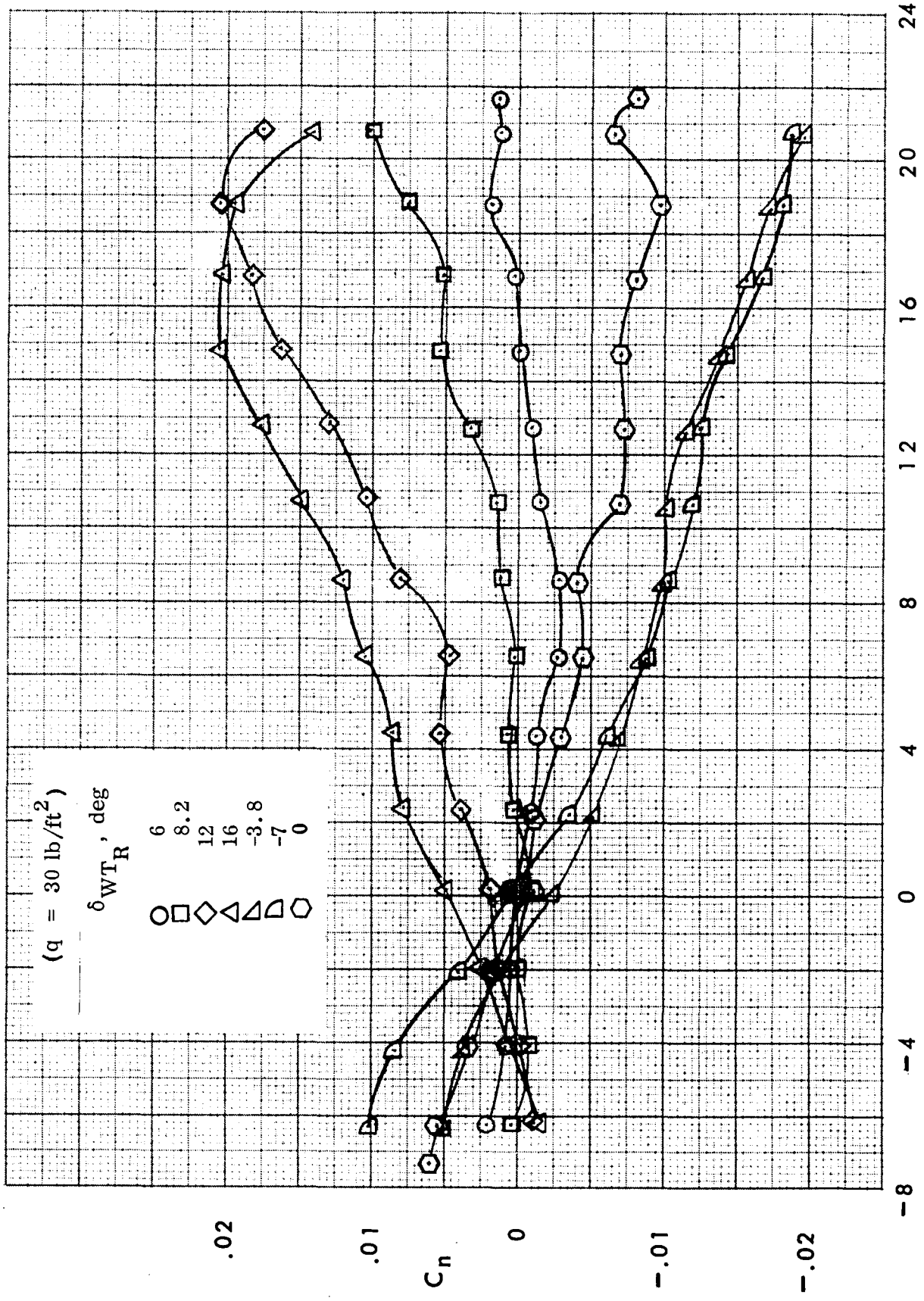


(a) $\beta = 1°$.

Figure 5-13. Variation of wing-body yawing moment coefficient with angle of attack for various wing tip deflections at q = 30 psf.

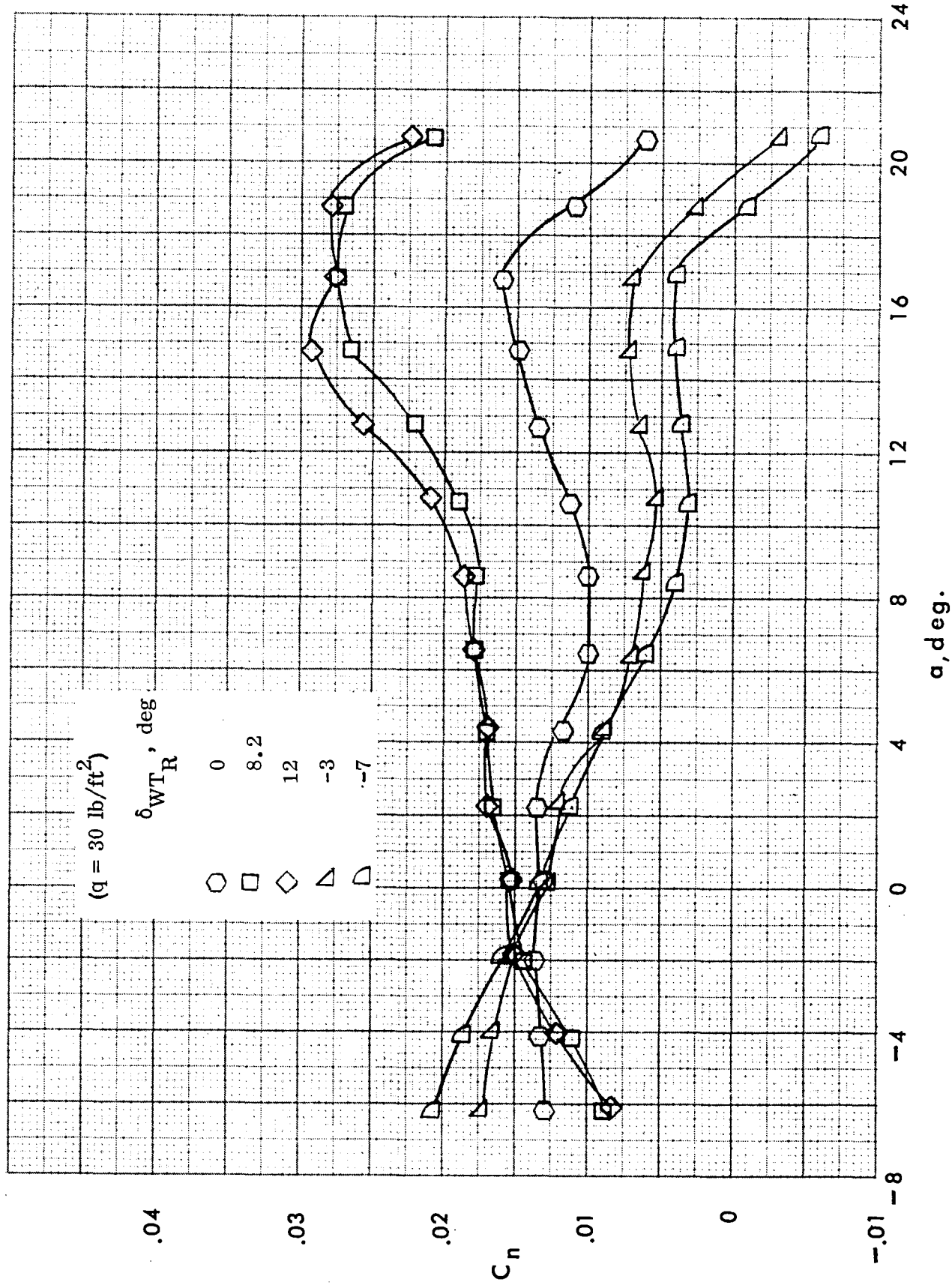


(b) $\beta = 6°$.

Figure 5-13. Continued.

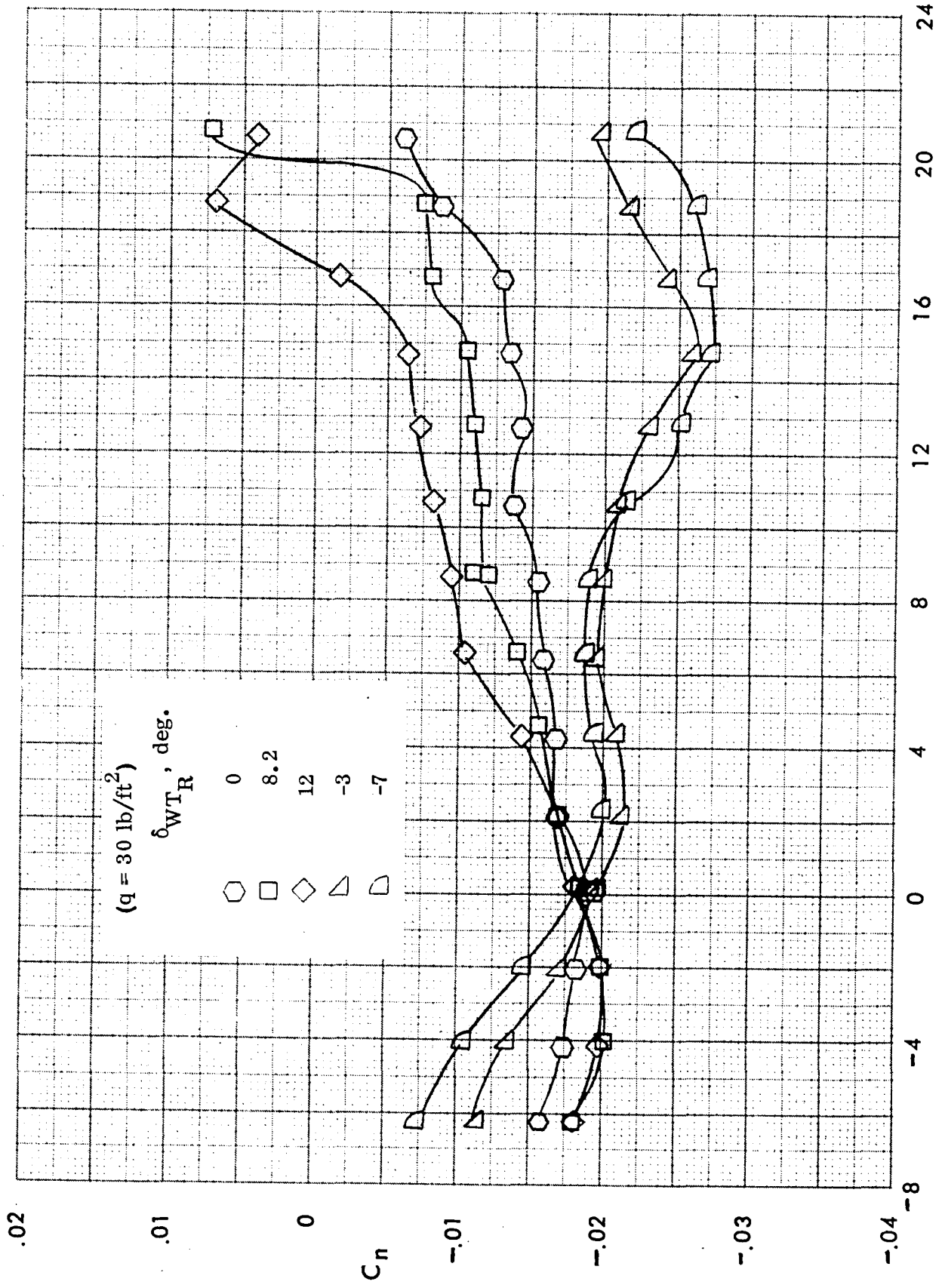


(c) $\beta = -6°$.

Figure 5-13. Concluded.

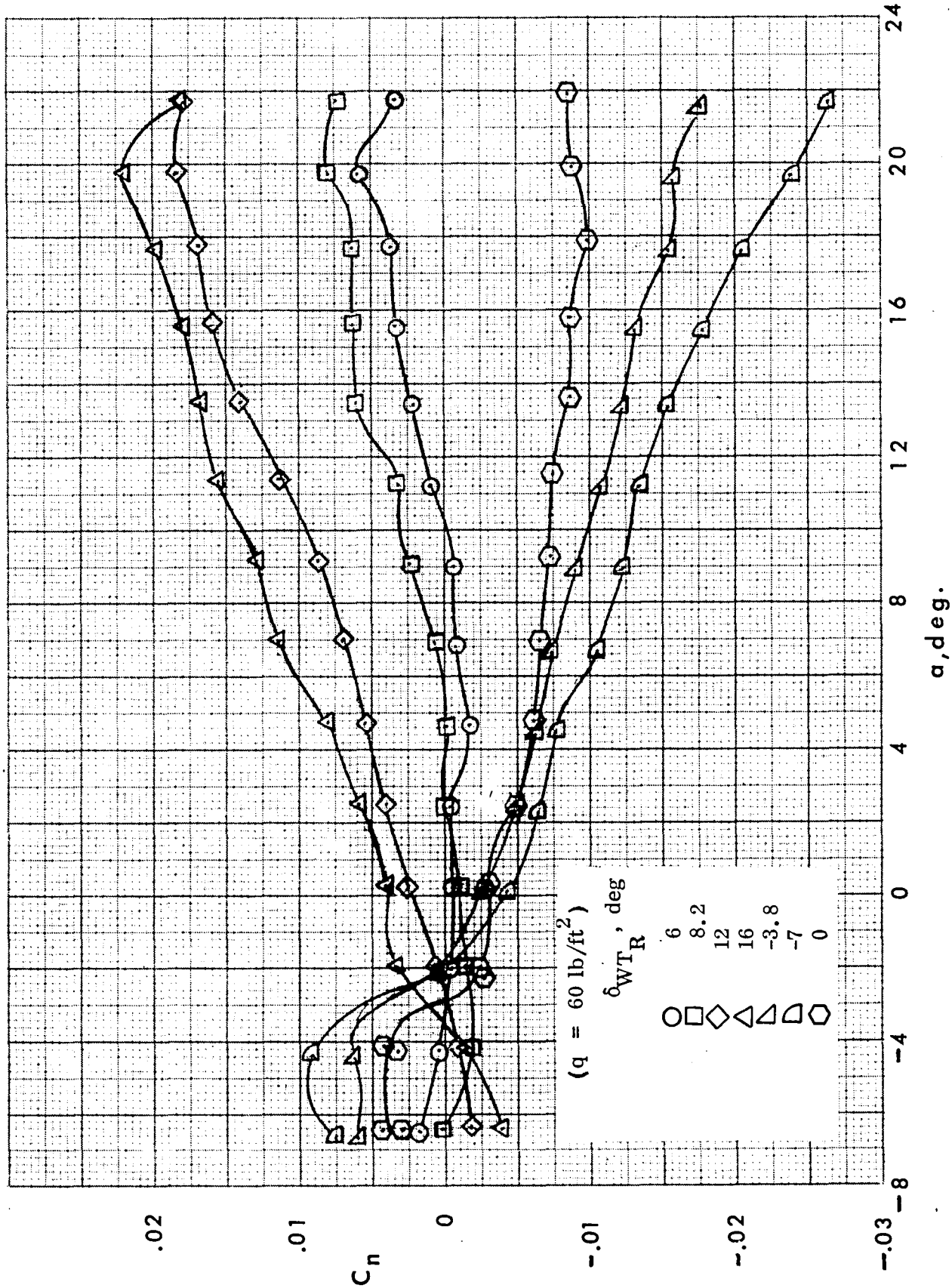


(a) $\beta = 1°$.

Figure 5-14. Variation of wing-body yawing moment coefficient with angle of attack at q = 60 psf.

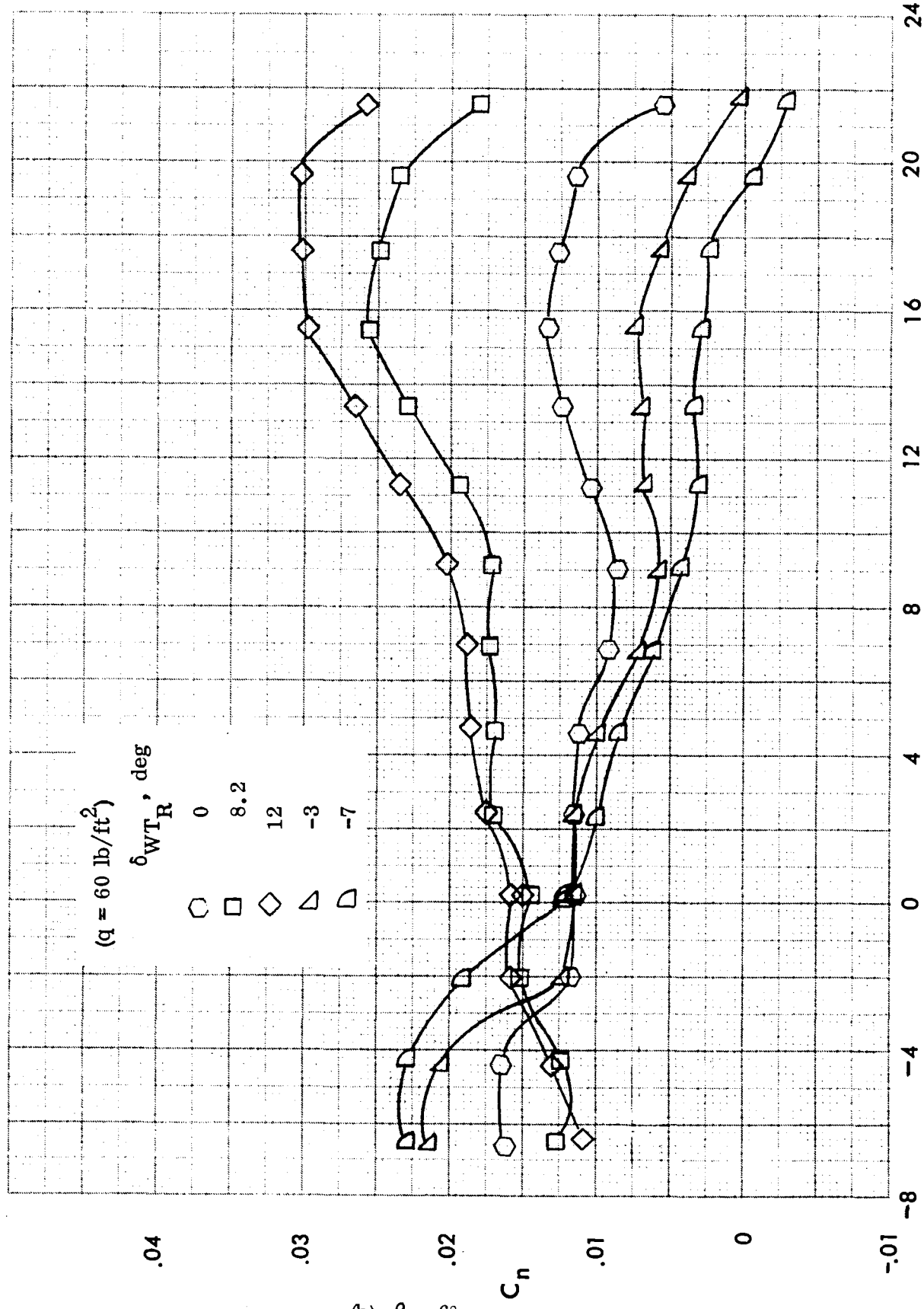


(b) $\beta = 6°$.

Figure 5-14. Continued.

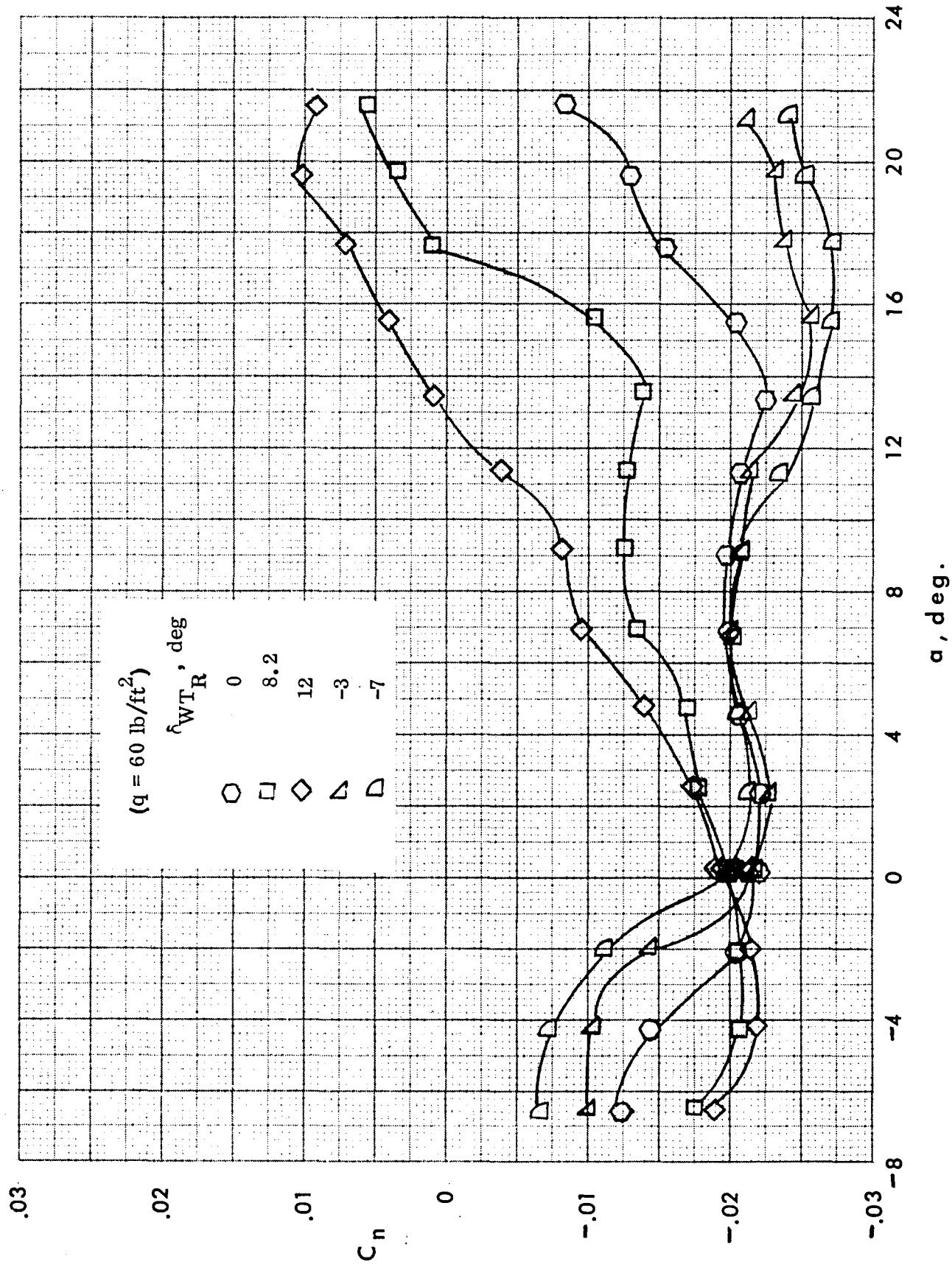


(c) $\beta = -6°$

Figure 5-14. Concluded

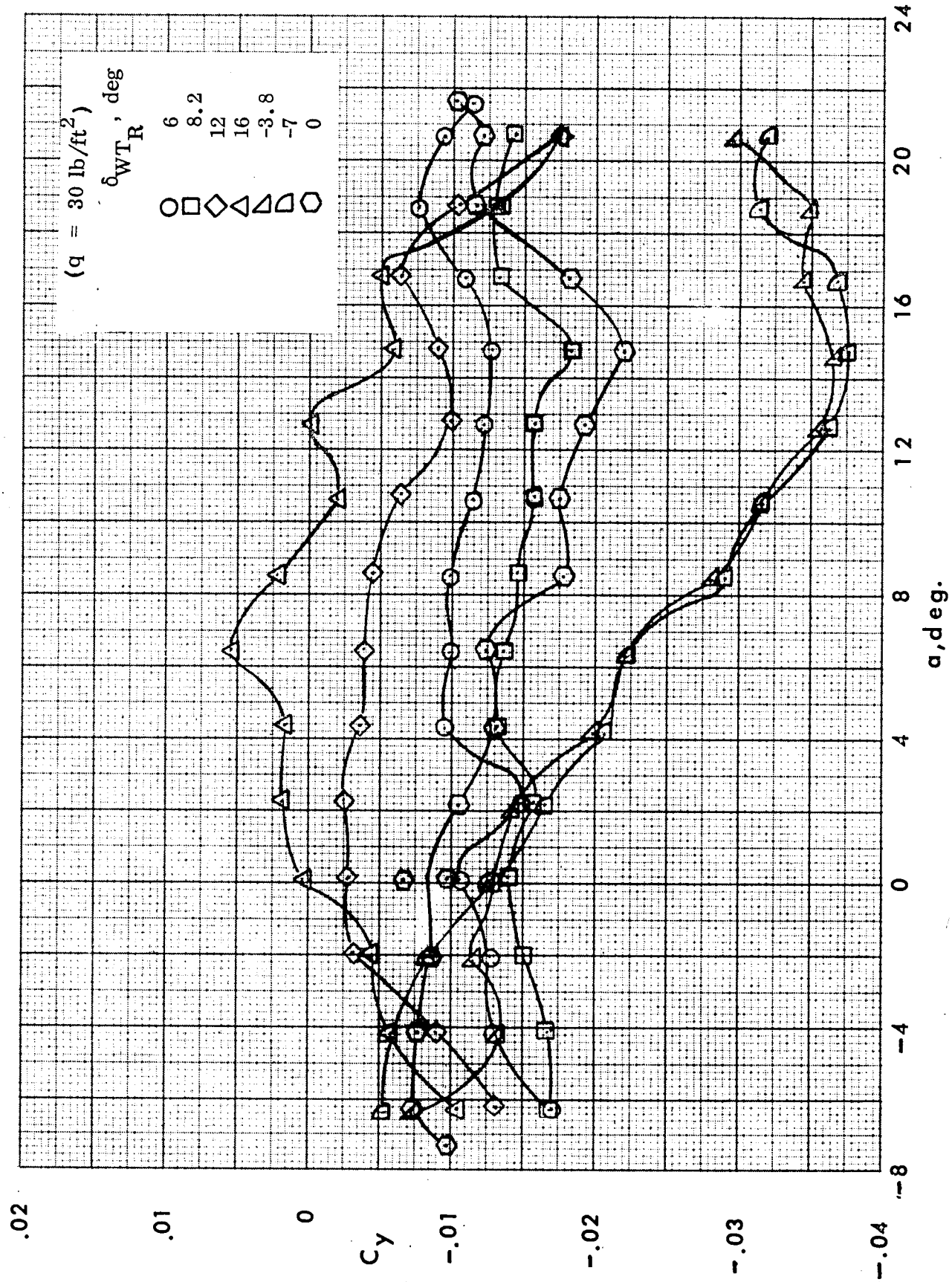


(a) $\beta = 1°$.

Figure 5-15. Variation of wing-body side force coefficient with angle of attack for various wing tip deflections at q = 30 psf.

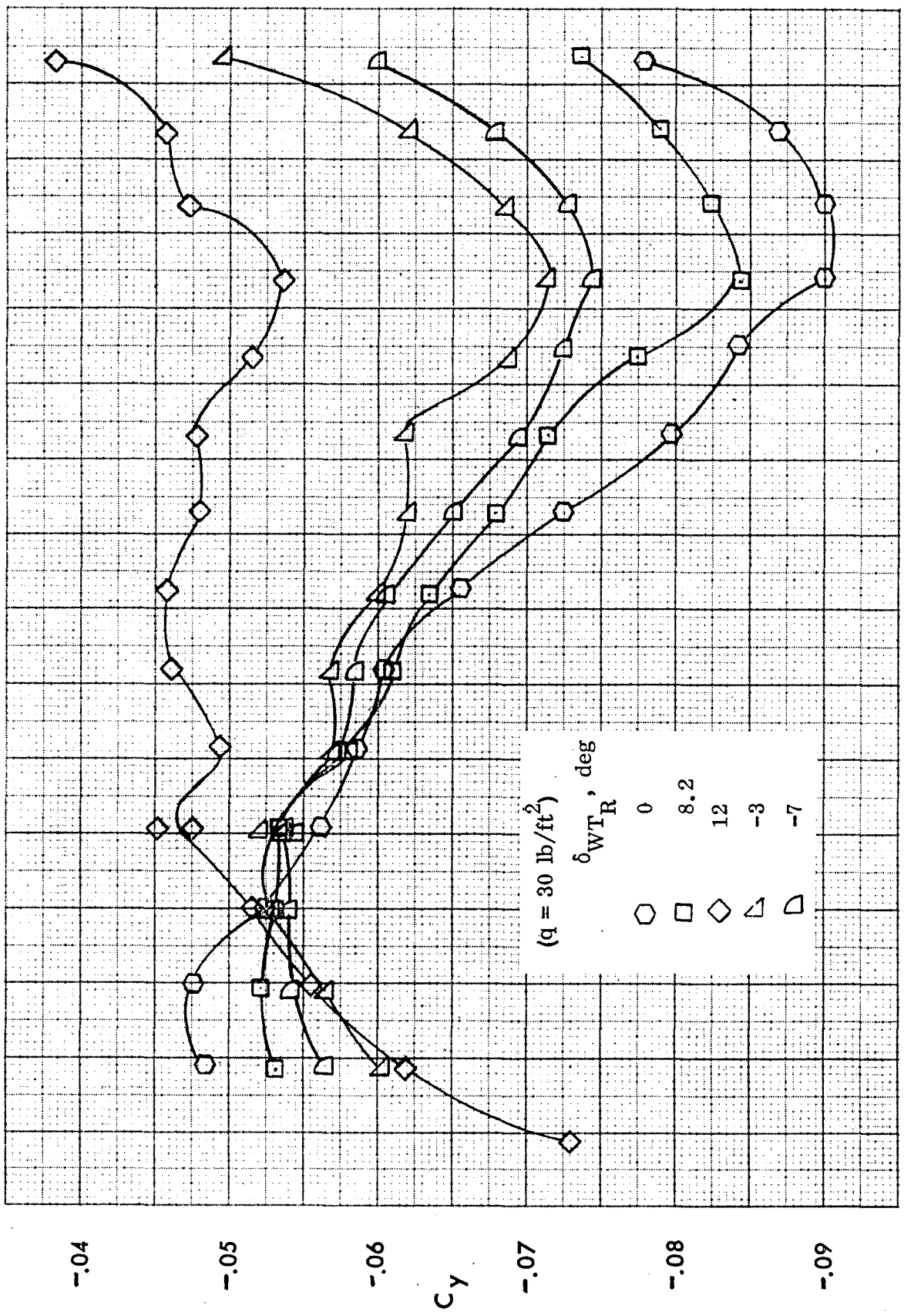


(b) $\beta = 6°$.

Figure 5-15. Continued.

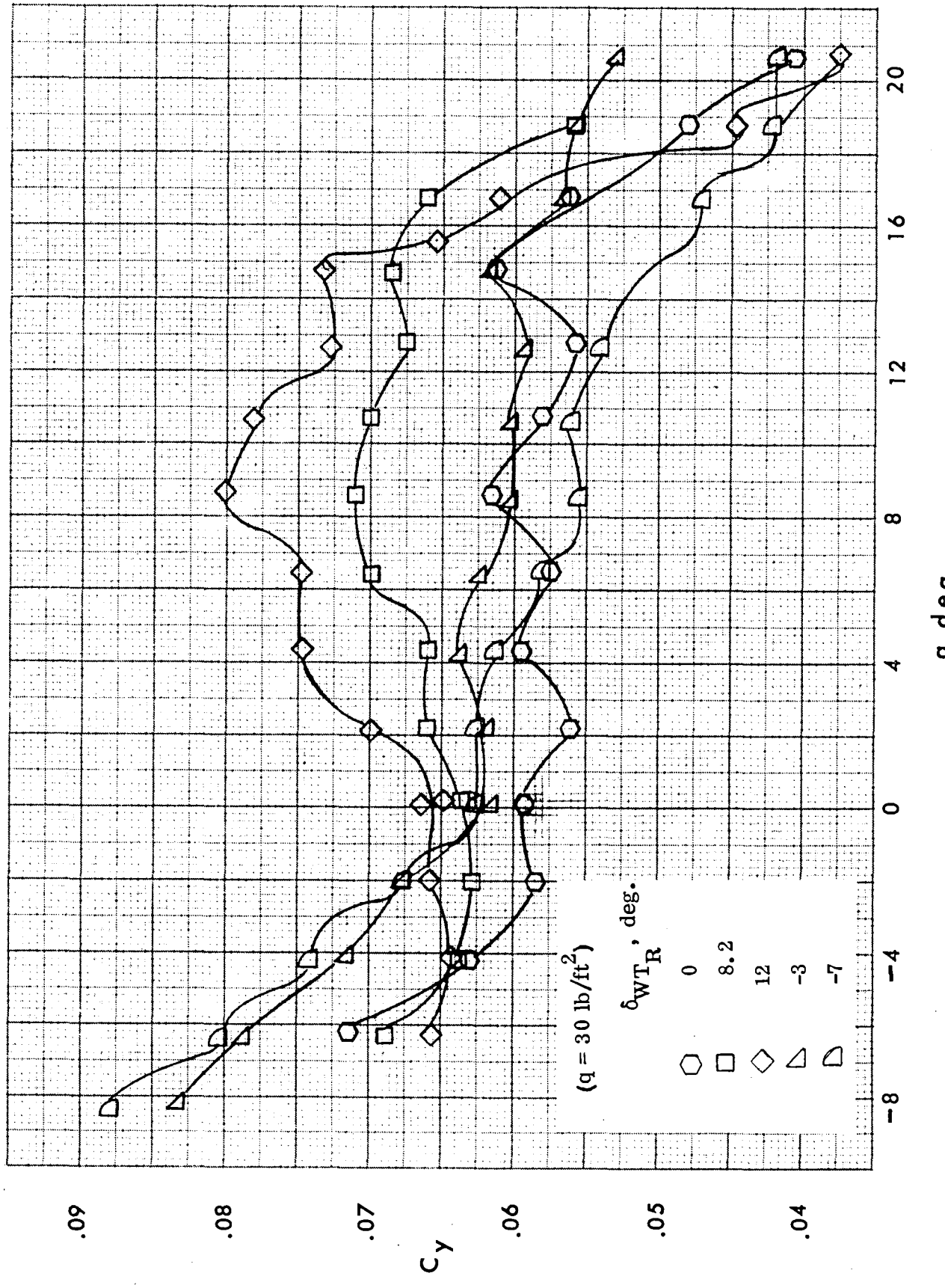


(c) $\beta = -6°$.

Figure 5-15. Concluded.

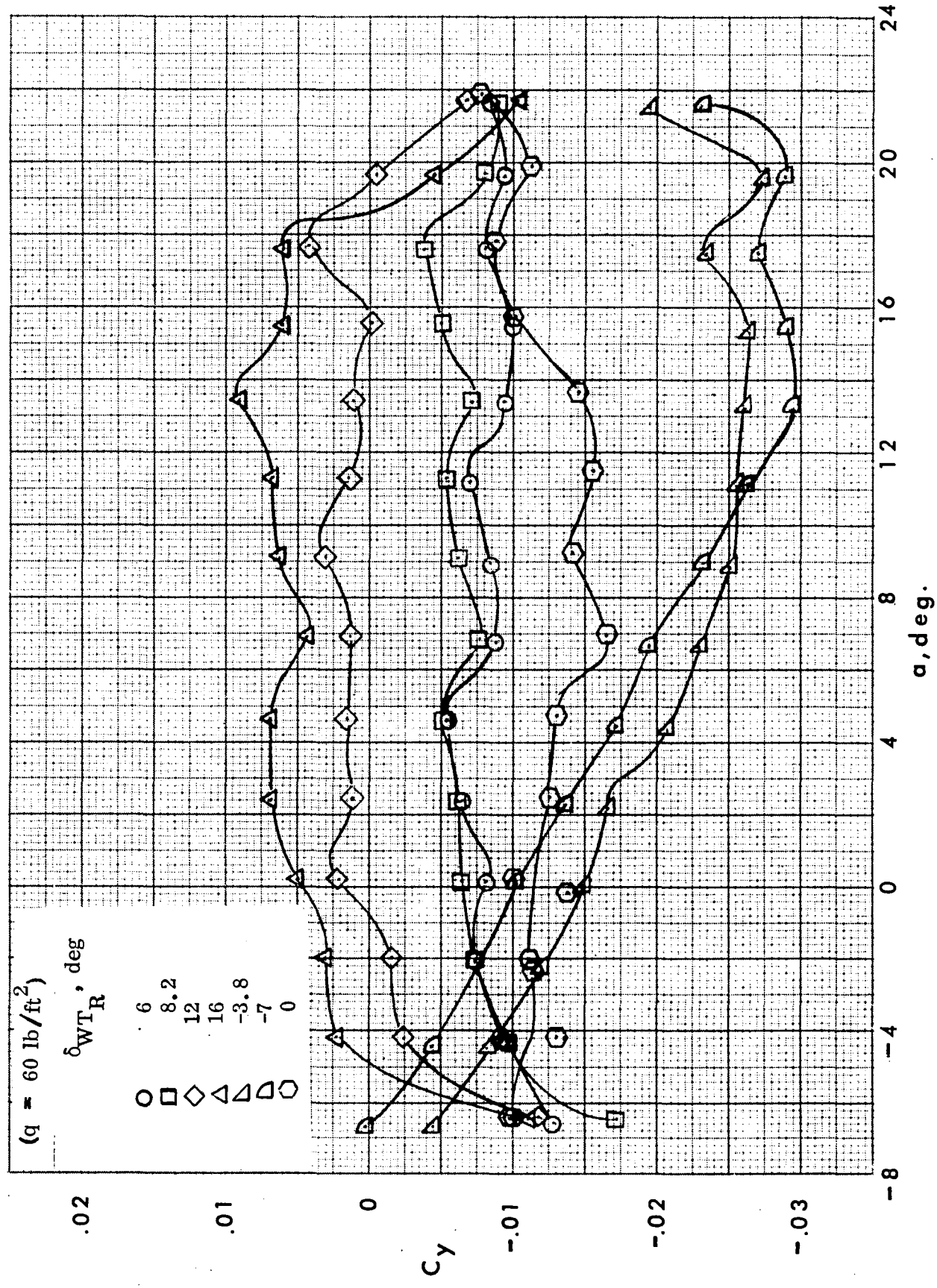


(a) $\beta = 1°$.

Figure 5-16. Variation of wing-body side force coefficient with angle of attack at q = 60 psf.

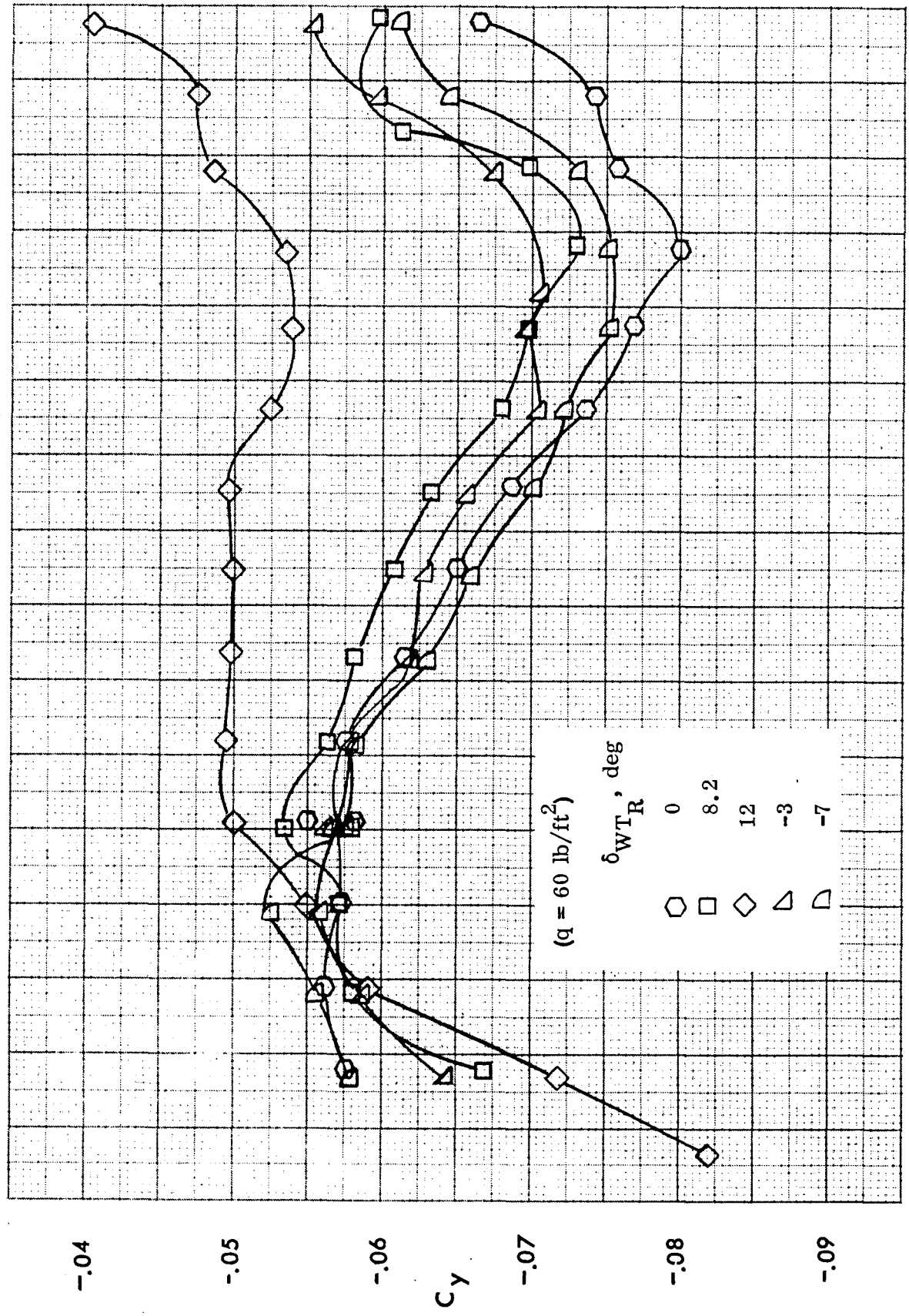


(b) $\beta = 6°$.

Figure 5-16. Continued.

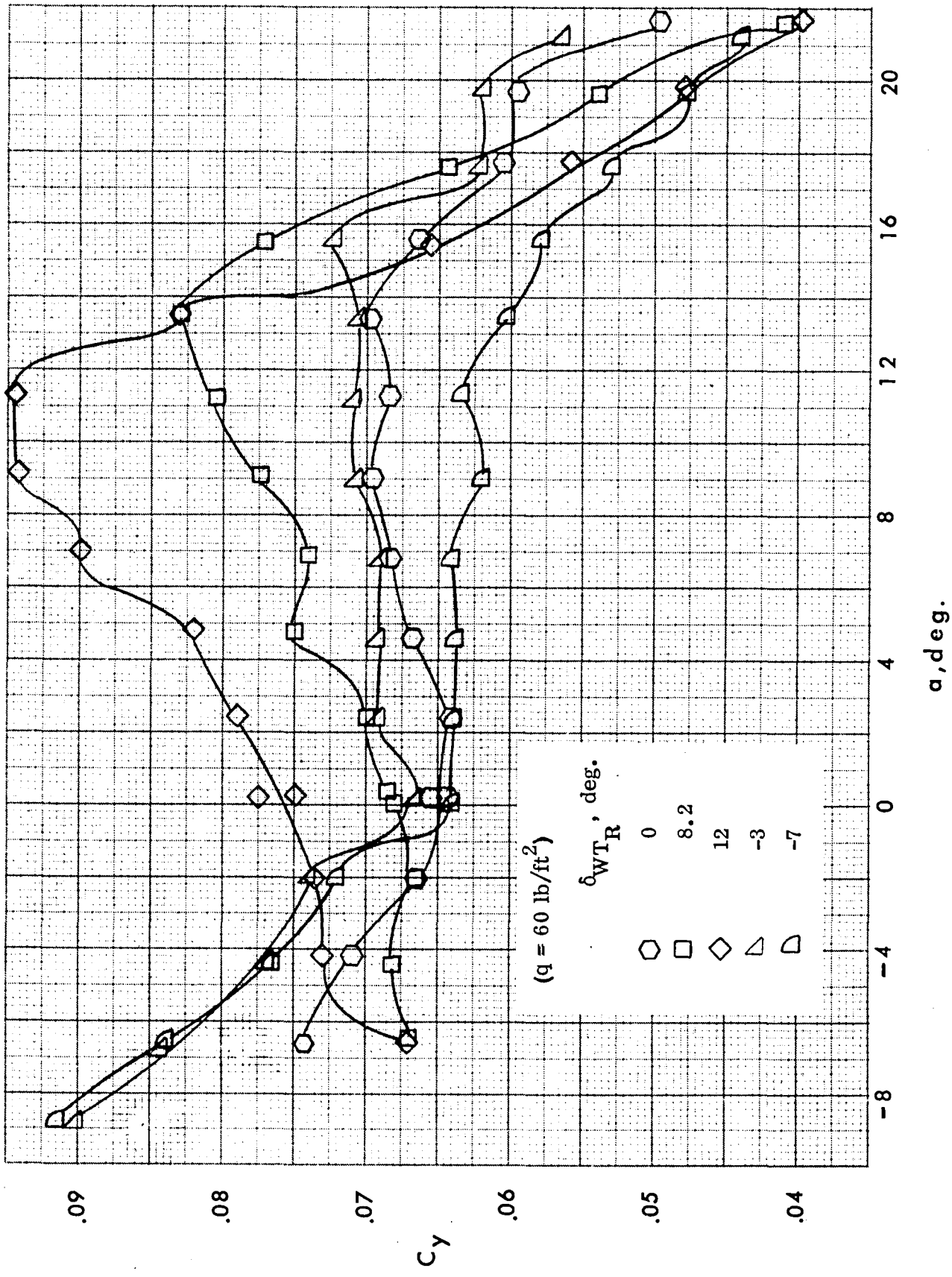


(c) $\beta = -6°$.

Figure 5-16. Concluded.

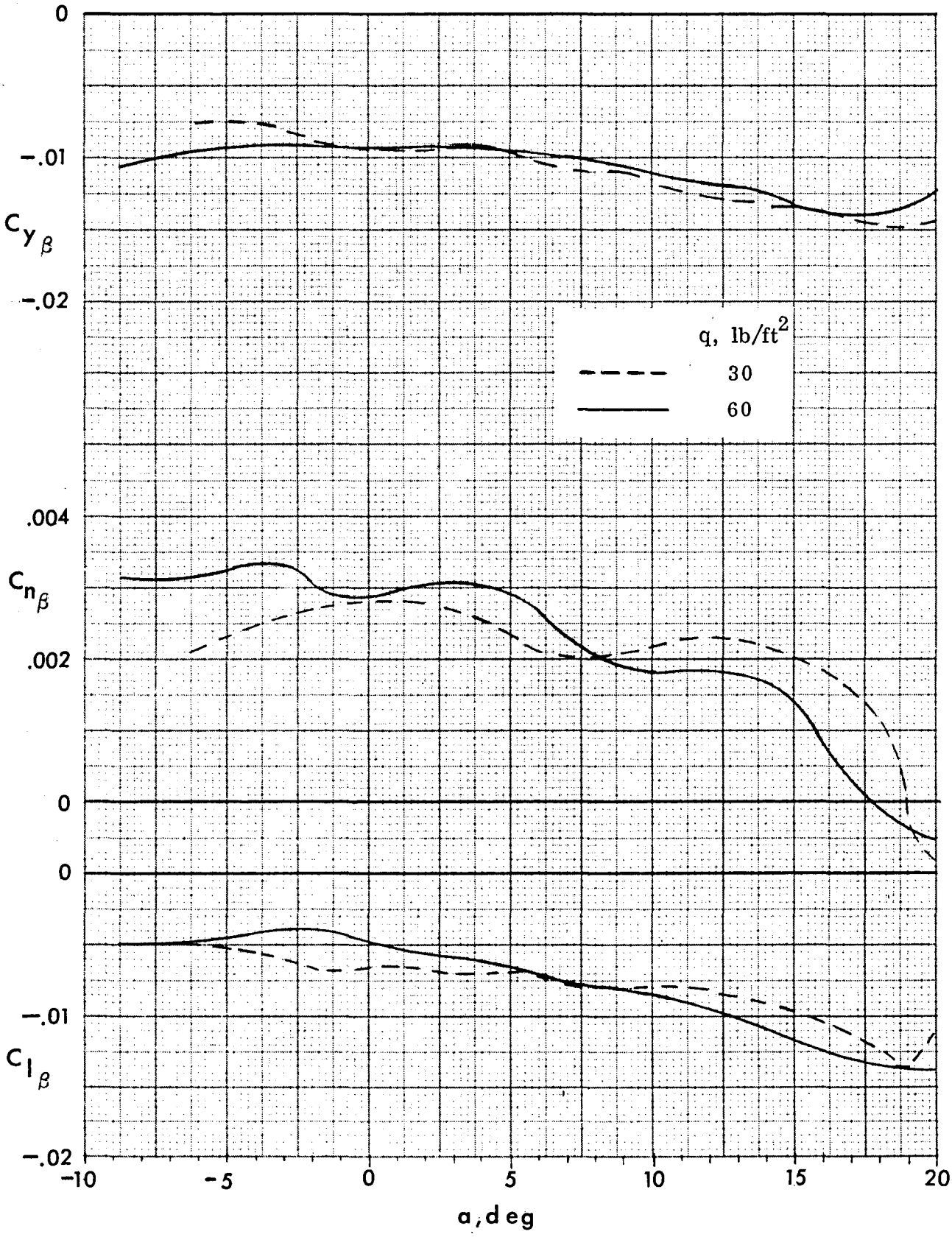


Figure 5-17. Variation of wing-body lateral-directional stability parameters with angle of attack. $\delta_{WT_R} = 0°$, $T_o = 80$ lbs.

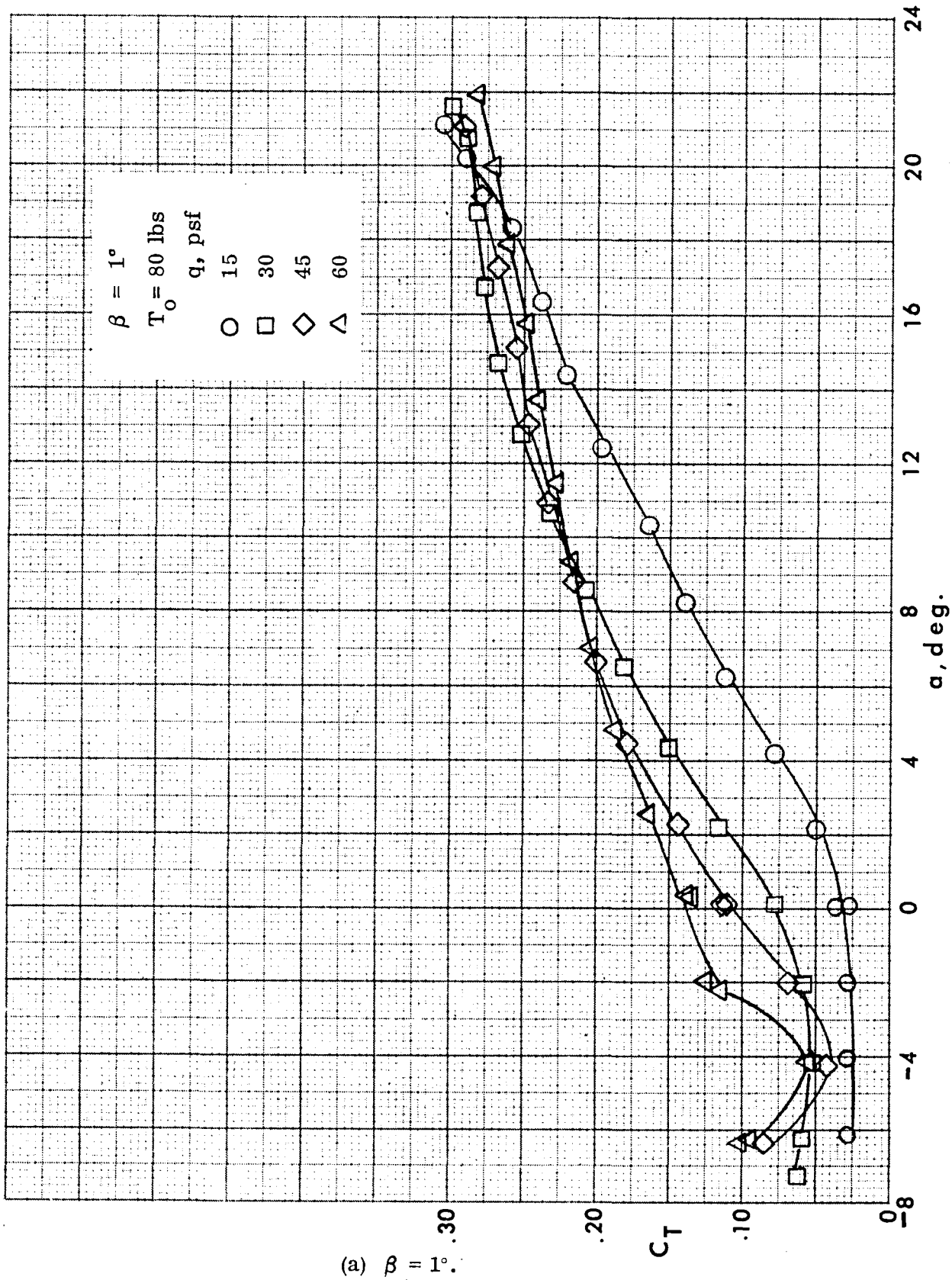


(a) $\beta = 1°$.

Figure 5-18. Effect of dynamic pressure and angle of attack on cable tension. $T_o = 80$ lbs, $\delta_{WT_R} = 0°$.

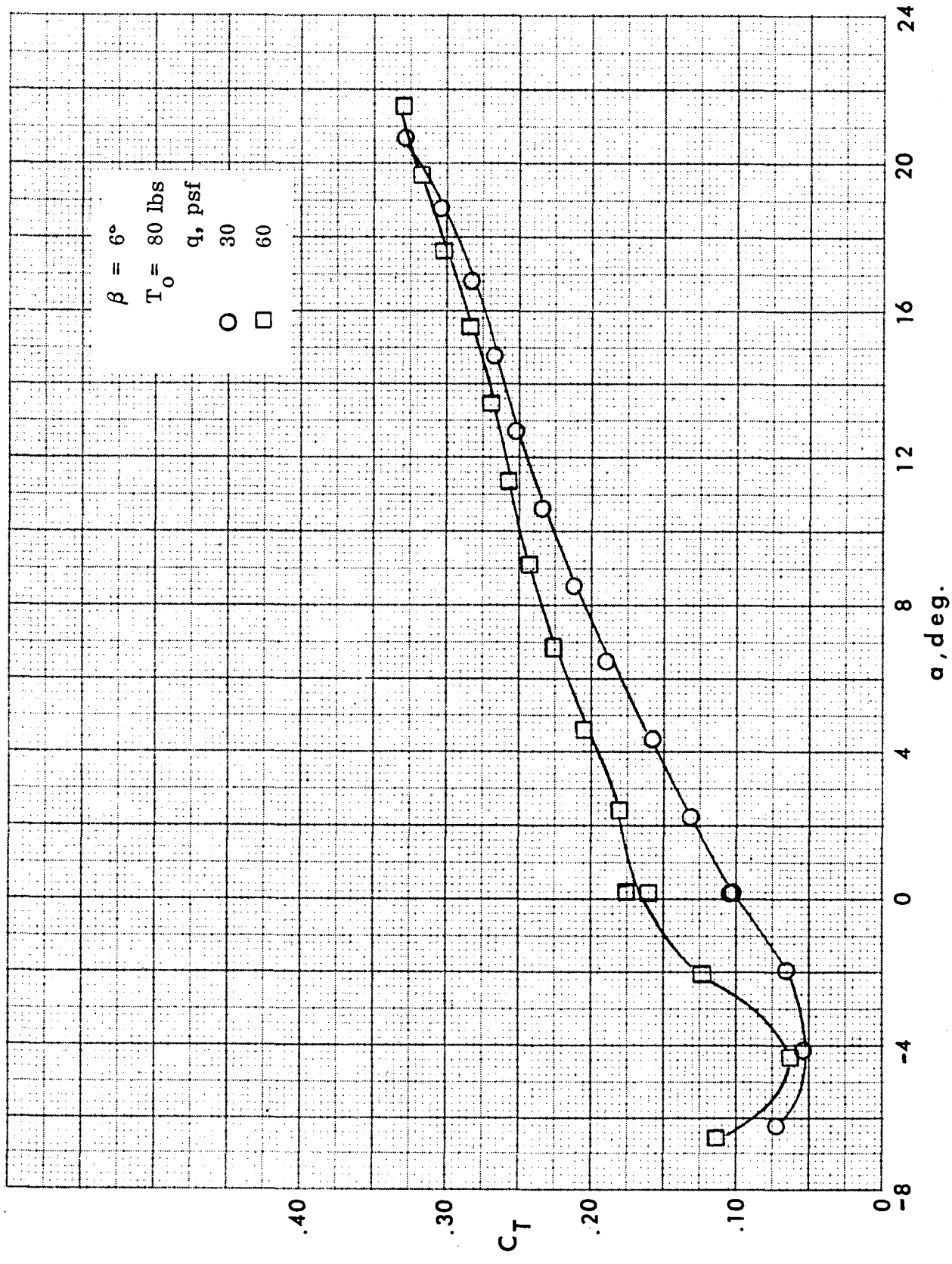


(b) $\beta = 6°$.

Figure 5-18. Continued.

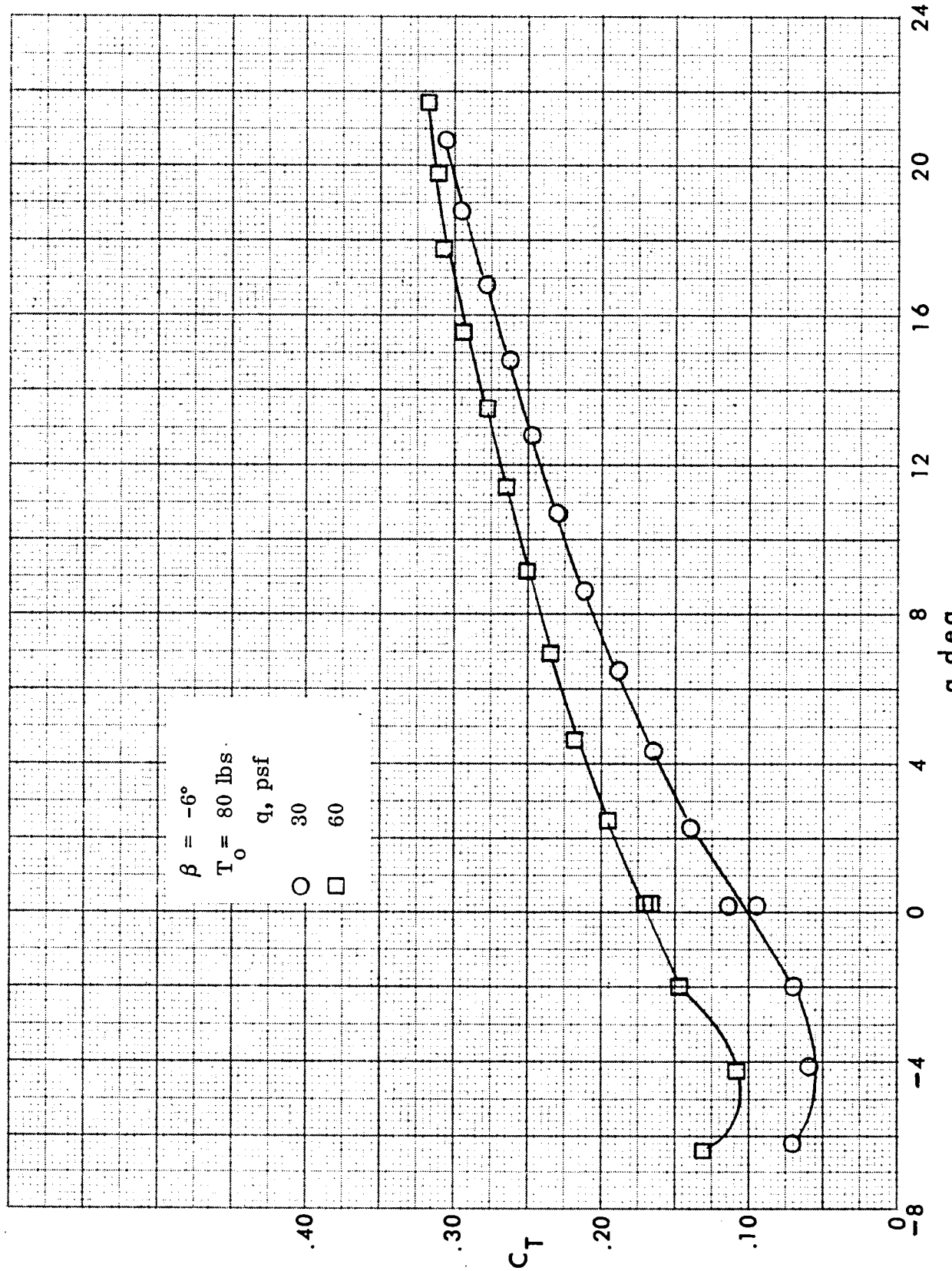


(c) $\beta = -6°$.

Figure 5-18. Concluded.

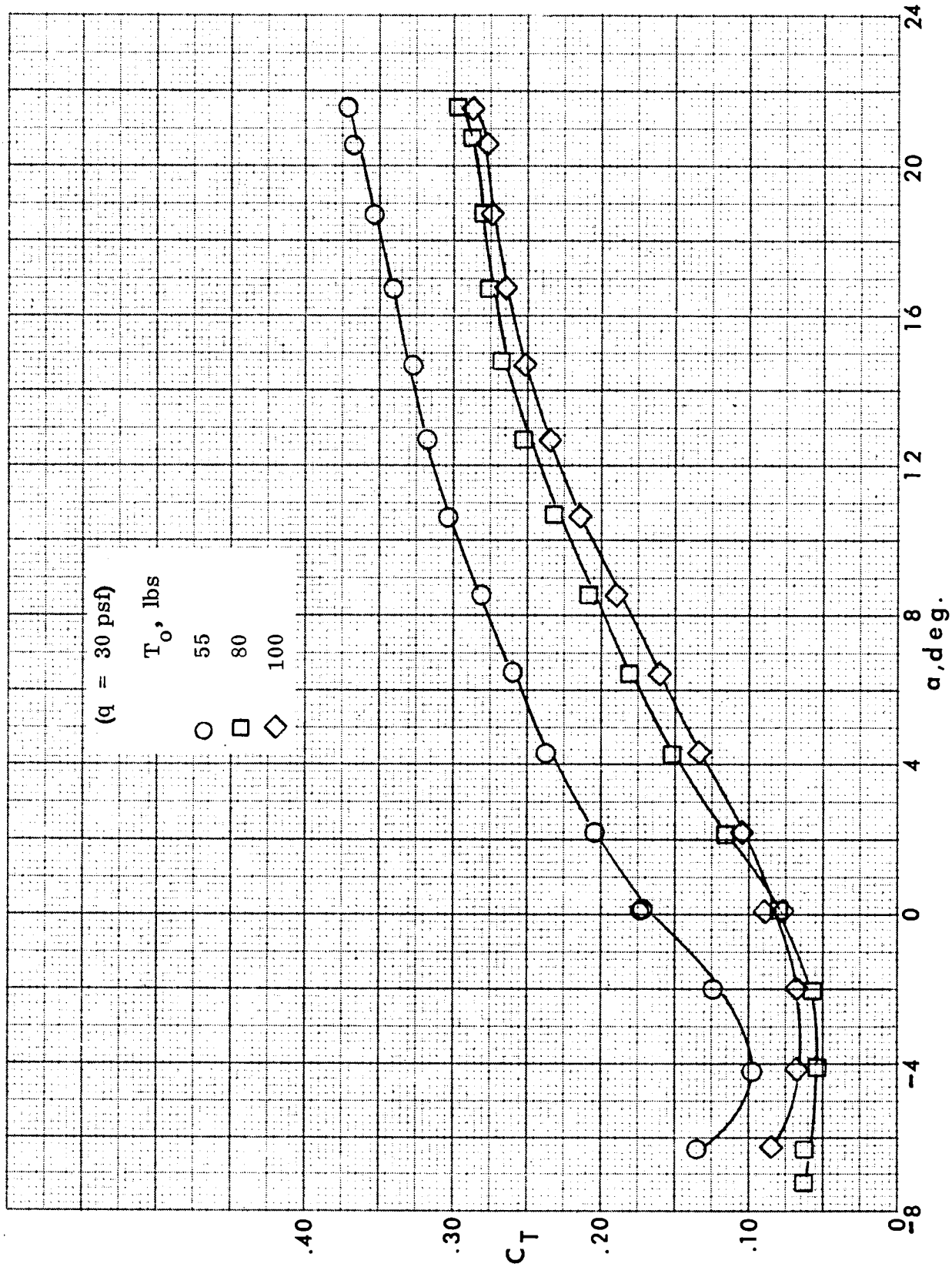


(a) q = 30 psf.

Figure 5-19. Effect of initial tension and angle of attack on cable tension. $\delta_{WT_R} = 0°$.

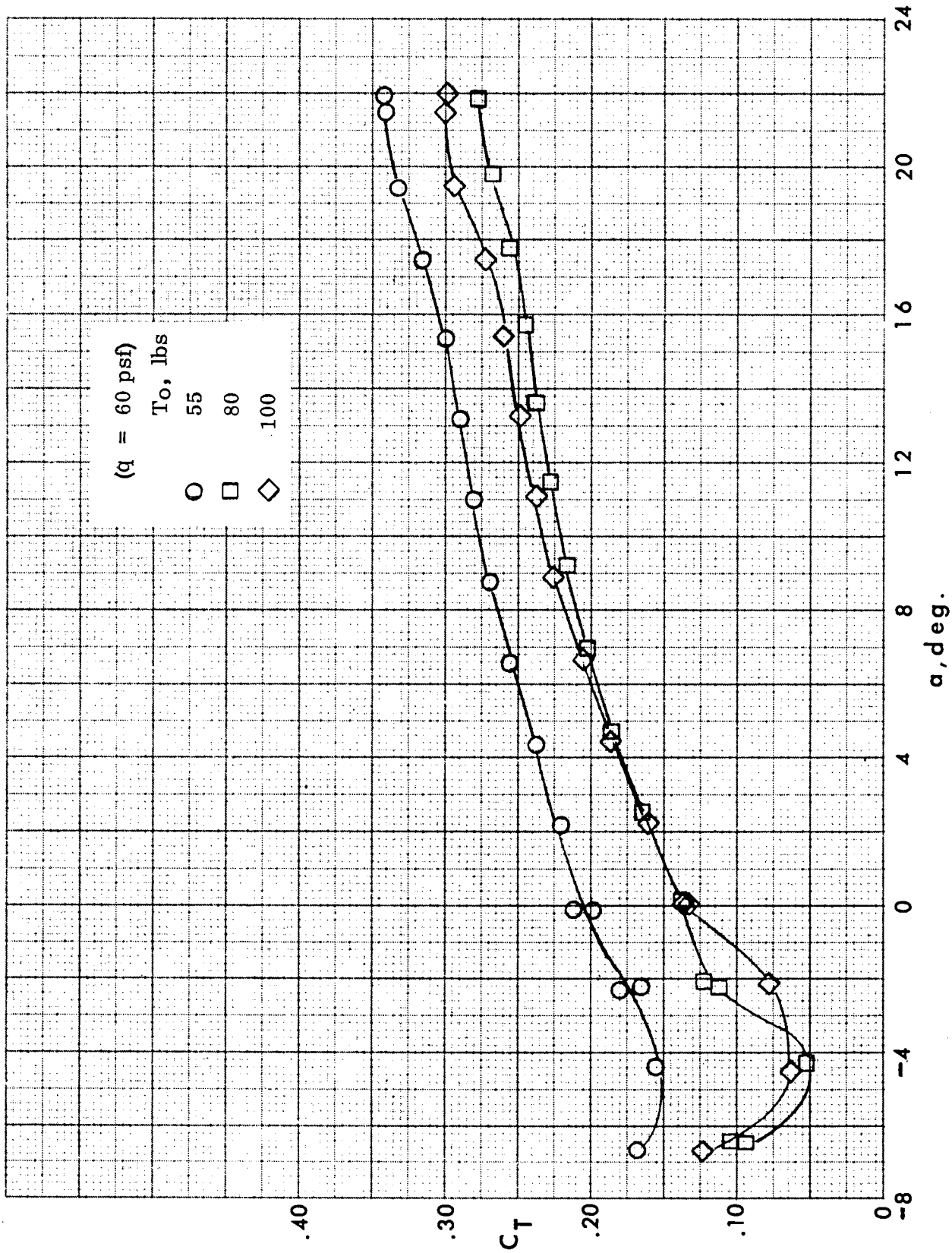


(b) q = 60 psf.
Figure 5-19. Concluded.

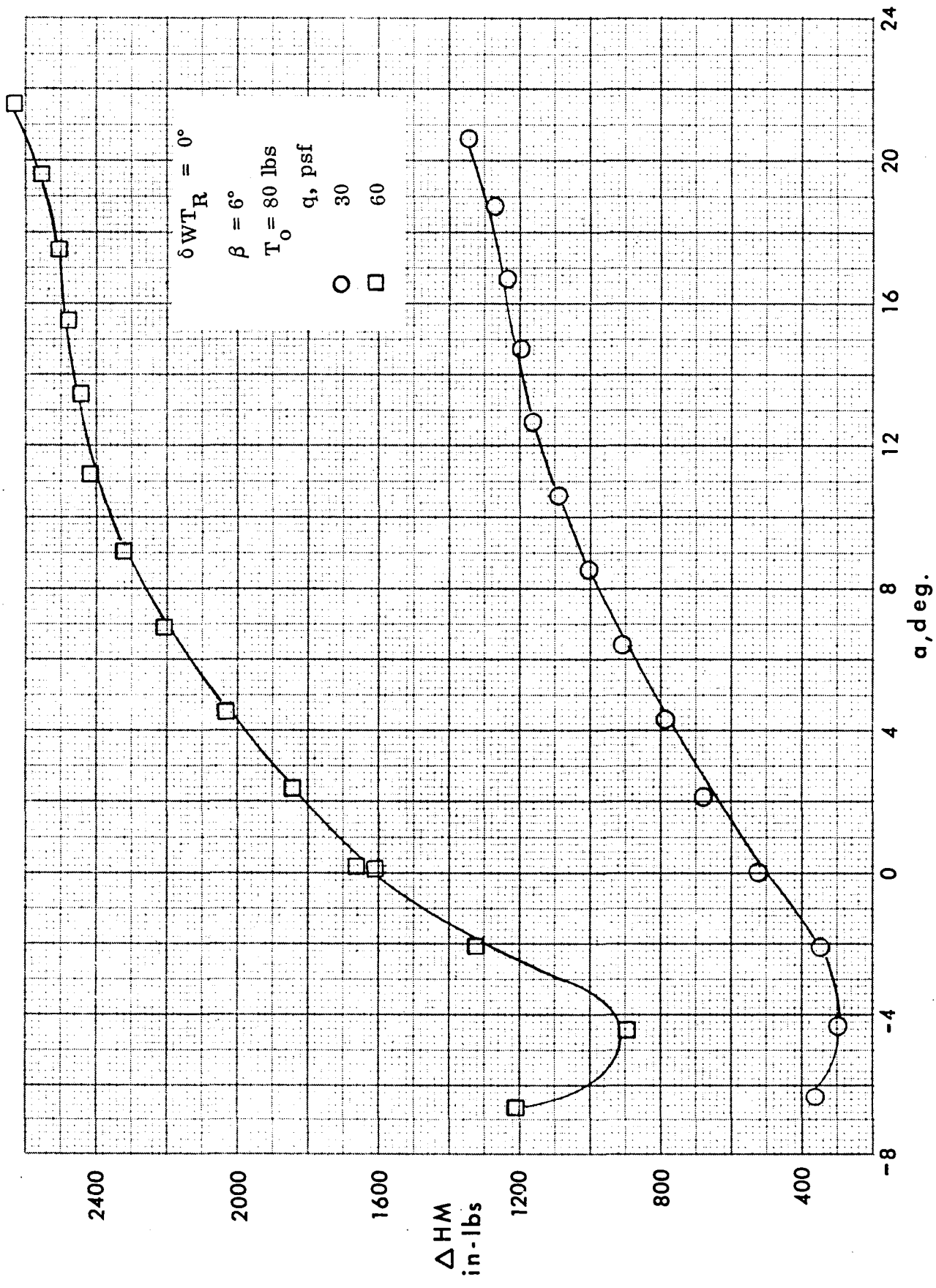


(a) $\beta = 6°$.

Figure 5-20. Effect of dynamic pressure and angle of attack on hinge moment. $T_o$ = 80 lbs, $\delta_{WT_R}$ = 0°.

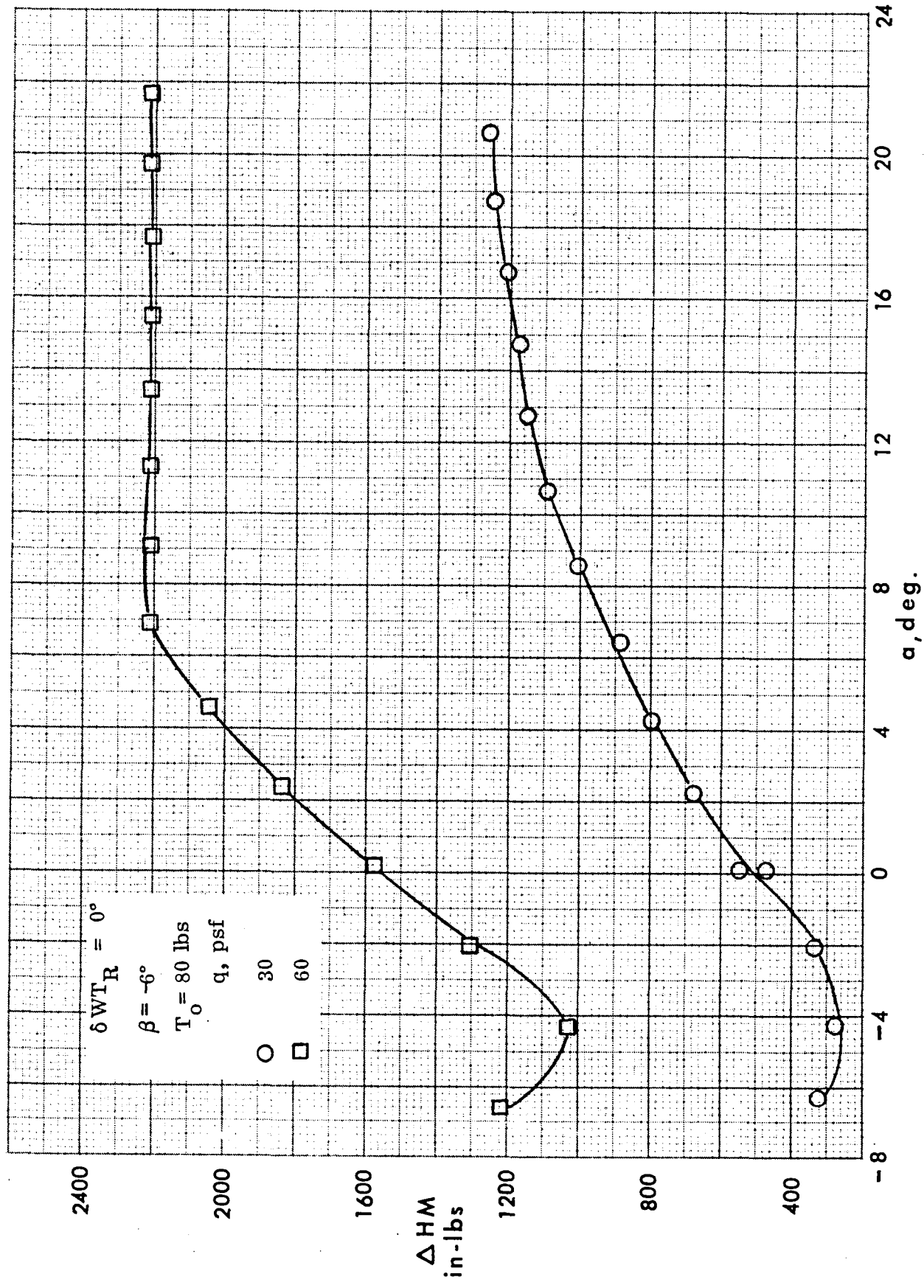


(b) $\beta = -6°$.

Figure 5-20. Concluded.

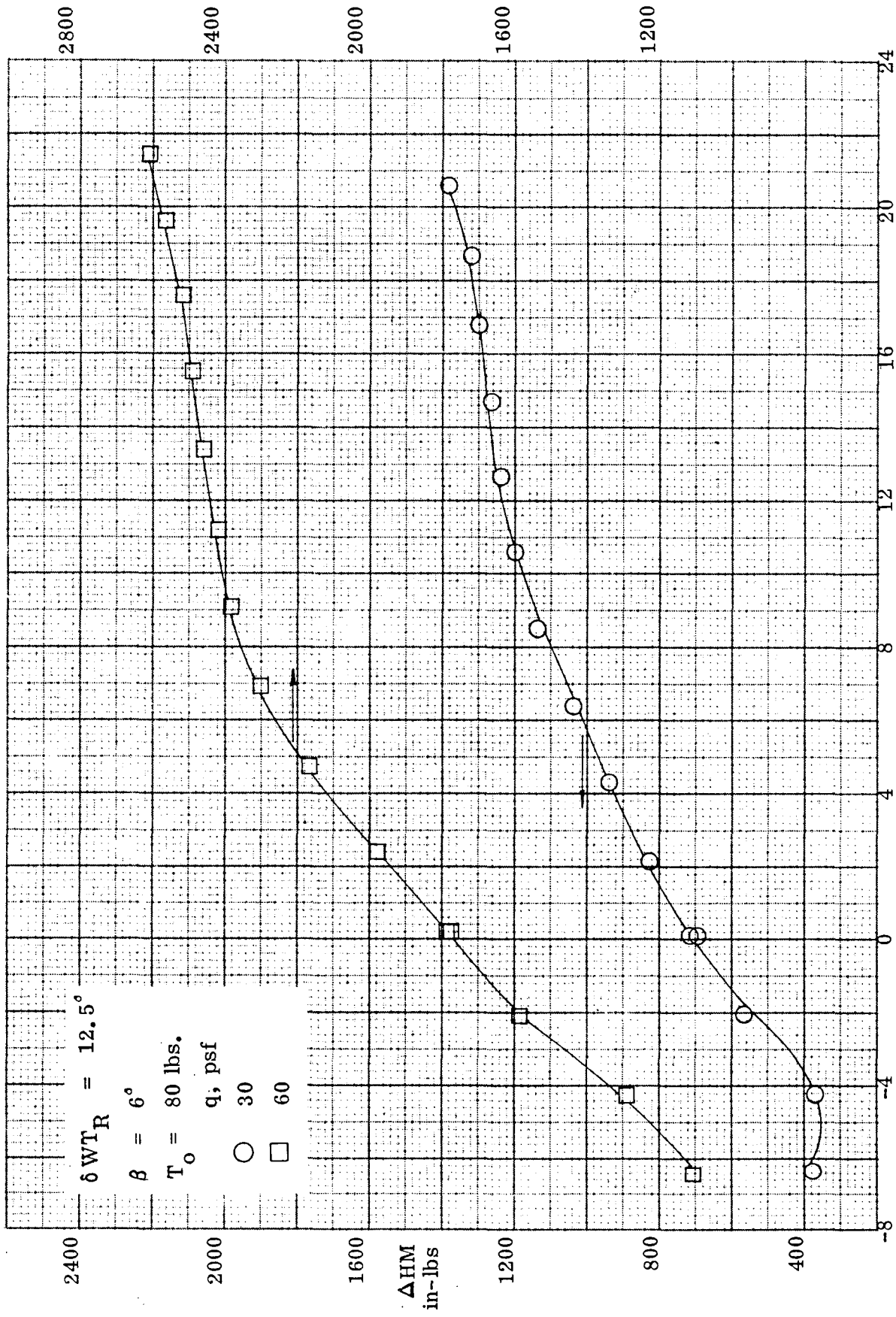


(a) $\beta = 6°$.

Figure 5-21. Effect of dynamic pressure and angle of attack on hinge moment. $T_o = 80$ lbs, $\delta_{WT_R} = 12.5°$.

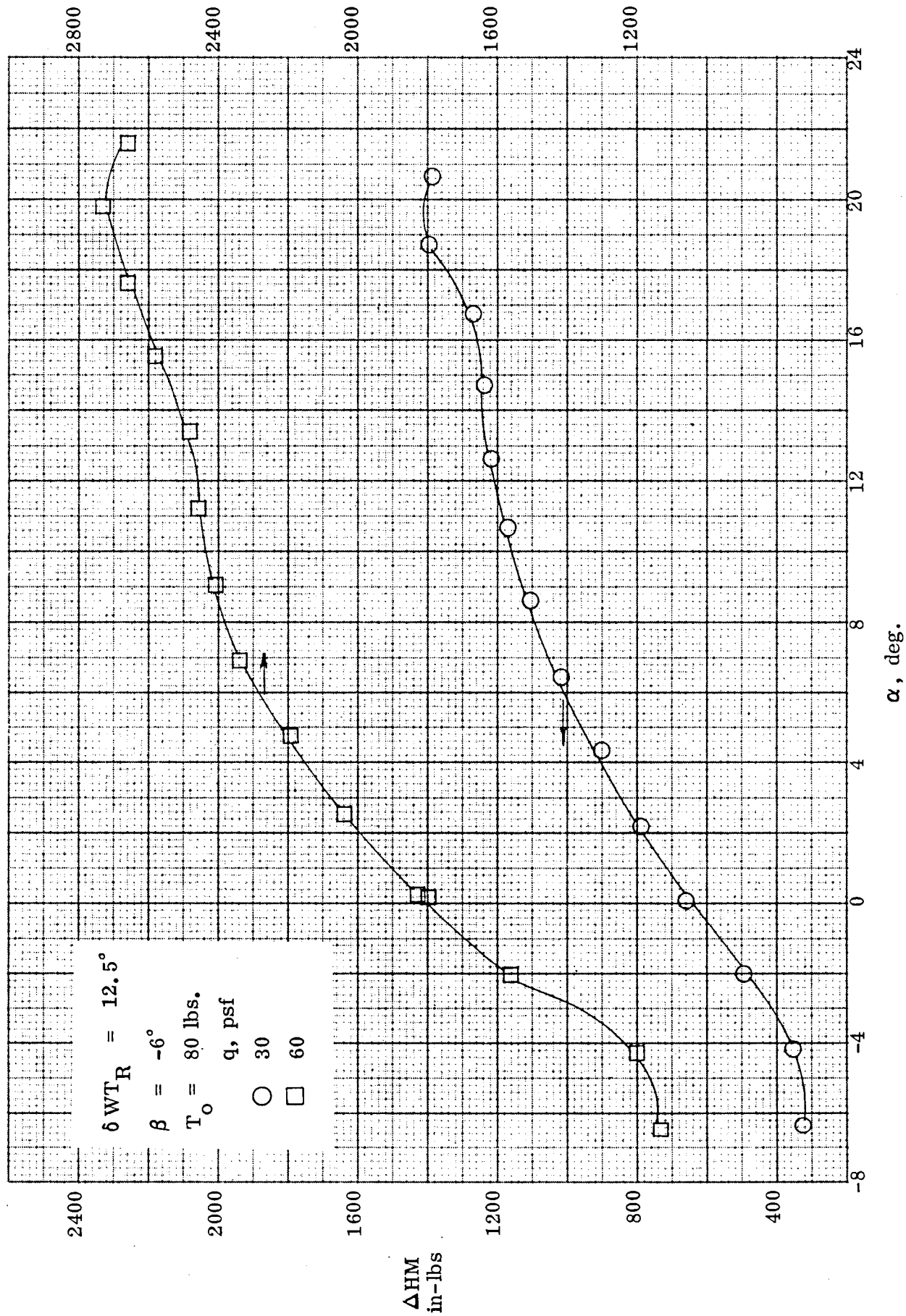


(b) $\beta = -6°$

Figure 5-21. Concluded.

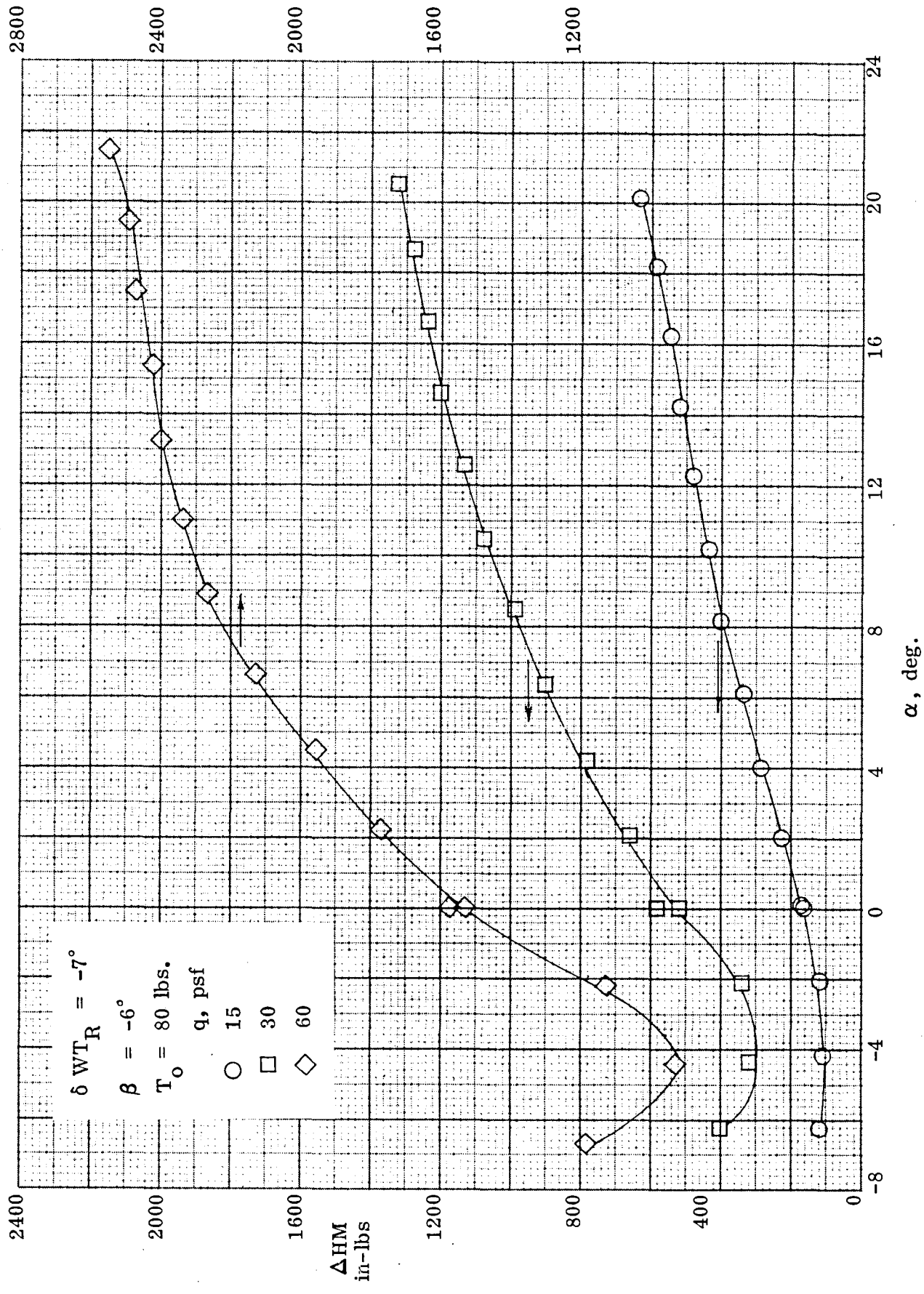


(a) $\beta = 6°$.

Figure 5-22. Effect of dynamic pressures and angle of attack on hinge moment. $T_o = 80$ lbs, $\delta_{WT_R} = -7°$.

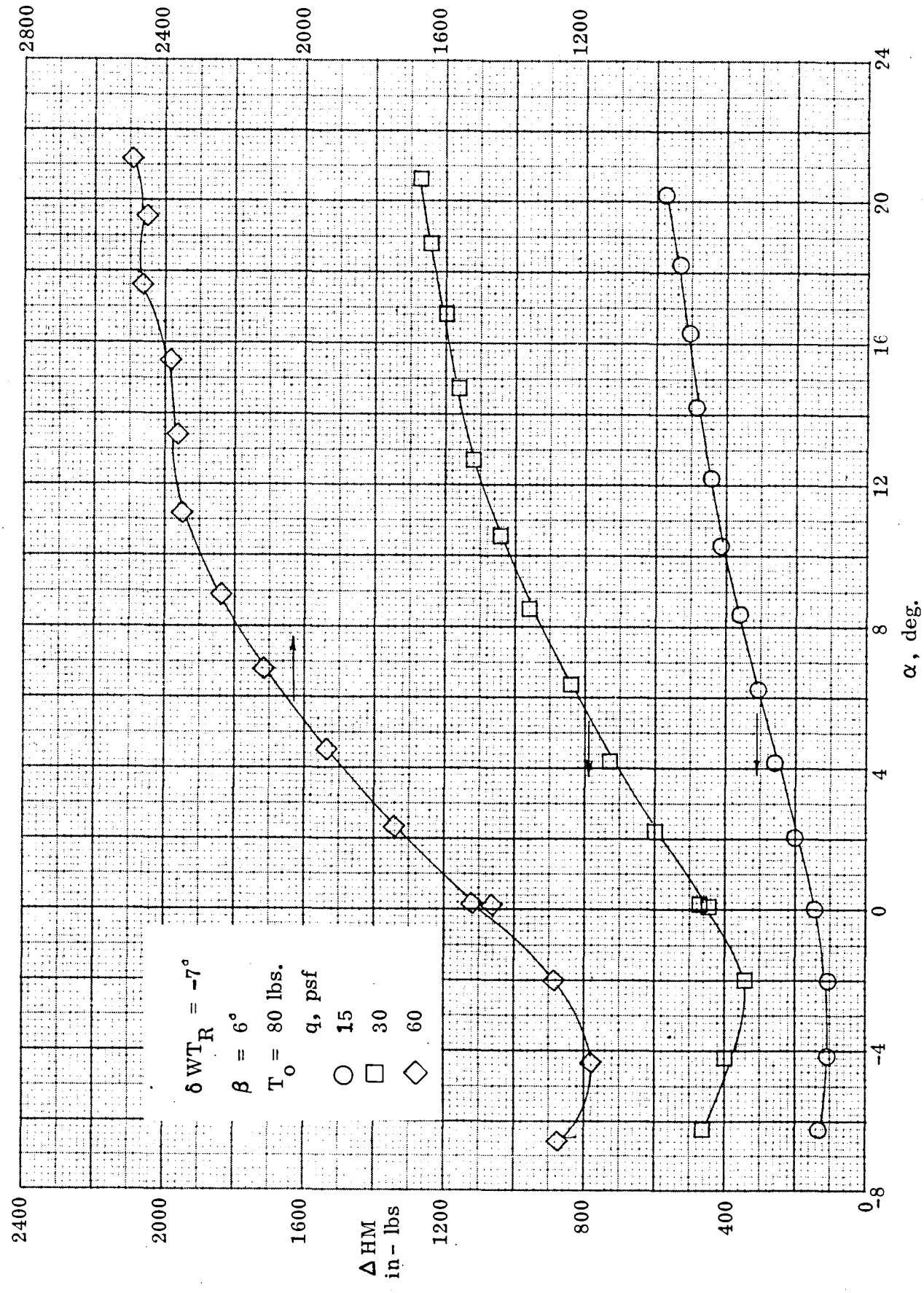


(b) $\beta = -6°$

Figure 5-22. Concluded

# SECTION 6
# DEPLOYMENT CHARACTERISTICS

The wing deployment investigation was conducted to gain insight into the manner of force build-up on the model during deployment, the importance of deployment rate, the effects of fabric flutter, and the forces on the wing structure during deployment. Scale factors are presented in the appendix which indicate how the results of the tests of this model may be extended to larger vehicles. Table 6-1 lists the test conditions used for each of the deployment test runs and the numbers of the figures in which the findings of the deployment tests are presented. The deployment time listed in Table 6-1 is the time it took to deploy the wing from a stowed position ($\Lambda = 80°$) to the fully extended position ($\Lambda = 20°$) using the deployment mechanism described earlier.

Figure 6-1 shows a wind-off deployment to check the rate of deployment and to identify the characteristics of the deployment system, so that later tests could show the effects of aerodynamic forces. The following important points are evident:

1) Due to the nature of the deployment mechanism, the deployment rate, as evidenced from the plot of $\dot{\Lambda}$, is not constant but varies with position as the wings tend to get ahead of the deployment system.

2) The hinge moment, measured by the compression (or tension) in a link of the deployment mechanism, begins at zero and drops to a small negative value, indicating that the link was under a small amount of compression when the wings were in their stowed position: the wings had to be restrained slightly to prevent unwanted movement. When deployment began, this restraint was removed and the link experienced no force; the reading is negative here because the zero-value of the data was taken while the wings were in their restrained position. The model was level and there was no wind, hence this value does not represent a force tending to assist the deployment mechanism.

   The hinge moment curve usually shows a positive peak immediately after deployment, which reflects the fact that the inertia of the wings and the

low mechanical advantage of the deployment mechanism in this position caused compression to build up in the linkage before it was relieved by wing movement. Once the wings moved, they swung out freely and compression in the link was reduced to almost zero.

The final rapid rise of hinge moment signifies the build-up of tension in the trailing edge cable and in the wing fabric, and occurs with no appreciable change of sweep angle.

TABLE 6-1. DEPLOYMENT TEST CONDITIONS

| Test Run No. | Dynamic Pressure ($lb/ft^2$) | $\alpha$ (deg) | Deployment Rate | Deployment Time (secs) | Figure Number |
|---|---|---|---|---|---|
| 33 | 0 | 0 | Fast | .90 | 6-1 |
| 34 | 15 | 0 | Fast | .89 | 6-2 |
| 36 | 15 | 5 | Fast | .77 | 6-3 |
| 37 | 15 | 10 | Fast | .78 | 6-4 |
| 38 | 15 | -5 | Fast | .57 | 6-5 |
| 42 | 15 | 0 | Slow | 1.86 | 6-6 |
| 43 | 15 | 10 | Slow | 2.02 | 6-7 |
| 45 | 30 | 0 | Slow | .99 | 6-8 |
| 46 | 30 | 10 | Slow | .94 | 6-9 |
| 47 | 60 | 0 | Slow | .66 | 6-10 |
| 48 | 60 | 10 | Slow | .80 | 6-11 |

3) The trailing edge cable tension behaves much like the hinge moment, since they are directly related through the deployment mechanism. The slight overshoot in both hinge moment and cable tension may be attributed to inertias in the system, both mechanical and fluid.

It will be noted that the final value of cable tension in the deployments is around 70 or 80 lbs, according to this data, while the tension measured by hand (using a tensometer) after each run showed (in most cases) the desired tension of 100 lbs, which was pre-set. There are two possible explanations of this:

1) The deployment system required a substantial length of time to build up to its final tension.

2) That part of the cable where the cable tension was measured by hand was under a different tension from that part of the cable containing the strain gage.

Of these, the first reflects the observation that, in some high -q deployments, the trailing edge cable tension and hinge moment climbed rapidly to peak value at the end of the deployment, then continued to increase at a very low rate, as long as the run lasted. This indicates that the deployment mechanism could not remove all the camber in the slack wing and stretch it to the fully-deployed position. This accounts for the more negative $C_m$ values obtained in the deployments, as is mentioned below. The first reason is also substantiated by the fact that in one run in particular the tension measured by hand after the run was considerably lower than the pre-set tension, but achieved the pre-set value after a wind-off recycling of the deployment actuator.

The second reason is suggested by the fact that some discrepancy in tension appears even in wind-off deployments, and that this difference may be due to the fact that between the strain gage location and the outboard part of the cable, where hand measurements were taken, was an eyelet against which the cable inadvertently pressed, and which possibly reduced through friction the tension seen by the strain gage.

Ideally, the final tension in the cable should equal the pre-set tension plus the increment of tension due to load discussed in Section 5. Examination of the deployment time histories reveals a large amount of scatter in the forces and moments, and this is due to the following:

1) Random signal noise in the recording system.

2) Stray vibrations in the tunnel which were picked up by the sting and appeared on the balance output.

3) Elastic couplings between sting and balance, and model and balance, and the presence of natural system frequencies.

The first was due to unavoidable electrical disturbances (lights, weak shielding, etc.) and the second to operations in an adjoining wind tunnel; the first is considerable in some runs, while the second is quite small and infrequent. The third is by far the most pronounced. All channels of force data show the presence of two vibrations, one at 25-30 cps and one at 5-10 cps, in addition to 13 cps in pitch and yaw and 11-12 cps in roll. These modes are excited at different times and under different conditions by unsteady airflow around the vehicle, and cause vibrations to appear in the data which reflect the lightly damped oscillation of the mechanism, and not true aerodynamic forces on the model.

The continuous data presented here is in fact comprised of discrete data points taken at a rate of 64 per second, and thus would not necessarily reveal any oscillation above about 30 cps. Such an oscillation was fabric flutter. As had been anticipated, the wing fabric fluttered rapidly in its loose condition before full extension, at from 50 to 60 cps as observed in oscillograph tracings. This rapid motion caused instantaneous peaks in the trailing edge cable at double this frequency and of a few pounds magnitude. This could have long-term detrimental effects on fabric seams along the trailing edge. In these wind tunnel model tests a gradual weakening of the stitching near the root-section trailing edge was observed which,in future applications,can be prevented by suitably reinforcing the fabric seams in this region. This gradual weakening of the stitching is believed to be partially responsible for the trailing edge cable tearing loose through the wing fabric on a deployment test with a dynamic pressure of 60 $lb/ft^2$ at a slow deployment rate corresponding to a deployment time of 6 seconds.

No investigation into means of reducing fabric flutter was conducted, although these tests suggest that very fast deployment may eliminate flutter, it was noted that in all cases flutter did not occur until the end of the initial high deployment rate, about halfway through the deployment. Once flutter begins, the force required to deploy the wing increases, with an attendant reduction in the deployment rate beyond this point.

Important factors gleaned from the structural and aerodynamic force data obtained in the wind-on tests and presented in Figures 6-2 through 6-10 are summarized in Table 6-2 and discussed below. The time periods denoted therein are relative to the time when the wing is first exposed to the air stream; this corresponds to a sweepback angle of about 80°.

With regard to hinge moment and cable tension (Table 6-2a, b) the final values represent the absolute values of these quantities, as opposed to the data of Section 5, wherein the increment above the pre-set (wind-off values) are presented. The data of Runs 45, 46 indicate that the highly-loaded wing was prevented from reaching full deployment by the forces trying to increase the camber; tension and hinge moment for those runs were slowly increasing from the end of deployment until the end of the run.

Final lift and pitching moment coefficient values attained in the deployment tests are presented in Table 6-3, where they are compared to the values presented in Section 5 which are referred to as static values-static in that the wing was fully deployed throughout the entire test run. The deployment test values of $C_m$ listed in the table include a slight correction to account for the forward travel of the model center-of-gravity when the wings move forward to their deployed position.

The differences between the deployment test values and the static test values of pitching moment coefficient can be explained on the basis of the differences in the camber shapes attained by the wing in static tests and the deployment tests.

The difference in camber is due to the inability of the model deployment mechanism to achieve full static deployment (corresponding to a leading edge sweep angle of 20°) because both the wing and trailing edge cable loaded up before full deployment was attained. In practice this could be overcome by using a deployment scheme which loads up the trailing edge cable only after the wing is fully deployed.

The increased camber in the trailing edge region apparently increased the pitching moment coefficient with no corresponding increase in lift coefficient. This is borne out by the fact that, as shown in Table 6-3, the agreement between the deployment and static test values of $C_L$ is quite good.

TABLE 6-2. SUMMARY OF DEPLOYMENT TESTS FORCE DATA

(a) Hinge Moment

| Test Run | $\alpha$ (deg) | q (psf) | Deployment Time (secs) | Maximum Build-up Period (secs) | $\Delta$HM in this Period (in-lbs) | Largest Variation Prior to Build-up (in-lbs) | Final Value (in-lbs) |
|---|---|---|---|---|---|---|---|
| 34 | 0 | 15 | .89 | .67- .89 | 0-2200 | 400,-300 | 2200 |
| 36 | 5 | 15 | .77 | .57- .77 | 0-2550 | 300,-240 | 2420 |
| 37 | 10 | 15 | .78 | .53- .78 | 0-2750 | 300,-130 | 2640 |
| 38 | -5 | 15 | .57 | .30- .57 | 100-2160 | 340, 0 | 2100 |
| 42 | 0 | 15 | 1.86 | 1.36-1.86 | 100-2480 | -120, 300 | 2400 |
| 43 | 10 | 15 | 2.02 | 1.36-2.02 | 300-2560 | - 80, 260 | 2620 |
| 45 | 0 | 30 | .99 | .68- .99 | 160-2420 | -320,1040 | 2550 |
| 46 | 10 | 30 | .94 | .63- .94 | 300-2200 | -120, 680 | 2280 |
| 47 | 0 | 60 | .66 | .55- .66 | 700-3680 | -100,1400 | 3660 |
| 48 | 10 | 60 | .80 | .55- .70 | 700-3750 | - 50, 95 | 3750 |

(b) Cable Tension

| Test Run | $\alpha$ (deg) | q (psf) | Build-up Period (secs) | Period of Maximum Build-up Rate (secs) |
|---|---|---|---|---|
| 34 | 0 | 15 | .30- .89 | .67- .89 |
| 36 | 5 | 15 | .27- .77 | .62- .77 |
| 37 | 10 | 15 | .23- .75 | .58- .75 |
| 38 | -5 | 15 | .26- .57 | .26- .57 |
| 42 | 0 | 15 | 1.15-1.86 | 1.35-1.86 |
| 43 | 10 | 15 | 1.00-2.02 | 1.37-2.02 |
| 45 | 0 | 30 | .41- .99 | .70- .99 |
| 46 | 10 | 30 | .39- .94 | .62- .94 |
| 47 | 0 | 60 | .36- .66 | .52- .66 |
| 48 | 10 | 60 | .36- .66 | .50- .66 |

(c) Wing Deployment Rate

| Test Run | Final Value (lbs) | Period of Maximum Rate (secs) | Maximum Rate (deg/sec) |
|---|---|---|---|
| 34 | 66 | .13-.39 | 160 |
| 36 | 72 | .04-.33 | 183 |
| 37 | 75 | .05-.31 | 204 |
| 38 | 65 | .05-.21 | 270 |
| 42 | 73 | .06-.30 | 88 |
| 43 | 79 | .05-.35 | 160 |
| 45 | 76 | .00-.21 | 230 |
| 46 | 63 | .00-.24 | 230 |
| 47 | 112 | .00-.20 | 280 |
| 48 | 110 | .00-.20 | 280 |

TABLE 6-2. SUMMARY OF DEPLOYMENT TESTS FORCE DATA (Cont'd)

(d) Lift Coefficient

| Test Run | $\alpha$ (deg) | q (psf) | Total $\Delta C_L/\Delta t$ (per sec) | Max. $\Delta C_L/\Delta t$ (per sec) | Time (secs) | Final Average Value of $C_L$ ($t \rightarrow \infty$) |
|---|---|---|---|---|---|---|
| 34 | 0 | 15 | .22 | .33 | .55 | .22 |
| 36 | 5 | 15 | .76 | 1.11 | .55 | .56 |
| 37 | 10 | 15 | 1.10 | 2.52 | .55 | .97 |
| 38 | -5 | 15 | -.30 | -1.12 | .50 | -.26 |
| 42 | 0 | 15 | .11 | .33 | 1.40 | .21 |
| 43 | 10 | 15 | .49 | 1.65 | 1.25 | 1.02 |
| 45 | 0 | 30 | .29 | 1.17 | .71 | .32 |
| 46 | 10 | 30 | 1.12 | 2.22 | .66 | 1.04 |
| 47 | 0 | 60 | .44 | 2.34 | .60 | .38 |
| 48 | 10 | 60 | 1.62 | 2.34 | .40 | 1.11 |

(e) Pitching Moment Coefficient

| Test Run | $\alpha$ (deg) | q (psf) | Initial Average Value | Final Average Value | Final Average $C_m$ Corrected |
|---|---|---|---|---|---|
| 34 | 0 | 15 | -.0036 | -.0032 | -.0015 |
| 36 | 5 | 15 | -.0029 | -.0039 | -.0022 |
| 37 | 10 | 15 | -.0018 | -.0019 | -.0015 |
| 38 | -5 | 15 | -.0036 | .0022 | .0390 |
| 42 | 0 | 15 | -.0036 | -.0041 | -.0230 |
| 43 | 10 | 15 | -.0032 | -.0033 | -.015 |
| 45 | 0 | 30 | -.0036 | -.0034 | -.026 |
| 46 | 10 | 30 | -.0032 | -.0033 | -.025 |
| 47 | 0 | 60 | -.0043 | .0036 | -.031 |
| 48 | 10 | 60 | -.0054 | -.0035 | -.030 |

TABLE 6-2. SUMMARY OF DEPLOYMENT TESTS FORCE DATA (Cont'd)

| | | | (f) Rolling Moment Coefficient | | | (g) Yawing Moment Coefficient | | |
|---|---|---|---|---|---|---|---|---|
| Test Run | α (deg) | q (psf) | Final Value | Maximum Avg. Value | Time (secs) | Maximum Peak Value | Maximum Peak Value | Time (secs) |
| 34 | 0 | 15 | .016 | .057 | .80 | ±.095 | ±.50<br>-.40 | .20 |
| 36 | 5 | 15 | .016 | .066 | .65 | +.21<br>-.090 | +.38<br>-.44 | .75 |
| 37 | 10 | 15 | .009 | .019 | .85 | +.090<br>-.06 | +.25<br>-.28 | .76 |
| 38 | -5 | 15 | .031 | .038 | .70 | ±.16 | >1.20 | .34 |
| 42 | 0 | 15 | .019 | .041 | 1.60 | +.095<br>-.06 | ±.19 | .14 |
| 43 | 10 | 15 | .013 | .054 | 1.15 | +.075<br>-.054 | ±.13 | .10 |
| 45 | 0 | 30 | .038 | .038 | 1.00 | +.088<br>-.060 | +.19<br>-.16 | .85 |
| 46 | 10 | 30 | .016 | .032 | .80 | +.14<br>-.04 | +.13<br>-.13 | .70 |
| 47 | 0 | 60 | .063 | .016 | .45 | +.060<br>-.041 | +.080<br>-.090 | .06 |
| 48 | 10 | 60 | -.016 | .016 | .40 | +.060<br>-.032 | +.047<br>-.038 | .30 |

TABLE 6-3. COMPARISON OF FINAL VALUES OF DEPLOYMENT TEST $C_L$ AND $C_m$ WITH STATIC TEST RESULTS

| Test Run | $\alpha$ (deg) | $q$ ($lb/ft^2$) | $C_{L_{dep}}$ | $C_{L_{stat}}$ | $C_{m_{dep}}$ | $C_{m_{stat}}$ |
|---|---|---|---|---|---|---|
| 34 | 0 | 15 | .222 | .197 | -.0146 | -.0066 |
| 36 | 5 | 15 | .562 | .597 | -.0219 | -.0055 |
| 37 | 10 | 15 | .970 | .980 | -.0015 | -.0030 |
| 38 | -5 | 15 | -.258 | -.198 | .0392 | -.0098 |
| 42 | 0 | 15 | .210 | .196 | -.0234 | -.0065 |
| 43 | 10 | 15 | 1.010 | .980 | -.0154 | -.0033 |
| 45 | 0 | 30 | .316 | .210 | -.0256 | -.0088 |
| 46 | 10 | 30 | 1.040 | 1.050 | -.0252 | -.0117 |
| 47 | 0 | 60 | .380 | .351 | -.0355 | -.023 |
| 48 | 10 | 60 | 1.110 | 1.110 | -.0347 | -.0200 |

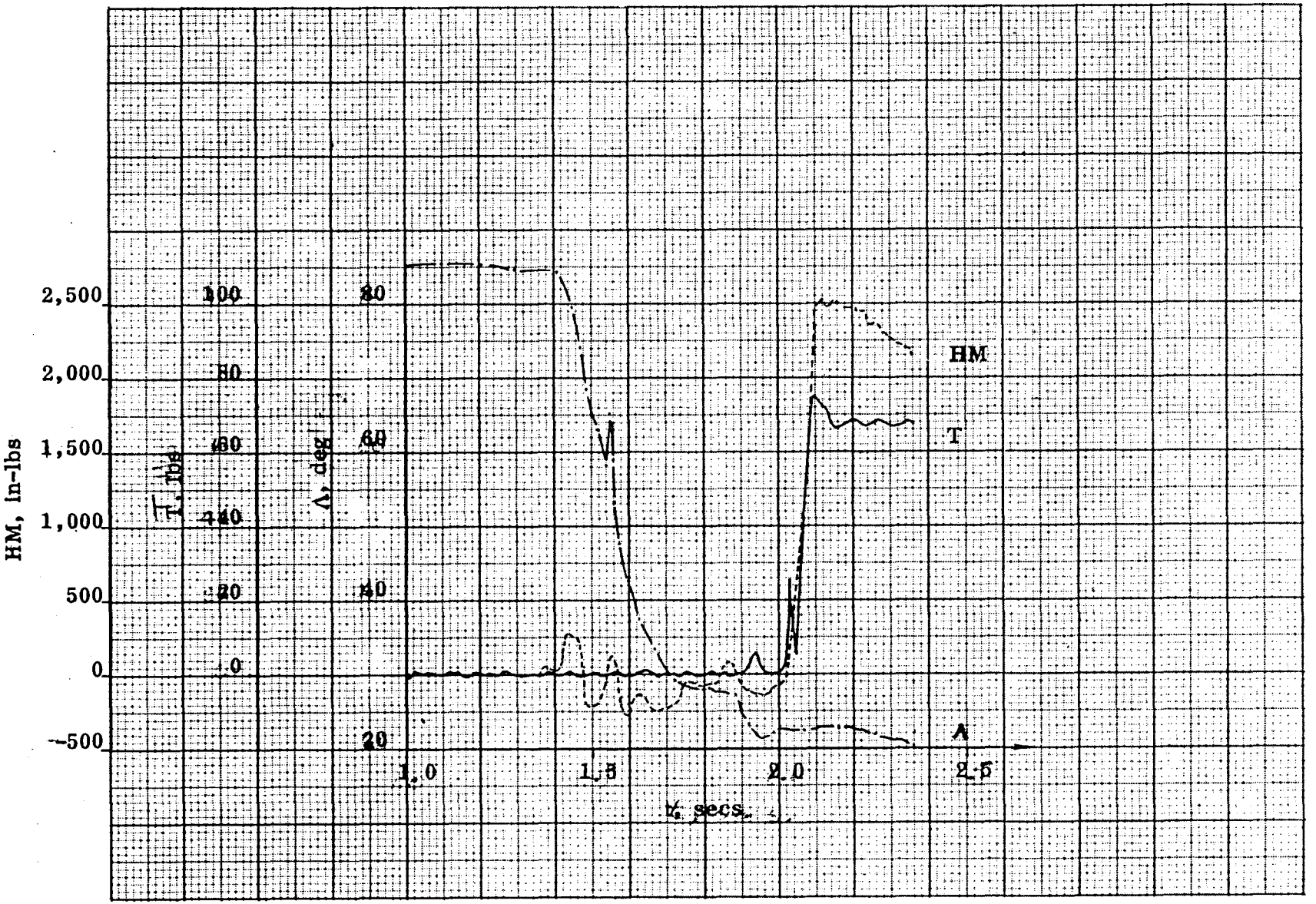


Figure 6-1. Deployment test run 33. q = 0, fast deployment rate.

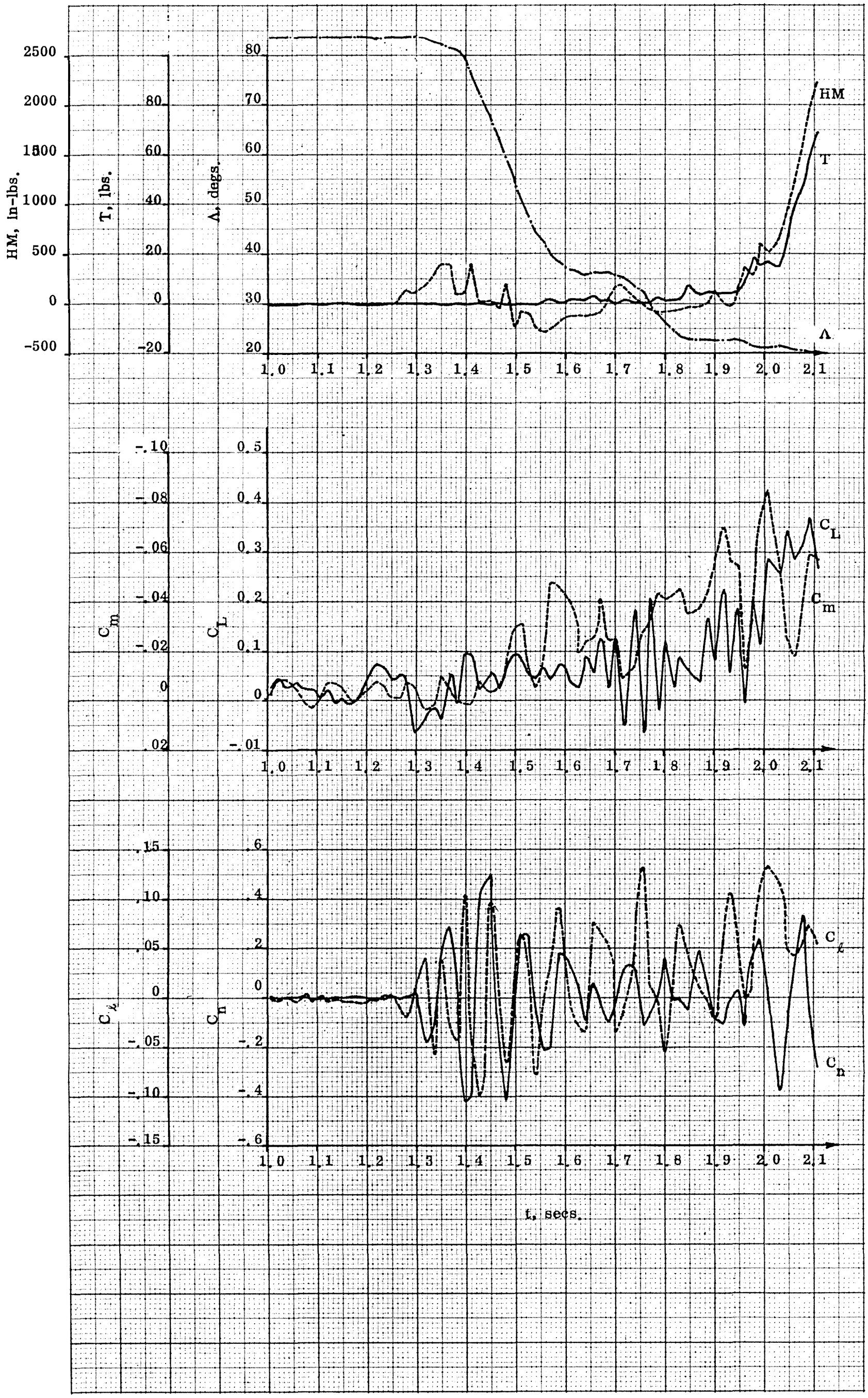


Figure 6-2. Deployment test run 34. q = 15 psf, $\alpha = 0°$, fast rate.

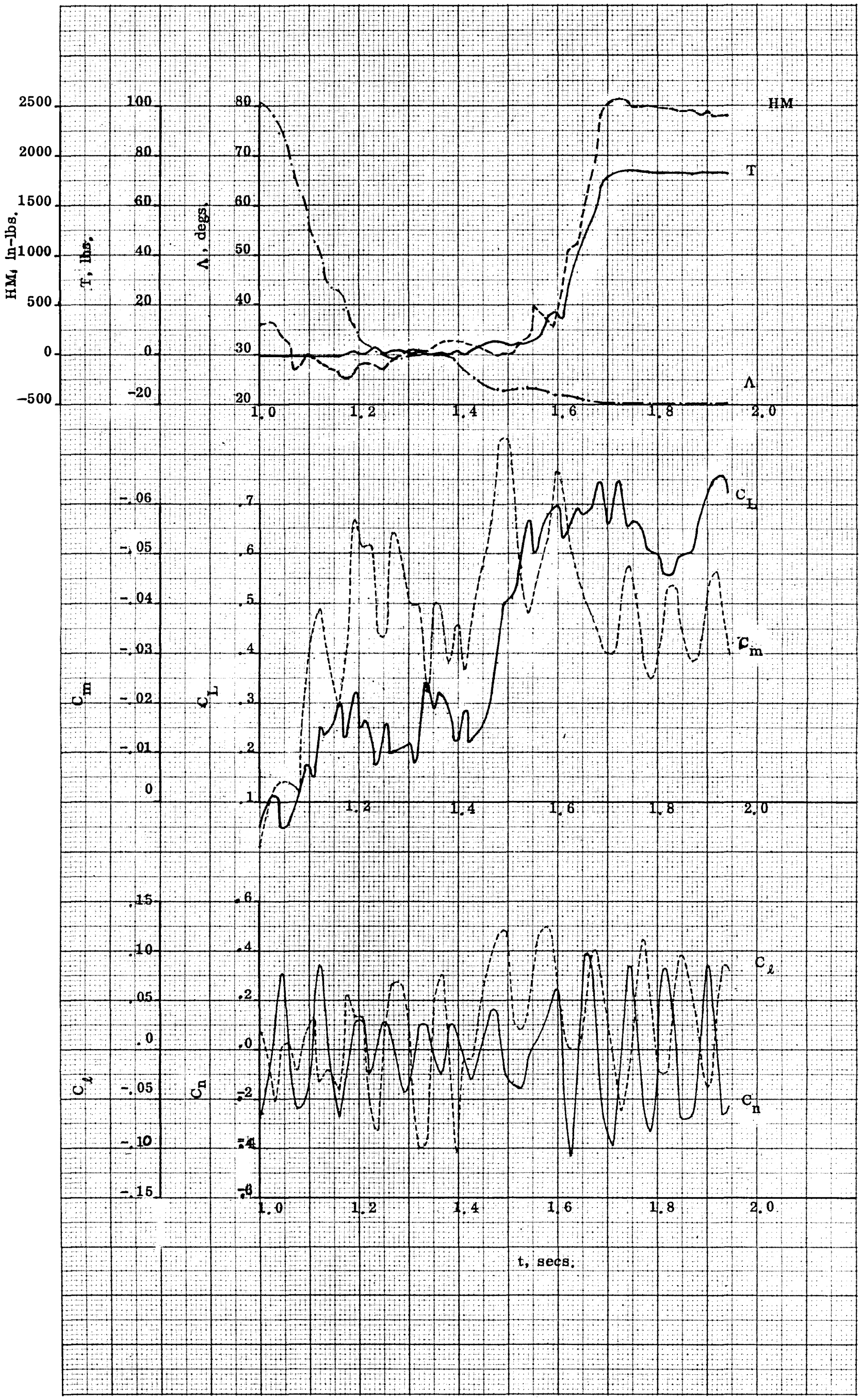


**Figure** 6-3. Deployment test run 36. q = 15 psf, $\alpha$ = 5°, fast rate.

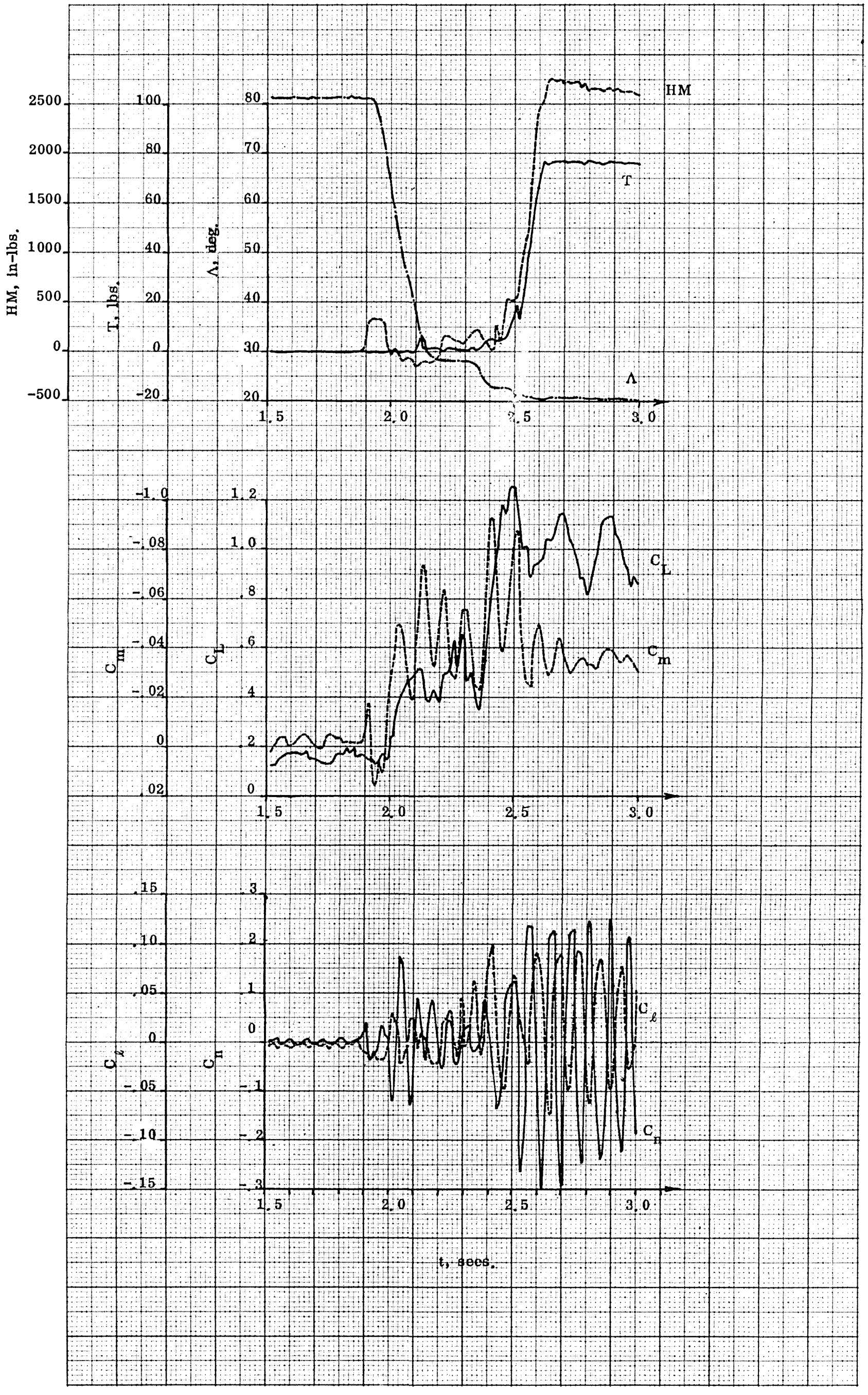


Figure 6-4. Deployment test run 37. q = 15 psf, $\alpha$ = 10°, fast rate.

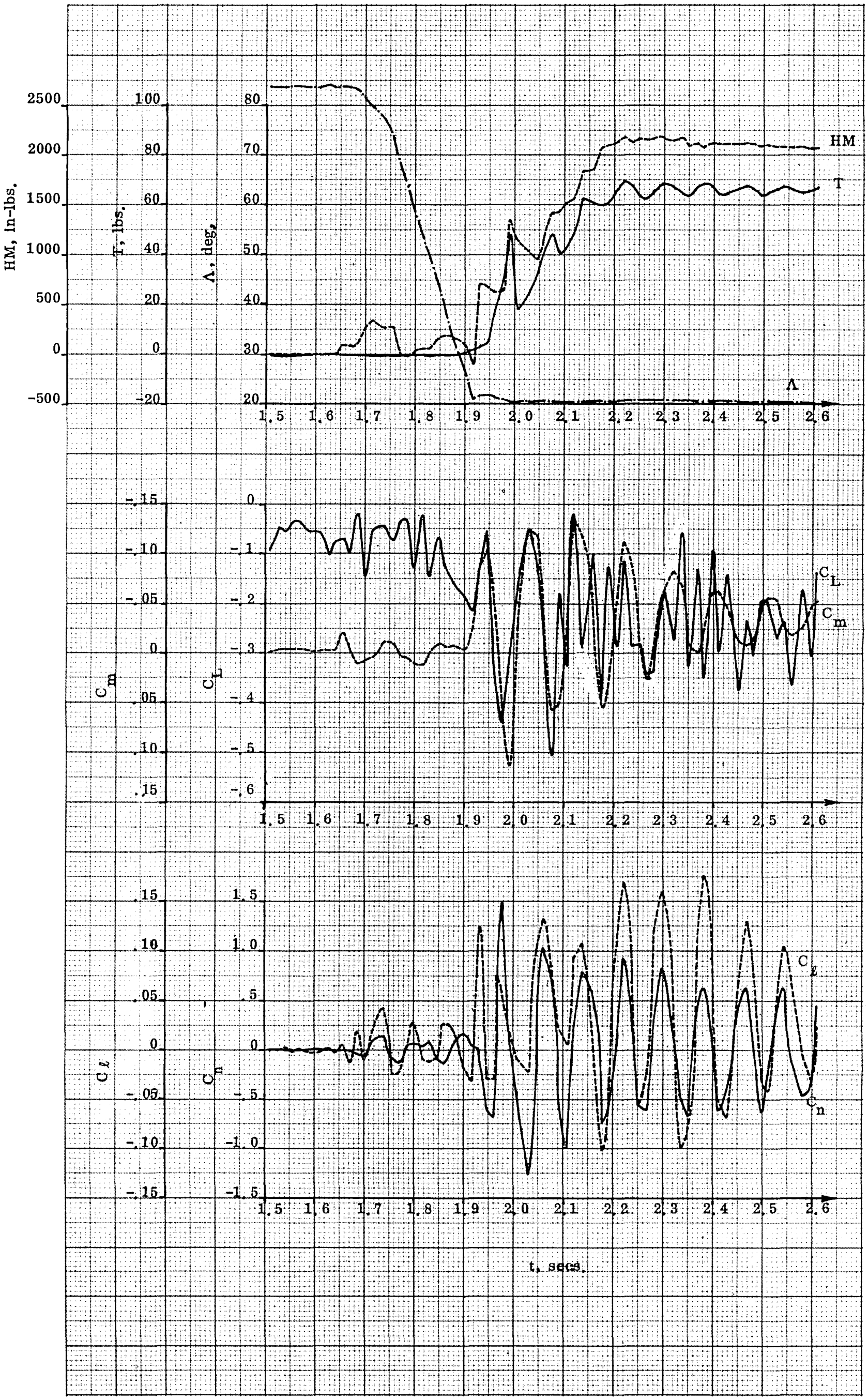


Figure 6-5. Deployment test run 38. q = 15 psf, $\alpha$ = -5°, fast rate.

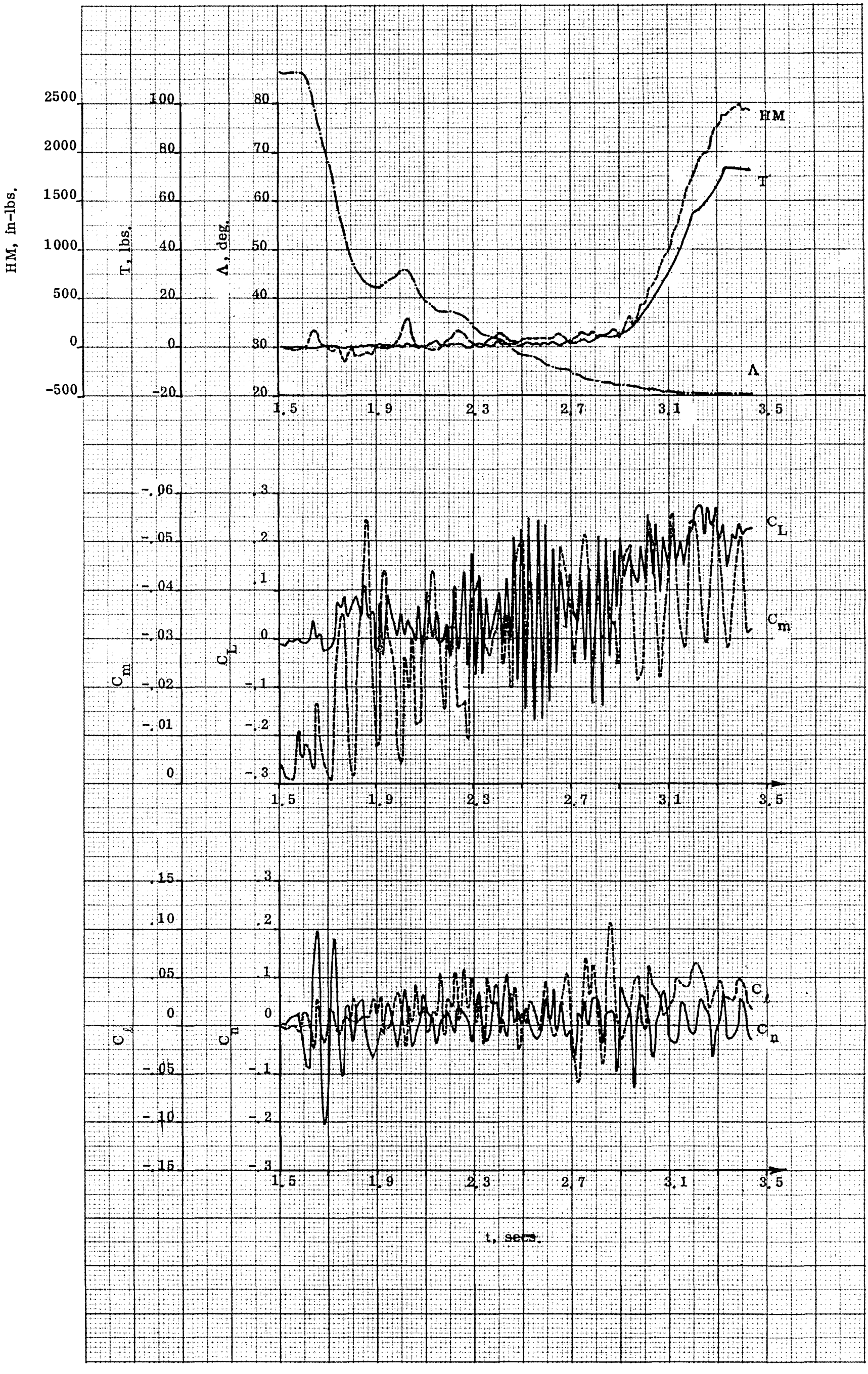


Figure 6-6. Deployment test run 42. q = 15 psf, $\alpha$ = 0°, slow rate.

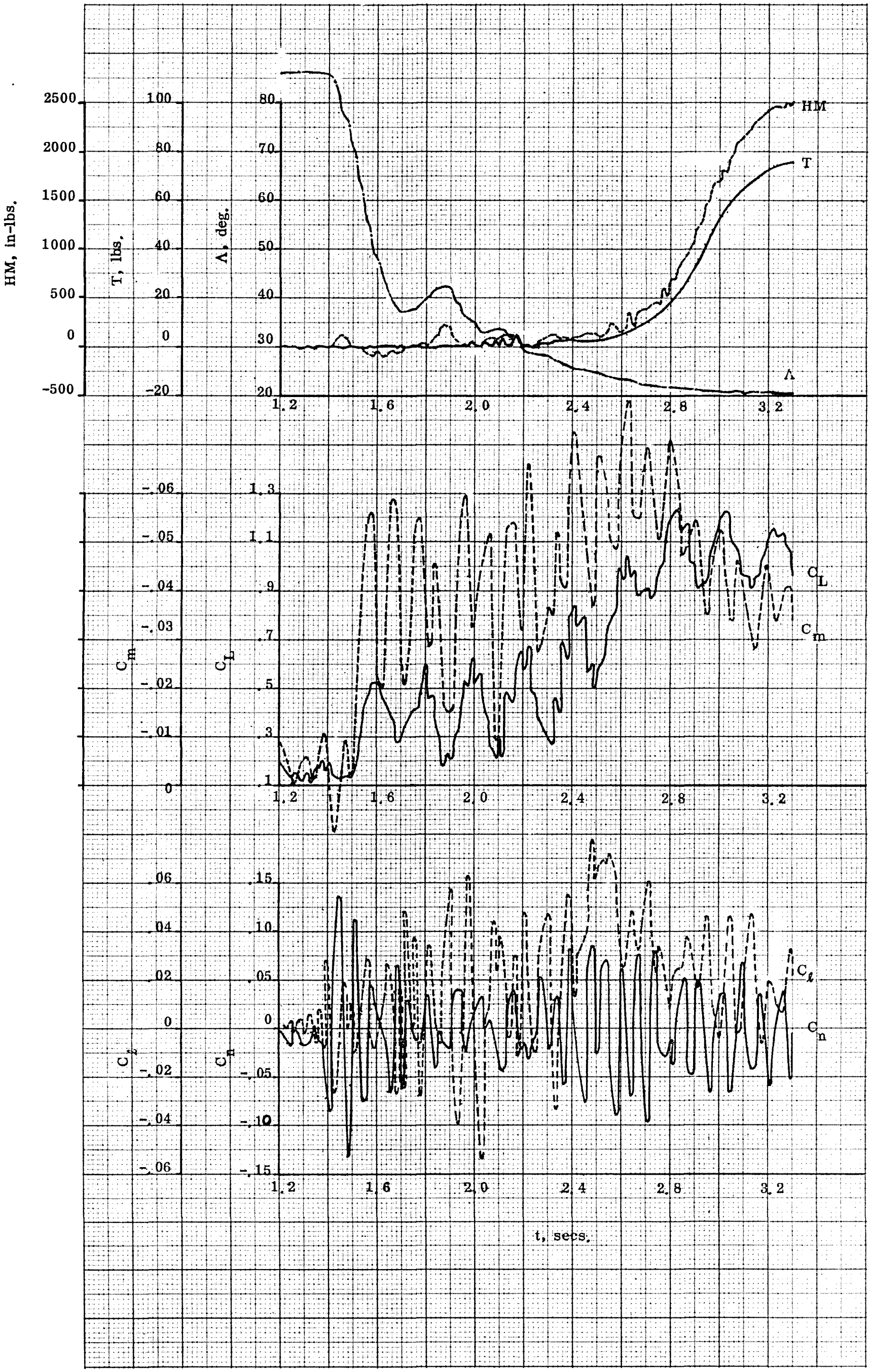


Figure 6-7. Deployment test run 43. q = 15 psf, $\alpha = 10°$, slow rate.

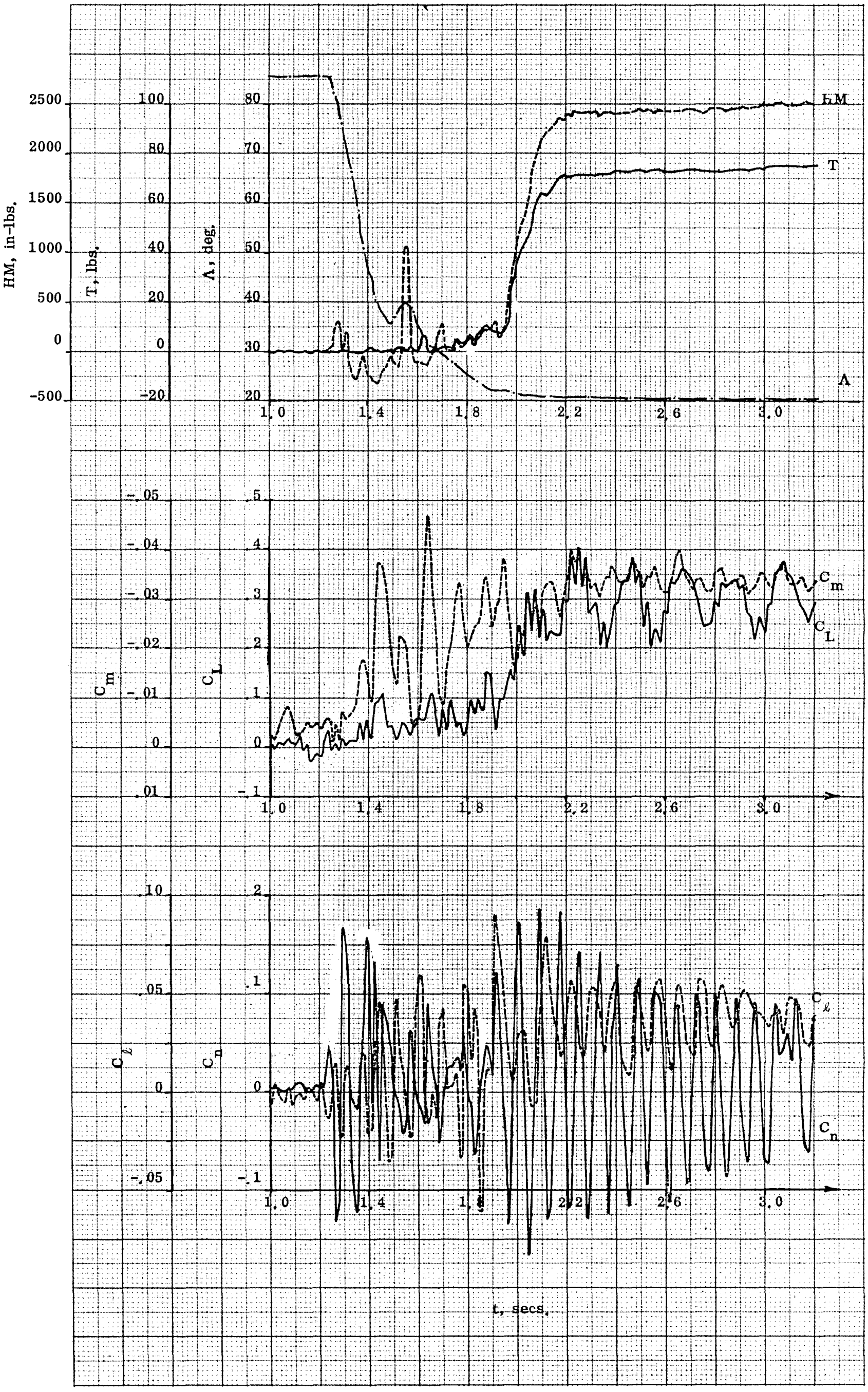


Figure 6-8. Deployment test run 45, q = 30 psf, $\alpha = 0°$, slow rate.

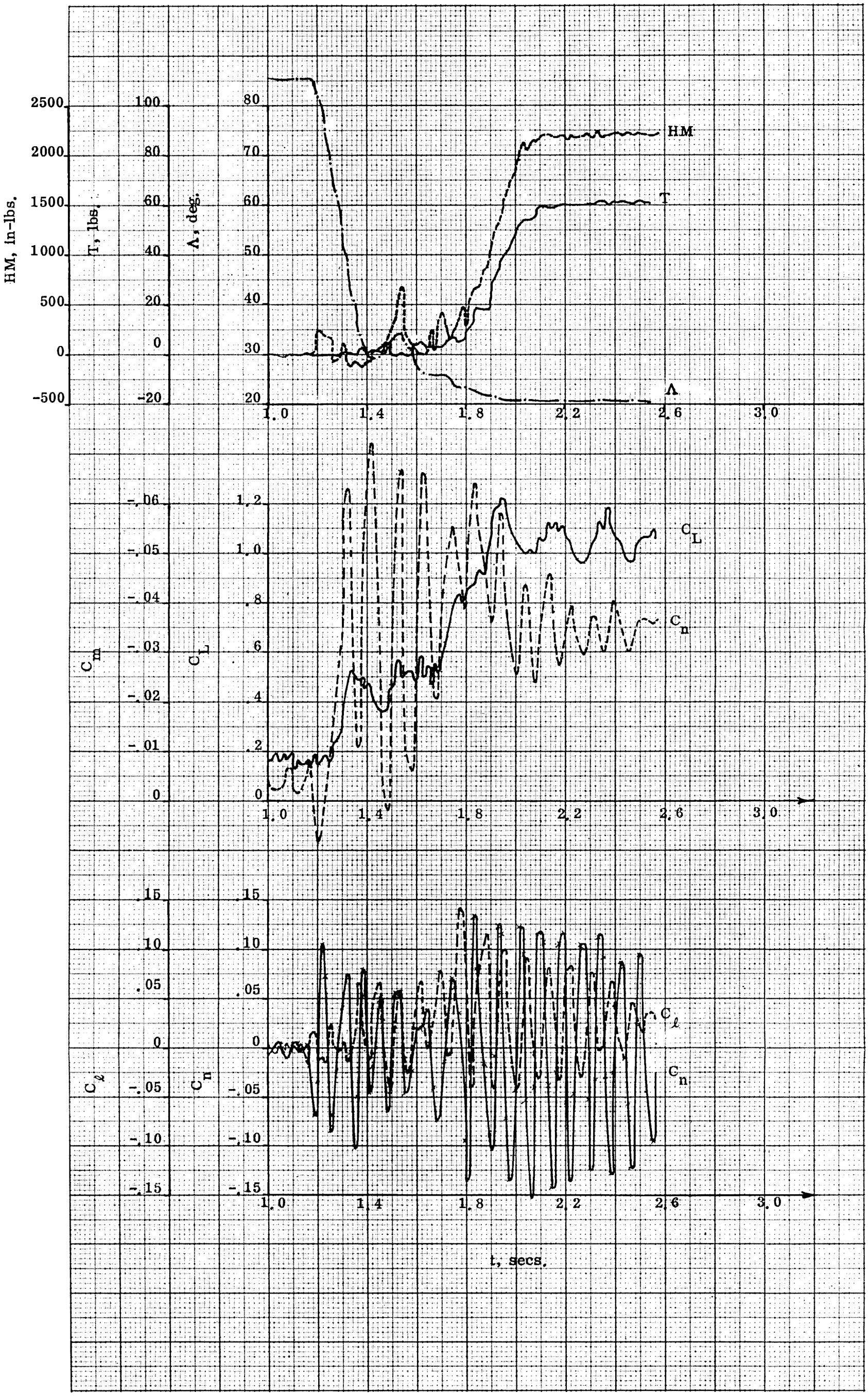


Figure 6-9. Deployment test run 46. q = 30 psf, $\alpha = 10°$, slow rate.

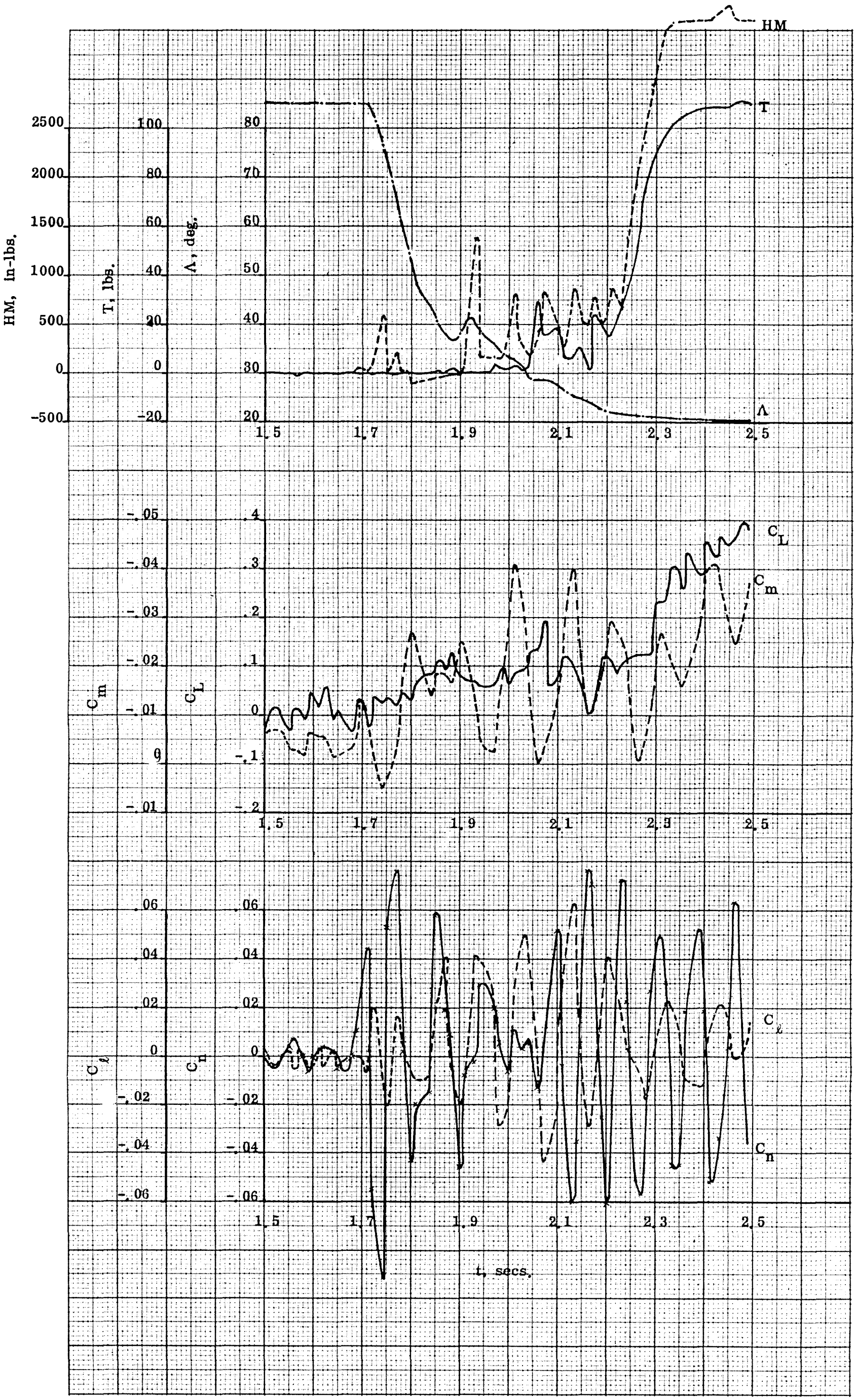


Figure 6-10. Deployment test run 47. q = 60 psf, $\alpha = 0°$, slow rate.

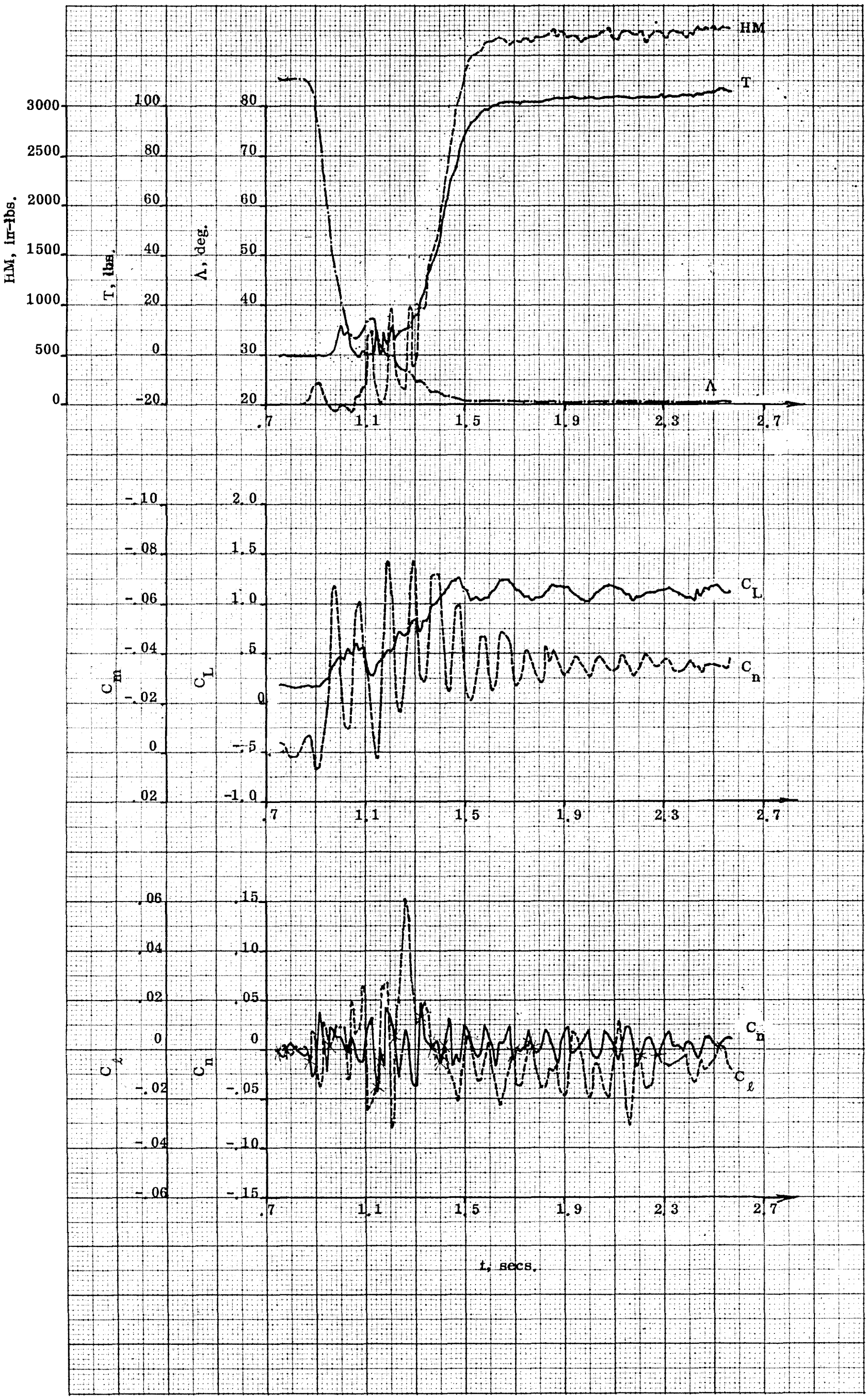


Figure 6-11. Deployment test run 48. q = 60 psf, $\alpha = 10°$, slow rate.

# SECTION 7
# BODY-ALONE AND WING-BODY LIFT-CURVE SLOPES COMPARISON

The lifting effectiveness of any wing added to a lifting body comes from three sources: a basic wing-alone lift which would be generated by the exposed wing area in the free stream, and lift increments produced by the mutual interference of wing-on-body, and body-on-wing. Each of these contributions may be calculated with a fairly high degree of certainty using methods such as those presented in Reference 5.

The methodology of that reference has been mechanized as a digital computer program by the contractor (Reference 6). This computer program was used in this investigation to estimate lift-curve slopes at zero angle of attack, in addition to the drag and longitudinal static stability characteristics of the test configurations. The geometry of the basic DL-4 body was inputted to this program, and three representative sailwings were added to the configuration. One of these was the sailwing under consideration here, and referred to subsequently as the nominal sized sailwing, and the others were wings with exposed areas of 0.5 and 1.5 times the exposed area of the nominal wing, and are referred to later as the downsized and upsized wings, respectively. These wings are shown in Figure 7-1 in which it is seen that they are geometrically similar, each having a leading edge sweep of 20°.

The estimated contributions to the total vehicle lift-curve slope are shown in Figure 7-2, as functions of exposed wing area. It is noted that the wing-on-body interference lift is always larger than the body-on-wing interference lift, since the wing with its higher aspect ratio is a more effective flow-inducer than the slender body. Moreover, the interference effects contribute about 30% of the lift of the wing-body vehicle. It is seen that the computer-program-predicted values of lift-curve slope for the body-alone and for the body with the nominal size sailwing agree very closely with the experimental values. The indication is, therefore, that the prediction methods are sufficiently accurate to evaluate the relative effectiveness, in terms of lift-curve slope, of wings of the given shape on the DL-4 body.

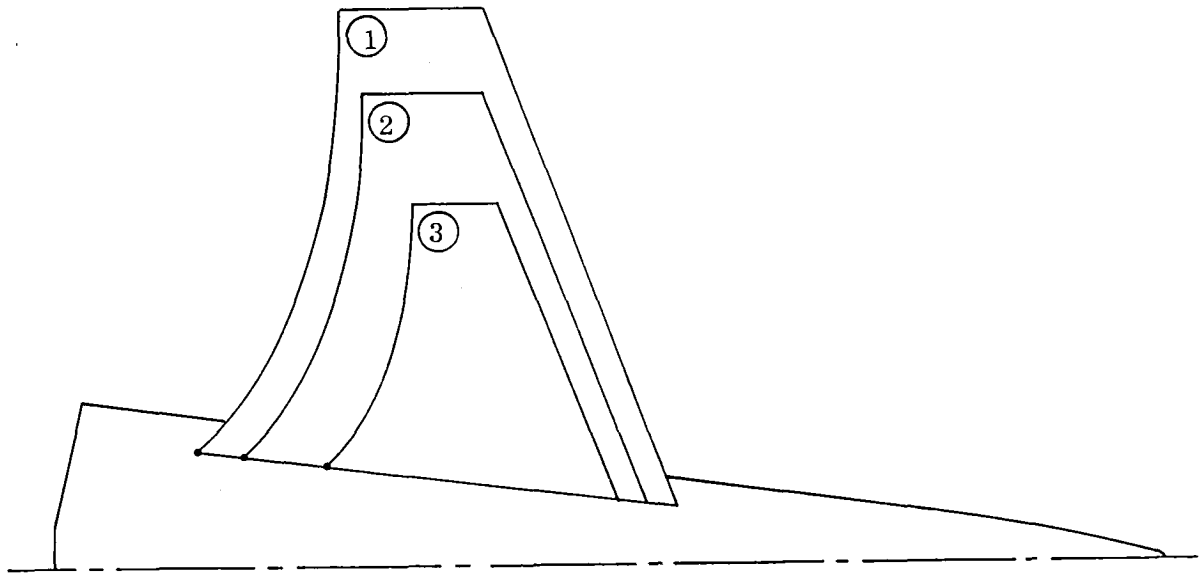


① Upscaled ($S_{exp}$ = 1.5 $S_{exp\,②}$)

② Nominal

③ Downscaled ($S_{exp}$ = 0.5 $S_{exp\,②}$)

Figure 7-1. DL-4 body with various size wings.

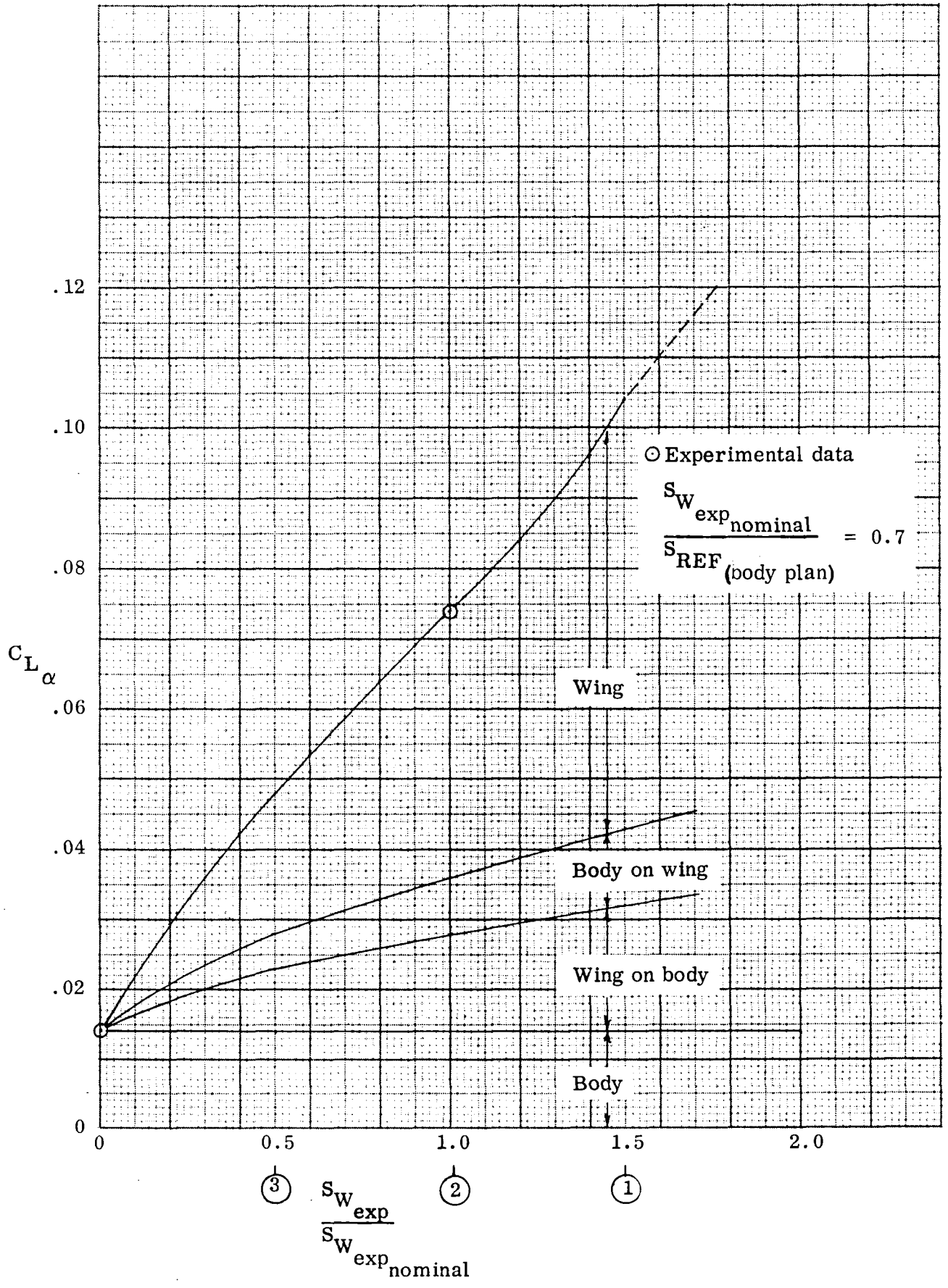


Figure 7-2. Wing-body lift curve slope breakdown

## SECTION 8

## SAILWING VS RIGID WING TRADE STUDY

### A. Vehicle Sizing Guidelines

The DL-4 body considered in this analysis was scaled up in size to that of a reusable orbiter vehicle portion of a space shuttle concept satisfying the following main guidelines:

1) 50,000 pound up/down payload capacity
2) Payload to be housed in a 15 ft dia x 60 ft long cargo bay
3) 260 nm orbit, provided by velocity increment ($\Delta V$) capability of 2000 ft/sec
4) Seven-day mission duration for a 2-man crew
5) Conventional landing on 10,000 ft runway with go-around capability
6) $LO_2$, $LH_2$ propellants
7) All propulsion system hardware reusable

The 2000 ft/sec velocity increment capability cited above is assumed to be required for transfer from a basic 45x100 nm orbit, of 55° inclination, to the 260 nm orbit via a 100 nm circular parking orbit; for rendezvous, docking and deorbit operations; and for contingencies. Accordingly, the trajectory assumptions used in the vehicle system sizing were that the vehicle is first boosted to an altitude of 45 nm and a velocity of 18,000 ft/sec using disposable strap-on tanks. The tanks are jettisoned at this point and the vehicle inserted in a 45x100 nm orbit. This velocity requirement, together with the 2000 ft/sec $\Delta V$ requirement determined the amount of onboard propellant required. Due allowance was made for velocity losses due to drag and gravity.

The configuration approach taken here is representative of the "one-stage-and-a-half" concept. This concept leads to much smaller launch weights, for a given payload, than does the fully-recoverable two-stage concepts, and was therefore selected here. The fuel required for boosting the orbiter vehicle from the ground would be carried in disposable strap-on tanks arranged in the shape of a "vee" nestled against the sides of the body. The booster engines are housed within the orbiter vehicle. These same engines are also used for orbit injection and subsequent maneuvers mentioned above.

Based upon the above constraints, including the requirement that no modifications were to be made to the DL-4 body shape, the vehicle which evolved is 170 ft long, and fully loaded with its internal fuel (none external) and payload weighs 448,570 pounds. As shown in Table 8-1, the vehicle carries 223,500 lbs of liquid oxygen and hydrogen

TABLE 8-1. DL-4 VEHICLE WEIGHT SUMMARY

| Component | Weight (lbs) |
|---|---|
| Fuselage and surfaces | 90,500 |
| Surface controls | 1,000 |
| Payload | 50,000 |
| Landing Gear | 6,850 |
| Communications equipment | 900 |
| Environmental Control | 1,800 |
| Stability augmentation | 250 |
| Guidance equipment | 1,500 |
| Reaction controls | 2,500 |
| Electrical system | 1,500 |
| Hydraulic system | 1,500 |
| Recovery engines (4 Rolls-Royce Allison XJ99's) | 3,520 |
| Recovery fuel (10 min. duration @ SFC = 1.18) | 12,000 |
| Crew (2-man) | 400 |
| Crew equipment | 400 |
| Wings | 14,800 |
| Main propulsion system and tankage | 38,000 |
| Instruments and engine controls | 300 |
| Aero weight empty | 227,720 |
| Propellant ($LH_2/LO_2$ for $\Delta V$ = 10,120 fps) | 223,500 |
| Launch weight | 451,220 |

propellants for its rocket engines, and some 12,000 lbs. of fuel for its 4 turbojet landing engines. The vehicle size permits sufficient volume for the 10,500 cubic-foot cargo cannister, the 13,000 cubic-foot of on-board propellants, and the requirements for crew quarters, equipment, rocket engines and landing engines, and wings. The 90,500 pounds listed in Table 8-1 for the fuselage and surfaces weights includes a structural weight allowance for enclosing and deploying the cruise engines and for the JP-4 fuel tanks for the recovery engine system. By optimizing the packaging of the various components, by departing from the cylindrical cargo canister shape, and by taking liberties with the basic body shape, a smaller overall vehicle size is possible.

An analysis of the boost requirements of such a vehicle indicates that the total lift-off weight of such a system will be about 2.66-million pounds. A system weight summary is presented in Table 8-2. Accordingly, three 1-million pound thrust $LO_2/LH_2$ rocket engines are required for lift-off and boost, and are housed within the DL-4 vehicle. The engine performance used for the sizing reflects current state-of-the art levels (460 seconds vacuum specific impulse, 390 seconds at sea level) for nozzle area ratios on the order of 50:1. Estimates of their weight and that of the associated tankage are included in the vehicle weight breakdown of Table 8-1. These, too, are based upon current state-of-the-art levels.

It is pointed out that the wing weight listed in Table 8-1 is the lowest in the group of four wings which were studied. This group consisted of a so-called nominal size sailwing, a downsized sail wing, and their rigid (metallic) wing counterparts. The rigid wings were designed to be aerodynamically equivalent to the sailwings, that is, they were sized to produce the same lift curves when the constraints on available internal volume made this possible for the particular wing in question.

For the heavier wings described in the following pages, the nominal payload of 50,000 lbs. would have to be reduced by an amount equal to the difference between the weight of the wing considered, and the 14,800 pounds shown in Table 8-1. If, on the other hand, lift-off weight is not a system design constraint, then the impact of the different wing weights will be reflected in much larger lift-off weights for the 50,000 pound payload. In this connection it should be noted that the ratio of lift-off weight to the weight at burnout of the "half-stage" is on the order of 5 to 1.

TABLE 8-2. SYSTEM WEIGHT SUMMARY

| Component | Weight (lbs) |
|---|---|
| Strap-on booster stage tanks | 80,879 |
| Booster propellants | 2,128,390 |
| DL-4 vehicle (empty) | 177,720 |
| DL-4 propellant ($LH_2/LO_2$) | 223,500 |
| DL-4 payload | 50,000 |
| Total launch weight | 2,660,489 |

B. Configuration Studies

1) Wing Sizing Considerations

In order to provide some indication of the sensitivity of the weight comparisons to geometric size, two differently sized sailwings and their equivalent rigid wing counterparts were designed as landing aids for the DL-4 vehicle application, and subjected to weight analyses which are described later. The size of the nominal sailwing was established by simply applying a scale factor of 170:5, based on the ratio of DL-4 orbiter vehicle length to that of the DL-4 wind tunnel model, to the model sailwing. A downsized sailwing, geometrically similar to the nominal one, but having only one-half its exposed area, was the second sailwing considered. These wings are shown mounted on the DL-4 vehicle body in Figure 8-1. Figure 8-2 shows their equivalent rigid wing counterparts.

The inverse taper of the rigid wings is a consequence of the constraints posed by available body volume and body shape. The lift curves of the nominal and downsized sailwings, together with their rigid wing counterparts are shown in Figure 8-3 and 8-4. Those for the rigid wings were estimated using available data for the 23012 and 23015 airfoil sections, together with single-slotted flap characteristics. The nominal size rigid wing was limited in span and area, and hence aspect ratio. Consequently, its lift-curve slope is less than that of the nominal sailwing. Use of a flap, however, produces a substantial gain in lift which makes it virtually equivalent, lift-wise, to the sailwing. The 23000 series airfoil section was selected for its good all-around aerodynamic characteristics and, from a structures standpoint, geometric shape.

The theoretical aspect ratios of the nominal and downsized sailwings are 3.27 and 3.31 respectively, and 9.45 and 8.10 for the corresponding rigid wings. A comparison of the exposed and theoretical wing planform areas, spans, and aspect ratios is presented in Table 8-3 below.

TABLE 8-3. ORBITER VEHICLE BODY AND WING AREAS

| Item | Planform Areas ($ft^2$) | | Span | Aspect Ratio |
|---|---|---|---|---|
| | Exposed | Theoretical | (ft) | (theoretical) |
| DL-4 Body | 5780 | 5780 | 55.2 | 0.52 |
| Nominal Sailwing | 3630 | 6760 | 141.7 | 3.27 |
| Downsized Sailwing | 1815 | 3820 | 112.5 | 3.31 |
| Nominal Rigid Wing | 1986 | 2380 | 150 | 9.45 |
| Downsized Rigid Wing | 1370 | 1835 | 122 | 8.10 |

2) Landing Performance Comparisons

Landing performance was estimated, for the body alone, and for the vehicle with the nominal and downsized wings. It was assumed in each case that the vehicle lands with no residual rocket propellant aboard, at a weight of 225,000 lbs. This weight does include, however, fuel for the four XJ99 recovery engines that enable the craft to abort a landing approach for another go-around. The following commonly used constraints were applied:

- Landing speed (speed at touchdown) is not to be less than 1.10 times stalling speed with flaps extended, if any,
- Approach speed (speed at 50 foot altitude) is 1.10 times touchdown speed

Moreover, the angle of attack at touchdown was not allowed to exceed 10°, compatible with ground clearance requirements. This value was dictated mainly by restrictions on the landing gear size and location posed by the center of gravity location, which is approximately the same as the moment reference center location of the wind tunnel model, namely: 0.61 of the body length from the nose. An increase in the allowable ground clearance angle of attack would require a much longer landing gear having prohibitively greater weight which would either degrade the payload weight or increase the lift-off weight, not to mention adverse effects on landing visibility. A ground friction coefficient of 0.30 was assumed for the landing distance estimation.

In addition, it was assumed that the engines were at idle (no thrust) throughout the maneuver.

The resulting landing performance is presented in Table 8-4 for the vehicle without wings, and for the vehicle equipped with the nominal and downsized sailwings respectively. Because the rigid wings were designed to produce the same lift curve as their sailwing counterparts, and because the drag differences between the vehicle fitted with the sailwings and with rigid wings are negligible, the results presented in Table 8-4 are also applicable to the vehicle fitted with the nominal and downsized rigid wings.

The high landing speed of the DL-4 orbiter vehicle without wings highlights the need for a landing aid because it falls well outside the 150 to 200 knots range of landing speeds envisaged for the space shuttle in Reference 7. Based upon a careful analysis of landing accident rate statistics, the results of Reference 7 indicate that landing speed per se is not the major cause of accidents; rather, inadequate runway length was found to be a major causative factor. Consequently, if routine landings are to be made at ordinary airports this speed should be reduced.

TABLE 8-4. LANDING PERFORMANCE COMPARISON

| Configuration | Speed (knots) | | Distance (ft) | |
|---|---|---|---|---|
| | Landing | Approach | Ground | Air |
| DL-4 Body Alone | 268 | 294 | 6310 | 1707 |
| Downsized Wing/Body | 134 | 148 | 2387 | 1304 |
| Nominal Wing/Body | 105 | 116 | 1598 | 1155 |

For the landing weight of 227,720 pounds, the wing loadings (based on theoretical wing areas) work out to be 33 and 59 psf for the nominal and downsized sailwings, and 95 and 120 for their rigid wing counterparts.

3) Nominal and Downsized Sailwing Details

The design approach to the sailwing was governed by the shape of the vehicle, the internal payload compartment, and the rocket propellant tanks.

The volume available for the sailwing in stowed position must provide for:

- A leading edge structural box.
- The upper and lower surface of the wing which consist of dacron fabric.
- A trailing edge cable.
- An extension actuator.
- A trailing edge cable feed-out system.

In conformity with the wind tunnel model a NACA 0012 airfoil section was used for the shape of the leading edge structural member at the root, and a NACA 0015 airfoil at the tip. The leading edge was drooped down at an angle of -10°, which has been found to give the best match of contours between the rigid leading edge and the dacron fabric covering when they are subject to aerodynamic lift.

The leading edge box is the only structural member in this cantilevered sailwing concept. Accordingly, it must be capable of handling bending, torsion, shear, column, and drag loads. The leading edge box design which evolved consists of two spars enclosed by an aluminum skin reinforced at the leading edge radius, as shown in Figure 8-5. At the inboard end the two spars pick up the wing pivot. The outboard end terminates in a hinge which permits the wing tip assembly to pivot and thereby function as an aileron.

The wing tip assembly consists of a hinged tip rib with a trailing edge cable retainer which allows the cable to slide through the fitting when the rib is collapsed for stowage. A folding brace connects the tip rib to the outboard hinge of the leading edge box which transmits the tension load of the trailing edge cable to the leading edge box. The upper and lower fabric covers are joined together at the trailing edge with a teflon sleeve which allows the fabric to slide on the cable without being damaged.

The trailing edge cable feed-out system was selected for the following reasons:

- The flexibility of the cable is limited due to its diameter.

- A storing drum is not applicable to this design since it would not allow the fabric to be collapsed for stowage and due to the minimum bend radius of the cable, the size of the drum would be prohibitive.

In the feed-out system envisioned, the inboard end of the cable is connected to a smaller cable which transports it from a forward location in stowed position, within the vehicle, to a socket at the end of an arm which sets up a predetermined tension load in the trailing edge cable. An actuated drum for the transporting cable is mounted on the tensioning arm which provides the necessary alignment of the trailing edge cable with the socket. A trough is provided in the vehicle to support the trailing edge cable while it is stowed and functions as a guide during the deployment of the wing.

4) Nominal and Down-sized Rigid Wing Details

The planform and size of the rigid wing was determined mostly by the volume available between the internal payload and external shape of the vehicle. As a result, the planform has an inverse taper. A NACA 23015 airfoil section is used at the root rib and a NACA 23012 is used at the tip rib.

The structure of the nominal wing consists of five spars of which three spars are full span and the other two terminate at the inboard rib of the aileron. The structure of the downsized wing consist of three full span spars with two-intermediate stringers which terminate at the inboard rib of the aileron. A closure rib incorporating the pivot is located at the inboard end of the wing.

A substantial gain in lift is obtained by the addition of a single slotted flap which makes up largely for the added weight of this lift device.

One problem associated with the rigid wing is that the main landing gear can be extended only after the wing has been extended. This difficulty is not encountered with the sailwing installation.

5) Internal Arrangement Comparison

The main difference in the internal arrangement of the vehicle due to the sailwing and the rigid wing is in the hydrogen tank configuration. The sailwing produces a wide slot in the side of the vehicle but does not project as deeply into the structure as does the rigid wing.

The rigid wing produces a narrow slot in the side of the vehicle but projects deeply into the structure. This condition is created by the necessity to obtain a maximum wing planform area for the allowable span. A stowage volume study was made for both wings which shows that the rigid wing requirement exceeds the sailwing by 15%.

6) Landing Propulsion System

A review of candidate engines for the landing phase of the vehicle showed that a substantial weight saving is obtained by using turbojets designed primarily for the direct-lift application concept. The engines used in the study are accordingly based on the Rolls Royce-Allison XJ-99 system.

The following Table presents a comparison of the two engine candidate of similar thrust.

TABLE 8-5. LANDING-ENGINE COMPARISON

| | Rolls Royce Allison Direct lift engine XJ-99 | Pratt and Whitney JT8D-11 Turbofan engine |
|---|---|---|
| Engine envelope | | |
| Length | 49.0 in. | 120.0 in. |
| Maximum diameter | 35.0 in. | 43.0 in. |
| Weight/engine | 880 lb. | 3310 lb. |
| S. F. C. | 1.18 | 0.62 |
| Total landing propulsion weight/vehicle | 3,520 lb. | 13,240 lb. |
| Landing fuel weight/vehicle | 12,000 lb. | 6,000 lb. |
| Total weight Fuel and engines | 15,520 lb. | 19,240 lb. |
| Weight difference | 3,720 lb. | |

A further weight saving is realized with the direct lift engines in that the structural cutout in the vehicle is substantially smaller than that required for a conventional turbofan engine.

C. Loads

The loads affecting the sailwing structure are the following, as illustrated in Figure 8-6:

1) Chordwise bending which is due primarily to the trailing edge cable tension, and, to a lesser extent, air loads acting on the spar directly, and those transmitted through the sail fabric.
2) Spanwise bending due to normal air loads.
3) Spar torsion induced through the rigid wing tip, and by the action of the aerodynamic lift force and moment at, and about, the aerodynamic center of each wing panel.
4) Column load on the spar due to the cable tension load.

The spanwise bending moment was determined from an estimated spanwise air load distribution. For this purpose the method due to Schrenk (Reference 8), which relates the load distribution to an averaged chord distribution, was considered adequate. The load distributions were modified slightly to account for the presence of body-on-wing interference lift, which increases the wing load. The amount of this increase was taken to be proportional to the estimated body-on-wing lift-curve slope contribution. Accordingly, the following relation between wing lift and total lift was assumed to apply

$$L_w = L_{TOT} \left[ \frac{C_{L_{\alpha_{w + BOW}}}}{C_{L_{\alpha_{TOT}}}} \right]$$

in which BOW denotes body-on-wing contribution.

From this it was determined that, for the nominal size sailwing, 61% of the vehicle weight is carried by the exposed wing, through wing-alone lift and body-on-wing interference lift. The remaining 39% of the vehicle weight is carried by body lift and wing-on-body interference lift. The load on each panel of the nominal size sailwing is thus 68,625 pounds for a load factor of one.

For the downsized sailwing it was estimated, on the basis of the above approach, that 52% of the vehicle lift is carried by the wing. The same percentages apply to the rigid wing counterparts of the sailwings because they are aerodynamically equivalent in terms of lift-producing capacity with flaps deflected.

The chordwise hinge moment, trailing edge cable tension, and the total vehicle lift and drag forces were determined from the experimental data for conditions commensurate with a load factor of 3.0 at a dynamic pressure of 60 psf. The lift and drag components of the wing panel air load were then estimated following the above approach, and the moment about the wing aerodynamic center due to sailwing camber was obtained from the data. The data for a pre-set cable tension of 55 pounds was used, and scaled up in accordance with the scaling criteria presented in the Appendix of this report. This case was used in the interest of keeping the cable size down without impairing the aerodynamic performance of the sailwing.

The sailwing loads, per panel, for a limit load factor of 3 used in the structural analysis are listed below in Table 8-6.

TABLE 8-6. SAILWING DESIGN LOADS

| Item | Nominal | Downsized |
|---|---|---|
| Hinge Moment (at root), ft-lbs | 8,183,000 | 5,041,000 |
| Cable Tension, lbs | 175,000 | 115,000 |
| Lift, lbs | 206,000 | 175,000 |
| Drag, lbs | 84,300 | 71,800 |
| Moment (about wing a.c.), ft-lbs | -885,000 | -442,500 |

The loads per panel used in the structural design of the rigid wings are tabulated below:

TABLE 8-7. RIGID WING DESIGN LOADS

| Item | Nominal | Downsized |
|---|---|---|
| Lift, lbs | 206,000 | 175,000 |
| Drag, lbs | 84,300 | 71,800 |
| Moment (about wing a.c.), ft-lbs | -136,000 | -86,800 |

It is noted that the loads listed for the rigid wing are with flaps deflected.

D. Weights Analyses

1) Structural Considerations

All of the wings, both sail and rigid were designed to a limit load factor of 3.0 g. Loads were generated for this condition and are described in greater detail in the preceding subsection. An ultimate factor of 1.5 was applied to all limit loads. The same basic materials of construction (aluminum and steel) were maintained for both types of wings with compatible allowables in order to minimize material selection as a significant factor in the trade study. Although potential weight savings might be realized by use of materials other than those selected for the study, the comparative standing of the two types of wings would remain unchanged since weight savings could be realized on both.

Upon examination of the load paths that exist for the sailwing, it becomes evident that the greater portion of the shear will be carried by the leading edge structure, which must also take large torques due to the absence of a conventional rear spar. In addition, the cable load must be quite large to hold the fabric taut and carry some shear thereby creating extremely large chordwise bending moments in the leading edge structure. Torques and chordwise bending moments of far less severity exist for the equivalent multispar rigid wings. Although somewhat larger spanwise bending moments are induced into the rigid wings because of increased span, the magnitudes are insufficient to cause major effects to the rigid wings.

An examination was also made of the column load on the sailwing spar structure produced by the cable tension load. The results indicated that its effect on the spar structural design is negligible. Therefore, the weight estimates presented here are valid.

When adding either the sailwing or rigid wing to the reentry body, it becomes necessary to provide wing support structure. This entails reenforcing the wing support frames and local longitudinal structure. In addition, the payload compartment doors must provide frame continuity when closed (shear and axial force continuity). This is accomplished by using pins placed in a longitudinal direction through the two halves of frame. Each door contains parts of the frames which are so designed to permit one to mesh with its counterpart allowing the pin holes to line up. Tapered pins are used to compensate for any small misalignments.

Care was taken in establishing the wing structure geometry to ensure that the body cutouts would not reach excessive proportions. Adequate frame depth has been maintained in all regions around the cutouts thereby assuring the body's structural integrity. The major difference in the slot requirements for the two types of wings is the orientation of the cutout. The cutout for the sailwing requires a greater vertical dimension and a smaller dimension for depth of cutout into the body than does the rigid wing. Although the leading edge structural box of the sailwings are narrower than the rigid wings, they are deeper. In addition, volume had to be provided for stowing the fabric and cable. Due to the large diameter cables required, it was necessary because of the cable rigidity to stow the cable longitudinally. This in turn necessitated the use of a cable stowing system which consumed additional space.

2) Nominal Size Wings

Detail weights were derived for both the sailwing and rigid wing on the basis of stress analysis and statistical weight data. The weight statement for the sailwing is presented in Table 8-8.

TABLE 8-8. WEIGHT STATEMENT - SAILWING

| Item | Weight (lbs) |
|---|---|
| Structure | (25,688) |
| Nose Structure | 13,218 |
| Wing Pivot Fittings | 2,866 |
| Wing Tip Ribs and Braces | 6,064 |
| Cable | 655 |
| Fabric | 2,885 |
| Flight Controls | (504) |
| Wing Extension & Stowage System | (2,698) |
| TOTAL | 28,890 |

The weight statement for the rigid wing is presented in Table 8-9 and a comparison summary in Table 8-10.

TABLE 8-9. WEIGHT STATEMENT - RIGID WING

| Item | Weight (lbs) |
|---|---|
| Structure | (23,403) |
| Structural Box | 14,098 |
| Leading Edge | 1,152 |
| Trailing Edge | 1,016 |
| Flaps & Ailerons | 1,612 |
| Wing Pivot Fittings | 5,525 |
| Flight Controls | (1,290) |
| Wing Extension System | (658) |
| TOTAL | 25,351 |

TABLE 8-10. COMPARISON SUMMARY

| Item | Weight (lbs) | |
|---|---|---|
| | Sailwing | Rigid Wing |
| Structure | 25,688 | 23,403 |
| Flight Controls | 504 | 1,290 |
| Wing Extension & Stowage System | 2,698 | 658 |
| TOTAL | 28,890 | 25,351 |

An examination of Table 8-10 indicates that the sailwing is heavier than the rigid wing by approximately 3,500 pounds. Both the structure and the wing extension

and stowage system for the sailwing are significantly heavier than for the rigid wing. However, the flight control system for the rigid wing is heavier due to the inclusion of a flap system. It may appear odd that such a large difference in weight should exist in the wing extension and stowage system. However, this difference is explained by examining the major elements within the system that make up the bulk of the difference. First, is the fact that the sailwing requires a stowage and tensioning system for the trailing edge cable (diameter = 2 inches) since it can not very easily be bent thereby requiring it to be stowed longitudinally. This system alone accounts for nearly 1000 pounds of the difference. The second factor that contributed to the large difference was the magnitude of the chordwise bending moment existing for the sailwing . The severity of this moment is due almost exclusively to the cable tension load. The drag component is small in comparison to the cable component. Although the wing extension system was not required to operate against this large moment, a static reaction force was required. This created an ultimate static load on the wing extension system of approximately 4.5 times that of the rigid wing.

In examining the structural details to determine the causes for the structural weight difference it again becomes apparent that the large chordwise bending moment is responsible for a significant portion of the weight difference. At first glance it appears strange that the nose structure (structural box) of the sailwing is approximately equal in weight to the structural box of the rigid wing since the rigid wing has slightly higher spanwise bending moments and smaller depths. However, this is more than offset by the material requirements for chordwise bending in sailwing nose structure.

Another interesting observation is the fact that the fabric and cable weight (3540 pounds) for the sailwing is only slightly lighter than the weight of the leading edge, trailing edge, flaps and ailerons (3780 pounds) of the rigid wing. This is caused largely by the larger sailwing area and high cable load requirement.

The wing pivot fittings of the sailwing are appreciably lighter because of the greater structural depth. However, a very significant weight is added to the sailwing for wing tip ribs and braces because of the large cable load.

3) Down Size Wings

Detail weights were derived for the downsized sailwing and rigid wing on the basis of stress analysis and statistical weight data. The weight statement for the

sailwing is presented in Table 8-11.

TABLE 8-11. WEIGHT STATEMENT - SAILWING

| Item | Weight (lbs) |
|---|---|
| Structure | (11,858) |
| Nose Structure | 6,009 |
| Wing Pivot Fittings | 1,451 |
| Wing Tip Ribs & Braces | 2,506 |
| Cable | 357 |
| Fabric | 1,535 |
| Flight Controls | (484) |
| Wing Extension & Stowage System | (2,451) |
| TOTAL | 14,793 |

The weight statement for the rigid wing is presented in Table 8-12 and a comparison summary in Table 8-13.

TABLE 8-12. WEIGHT STATEMENT - RIGID WING

| Item | Weight (lbs) |
|---|---|
| Structure | (14,935) |
| Structural Box | 8,426 |
| Leading Edge | 825 |
| Trailing Edge | 729 |
| Flaps & Ailerons | 1,138 |
| Wing Pivot Fittings | 3,817 |
| Flight Controls | (910) |
| Wing Extension System | (562) |
| TOTAL | 16,407 |

TABLE 8-13. COMPARISON SUMMARY

| Item | Weight (lbs) | |
|---|---|---|
| | Sailwing | Rigid Wing |
| Structure | 11,858 | 14,935 |
| Flight Controls | 484 | 910 |
| Wing Extension & Stowage System | 2,451 | 562 |
| TOTAL | 14,793 | 16,407 |

For the downsized wings it is interesting to note that the sailwing weight is lighter than the rigid wing. The major cause of this trend was the far larger reduction in structural weight of the sailwing as compared to the rigid wing. The weight changes in the flight control and wing extension and stowage systems were far less significant when compared to the structural change.

As was explained in the discussion of the nominal size sailwing, the major factor contributing to the large structural weights was the magnitude of the chordwise bending moments. Since the downsized sailwing has a reduced cable load and smaller chords, the chordwise bending moments were far smaller with the consequent large reduction in structural weight.

The chordwise bending moment reduction at the pivot amounted to approximately 34% but the width of the leading edge structure was only reduced approximately 13% thereby creating a relatively more efficient structural beam.

The weights of the flight controls and the wing extension and stowage systems were smaller for both the downsized sail and rigid wings. No significant changes occurred between the two wings.

4) Conclusions

The basic conclusion that can be drawn from this limited study is that the sailwing becomes more attractive in the smaller sizes. Table 8-13 shows a significant weight saving for the downsized sailwing when compared against the downsized rigid

wing. On the other hand, the nominal sailwing was approximately 3500 pounds heavier than the nominal rigid wing.

It appears that there is a cross-over between the sail and rigid wings as a function of size. However, the point of cross-over was not determined because it would require more time than was available. It also appears that further study of the sailwing is in order to further optimize the construction which would result in weight savings. In this connection it is worth noting that for applications other than the one considered in this study, it will be possible to deviate from the cantilever type structure used here. In such cases, a bridle arrangement for imparting tension to the wing trailing edge, in conjunction with a drag-wire type of bracing of the sailwing spar, to reduce the chordwise moment at the root, should yield further weight reductions for the sailwing.

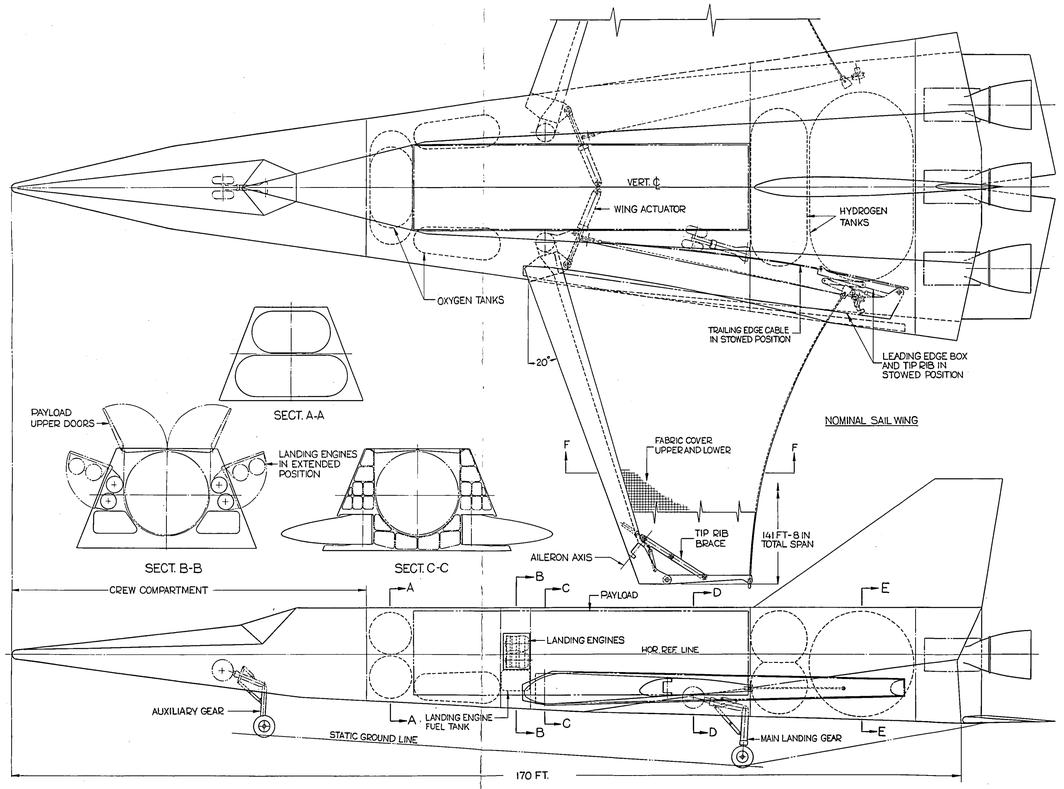


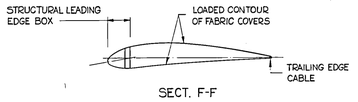


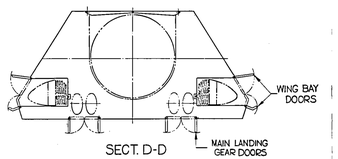


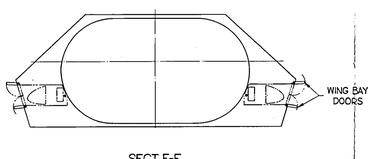


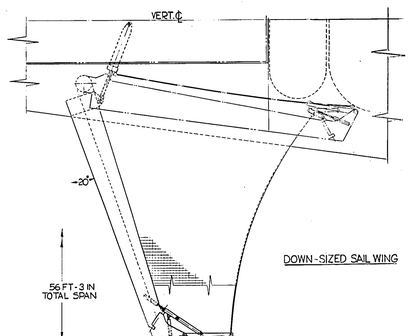


Figure 8-1. 170-foot Vehicle with nominal size and downsized sailwings.

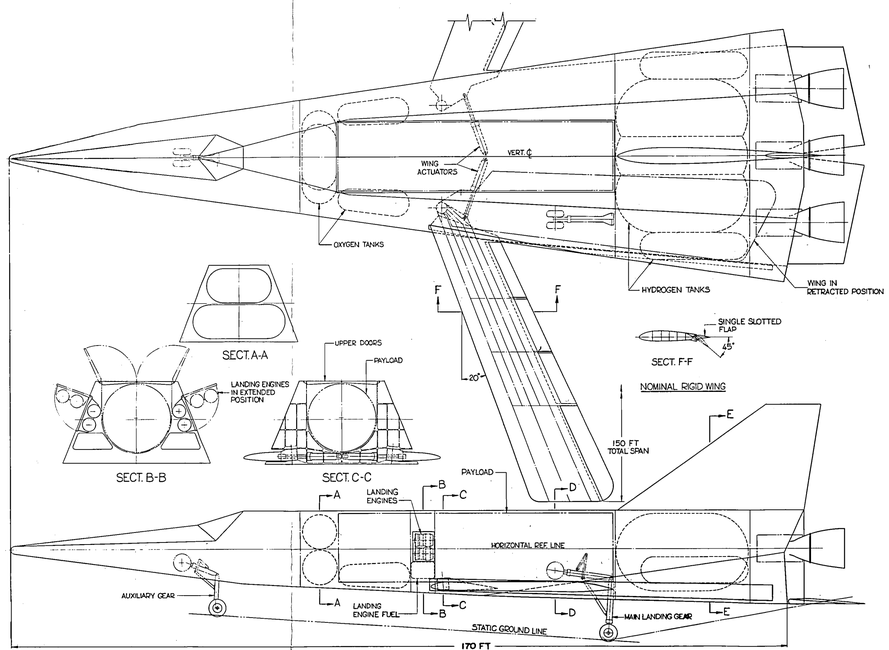


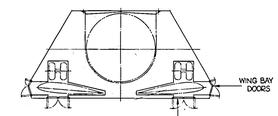


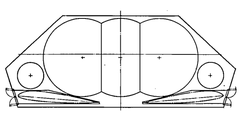


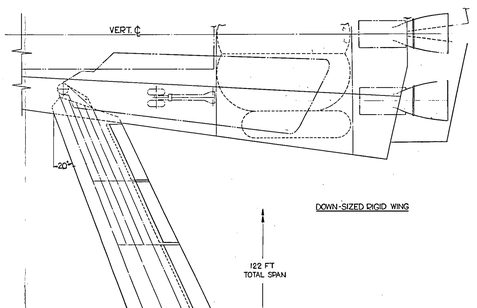


Figure 8-2. 170-foot Vehicle with nominal size and downsized rigid wings.

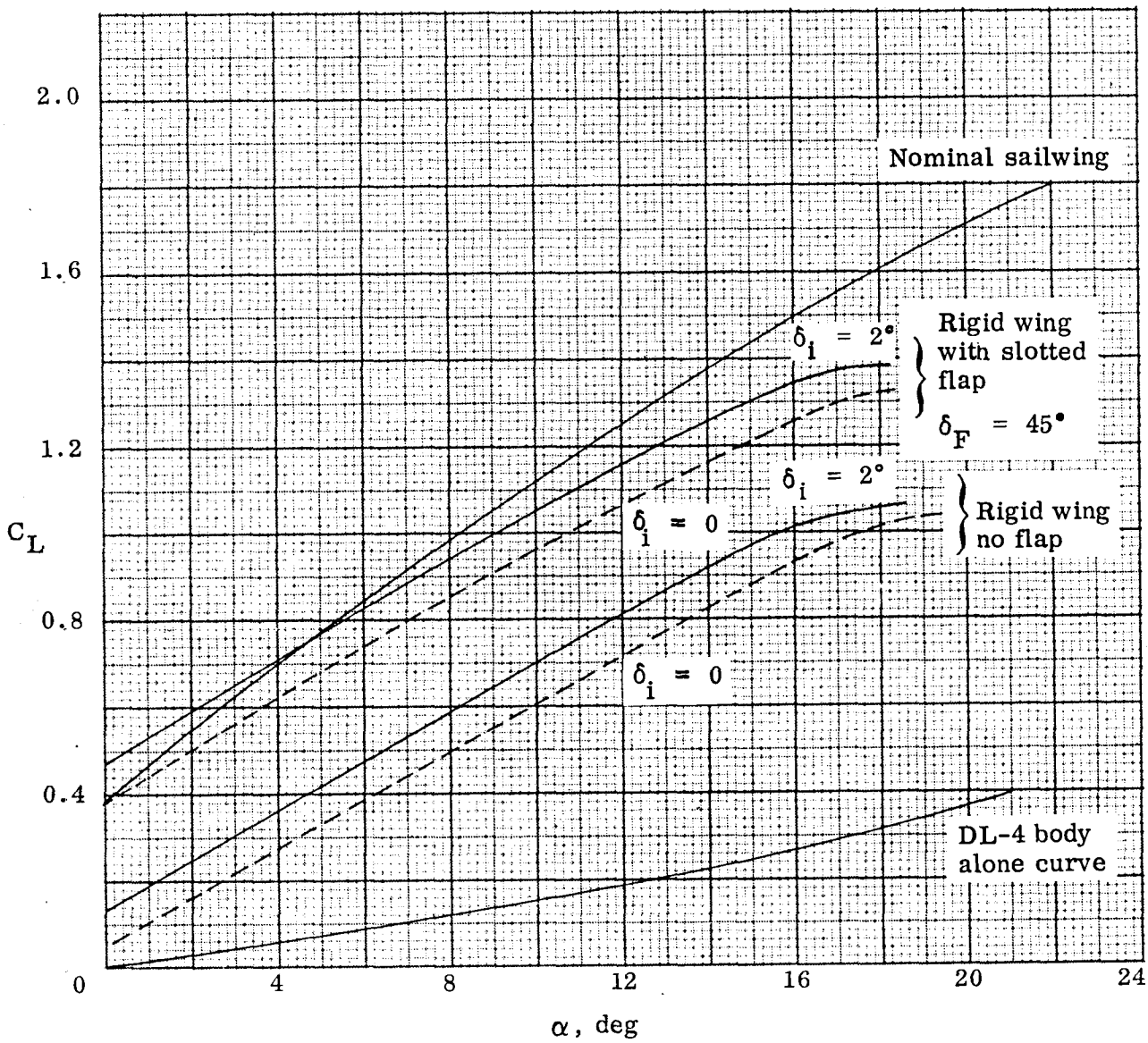


Figure 8-3. Lift curves of nominal sailwing and rigid wing.

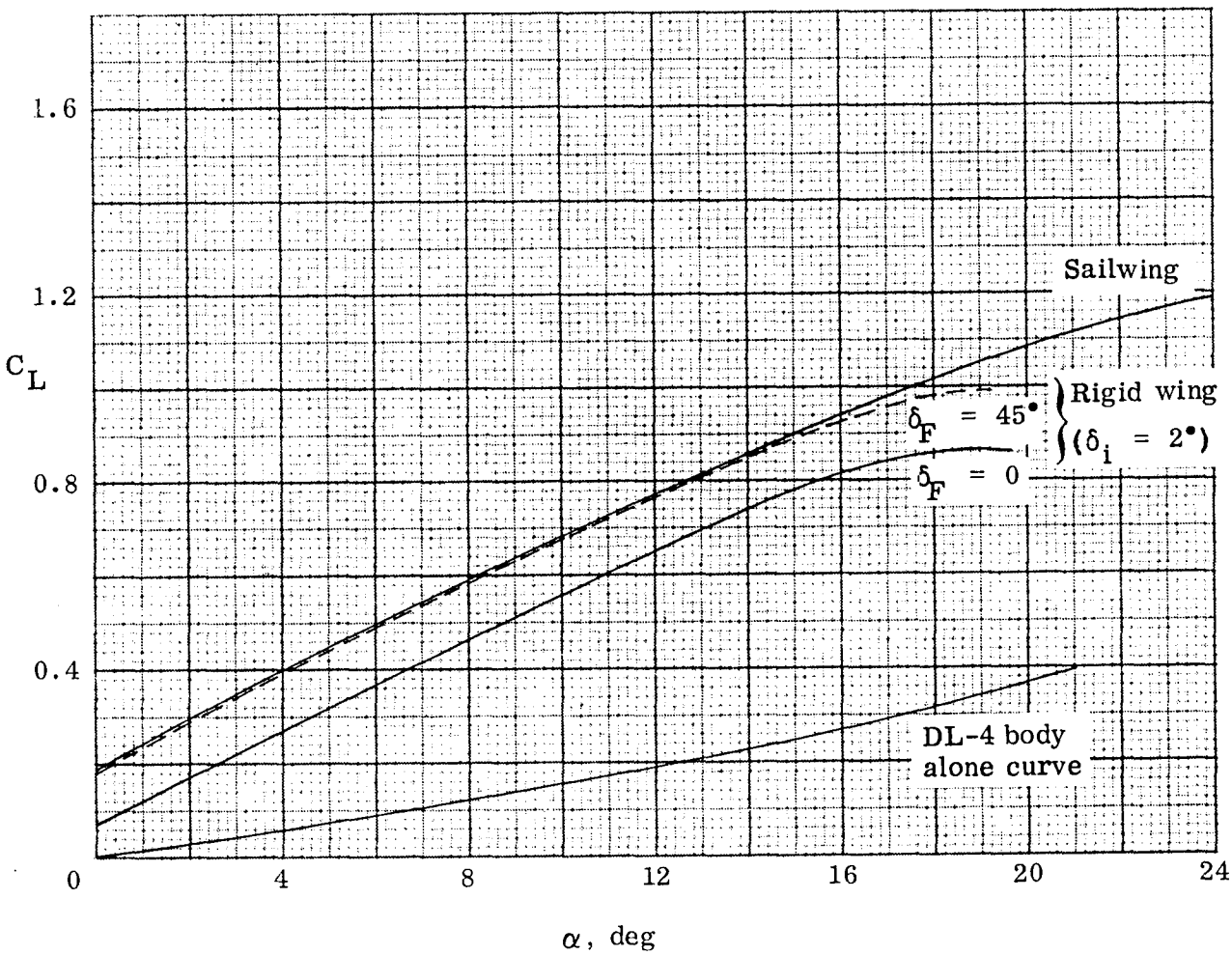


Figure 8-4. Lift curves of downsized sailwing and rigid wing.

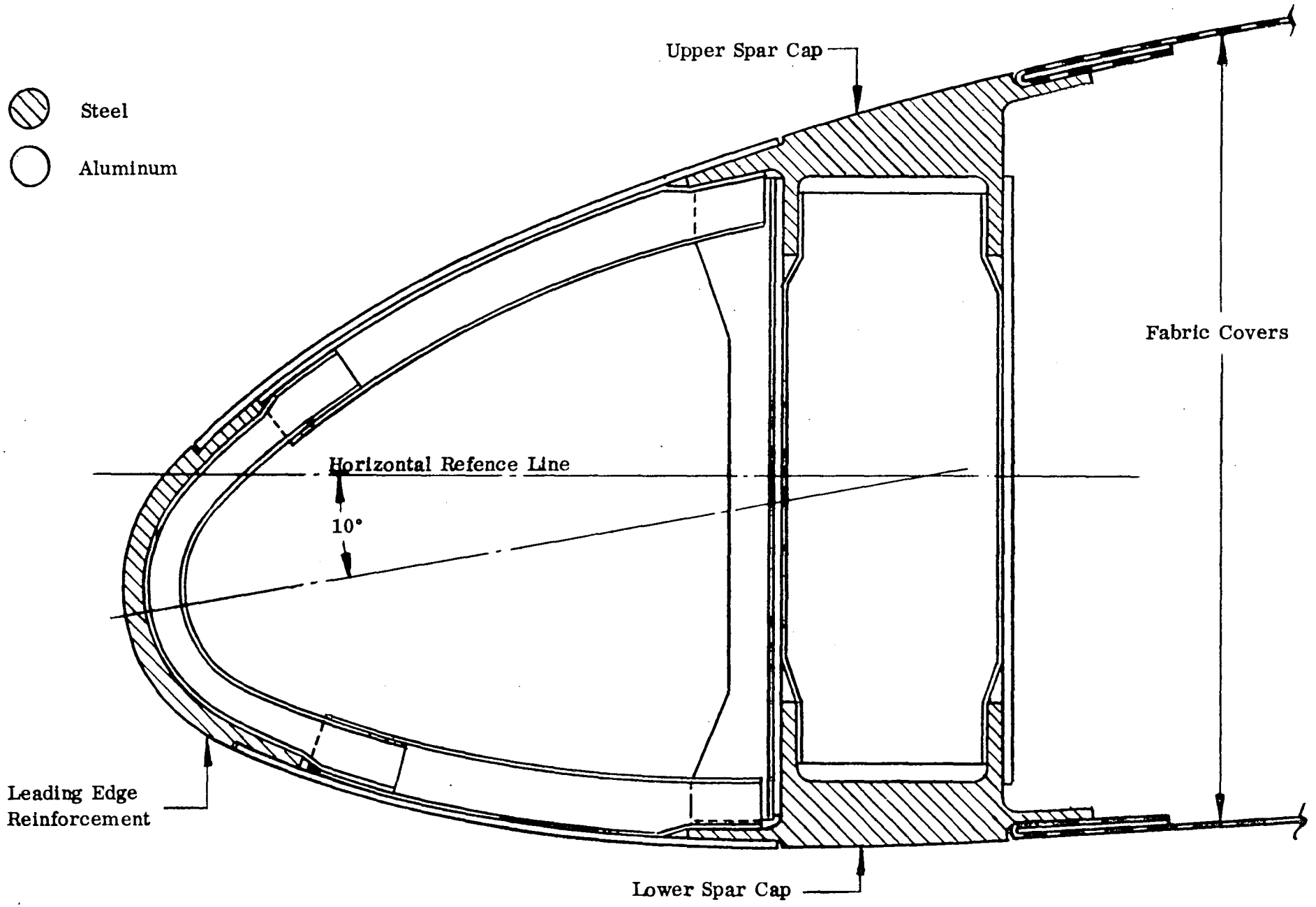


Figure 8-5. Typical section through leading edge box.

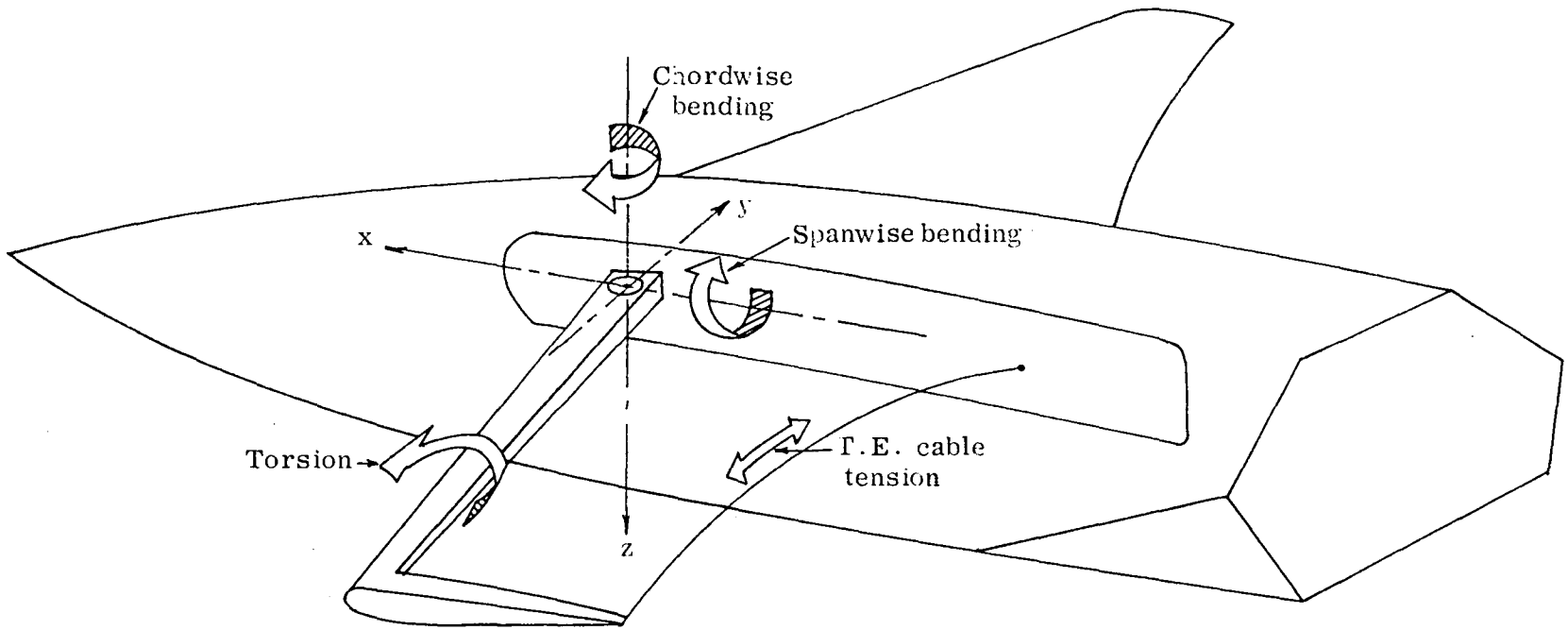


Figure 8-6. Sailwing structural loads schematic.

## SECTION 9

## CONCLUSIONS

The more important conclusions which can be drawn from the experimental and design study portions of this investigation are summarized below.

A. DL-4 Body Alone Tests

Based upon the results of the DL-4 body-alone wind tunnel tests the following conclusions apply:

1) The elevons provide effective control of both pitch and roll for the body alone. Sideslip was found to have no appreciable effect on elevon effectiveness.

2) The body-alone maximum lift-to-drag ratios ranged from only 1.85 to 2.20 over the range of elevon deflections tested.

3) Attempts to improve the flow in the base region of the body by means of a base shield had virtually no effect on the base pressure, and hence drag, and decreased the effectiveness of the elevons by about 30%.

B. Sailwing/DL-4 Body Tests

The results of the tests on the wing-body combination indicate that:

1) A significant increase in the maximum lift-to-drag ratio to a value of 7.1 is provided by the sailwing.

2) The effect of cable tension on the lift-to-drag ratio over the range of cable tension values tested was found to be small, as were the effects of dynamic pressure.

3) Due to its flexibility the sailwing undergoes a camber reversal in the neighborhood of zero lift which produces a steepening of the lift curve in this region. This was found to vary with the ratio of dynamic pressure to the preset tension in the trailing edge cable. The camber reversal becomes less abrupt with decreasing dynamic pressure and increasing cable tension.

4) The sailwing introduces a negative $C_{m_o}$ in the pitching moment characteristics of the wing-body combination. This is due to the cambered shape which the sailwing assumes when loaded. As a result, for the size wing tested, the body elevons lack the control power required for trim over the whole angle of attack range tested. A reduction in the exposed area of the sailwing of roughly 50%, however, would make it possible for the size elevons tested to provide trim over the whole angle of attack range. Such a downsized sailwing would still provide a significant improvement in the subsonic aerodynamic characteristics of the DL-4 body.

5) Wing warping by deflecting a wing tip is an effective roll control device up to angles of attack near wing stall where control effectiveness falls off. The sailwing was found to add to both the directional stability of the body, and to the effective dihedral parameter.

6) The sailwing displayed no serious flutter, buffing, or other sail misbehavior in its deployed position at any angle of attack tested.

C. Wing Deployment

The wing deployment test results demonstrated that:

1) Sailwing deployment at dynamic pressures of up to 60 psf is feasible.

2) On the basis of the scaling factors presented in this report, the deployment rates used in these tests translate to full-scale rates which can be attained without difficulty.

3) Banner-like flutter of the sailwing fabric was found to occur only during the later stages of a deployment, This flutter can be reduced by rapid deployment, by restraining the trailing edge of the sailwing during deployment, or by a combination of these means.

D. Sailwing vs. Rigid Wing Trade Study

The results of the design study, in which the DL-4 body configuration and sailwing were scaled up in size for an orbiter vehicle application, meeting certain system design constraints, indicate the following:

1) Without the use of a landing aid, such as a deployable sailwing or a rigid (metallic) wing, the landing speed would be excessively high (270 knots).

2) Use of a sailwing of the proportions tested, or of an equivalent (lift-wise) rigid wing would reduce the landing speed significantly (105 knots).

3) A sailwing of smaller proportions, having only one half the exposed area of the nominal one, would still give an appreciable improvement in the landing speed (134 knots).

4) The weight differences between a sailwing and its rigid wing counterpart are found to be sensitive to size. Whereas the nominal size sailwing was found to be slightly heavier than its rigid counterpart, the downsized sailwing was lighter. The weight advantage of this downsized sailwing could undoubtedly be improved still further by modifying the sailwing structural arrangement. No attempt was made in this study to optimize the cantilever-type structural design used for the sailwing, or to determine the crossover point, i.e., the wing size where the weights of the sailwing and rigid wing would be equal.

## SECTION 10
## REFERENCES


1. Ormiston, R. A., Fox, R. D., "The Sailwing Lifting Body Concept," Princeton University Report No. 825, February, 1968.

2. Sweeney, T. E., Ormiston, R. A., Mercer, J. E., et al., "Sailwing Wind Tunnel Test Program," Fairchild Hiller Report No. R540A-002, September, 1966.

3. Bartlett, G. E., Vidal, R. J., "Experimental Investigation of Influence of Edge Shapes on the Aerodynamic Characteristics of Low Aspect Ratio Wings at Low Speeds," Journal of Aeronautical Sciences, Vol. 22, pp 517-533, August, 1955.

4. Ellison, D. E., et al., "USAF Stability and Control Datcom," Air Force Flight Dynamics Laboratory Report, October, 1960, Revised November, 1965.

5. Pitts, W. C., Nielsen, J. N., and Kaatari, G. E., "Lift and Center of Pressure of Wing-Body-Tail Combinations at Subsonic, Transonic, and Supersonic Speeds," NACA Report 1307, 1957.

6. Torrillo, D. T., and Muller, E., "Users Manual for Aerodynamics Computer Program FHR 620214," Fairchild Hiller Report FHR 3576, 1968.

7. Love, E. S., "Reusable Launch Vehicle Concepts," paper presented at the Joint National Meeting, AAS/ORSA "Planning Challenges of the 70's in Space and the Public Domain," Denver, Colorado, June 17-20, 1969.

8. Schrenk, O., "A Simple Approximation Method for Obtaining the Spanwise Lift Distribution," NACA TM 948, 1940.

9. Kuethe, A. M., and Schetzer, J. D., Foundations of Aerodynamics (New York: John Wiley and Sons, Inc., 1959), Appendix A.

# APPENDIX
## SAILWING SCALING ANALYSIS

In considering the application of a sailwing to a full-size vehicle, it is necessary to know how the forces on, and in, such a model translate up to those of a full scale vehicle. Some insight into this problem is afforded by the application of dimensional analysis to establish groupings of physical variables (similitude parameters) that are dimensionless, hence independent of the scale of the system.

In considering here the variables which affect the aerodynamic force, F, produced by a sailwing, certain physical variables such as coefficient of viscosity, and speed of sound are excluded since they would only lead to the well known similitude parameters of Reynolds number and Mach number which, of course, apply in any case.

Camber is an important geometric parameter known to affect the aerodynamic properties of wings and, for a sailwing, can be expected to vary with dynamic pressure, the fabric tension, and a characteristic wing dimension such as chord.

The fabric tension of the loaded sailwing will be determined by both the initial (wind-off)cable tension, and the product of the modulus, E, and the thickness, t, of the material. This product is essentially a material spring constant, and is a measure of the elasticity of the wing covering, and therefore, affects the shape the wing assumes under load.

The set of primary parameters,including the generalized aerodynamic force F, from which the similitude parameters will be formed are listed as:

| Symbol | Name | Dimensions |
|---|---|---|
| F | aerodynamic force (lbs) | $MLT^{-2}$ |
| q | dynamic pressure ($lbs/ft^2$) | $ML^{-1}T^{-2}$ |
| Et | elasticity index (spring constant, lb/ft) | $MT^{-2}$ |
| c | chord length (ft) | L |
| $T_o$ | preset trailing edge cable tension (lbs) | $MLT^{-2}$ |
| $\Omega$ | wing deployment rate (rads/sec) | $T^{-1}$ |
| V | free stream velocity (ft/sec) | $LT^{-1}$ |

where M, L, T denote the dimensions of the basic units of mass, length, and time. The wing deployment rate and velocity are included since these variables affect the build-up of the aerodynamic force during deployment.

Now, choosing as our primary variables q, c, and $\Omega$, and following the usual dimensional analysis procedure, as presented in Reference 9, for example, the following dimensionless "pi" ratios are obtained.

$$\pi_F = \frac{F}{qc^2} \quad (= C_F) \tag{1}$$

$$\pi_{T_o} = \frac{T_o}{qc^2} \tag{2}$$

$$\pi_{Et} = \frac{Et}{qc} \tag{3}$$

$$\pi_{\Omega} = \frac{\Omega c}{V} \tag{4}$$

in terms of which the functional dependence of F can be written as:

$$\frac{F}{qc^2} = f\left(\frac{T_o}{qc^2}, \frac{Et}{qc}, \frac{\Omega c}{V}\right) \tag{5}$$

By considering the parameters upon which the frequency, $\omega$, of fabric flutter, or membrane-like, vibration depends, namely fabric areal density $\rho_f$ (slugs/ft$^2$), $T_o$, Et, q, and c, and by choosing as primary variables $\rho_f$, q, c, and following the same procedure, one obtains three additional dimemsionless ratios. One of these is new and is

$$\pi_{\omega} = \omega\sqrt{\frac{\rho_f c}{q}} \tag{6}$$

whereas the other two are merely repeats of (2) and (3) above. Consequently, the functional dependence of the flutter frequency, $\omega$, can be expressed in the form

$$\omega\sqrt{\frac{\rho_f c}{q}} = f\left(\frac{T_o}{qc^2}, \frac{Et}{qc}\right) \tag{7}$$

By equating these ratios for the model and for a vehicle of some scaled-up size, one gets the following, in which the subscripts, v and m, are used to denote vehicle and model values, respectively:

$$\frac{T_{o_v}}{T_{o_m}} = \frac{q_v}{q_m}\left(\frac{c_v}{c_m}\right)^2 \tag{8}$$

$$\frac{(Et)_v}{(Et)_m} = \frac{q_v}{q_m}\left(\frac{c_v}{c_m}\right) \tag{9}$$

$$\frac{\omega_v}{\omega_m} = \sqrt{\frac{c_m}{c_v}\frac{(\rho_f/q)_m}{(\rho_f/q)_v}} \tag{10}$$

$$\frac{\Omega_v}{\Omega_m} = \frac{c_m}{c_v}\frac{V_v}{V_m} \tag{11}$$

The significance of these ratios is as follows. The ratios $\pi_{T_o}$ and $\pi_{Et}$ indicate that the trailing edge cable tension scales directly as the square of the vehicle scale factor $\left(\frac{c_v}{c_m}\right)$, while the elasticity index scales as the first power of the scale factor. The former suggests a source of structural difficulties in very large vehicles. These ratios also indicate that both tensions scale directly with the first power of the dynamic pressure ratio.

The similitude parameter $\pi_\omega$ reveals that the flutter frequency of the sail fabric, in this case, scales directly with the root of the dynamic pressure ratio, and inversely with the roots of the sail fabric density and chord length ratios. Thus, increasing the dynamic pressure will increase the flutter frequency, while increasing fabric density or wing size will decrease it.

The ratio $\pi_\Omega$ is essentially a time-scaling parameter. It states that the angular velocity of wing deployment scales inversely as the scale factor and directly as the velocity ratio. If a vehicle's velocity were measured in vehicle lengths per unit time, it is evident that for equal airspeeds a small vehicle travels c-times "faster" than a

vehicle c-times larger. To travel at an equal "dimensional" speed the larger vehicle would have to travel at c-times greater airspeed than the smaller one.

The impact of these parameters on the application of the data from the five-foot wind-tunnel model of this investigation to the 170-foot DL-4 vehicle application study is reflected in the following summary, obtained by using relations (7) through (10) together with the conditions shown below:

Conditions:

$$q_v = q_m = 60 \text{ psf}$$

$$\frac{c_v}{c_m} = 34$$

$$V_v = V_m$$

$$E_v = E_m \quad \text{(same material)}$$

Whence, to obtain same aerodynamic characteristics of sailwing:

$$T_{o_v} = 1{,}156\, T_{o_m}$$

$$\Omega_v = \frac{1}{34}\, \Omega_m$$

$$t_v = 34\, t_m$$

and, as a consequence,

$$\rho_{f_v} = 34\, \rho_{f_m}$$

so that, as a result $\omega_v = \frac{1}{34}\ \omega_m$. This reduction in the membrane-like vibrational frequency of the scaled-up sailwing should be beneficial as regards fatigue life.

## ABSTRACT

Wind tunnel tests and structural weight analyses were conducted. Sailwing deployment at dynamic pressures up to 60 psf is feasible. The sailwing increased the body alone subsonic lift-to-drag ratio from 2.2 to 7.1, and, for the size tested, reduced vehicle landing speed from 270 knots to 105 knots. For sizes less than about 50 percent of the body planform area the sailwing is lighter than an equivalent rigid wing. Scaling factors are presented for use in applying sailwing test data to full scale configurations.

FAIRCHILD HILLER
REPUBLIC AVIATION DIVISION
FARMINGDALE, LONG ISLAND, NEW YORK